

BAW-1203(Vol. 1)

NUCLEAR MERCHANT SHIP REACTOR PROJECT

Extended Zero Power Tests—NS Savannah Core I. Final Report

January 1961

Atomic Energy Division
Babcock and Wilcox Company
Lynchburg, Virginia

DISCLAIMER

This report was prepared as an account of work sponsored by an agency of the United States Government. Neither the United States Government nor any agency Thereof, nor any of their employees, makes any warranty, express or implied, or assumes any legal liability or responsibility for the accuracy, completeness, or usefulness of any information, apparatus, product, or process disclosed, or represents that its use would not infringe privately owned rights. Reference herein to any specific commercial product, process, or service by trade name, trademark, manufacturer, or otherwise does not necessarily constitute or imply its endorsement, recommendation, or favoring by the United States Government or any agency thereof. The views and opinions of authors expressed herein do not necessarily state or reflect those of the United States Government or any agency thereof.

DISCLAIMER

Portions of this document may be illegible in electronic image products. Images are produced from the best available original document.

LEGAL NOTICE

This report was prepared as an account of Government sponsored work. Neither the United States, nor the Commission, nor any person acting on behalf of the Commission:

A. Makes any warranty or representation, expressed or implied, with respect to the accuracy, completeness, or usefulness of the information contained in this report, or that the use of any information, apparatus, method, or process disclosed in this report may not infringe privately owned rights; or

B. Assumes any liabilities with respect to the use of, or for damages resulting from the use of any information, apparatus, method, or process disclosed in this report.

As used in the above, "person acting on behalf of the Commission" includes any employee or contractor of the Commission, or employee of such contractor, to the extent that such employee or contractor of the Commission, or employee of such contractor prepares, disseminates, or provides access to, any information pursuant to his employment or contract with the Commission, or his employment with such contractor.

This report has been reproduced directly from the best available copy.

Printed in USA. Price \$2.75. Available from the Office of Technical Services, Department of Commerce, Washington 25, D. C.

NUCLEAR MERCHANT SHIP REACTOR PROJECT
EXTENDED ZERO POWER TESTS
NS SAVANNAH CORE I
FINAL REPORT

January 1961

AEC CONTRACT NO. AT(30-1)-2534
B&W CONTRACT NO. 596-3044

SUBMITTED TO THE
UNITED STATES ATOMIC ENERGY COMMISSION
BY
THE BABCOCK & WILCOX COMPANY

THIS PAGE
WAS INTENTIONALLY
LEFT BLANK

CONTRIBUTORS

Edited by A. L. MacKinney

Written by

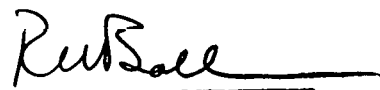
R. M. Ball	R. H. Lewis
C. E. Barksdale	A. L. MacKinney
M. L. Batch	J. H. Mortenson
J. W. Cure	T. G. Pitts
J. P. Farrar	S. W. Spetz
R. N. Kubik	H. J. Worsham

Development Department
Critical Experiment Laboratory
Atomic Energy Division

D. A. Ross
Service Department
Boiler Division

D. E. Crouter
States Marine Lines
Camden, New Jersey

Reviewed by:



R. M. Ball

Approved by:



D. V. P. Williams

THIS PAGE
WAS INTENTIONALLY
LEFT BLANK

CONTENTS

	Page
List of Tables	vi
List of Figures	vii
Abstract	xi
1. INTRODUCTION	1
2. DESCRIPTION OF THE FACILITY	3
3. INSTRUMENTATION TESTS	5
3.1 Description of Instrumentation	5
3.2 Relation of CEL to Ship Instrument Response	8
3.3 Loading Response of Instruments	10
3.4 Rod Withdrawal Response on Instruments	10
3.5 Extrapolation to Shipboard Use	10
4. POWER LEVEL CALIBRATION	15
4.1 Introduction	15
4.2 Experimental Procedures	15
4.3 Results	18
4.4 Discussion of Errors	18
5. FAST NEUTRON FLUX MEASUREMENTS	21
5.1 Introduction	21
5.2 Theory of Experiments	22
5.3 Experimental Procedures	26
5.4 Conclusions	30
6. STUCK ROD TESTS	33
7. NEUTRON FLUX DISTRIBUTION MEASUREMENTS	35
7.1 Neutron Flux Detectors	35
7.2 Wire Scanner	35
7.3 Description of Measurements	37
7.4 Wire Quality Control Program	38
8. SUPPLEMENTARY FLUX DISTRIBUTION MEASUREMENTS	41
8.1 Partial Water Height Traverses	41
8.2 MARTY Can Measurements	41
8.3 Cadmium Fraction Measurements	42
8.4 Cocked Rod Measurements	43
8.5 Flux Gradient Measurements	43
8.6 Reproducibility Check	43

CONTENTS (CONT'D)

	Page
9. FLUX MAP ANALYSIS	45
9.1 Data Reduction Program	45
9.2 Radial Weighting Factor Selection	46
9.3 Power Peaking Analysis	47
10. THREE DIMENSIONAL CALCULATION	51
10.1 Introduction	51
10.2 Westinghouse TKO Program for the IBM 704 Computer	51
10.3 TKO Input Preparation	53
10.4 Comparison of TKO and Experimental Results	54
10.5 Conclusions and Recommendations	55
11. APPENDIX	57
12. TABLES AND FIGURES.	59
13. REFERENCES	179

LIST OF TABLES

Table	Page
I. Instrument Response During Fuel Loading	60
II. Approach to Critical by Rod Withdrawal	61
III. Absolute Flux Measurements	62
IV. Power Calculations	63
V. Ship Instrument Calibration at CEL	64
VI. Estimate of Power Calibration Errors	64
VII. Integral Counts of Nickel Foils	65
VIII. Summary of "Stuck Rod Group" Measurements	66
IX. Borated Plastic Sample Weights	67
X. Flux Map Exposures	68
XI. Rod Positions for Flux Map Exposures	69
XII. Standard Deviation of Color Flag Groups	70
XIII. MARTY Element Measurements	71
XIV. Summary of Cadmium Fraction Measurements	72
XV. Cocked Rod Measurements	73
XVI. Cocked Rod Measurements	74
XVII. Peak Flux and Peak Power Factors	75
XVIII. Atom Concentrations	76
XIX. Disadvantage Factors	76
XX. Experimental and Calculated Flux and Power Peaks	77

LIST OF FIGURES

(All Figures Follow Page 77)

Figure

- 1 Elevation Diagram of SAVANNAH Control Rods and Fuel Elements in Test Facility
- 2 Normal Instrument Location Around Critical Facility
- 3 Photograph of SAVANNAH Core
- 4 Block Diagram of Instrumentation for Zero Power Extension Tests on Core I
- 5 Voltage Plateau for SAVANNAH BF_3 Counter, WL-7087
- 6 Bias Curve With Reactor for SAVANNAH Fission Counter, WL-6376
- 7 Bias Curve With Po-Be Source for SAVANNAH Fission Counter; WL-6376
- 8 Simultaneous Response of Three Ship Detectors
- 9 Location of Instruments in Shield Mockup at CEL - Top View
- 10 Relative Distances of Instruments From Reactor - Side View
- 11 Placement of Detectors Around Core Aboard NS SAVANNAH
- 12 Flux Distribution Vs Distance From Thermal Shield at CEL
- 13 Ship Detector Response Vs Fuel Elements Loaded
- 14 Normalized Inverse Count Rate of Ship BF_3 in CEL Mockup - NS SAVANNAH Core I
- 15 Temperature Effects on Detector Response
- 16 Wire and Foil Location for Power Calibration
- 17 Ni and Au Foil Location in Core for Fast Flux Measurement
- 18 Gold Foil Traverse at Core Centerline From Core Tank to Thermal Shield
- 19 Gold Foil Traverse at Top of Fuel From Core Tank to Thermal Shield
- 20 Spatial Resolution of Wire Scanner
- 21 Block Diagram of Wire Scanner
- 22 Resolution Loss of Wire Scanner With Mn-Cu Wire
- 23 Radial Profile of Axially Averaged Flux
- 24 Radial Profile of Axially Averaged Flux
- 25 Radial Profile of Axially Averaged Flux
- 26 Cadmium Fraction Vs Axial Position
- 27 Cadmium Fraction Vs Axial Position
- 28 Cadmium Fraction Vs Axial Position
- 29 Cadmium Fraction Vs Axial Position
- 30 Cadmium Fraction Vs Axial Position
- 31 Cadmium Fraction Vs Axial Position
- 32 Cadmium Fraction Vs Axial Position
- 33 Cadmium Fraction Vs Axial Position
- 34 Cadmium Fraction Vs Axial Position
- 35 Cadmium Fraction Vs Axial Position
- 36 Cadmium Fraction Vs Axial Position
- 37 Cadmium Fraction Across Can

FIGURES (CONT'D)

Figure

- 38 Fine Structure Through Corner of SAVANNAH Fuel Bundle
- 39 Wire Activities Adjacent to Corner Fuel Pins
- 40 Location Matrix for Pin and Wire Positions
- 41 Radial Profile of Axially Averaged Flux
- 42 Radial Profile of Axially Averaged Flux
- 43 Radial Profile of Axially Averaged Flux
- 44 Radial Profile of Axially Averaged Flux
- 45 Radial Profile of Axially Averaged Flux
- 46 Radial Profile of Axially Averaged Flux
- 47 Radial Profile of Axially Averaged Flux
- 48 Radial Profile of Axially Averaged Flux
- 49 Radial Profile of Axially Averaged Flux
- 50 Radial Profile of Axially Averaged Flux
- 51 Radial Profile of Axially Averaged Flux
- 52 Radial Profile of Axially Averaged Flux
- 53 Radial Profile of Axially Averaged Flux
- 54 Radial Profile of Axially Averaged Flux
- 55 Radial Profile of Axially Averaged Flux
- 56 Radial Profile of Axially Averaged Flux
- 57 Radial Profile of Axially Averaged Flux
- 58 Radial Profile of Axially Averaged Flux
- 59 Radial Profile of Axially Averaged Flux
- 60 Radial Profile of Axially Averaged Flux
- 61 Radial Profile of Axially Averaged Flux
- 62 Radial Profile of Axially Averaged Flux
- 63 Radial Profile of Axially Averaged Flux
- 64 Radial Profile of Axially Averaged Flux
- 65 Can Flux and Power Averages
- 66 Can Flux and Power Averages
- 67 Can Flux and Power Averages
- 68 Can Flux and Power Averages
- 69 Can Flux and Power Averages
- 70 Can Flux and Power Averages
- 71 Can Flux and Power Averages
- 72 Can Flux and Power Averages
- 73 Can Flux and Power Averages
- 74 Can Flux and Power Averages
- 75 Can Flux and Power Averages
- 76 Can Flux and Power Averages
- 77 Can Flux and Power Averages
- 78 Can Flux and Power Averages
- 79 Can Flux and Power Averages
- 80 Can Flux and Power Averages
- 81 Can Flux and Power Averages
- 82 Can Flux and Power Averages
- 83 Can Flux and Power Averages
- 84 Can Flux and Power Averages
- 85 Can Flux and Power Averages
- 86 Can Flux and Power Averages

FIGURES (CONT'D)

Figure

- 87 XY Mesh for TKO Code
- 88 Z Mesh for TKO Code — Run 418
- 89 Z Mesh for TKO Code — Run 420
- 90 Axial Flux Traverse
- 91 Axial Flux Traverse
- 92 Axial Flux Traverse
- 93 Axial Flux Traverse
- 94 Axial Flux Traverse
- 95 Axial Flux Traverse
- 96 Axial Flux Traverse
- 97 Axial Flux Traverse
- 98 Axial Flux Traverse
- 99 Axial Flux Traverse
- 100 Can Flux and Power Averages
- 101 Can Flux and Power Averages

THIS PAGE
WAS INTENTIONALLY
LEFT BLANK

ABSTRACT

Experiments were performed on the NS SAVANNAH Service Core I to supply information on future shipboard operation of the Nuclear Merchant Ship Reactor.

Testing of instrumentation equipment shipped to The Babcock and Wilcox Company from New York Shipbuilding Corporation was satisfactory. Correction factors for shipboard use were determined.

Fast neutron flux, neutron flux distribution, and stuck control rod studies were carried out successfully, as was a three-dimensional calculation (TKO) to match two critical rod patterns.

1. INTRODUCTION

The extended zero power studies on the NS SAVANNAH Service Core I were conducted by The Babcock and Wilcox Company (B&W) at its Critical Experiment Laboratory (CEL). The CEL facilities afforded simpler operation and better access to the core than would have been possible on board ship.

All tests were designed to provide information for the future operation of the Nuclear Merchant Ship Reactor (NMSR) on board ship. The following areas were investigated.

1. Characteristics of instrumentation to be installed aboard the NS SAVANNAH.
2. Manner in which a stuck rod within a rod group affected reactivity and reactor operation.
3. Neutron flux distribution with a variety of control rod patterns.
4. Measurements leading to an estimate of the fast flux at the pressure vessel wall.

THIS PAGE
WAS INTENTIONALLY
LEFT BLANK

2. DESCRIPTION OF THE FACILITY

Bay number one in the CEL has a core tank adapted to accept the SAVANNAH service core internals, lower flow baffle, fuel elements, and control rods with followers attached.

Two sets of control rod drives were used. The first was the cable-drum drives used with the MARTY experiments. These drives position to within 0.01 cm and will operate the SAVANNAH rods, but they do not have adequate snubbing action to handle a rod under scram conditions. The shafts of these drives, therefore, have been securely pinned to prevent scram. A second set of four hydraulically operated rod drives was adapted to handle scrams. Snubbing is done by a hydraulic orifice. These rod drives position to within 0.1 cm.

All rod positions — as in the case of the Zero Power Tests — are measured with reference to the position where the rod rests on the emergency snubber.¹ Rod indicators read zero at this point, so that the bottom of the active poison of the rods is 7.5 cm above the bottom of the active fuel, as shown in Figure 1.

The normal core instrumentation consists of two linear channels, both using Neutronics Model BR ion chambers; two linear safety channels, both using "beanpole"* chambers; a logarithmic channel, reading the current from a Neutronics Model BR chamber; and a fission chamber, Westinghouse Model WL-6376. Figure 2 shows the location of these instruments, and Figure 3 shows the core. Additional details of the facility are given in BAW-1202.¹

Reactor runs reported here are numbered serially. These numbers are carried through this report as positive identifications for each run.

* "Beanpole" is the name of a long ionization chamber, designed and constructed at the CEL.

**THIS PAGE
WAS INTENTIONALLY
LEFT BLANK**

3. INSTRUMENTATION TESTS

Work for this contract included the determination of operational characteristics of instrumentation to be installed aboard ship. The items sent to the CEL from the shipyard were instrumentation cabinet A, instrumentation cabinet D, a BF_3 multiple counter, a fission counter, a compensated ion current chamber, and the associated cables and connectors. This equipment was tested in conjunction with the reactor, and the expected operating conditions aboard ship were determined.

3.1 DESCRIPTION OF INSTRUMENTATION

3.1.1 General

Figure 4 shows the connections between the detectors and their associated amplifiers and indicators. The digital scalers — used for the ship BF_3 and fission counters — were connected at the "amp out" jack of the pulse amplifier-integrator. During measurements with the log microammeters, these scalers were disconnected to eliminate any loading effect. The Keithley micromicroammeter was used for the compensated chamber rather than the ship instrument because it was readable down to 10^{-13} amps, as opposed to 10^{-10} amps for the ship instrument.

3.1.2 Shipboard Instrument Calibration and Installation

The ship cabinets were set up and calibrated in accordance with the instruction manual.² The microammeter in cabinet D and the linear power channel in cabinet A required service to correct defects. A series of electrical disturbance measurements, taken throughout the work at the CEL, indicated that both the BF_3 and the fission counter amplifiers were sensitive to electrical transients caused by switching pumps and other power equipment on and off. Of various methods of shielding tried, the most successful was standard, magnetic, thin-wall house conduit. The power consumption of the two cabinets was 440 w, as measured on a Simpson model 390 wattmeter. The temperature in

the cabinets was taken by a thermometer suspended in air at the mid-plane. After a 17-hour run with the cabinets closed, and an outside ambient of 70° F, cabinet A was at 98° F and cabinet D was at 120° F.

3.1.3 Cable and Gain Measurements

Using in turn the fission counter, the BF₃ counter, and a pulse generator, the attenuation caused by the insertion of 200 ft of tri-axial cable was measured. The amplifier outputs were viewed directly on a Tektronix type 531 oscilloscope.

On the BF₃ amplifier, the peak pulses (caused by neutrons) with 200 ft of cable were 11 v 0.6 μ sec wide. With the 5-ft cable attached to the chamber, the peak pulses were 16 v. The pulser with either length of cable gave a 4-v output pulse for a 1-mv input pulse, indicating a gain of 4000. The normal noise level with or without the cable connected at the amplifier output was 0.5 v peak-to-peak.

On the fission counter amplifier, the peak pulses (caused by neutrons) with 200 ft and also with 5 ft of cable, were 4 v. The pulser with either length of cable gave a 2-v pulse out for a 100-μv pulse in, indicating a gain of 20,000. The normal noise level at the amplifier output was 0.8 v peak-to-peak.

3.1.4 Discriminator Measurements

Section II-5-18, Step 14 of the manual states that the discriminator is to be set at a point where the noise generates about 10 c/sec and then the bias is to be reduced by about 3 v.² Using this information, the minimum pulse level counted from the fission counter is 190 μv and from the BF₃ counter it is 870 μv.

3.1.5 BF₃ Counter, Plateau and Sensitivity Requirements

The ship BF₃, WL-7087, is specified as having a sensitivity of 40 c/sec/nv_{th}. Figure 5 shows the counting rate versus voltage applied to the counter. A neutron source was placed near the counter, and 200 ft of tri-axial cable was used between the counter and the ship amplifier. The voltage was measured with a University model electrostatic voltmeter. The discriminator setting was 21 v, 3 v below the 10 c/sec noise setting. From the plateau, a 2200-v setting was selected as the operating point for all subsequent measurements with this counter.

3.1.6 Fission Counter, Pulse Height Curves, and Sensitivity Measurements

The ship fission counter, WL-6376, is specified to have a sensitivity of $0.4 \text{ c/sec/nv}_{\text{th}}$. However, the sensitivity was found to be a function of the discriminator setting. Several measurements were taken with a constant source (either the reactor source or polonium-beryllium) of count rate versus discriminator setting. Curves shown in Figures 6 and 7 show the loss of sensitivity as a function of discriminator setting. The procedure given in the manual for setting the discriminator will reduce sensitivity of the fission counter more than a factor of 20 compared with the setting found operable at the CEL. In Figure 6, the one volt bias point is 690; in Figure 7, the one-volt bias point is 345. The relationships are linear.

3.1.7 Compensated Ion Chamber, Compensation and Sensitivity Measurements

The ship compensated ion chamber, WL-6377, is specified to have a sensitivity of $4 \times 10^{-14} \text{ amp/nv}_{\text{th}}$. This chamber was placed in the mockup shield water tank and the effect of changing the compensating voltage while the reactor was at power was determined. With the compensating voltage at 0 (measured on an RCA voltohmyst model 98A), the output current from the chamber was $57 \mu\text{amp}$. With the compensating voltage at -5.0 v , the current dropped 32% to $43 \mu\text{amp}$ and remained there as the compensating voltage was changed in 5-v increments to -90.0 v .

In another experiment, the output of the compensated chamber as a function of reactor power was determined. The deviation from linearity is about 10% over the decade from 4 to $40 \mu\text{amp}$, as shown below.

<u>Reactor Power, Arbitrary Units</u>	<u>Chamber Output, μamp</u>
1	4.6
2	8.3
5	22
10	46

3.1.8 Intersensitivity Comparison

The three ship detectors were inserted in wells (the BF_3 in a non-metallic 6-in. -ID pipe, others in metallic 6-in. -ID pipe) in

the mockup shield water tank; and during a reactor run, the outputs were read simultaneously. The BF_3 and the fission chamber were connected to the ship amplifiers and indicators and the compensated chamber with -10.0 v compensation was connected to the Keithley micromicroammeter. As seen in Figure 8, all instruments indicated linearly with reactor power. Although the detectors were at slightly different distances from the reactor, the ratio of BF_3 counts to fission counts should be in about the same ratio as their neutron sensitivity. The fact that the fission counter appears less sensitive by a factor of 20 than expected is attributed to the 3-v bias setting of the discriminator (according to the manual).

3.1.9 Non-Ship Instrumentation

In addition to the ship instruments in the shield water tank mockup, there were fission chambers and ion chambers located around the core in the core tank as shown in Figure 9. One additional BF_3 was placed in the shield water tank and is labeled "Auxiliary BF_3 ".

3.1.10 Instrument Location and Shield Water Tank Description

Figures 9 and 10 show the mockup shield water tank in plan and side views. The wells are 6-in. diameter pipe. The distances are shown in the figure for both the shipboard installation and the CEL mockup. Figure 11 shows the location of various instruments around the core when installed on board ship.

3.2 RELATIONSHIP OF CEL TO SHIP INSTRUMENT RESPONSE

3.2.1 Flux Scans

Flux was measured in the water from the outer wall of the inner thermal shield to determine the attenuation of neutrons as a function of distance from the core. This information is used to establish the relationship between the shipboard and CEL instrument locations. Figure 12 shows that the attenuation in water is approximately exponential with a 6.2 cm relaxation length. The measurements were taken with pure indium foils 0.5 in. diameter, 96 mg/cm², loaded in a lucite holder and placed at the core vertical centerline. The exposure was made at full water height with all of the control rods inserted and

the two sources in place in the core. The strength of the sources on the date of exposure (23 March 1960) was 4.07×10^8 neut/sec. The activity plotted in Figure 12 is the saturated activity of the foils; the flux ($n v_{th}$) is about eight times this value.

3.2.2 Attenuation Factors

The thickness of steel between the outer wall of the inner thermal shield and the BF_3 detector is 25.7 cm on board ship, and 19.4 cm at the CEL. The thickness of water between the outer wall of the inner thermal shield and the BF_3 detector is 33.7 cm on board ship and 57.8 cm at the CEL. The removal cross section of steel for fission neutrons is $\Sigma_r = 0.17 \text{ cm}^{-1}$ using data in ORNL-1843.³ The relationship (cold) between ship and CEL is

$$R \left[\frac{\text{Ship}}{\text{CEL}} \right] = \frac{D^2_{\text{(CEL)}} A_{\text{(Ship)}} e^{-\Sigma_r t_{\text{(Ship)}}}}{D^2_{\text{(Ship)}} A_{\text{(CEL)}} e^{-\Sigma_r t_{\text{(CEL)}}}}$$

where D is the distance from the core center to the instruments in (CEL) or (Ship), $D(\text{CEL}) = 80.3 \text{ cm}$, $D(\text{Ship}) = 67.9 \text{ cm}$,

A is the attenuation factor for water taken from relaxation length of Figure 12 using the thickness of water for (CEL) or (Ship), $A(\text{Ship})/A(\text{CEL}) = 49$,

Σ_r is the removal cross section of steel, 0.17 cm^{-1} , and

t is the thickness (in cm) of steel between the inner thermal shield and the instruments for the (CEL) or (Ship), $t_{\text{(CEL)}} = 19.4$, $t_{\text{(Ship)}} = 25.7$.

R the ratio between ship and CEL readings due to geometry is 23.5.

3.2.3 Differences Due to Source Strength

Startup source decay will reduce the absolute count rate measured on board ship as compared with the CEL measurements. The two polonium-beryllium sources decay with a 138-day half life. The total strength on 18 January 1960, as calibrated by Mound Laboratory was 5.63×10^8 neut/sec or 256.6 curies. According to the plotted decay as shown in BAW-1202, the strength on 1 September 1960 would be 1.8×10^8 neut/sec.¹ Another source of neutrons is the spontaneous fission

of the U-238 in the fuel. Using data from Weinberg and Wigner, this rate is 1.8×10^5 neut/sec.⁴

3.3 LOADING RESPONSE OF INSTRUMENTS

The location of instruments around the core is shown in Figures 2 and 9. Table I shows the indication of the various instruments as fuel was added to the core. More detailed information on the nonship instrumentation loading response is found in BAW-1202.¹ Figure 13 is a plot of the ship detector response as the fuel was loaded, starting on 25 March 1960 with a source strength of 3.9×10^8 n/sec. The level of 2.7 c/sec is considered primarily neutron or instrument background although all sources and fuel were removed from the vicinity of the experiment. Using a corrected indication for the fully loaded core of 1.8 c/sec and the corrections for differences in source strength and attenuation, it was expected that on 1 September 1960 the ship BF₃ (aboard ship) would read higher by a factor of 10.8 or 20 c/sec.

3.4 ROD WITHDRAWAL RESPONSE OF INSTRUMENTS

Continuing the approach to criticality, safety rods were cocked in the fully loaded core, and water was admitted until the core was completely covered. Starting from the fully inserted position of all rods the E group, and then the D group, were withdrawn until the reactor became critical. The instrument location is the same as before and the response is shown in Table II. A normalized plot of the ship detector response is shown in Figure 14, where the inverse count rate is plotted to show the approach to criticality. A similar plot should result during the approach to criticality aboard ship.

3.5 EXTRAPOLATION TO SHIPBOARD USE

3.5.1 Source Power Calibration With All Rods In

A convenient base point for power calibration (identical for the ship and the CEL) is the case with full water, the sources in their normal locations, and all control rods fully inserted. This will provide the first power information available on board ship.

3.5.2 Measurement of Power

During the power calibration run the CEL BF₃ in the shield water tank indicated 250 c/sec, corresponding to a power of 135 ± 28 w. The same BF₃ in the same location indicated 0.42 c/sec (see Table I) when all of the fuel was loaded, the sources located normally, and the rods full in with full water height. Thus, as of 25 March 1960, the source power was 0.23 ± 0.06 w.

3.5.3 Calculation of Power

The neutrons emitted from the source at shutdown are multiplied by an amount dependent on the degree of subcriticality. The subcriticality of the core, as measured by pulse neutron techniques, was -2.9 ± 0.47 . The k_{eff} is 0.98 ± 0.03 .

The multiplication of the core is

$$M = 1/1 - k_{\text{eff}} = 50 \pm 8.$$

Knowing that for every source neutron emitted, 50 fission neutrons are created, the core power may be determined. The yield of 2.47 neutrons per fission indicates that the number of fissions per source neutron, and thus the source power, can be calculated from

$$P = \frac{M S_0}{\nu_0 K_0}$$

where

P = power, w,

M = multiplication, 50,

ν_0 = neutrons per fission, 2.47,

K_0 = fissions/sec/w, 3.12×10^{10} , and

S_0 = source strength in neut/sec.

Using the above information, the calculated source power on 25 March 1960 was 0.25 ± 0.04 w, in good agreement with the measured value.

3.5.4 Anticipated Ship Indications

This information can be used to extrapolate to the anticipated ship indication for a given date. The arbitrary date selected is 1 February 1961; other dates can be used by applying source decay corrections.

3.5.5 Startup Channel at Source Power, Cold

The anticipated source power on 1 February 1961 is 0.048 watts (0.19 of 25 March 1960 value); the anticipated BF_3 reading is 8.9 c/s. Both conditions should exist with full water, source in, and rods fully inserted.

3.5.6 Startup Channel at Source Power, Hot

As water temperature increases, three effects are noted: (1) a change in the leakage of neutrons from the core, (2) a change in the shielding of neutrons by the water between the core and the neutron detectors, and (3) a decrease in k_{eff} resulting from the temperature defect.

The first of these effects may be estimated from the one-group model:

$$k_{\text{eff}} = \frac{k_{\infty}}{1 + M^2 B^2},$$

where the non-leakage probability is $\frac{1}{1 + M^2 B^2}$. The leakage probability, therefore, is $1 - \frac{1}{1 + M^2 B^2}$, or $\frac{M^2 B^2}{1 + M^2 B^2}$. The change in leakage as the core water is heated is attributed to the increase of the migration area. The ratio of leakage hot to leakage cold is then given by

$$R = \frac{\left[\frac{M^2 B^2}{1 + M^2 B^2} \right]_{\text{hot}}}{\left[\frac{M^2 B^2}{1 + M^2 B^2} \right]_{\text{cold}}} = 1.35$$

using migration areas calculated in connection with the Savannah core physics program.

The effect of decreased water shielding may be regarded as an effective decrease in the shielding thickness of hot shield water compared with cold shield water. Within the pressure vessel, between the active core and the shield water tank, 35.1 cm of water is heated to approximately 508° F, changing the water density from 0.998 to 0.793. The change in neutron leakage may be determined from Figure 12, comparing the flux at 35.1 cm to that at $35.1 \times \frac{0.793}{0.998}$. This ratio is 3.47.

Assuming a temperature defect of 3.2% k_{eff} , the effect on source power may be calculated by considering the multiplication:

$$M_{\text{cold}} = \frac{1}{1 - 0.98} = 50$$

$$M_{\text{hot}} = \frac{1}{1 - 0.95} = 20$$

Thus, the hot source power will be reduced by a factor of 0.4.

Combining these effects, the instrument response at critical will be increased by 1.34×3.47 , or 4.65. These effects are shown as a function of temperature in Figure 15. The source power response of the instruments will increase by $1.34 \times 3.47 \times 0.4$, or 1.85. A table of source power response is shown below:

<u>Date</u>	Expected Indication on Startup Channel	
	<u>Cold</u> c/s	<u>Hot</u> c/s
January 1, 1961	10.4	19.2
February 1, 1961	8.9	16.5
March 1, 1961	7.8	14.4
April 1, 1961	6.6	12.2
May 1, 1961	5.7	10.5
June 1, 1961	4.9	9.1
July 1, 1961	4.2	7.8
August 1, 1961	3.6	6.7
September 1, 1961	3.1	5.7
October 1, 1961	2.6	4.8
November 1, 1961	2.4	4.4
December 1, 1961	1.9	3.5
January 1, 1962	1.6	3.0

THIS PAGE
WAS INTENTIONALLY
LEFT BLANK

4. POWER LEVEL CALIBRATION

4.1 INTRODUCTION

This experiment measured the total power generation of a specific clean, cold, critical configuration of the NS SAVANNAH service core, and correlated this power with observed reactor control instrumentation readings. The experimental procedures for the measurement can be analyzed into four distinct steps.

Step 1 was the measuring of the relative neutron flux distribution in the core (both vertically and radially) by scanning the induced activity on Mn-Cu alloy wires. Because of loading symmetry only one-quarter of the core was analyzed.

Step 2 analyzed the fine structure of the neutron flux (as shown by the wire data); this yielded an estimate of the average radial and vertical flux in each fuel can. At this point, the flux numbers are only relative, since no attempt was made to calibrate the Mn-Cu wires to measure absolute neutron flux.

Step 3 was the measurement of the absolute neutron flux in a specific location with calibrated Dy-Al alloy foils, and the conversion of the relative wire data in Step 2 to absolute 2200 meter/sec flux.

Step 4 was the final calculation of fission rate for the core by the activation formula and its conversion to total power.

4.2 EXPERIMENTAL PROCEDURES

4.2.1 Step 1

The core that was calibrated is shown in Figure 16 and the positions of the Mn-Cu wires are indicated. The procedures for loading and counting the wires were identical with those described in Section 7 of this report.

4.2.2 Step 2

To analyze the fine structure of the neutron flux in each can, the flux must be averaged in the vertical direction, and then, in the radial direction. The vertical average is readily obtained by numerically averaging the data points from a vertical scan of almost any Mn-Cu wire, since the vertical flux shape is relatively constant throughout each can. For this reason, a Mn-Cu wire was irradiated in the center of each can and a vertical average count rate computed from the scan data. The absolute flux determinations (as explained in Step 3) were made at a vertical height of 80 cm above the bottom of the fuel. Therefore it was necessary to ratio the average count rate of each center wire to the 80-cm count rate on that wire, so that count rate could be converted to flux. These ratios are given in the fourth column of Table IV.

The radial average is not so readily available. Ideally, a Mn-Cu wire should be irradiated in every water channel in each can, but this was ruled out by the time and effort required. As explained in Section 9.2 an eight-wire pattern was established for estimating the radial averages in each can. When many sets of radial averages were inspected, it was found that the center wire data could be corrected for the radial effects by a single factor dependent only on the rod configuration around each can. These factors were estimated to be as follows: 0.85 for a can surrounded by completely inserted rods; 0.95 for a can surrounded by partially inserted rods; and 1.00 for a can surrounded by completely withdrawn rods (see Table IV).

4.2.3 Step 3

The absolute flux determinations were done with four Dy Al foils irradiated in each of three cans in Run 352 as shown in Figure 16. The foils were vertically located 80 cm above the bottom of the fuel, and were calibrated such that their saturated activities could be converted to absolute 2200 meter/sec neutron flux. The foil data are shown in Table III. An average flux was computed from the four foils and a ratio was found between the flux and the corresponding center wire count rate for the three cans. The flux-to-count rate ratios were averaged and applied to all center wire data, thereby converting all center wire count rates at

80 cm to absolute 2200 meter/sec flux, as shown in Table IV. The average 2200 meter/sec flux for each can was computed by applying the vertical (f_v) and the radial (f_r) correction factors to the 80-cm flux values.

4.2.4 Step 4

To compute the power generated in each can, the total fission rate in each can must be determined. The fission rate may be calculated from the basic activation formula and several correction factors (refinements necessary to calculate total fissions rather than just thermal fissions). The power formula in its refined form is as follows.

$$\text{power} = \frac{\text{fiss/sec}}{3.1 \times 10^{10} \text{ fiss/sec/watt}} \times \text{correction factors or,}$$

$$\text{watts} = \frac{N_{25} (\sigma_f)_{2200} \bar{\phi}_{2200}}{3.1 \times 10^{10}} \times \text{VFRE,}$$

where N_{25} = number of U-235 atoms per can,

= 24.6×10^{24} atoms per can (for cans with 4.2% enrichment),

= 27.0×10^{24} atoms per can (for cans with 4.6% enrichment);

$(\sigma_f)_{2200}$ = fission cross section for U-235 at 2200 meters/sec,

= 579 barns;

$\bar{\phi}_{2200}$ = averaged 2200 meter/sec neutron flux for entire can;

V = non $1/v$ correction to the U-235 thermal cross section,

= 0.98;

F = $\frac{\bar{\phi}_{\text{fuel}}}{\bar{\phi}_{\text{water}}}$ (This correction is needed since the flux values were obtained in water channels and not in the fuel; the factor was calculated from MARTY critical experiment data.)

= 0.696 for 4.2% enrichment,

= 0.678 for 4.6% enrichment;

$$R = \frac{\text{total U-235 fissions}}{\text{sub-cadmium U-235 fissions}}$$

$$= 1.18 \text{ (This correction is to account for non-thermal fissions in U-235; data is given in 8.2.2.)}$$

$$E = \frac{\text{U-235 fissions} + \text{U-238 fissions}}{\text{U-235 fissions}} = 1.05$$

(This correction accounts for the U-238 fast fissions determined in MARTY Critical Experiments.)

Thus by inserting the values for all factors into the power formula, two constants are generated.

1. For cans with 4.2% enrichment, power = $3.88 \times 10^{-7} \times \phi_{2200}$ watts.

2. For cans with 4.6% enrichment, power = $4.15 \times 10^{-7} \times \bar{\phi}_{2200}$ watts.

The power for each can as calculated by the above formula is shown in Table IV.

4.3 RESULTS

The ship BF₃ counter and the ship fission chamber, located as shown in Figures 9 and 10, were observed during the power calibration run. Table V lists the resulting correlation between reactor power and count rate for each detector.

Although the instrument-power calibration was measured for only one rod configuration, it should be approximately valid for most standard rod patterns. The calibration is limited, however, since it was calculated from data taken at room temperature and thus will not apply to determinations at operating power and pressure. It may be used only for the critical experiment and initial startup power determinations.

4.4 DISCUSSION OF ERRORS

Since the power formula is made up of only multiplying factors, the best estimate of the total percentage error is the square root of the sum of the squares of each individual percentage error. A tabulation of the estimated errors shows that the error in ϕ_{2200} dominates all others. This large error is due to the uncertainty in correction factors used to average the radial flux. The available fine structure data indicate that

the outer row of pins in each can are the ones most affected by rod positions, but there were not many data taken in these regions that could be used for the radial correction factors. The error in the absolute flux calibration by the Dy-Al alloy foils is also included in $\bar{\phi}_{2200}$ and is estimated to be $\pm 5\%$. Table VI lists the estimated errors for each factor of the power formula and the calculated total error for the power calibration is $\pm 21\%$.

THIS PAGE
WAS INTENTIONALLY
LEFT BLANK

5. FAST NEUTRON FLUX MEASUREMENTS

5.1 INTRODUCTION

Several A212 carbon steel samples will be irradiated in a test well (see Fig. 17) just outside the SAVANNAH core. These samples will be used for radiation damage effect studies that can be correlated with the expected pressure vessel life. Since the test samples can be removed only during a complete reactor shutdown, it is expected that they will be irradiated for about two years. The long range irradiation time, coupled with the fact that the test well is inaccessible once full-power operation is reached, makes the flux monitoring extremely difficult.

Usually, the experimental program for a radiation effects study includes many irradiations of monitor foils in the test facility to measure the 2200 meter/sec flux, the 1/E flux, and the fast neutron flux above 1 Mev. These measurements require cadmium ratios, threshold detectors, and variable power levels to accommodate the wide range of activation characteristics of the monitors. Most of the neutron spectrum measurements are made at the beginning of the experiment, and several monitors are then left with the test samples for the duration of the experiment to obtain the time-integrated neutron flux. If necessary, the integrating monitors are replaced during experiments that continue for many months. All of these operations are possible in most research or test reactors, but they are virtually impossible in the SAVANNAH core. Thus the following experiments were devised during the zero power tests to provide a limited number of fast neutron measurements that will help fill the obvious gap of the flux data required for adequate interpretation of the steel test samples in the SAVANNAH program.

The first experiment was the correlation of a threshold-type reaction (which is primarily sensitive to fast neutrons) with a long-lived thermal neutron reaction product that would be a good integrator for the power-time history of the long time irradiation for the steel test samples.

This experiment was considered necessary for two reasons. First, no flux monitors are to be used with the steel test samples. Second, none of the threshold reactions that are currently being used in fast neutron damage effect studies result in nuclides with half-lives that are long enough to integrate properly a 2-year, or longer, irradiation. The Ni-58(n,p)Co-58 reaction was chosen for the threshold measurements, primarily because of its current popularity in fast neutron damage studies in steels. The resulting nuclide, Co-58, has a half-life of 71 days. The Co-59(n, γ)Co-60 reaction was chosen for the thermal neutron reaction inasmuch as the natural Co-59 impurities (measured by ORNL to be 103 ppm in A212 carbon steel) in the test samples would allow the samples to be their own monitors.³ The Co-60 half-life, 5.24 years, thus fulfills the long-lived requirements.

The second experiment was the measurement of the attenuation of the fast neutron flux (as measured by the Ni-58 reaction) at the pressure vessel wall from the test sample location. In addition, a complete mapping of the thermal and epithermal neutron flux in this region was made with bare and cadmium-covered gold foils.

5.2 THEORY OF EXPERIMENTS

5.2.1 Correlation of Ni-58 Reaction With Co-59 Reaction

It is assumed that the damage effects observed in the steel test samples will be proportional to the total number of interactions of neutrons above some energy with the samples. At present, the exact relationship between damage effects and the type of fast neutron spectra is not fully understood. However, widespread research is being conducted at many laboratories in an attempt to correlate damage effects in steels with fast neutron spectra as measured by several types of threshold and fast-fission detectors. As indicated above, one popular reaction under study is the Ni-58(n,p)Co-58 reaction. If the total number of Co-58 atoms formed in a nickel foil could be determined — assuming the foil had been irradiated along side the steel test samples — then some correlation of the SAVANNAH steel test samples could be made with data from other laboratories. Unfortunately, even if a nickel foil were to be irradiated with the SAVANNAH steel test samples, the relatively short

71-day half-life for Co-58 would make it essentially impossible to calculate the total number of Co-58 atoms formed in the foil during a 2-yr irradiation.

The Co-59(n, γ)Co-60 reaction that occurs in the natural cobalt impurities in the steel test samples will allow a moderately accurate determination of the total number of Co-60 atoms formed in the samples during a 2-yr irradiation, provided that the power versus time history is known and that the absolute disintegration rate of the Co-60 can be measured.

Although the number of Co-60 atoms formed is proportional to the thermal neutron absorptions primarily, and, although the thermal neutrons are not the neutrons causing damage interactions in the steel samples, it is assumed that the ratio of the thermal neutron flux to the damaging fast neutron flux will remain constant throughout the irradiation. This assumption may be in error; however, for a first approximation, it allows the only practical approach to the problem.

It can be shown that the ratio of specific activity of Co-60 to the specific activity of Co-58, in a pair of cobalt and nickel foils simultaneously irradiated for a few minutes in the steel test sample location at low power, is the ratio of the total number of Co-60 atoms formed in the cobalt foil to the total number of Co-58 atoms formed in the nickel foil. For example, the activation formula can be written as follows:

$$\lambda N = W A \sigma \phi (1 - e^{-\lambda t_{\text{exp}}}),$$

- where λN = disintegrations per second of nuclide formed
 W = weight in grams per atomic weight of isotope being irradiated
 A = Avagadro's number
 σ = cross section for the reaction involved
 ϕ = neutron flux causing the reaction in neutrons/cm²/sec
 t_{exp} = irradiation time in same units as λ is expressed
 λ = decay constant for nuclide being formed, and is in units of reciprocal seconds when multiplying N , and is in same reciprocal time units as t_{exp} in the exponential.
 N = number of atoms of nuclide formed at the end of the irradiation

For the cobalt foil then,

$$\lambda_{\text{Co}^{60}} N_{\text{Co}^{60}} / \text{gram} = \frac{1}{59} A \sigma_{\text{th}} \phi_{\text{th}} (1 - e^{-\lambda_{\text{Co}^{60}} t_{\text{exp}}}),$$

and when the exposure time is very small compared to the half-life,

$$\lambda_{\text{Co}^{60}} N_{\text{Co}^{60}} / \text{gram} = \frac{1}{59} A \sigma_{\text{th}} \phi_{\text{th}} \lambda_{\text{Co}^{60}} t_{\text{exp}}.$$

Likewise, for the nickel foil,

$$\lambda_{\text{Co}^{58}} N_{\text{Co}^{58}} / \text{gram} = \frac{1}{58} A \int_{E_{\text{eff}}}^{\infty} \sigma(E) \phi(E) dE \cdot \lambda_{\text{Co}^{58}} t_{\text{exp}},$$

where $\int_{E_{\text{eff}}}^{\infty} \sigma(E) \phi(E) dE$ is the complicated relationship of cross section and fast neutron spectrum for the reaction.

Thus the ratio of the specific activities is

$$\frac{\lambda_{\text{Co}^{60}} N_{\text{Co}^{60}}}{\lambda_{\text{Co}^{58}} N_{\text{Co}^{58}}} = \frac{58}{59} \cdot \frac{\sigma_{\text{th}} \phi_{\text{th}}}{\int_{E_{\text{eff}}}^{\infty} \sigma(E) \phi(E) dE} \cdot \frac{\lambda_{\text{Co}^{60}} t_{\text{exp}}}{\lambda_{\text{Co}^{58}} t_{\text{exp}}}.$$

Simplifying,

$$\frac{N_{\text{Co}^{60}}}{N_{\text{Co}^{58}}} = 0.983 \left[\frac{\sigma_{\text{th}} \phi_{\text{th}}}{\int_{E_{\text{eff}}}^{\infty} \sigma(E) \phi(E) dE} \right].$$

In the Co-60 activation, no consideration was given to the epithermal or resonance neutron activation. It is estimated that this error is less than 10% so, in lieu of the other assumptions used in this treatment, it has been neglected. Also, it is realized that the use of an E_{eff} in the threshold reaction may be somewhat fictitious; it is assumed that at some fast neutron energy, namely E_{eff} , the cross section for the reaction becomes significant.

We assume that to good approximation the ratio of the thermal flux to the fast neutron flux remains constant at all power levels, operating temperatures, and time, so that the ratio

$$\frac{N_{\text{Co}^{60}}}{N_{\text{Co}^{58}}} = \text{constant}$$

for any given irradiation time. Thus, that constant can be measured by observing the ratio of the specific activities of a cobalt and nickel foil that were exposed at low power for a short duration. $N_{Co^{60}}$ can be determined from the Co-60 activity in steel test samples following the 2-yr irradiation, by considering the saturation factors and the power-time history, and $N_{Co^{58}}$ can be estimated from the above relationship. This gives an estimate of the total number of Co-58 atoms that would have been formed if a nickel monitor foil had been present. This information along with the observed damage effects in the steel samples can then be correlated.

5.2.2 Fast Neutron Flux Attenuation

It is also desired to know the ratio of the fast neutron flux at the steel sample test location and at the pressure vessel wall. Two problems occur in this measurement. The first is that the fast neutron flux level was too low in the zero power tests to measure the Ni-58(n,p) Co-58 reaction at the pressure vessel wall. The second is that a correction must be made for any room temperature measurements in extrapolating to operating temperature of the SAVANNAH core.

In order to estimate the fast neutron flux at the pressure vessel wall, a partial traverse of the water gap between the test well and the pressure vessel wall was made with nickel foils. Simultaneously, a complete map of the entire gap was made with both bare and cadmium-covered gold foils. Based on previous data obtained in bulk shielding experiments, it is reasonable to assume that the slope of the fast flux will be essentially that of the thermal flux in the water gap. The partial nickel traverse was thus extrapolated on this basis to the pressure vessel wall.

Since the water density decreases as the temperature increases, the ratio of the nickel activities between the test sample location and the pressure vessel wall will decrease at operating temperature from that value observed at room temperature. The density of water decreases from 0.997 gm/cm³ at room temperature to 0.765 gm/cm³ at 512°F. This change effectively moves the pressure vessel wall closer to the test well, so that

$$\begin{aligned} \text{effective distance} &= \text{actual distance} \times \frac{0.765}{0.997} \\ &= \text{actual distance} \times 0.767 \end{aligned}$$

5.3 EXPERIMENTAL PROCEDURES

5.3.1 Irradiation Conditions

Figure 17 shows the location of the nickel foils, bare and cadmium-covered gold foils, and the cobalt foils that were irradiated simultaneously for this experiment. The exposure time was 660 sec, and the integrated power was estimated to be 10.8 kilowatt-hours.

The gold foils were calibrated so that their saturated activities could be converted directly to absolute thermal neutron flux, based on an intercomparison with the standard neutron flux at the National Bureau of Standards, Washington, D. C.

The nickel foils were counted 13 days following the irradiation, and this decay time was considered in the calculation of their absolute disintegration rates. The 13-day decay time was neglected in the calculation of the Co-60 disintegration rate. Counting times on these foils ranged from one to thirty minutes, and all data were reported in net counts per minute.

5.3.2 Step 1

Following activation, the nickel foils (approximately 1 in. x 1 in. x 0.020 in. and 99+% pure) were counted on a gamma-ray single-channel spectrometer similar to that of R. L. Heath.^{5,6} The detector was a right-circular cylinder of NaI(Tl), 1-3/4 in. diameter by 2 in. high, located inside a 2-in.-thick lead shield which was 16 inches wide, 16 inches deep and 24 inches high. Some of the factors for calculating the absolute disintegration rate must be estimated since the detector was not exactly the same size as that given in the references.^{5,6} Inspection of the gamma-ray spectra from the nickel samples several days after activation indicated that the activity contribution from impurities was negligible, and that the foil activities were quite small. Thus, to enhance the counting statistics, the integral count rate of each foil was determined rather than obtaining a complete spectrum analysis. The count rates of the nickel foils are given in Table VII.

In order to calculate the absolute disintegration rate of the nickel foils, a complete spectrum analysis was performed on nickel foil No. 8 which had been activated near the center of the core to a much higher nvt than the foils near the test sample location. Using Heath's formula

$$N_o = \frac{N_p}{\epsilon_t P A e^{-\lambda t_w}} = \frac{2.129 N_m a}{\epsilon_t w P A e^{-\lambda t_w}}$$

where

- N_o = the number of gamma-rays per minute emitted by the foil at end of irradiation;
- N_p = the area under the photo peak in counts per minute
 $= \frac{2.129 N_m a}{w}$;
- A = the correction factor for absorption in the source and any beta absorber used,
 $= 1.0$;
- N_m = the peak counting rate in counts per minute,
 $= 92$ counts per minute;
- a = the half width at one-half maximum of the photo peak in pulse height units (PHU),
 $= 20.0$ PHU;
- w = measured width of the "window" of the single-channel analyzer,
 $= 9.0$ PHU;
- P = the peak to total ratio,
 $= 0.317$ (based on an extrapolation of Heath's data on a volume basis for the size of the NaI crystal);
- ϵ_t = the total absolute detection efficiency for the source-detector geometry used,
 $= 0.0180$ (based on an extrapolation of Heath's data on a volume basis for the size of the NaI crystal); and
- $e^{-\lambda t_w}$ = decay factor, where t_w is the elapsed time of 13 days between counting of the foil and end of exposure, and λ is the decay constant for Co-58,
 $= 0.881$.

The activity of nickel foil No. 8 is

$$N_o = \frac{2.129 \times 92 \times 20}{0.0180 \times 9.0 \times 0.317 \times 1.0 \times 0.881}$$

$$= 8.65 \times 10^4 \text{ disintegrations per minute.}$$

The absolute disintegration rate of nickel foil No. 6 (irradiated in the test well for the steel samples) can now be computed by comparing the integral count rate with that for nickel foil No. 8.

Thus,

$$(N_o)_{Ni\ 6} = 8.65 \times 10^4 \times \frac{399}{20,765}$$

$$= 1.67 \times 10^3 \text{ disintegrations per minute.}$$

Since foil No. 6 weighs 2.58 gm, its specific activity is

$$(N_o)_{Ni\ 6} = 6.45 \times 10^2 \text{ disintegrations per minute of Co-58 per gram of nickel.}$$

5.3.3 Step 2

The 2200 m/sec flux measured at the steel sample test well with bare and cadmium-covered gold foils was 5.9×10^8 neut/cm²/sec at the power level of this experiment. The low neutron flux level prohibited direct cobalt activity measurement due to the Co-59 impurity in the A212 carbon steel samples. To determine the total cobalt activity in this location, a pure cobalt foil (1 in. x 0.5 in. x 0.020 in.) was irradiated, and its disintegration rate was determined by comparing the count rate with that of a calibrated Co-60 standard.

Thus,

$$(\text{Dis/min})_{Co\ \text{foil}} = \frac{(\text{count rate})_{Co\ \text{foil}}}{(\text{count rate})_{Co\ \text{Std}}} \times (\text{dis/min})_{Co\ \text{Std}}$$

$$= \frac{1,163}{57,548} \times 1.56 \times 10^6 \text{ dis/min}$$

$$= 3.15 \times 10^4 \text{ dis/min,}$$

and dividing by the weight of the foil (0.9566 grams)

$$(\text{Specific Activity})_{Co\ \text{foil}} = \frac{3.15 \times 10^4}{0.9566}$$

$$= 3.30 \times 10^4 \text{ dis/min of Co-60 per gram cobalt.}$$

As a check for the absolute disintegration rate of the cobalt foil, one may use the activation formula and calculate the neutron flux to which the foil had been exposed. Using 34 barns for the cross section, an

exposure time of 660 seconds and a half-life of 5.24 years for Co-60, the thermal flux is computed to be 5.7×10^8 neut/cm²/sec. This is in good agreement with the 5.9×10^8 measured by the calibrated gold foils.

Assuming that the Co-59 impurity in the A212 carbon steel samples will be 103 ppm \pm 10% (by weight), the calculated cobalt specific activity in the test samples (had they actually been exposed in this experiment) would be

$$(N_o)_{Co^{60}} = 3.4 \text{ dis/min of Co-60 per gram of A212 carbon steel.}$$

Combining this result with the specific activity of nickel foil #6, as computed in 5.3.2, the following ratio is obtained:

$$\frac{\text{No. of atoms of Co-60 per gram steel}}{\text{No. of atoms of Co-58 per gram nickel}} = \frac{3.4}{6.45 \times 10^2} = 5.27 \times 10^{-3}$$

One correction for this ratio is necessary. The cross section of Co-59 is essentially reduced at the operating temperatures due to the spectrum shift of the thermal neutrons. If the cross section is reduced, then the specific activity of the Co-60 is likewise reduced. The correction is estimated as follows:

Let

σ_1 = cross section of Co-59 at room temperature

σ_2 = cross section of Co-59 at operating temperature

T_1 = room temperature = 293 K

T_2 = operating temperature = 538 K,

then

$$\frac{\sigma_2}{\sigma_1} \approx \sqrt{\frac{T_1}{T_2}} \approx \sqrt{\frac{293}{538}} \approx \sqrt{0.544} \approx 0.740$$

$$\begin{aligned} \frac{\text{No. of atoms of Co-60 per gram steel}}{\text{No. of atoms of Co-58 per gram nickel}} &= 5.27 \times 10^{-3} \times 0.740 \\ &\text{at } 508^\circ\text{F} \\ &= 3.9 \times 10^{-3} \end{aligned}$$

5.3.4 Step 3

Ideally, the fast neutron flux should be measured at the test sample location and at the pressure vessel wall. However, the fast neutron flux was not high enough to activate a nickel foil at the pressure vessel wall, but it was high enough to obtain a partial traverse in the water gap. This was done with five nickel foils equally spaced

3 cm apart. (See Fig. 17.) The count rates of these foils are shown in Table VII, and their normalized activities are shown in Figure 18. To obtain a complete flux picture, bare and cadmium-covered foils were irradiated on lucite strips (Fig. 17) that traversed the entire distance between the test well and the pressure vessel wall. The gold foil activities are also plotted in Figure 18, and the slope of the nickel data appears to agree with the slope of the bare gold data. Assuming that the nickel activations do follow the slope of the bare gold data, the nickel activity at the pressure vessel wall can be estimated. This estimate, when compared with the nickel activity at the test well, yields an attenuation of approximately 100. However, this factor must be corrected for the change in moderator density that occurs at NS SAVANNAH operating temperatures. Since water density decreases as temperature increases, the ratio of the nickel activities between the test sample location and the pressure vessel wall will be decreased from that observed at room temperatures. The density of the water decreases from 0.997 gm/cm³ at room temperature to 0.765 gm/cm³ at 512°F. This change in density effectively moves the pressure vessel wall closer to the test well, so that

$$\begin{aligned}
 \text{effective distance} &= \text{actual distance} \times \frac{0.765}{0.997} \\
 &= 32.4 \text{ cm} \times 0.767 \\
 &= 24.8 \text{ cm.}
 \end{aligned}$$

Referring to the extrapolated nickel curve (Fig. 18), the ratio of the activity at the test well to activity at 24.8 cm is 34.

Some of the A212 carbon steel samples will be placed at the top of the fuel in the test well, in addition to those placed at the reactor fuel centerline. Thus the moderator gap was traversed at this level with bare gold foils, in the same manner as described above. The slope of this traverse (Fig. 19) is approximately the same as the bare gold curve in Figure 18. The attenuation factor for the fast neutron flux is expected to be similar to that measured at the reactor fuel center line.

5.4 CONCLUSIONS

Combining the data in Steps 1, 2, and 3, the following general relationships can be formulated for the test well location.

1. The thermal nvt (neglecting episcadmium contribution) can be calculated from the Co-60 disintegration rate observed in the steel test samples, by using the activation formula and the power-time history of the irradiation.

2. The number of atoms of Co-58 that would have been formed in a nickel foil placed along side the test samples can be obtained from

$$(\text{No. of atoms of Co-58 per gm nickel})_{\text{at } 500^\circ\text{F}} = \frac{(\text{No. of atoms of Co-60 per gm steel})}{3.9 \times 10^{-3}}$$

assuming that the number of atoms of Co-60 formed can be calculated from the Co-60 disintegration rate observed in the steel samples.

3. The ratio of the fast flux at the test well to the fast flux at the pressure vessel wall (as measured by the Ni-58(n,p)Co-58 reaction) can be obtained by

$$\left(\frac{\text{Co-58 activity at test well}}{\text{Co-58 activity at pressure vessel wall}} \right)_{\text{at } 512^\circ\text{F}} = 34$$

For example, assume the following radiation history:

$$T_{\text{exp}} = 2 \text{ yr} = 6.3 \times 10^7 \text{ sec}$$

$$\text{Power Level} = \text{constant} = 69 \text{ MW}$$

$$\text{Weight of A212-Steel Sample} = 1 \text{ gram}$$

$$\text{Co-60 Disintegration Rate} = 4.25 \times 10^6 \text{ dis/sec per gram steel. (at end of irradiation)}$$

Then,

(1) The thermal nvt may be estimated by

$$A_{\text{Co}60} = \text{dis/sec} = \frac{103 \times 10^{-6}}{59} \times 6.02 \times 10^{23} \times \bar{\phi}_{\text{th}} \times 25.2 \times 10^{-24} \times (1 - e^{-\lambda t})_{\text{exp}}$$

$$\text{or } 4.25 \times 10^6 = \frac{103}{59} \times 10^{-6} \times 6.02 \times 10^{23} \times \bar{\phi}_{\text{th}} \times 25.2 \times 10^{-24} \times 0.2325.$$

Solving for the average ϕ_{thermal} ,

$$\bar{\phi}_{\text{th}} = 6.9 \times 10^{11} \text{ neut/cm}^2/\text{sec},$$

and the total integrated thermal nvt,

$$(\text{nvt})_{\text{th}} = 6.9 \times 10^{11} \times 6.3 \times 10^7 = 4.3 \times 10^{19} \text{ neut/cm}^2.$$

* Note that the σ_{th} for Co-59 has been reduced from 34 barns to 25.2 barns to account for the energy shift in the thermal neutron distribution at the operating temperatures of 508 °F.

(2) The total number of Co-60 atoms formed during irradiation may be found as follows.

$$\begin{aligned}
 N_{\text{Co}^{60}} &= N_{\text{Co}^{59}} \cdot \sigma_{\text{th}} \cdot (\text{nvt})_{\text{th}} \\
 &= \frac{103 \times 10^{-6}}{59} \times 6.02 \times 10^{23} \times 25.2 \times 10^{-24}^* \times 4.3 \times 10^{19} \\
 &= 1.14 \times 10^{15} \text{ atoms Co-60 per gram steel.}
 \end{aligned}$$

(3) The total number of Co-58 atoms that would have been formed during the irradiation in the test well if a nickel monitor had been used would be

$$\begin{aligned}
 \left[N_{\text{Co}^{58}} \right]_{512^\circ\text{F}} &= \frac{N_{\text{Co}^{60}}}{3.9 \times 10^{-3}} \\
 \left[N_{\text{Co}^{58}} \right]_{512^\circ\text{F}} &= \frac{1.14 \times 10^{15}}{3.9 \times 10^{-3}} \\
 \left[N_{\text{Co}^{58}} \right]_{512^\circ\text{F}} &= 2.93 \times 10^{17} \text{ atoms of Co-58 per gram nickel.}
 \end{aligned}$$

The observed damage effects in the A212 carbon steel samples can now be correlated to the total number of fast neutron interactions that would have been suffered by the Ni-58(n,p)Co-58 reaction.

(4) The total number of Co-58 atoms that would have been formed during the irradiation at the pressure vessel wall, if a nickel monitor had been used, would be

$$\begin{aligned}
 \left[N_{\text{Co}^{58}} \right]_{\text{P.V. Wall}} &= \frac{\left[N_{\text{Co}^{58}} \right]_{\text{Test Well}}}{34} \\
 &= \frac{2.93 \times 10^{17}}{34} = 8.60 \times 10^{15} \text{ atoms of Co-58} \\
 &\quad \text{per gram nickel.}
 \end{aligned}$$

Obviously, this is an indirect method for obtaining neutron flux data for correlation with the steel damage effects; however, in the case of the SAVANNAH samples, it appears to be the only feasible method for obtaining neutron flux information.

* Note that the σ_{th} for Co-59 has been reduced from 34 barns to 25.2 barns to account for the energy shift in the thermal neutron distribution at the operating temperatures of 508°F.

6. STUCK ROD TESTS

Each rod group was withdrawn from a pattern of fully inserted rods to determine if the reactor would remain subcritical in case of control rod drive malfunction. It was established that the reactor was subcritical if either the X, C, D, or E group is independently withdrawn. The reactor becomes critical as the third rod of the A group is withdrawn and as the fourth rod of the B group is withdrawn. Measurements were done at room temperature, 15.8° C, the point of maximum reactivity. Results are shown in Table VIII.

**THIS PAGE
WAS INTENTIONALLY
LEFT BLANK**

7. NEUTRON FLUX DISTRIBUTION MEASUREMENTS

7.1 NEUTRON FLUX DETECTORS

The detectors used for determining flux distributions were 0.020-in. - diameter wires of a manganese copper alloy. Two alloys were used, a nominal 20 w/o Mn-80 w/o Cu, and a nominal 80 w/o Mn-20 w/o Cu. The deviation from nominal composition is discussed elsewhere in this report.

The wires were inserted into two different sizes of acrylic plastic tubes depending upon the proposed location of the wire in the core. The smaller tubes were 3/16-in. OD and 1/16-in. ID; the larger tubes were 5/16-in. OD and 3/16-in. ID. Both were approximately 6 ft long.

The "wired" plastic tubes were inserted into selected positions in the core in spaces within the ferrules. The smaller plastic tubes were used at positions near the corners of fuel bundles.

The wires were drawn taut within the plastic tubes but some horizontal displacement was still possible. The maximum displacement was equivalent to the tolerance of the wire within the tube plus the tolerance of the tube within the ferrule, for a total maximum displacement of 0.135 in. from centerline.

Several experiments were performed to determine the maximum possible activation error for maximum displacement in a position of maximum flux gradient. (See Section 8.5.) The results indicate a maximum possible error of $\pm 6\%$ for a given point, but the maximum possible error for the integrated activity over the full length of a wire should be considerably less since a loose wire has a tendency to spiral in a tube and thus average out errors.

7.2 WIRE SCANNER

The activity at increments along the length of the wire was determined by an automatic scanning device similar to that described

for fuel pins by Mortenson and Ball.⁷

The irradiated wires were removed from the plastic tubes and positioned under tension on an aluminum bed. A friction-drive mechanism moved the bed under a lead shield containing a collimating hole and a beta-sensitive scintillation detector. At a predetermined position, the bed was arrested by a mechanical stop, and the activity of the wire under the collimating hole was counted for a time interval. At the conclusion of the time interval the bed was advanced to the next mechanical stop and the cycle was repeated.

The mechanical stops were positioned within ± 0.05 cm. The position of the wire under the collimator was rigidly controlled by forcing the wire through a groove in a teflon block, allowing about 0.02 cm tolerance. The distance between the wire and the anthracene scintillation crystal (depth of the 2.54-cm ID collimating hole) was approximately 5.0 cm. Figure 20 shows the resolution of the collimating hole.

Figure 21 shows a block diagram of the instrumentation, which is divided into two identical channels, the master channel and the slave channel. The master channel monitors one small section of an irradiated wire during a counting session, and the activity of this wire is displayed on the master scaler. The counting interval of both counting channels is determined by the time necessary for the master scaler to accumulate a preset count. As the activity of the master wire decreases, the counting intervals increase proportionately, thus correcting all data accumulated in the slave channel for radioactive decay. Data from the slave channel was recorded on paper tape by a Berkeley digital printer and simultaneously punched into IBM cards by an IBM serial card punch.

The uncertainty of an individual count, due to the statistical nature of the radioactive decay process, is a function of the total number of counts accumulated on both scalers. From Mortenson and Ball, the standard deviation of an individual count is

$$\sigma = \pm \sqrt{N_s + \frac{N_s^2}{N_m^2} N_m}$$

where N_s and N_m are the total number of counts accumulated on the slave and master scalers, respectively.² For all wire mapping data reported here, N_m was preset to 10,000 counts; therefore, the standard deviation, due to counting statistics, for any single activity measurement reported in Volumes I, II, and III of this report may be determined from the relation

$$\sigma = \pm \sqrt{10,000 N_s + N_s^2/100}.$$

Several experiments were performed to determine the dead time resolution losses of the entire scanner system (see Fig. 22). Although resolution losses at count rates above 20,000 c/sec are indicated, in practice count rates were never allowed to exceed 10,000 c/sec. Deviation of the decay curves from the straight line at the extreme right is due to the contribution of the longer half life copper isotope. The decay curve represents the decay from 8 to 31 hr after reactor shutdown. In practice all wires are counted within 8 hr after shutdown.

7.3 DESCRIPTION OF MEASUREMENTS

Each flux experiment was performed in a similar manner. The first activation was performed by exposing the wires to a steady neutron flux for ten minutes; each subsequent activation was accomplished by exposing the wires to an exponentially rising flux.

Tables X and XI list the reactor conditions for each flux measuring run, including control rod settings, boron plastic inventory, peak instrument readings, and doubling time when ascending to peak power. In addition to normal reactor instrumentation, some of the runs used a Neutronics Model BR ion chamber in the shield tank mockup. These readings, where available, are also shown in Table X.

7.3.1 Wire Identification

For the purposes of wire position identification, a standard nomenclature was adopted. Each wire is assigned a series of three numbers which completely define its position. The first number identifies the can in which it is located; the second number identifies the x position in the can, and the third number identifies the y position within the can. Figure 40 shows the location matrix.

7.3.2 Borated Polyethylene

Many of the rod patterns required the addition of borated polyethylene rods to attain full water height. These rods consisted of 25% by weight of natural enrichment boron carbide and 75% by weight polyethylene. The rods are $0.250^{+0.002}_{-0.010}$ in. in diameter, $6 \text{ ft} \pm 1/2 \text{ in.}$ long. To test their uniformity, 34 samples were cut at random from a few of the poison rods. These samples were 10 cm long, and their weights are shown in Table IX. Note that, since the density of the boron carbide is approximately 2.5 times the density of normal polyethylene, slight variations in uniformity will show up as differences in density of the mixture. Table IX therefore, gives an indication of both dimensional and composition uniformity.

7.4 WIRE QUALITY CONTROL

An extensive program of wire calibration was undertaken to investigate uniformity of the wire as received from the vendor. Wire spools were spot-checked as they were received from the vendor, until large variations in wire activity were observed. At this point, the wire quality control program was expanded, beginning with run 405.

Samples 2-in. long were taken from each section of each roll as it was received from the vendor. These were irradiated as described below, and the wires were separated for use as determined by the results.

As the wires were loaded into the lucite wire holders, a 1 1/2 to 2-in. section was taken from each wire and set aside for "quality control" testing. Samples were chosen at random from these sections for an irradiation test.

After separating the wire into groups for loading into the lucite tubes, colored tape was applied for permanent identification; and, where possible, wires with a common color identification were used in a given run.

The wire samples, approximately 0.47-in. long, were irradiated in a lucite wheel 3.07 in. in diameter by 0.48 in. thick. The wheel has fifty-five 0.42-in. indexed holes on a 2.72-in. diameter. There is an 0.25-in. thick undercut top piece to hold the wires in place.

The loaded wheel was placed on the end of an adjustable length shaft and driven by an electric motor. The wheel assembly was then hung from the top and on the outside of the thermal shield with the wheel at the vertical center of the core. The wheel was rotated at 60 rpm throughout the irradiation. The wires were irradiated at the same power level that the flux map required.

After irradiation, the wires were put in small envelopes, and the envelopes were indexed. Each wire was counted for one minute on each of three gas-flow proportional beta counters, and then weighed.

All data were corrected to saturated activity and divided by mass on the Burroughs 205 Computer, so results are given in units of counts per minute per gram (c/min/gm).

Table XII summarizes the results of each colored flag group and identifies the run where this group was used.

THIS PAGE
WAS INTENTIONALLY
LEFT BLANK

8. SUPPLEMENTARY FLUX DISTRIBUTION MEASUREMENTS

8.1 PARTIAL WATER HEIGHT TRAVERSES

A set of three wire traverses were done with all rods withdrawn. For these traverses, run 401 had 594 boron plastic strips in the core, run 404 had 256 strips, and run 405 had no boron plastic strips; the reactivity differences being adjusted by water height. These runs gave information to determine the effects of the boron plastic strips on corner peaking. The data are shown in Figures 23 through 25 and in Volume III of this report.

8.2 MARTY CAN MEASUREMENTS

A bundle of MARTY pins was constructed on a 0.663-in. pitch, using a specially designed tube sheet arrangement that allows the bundle to fit within the NS SAVANNAH internals. This bundle, although constructed using 4% enriched fuel, differed in reactivity by only about 2 cents from the NS SAVANNAH element (the MARTY bundle is slightly more reactive because of its smaller amount of steel).

This bundle was completely instrumented with wires. Using the wire scanner to count the wires and the MARTY pin scanner to determine the gamma activity of the fuel pins, data were taken in half of the symmetrically located can. The experiments were designed to investigate the effects of borated plastic strips on peaking factors and wire flux to pin power conversion.

The MARTY can was exposed five separate times. Table XIII gives the runs, conditions, and comments. In each case, the pin activities were normalized to the average pin activity, and the wire activities were normalized to the average wire activity. The data for each run are shown in Volume III of this report.

8.3 CADMIUM FRACTION MEASUREMENTS

These measurements were undertaken to determine the spectral similarity of manganese and fuel in various positions in the can.

8.3.1 Mn-Cu Cadmium Fractions

The wire used in this measurement was the same Mn-Cu wire that was used in the power maps. The cadmium tubing used was 0.075-in. OD with a 0.020-in. wall thickness.

The thermal component of the bare Mn-Cu wire is given by $A_{th} = F_{cd} \cdot A$, where $F_{cd} = \frac{\text{Total Activity minus Cadmium-covered Activity}}{\text{Total Activity}}$

The quantity, F_{cd} , the cadmium fraction, represents the percentage of thermal activations. The variation of the Mn-Cu cadmium fraction was measured in an axial direction, and the change was not appreciable in the regions unperturbed by the control blades. A total of 11 different sets of data were taken, varying the control blade positions and the wire locations in different cans. These data are shown in Figures 26 through 36.

A composite curve was then constructed to give the F_{cd} in the horizontal direction in a fuel can. This was done by measuring the Mn-Cu cadmium fractions at a point on the wires 49.4 cm above the bottom of the fuel. In all cases the control blades were out of the core in the regions measured. The F_{cd} was found to vary from 0.96 near the edge of the can to an apparent asymptotic value of 0.74 near the center portion of the can (see Fig. 37).

8.3.2 U-235 Cadmium Fractions

Two U-235 cadmium fractions were taken with fully enriched U-Al foils. Figure 37 shows a value of 0.875 near the edge of the fuel can, but near the center region the value drops to 0.845. Cadmium boxes 0.020 in. thick were used in these cases.

Core symmetry was used in both uranium and Mn-Cu cadmium fraction measurements to establish equal fluxes at the cadmium-covered and bare wire locations. A summary of the data is shown in Table XIV.

8.4 COCKED ROD MEASUREMENTS

Two sets of experiments were performed in which the control rod was intentionally cocked in its channel. In run 456, rod A-4 was wedged toward can No. 12. Table XV shows the ratio of the wire activities in symmetrical cans. In run 458, rod A-2 was wedged toward the MARTY element in can 20, and rod A-3 was wedged away from this element. Table XVI shows the analysis of this experiment, based on fuel pin activity.

From either run, it is difficult to evaluate effects of the cocked rods on peaking factors. In only one case did the ratio between flux in the pin away from the cocked rod and the flux in the pin against the cocked rod exceed 1.05. In this case, wires located one position away from the rods gave a ratio of less than one.

8.5 FLUX GRADIENT MEASUREMENTS

Small sections of manganese-copper wire were loaded into a lucite rod which had holes drilled along its diameter. This rod was attached to a smaller rod and inserted into a ferrule in position 13-25-25. The results of this traverse are shown in Figure 38.

In a second set of measurements (Run 422), wires were taped to the fuel pins in can 31 at a point 49.4 cm above the bottom of the active fuel. The results of this measurement — compared to the same point on wire 31-3-25 — are shown in Figure 39.

8.6 REPRODUCIBILITY CHECK

The conditions of run 418 were repeated in run 459, with the A rod group banked at 79.0 cm.

A direct comparison may be made by comparing Figures 48 and 63, and Figures 75 and 86. The data for runs 418 and 459 are in Volume II of this Report. There are slight differences in point-by-point activity, with the worst disagreement occurring in the corners. As stated earlier, if a corner wire is cocked to one extreme in run 418, and to the other extreme in run 459, a 12% difference would exist, although each wire is only 6% off of the true corner position activity.

It may be seen in Table XVII that the axial position of the peak is not the same in runs 418 and 459. Actually the true peak probably falls between the two points, and the differences are not statistically significant.

THIS PAGE
WAS INTENTIONALLY
LEFT BLANK

9. FLUX MAP ANALYSIS

9.1 DATA REDUCTION PROGRAM

To expedite the data reduction and to prepare a printed record of the data points measured, the data were punched automatically into IBM cards. A computer program was prepared to average and normalize the data, to arrange it in a reasonable order, and to print the raw data, along with the normalized data, on paper offset plates. Details of this computer program are given in Volume II of this report. In summary, the program first computes by numerical methods, the average axial activity by performing the operation

$$\bar{\phi}_z = \frac{\int_{z_0}^{z_m} \phi(z) dz}{\int_{z_0}^{z_m} dz}$$

where $\phi(z)$ = the activity at each axial position along a wire,
 z_0 = the first point counted, and
 z_m = the last point counted.

A total core average is then computed by

$$\bar{\phi} = \frac{\sum W_i \bar{\phi}_z}{\sum W_i}$$

where W_i is a weighting factor, denoting the importance of this wire in representing the flux of a region.

The computer then normalizes each point by dividing the data point by the average activity. This number is printed, along with the measured data, at its respective position, identified by can number, x, y, and z position as defined in Section 7.3.1 and Figure 40.

9.2 RADIAL WEIGHTING FACTOR SELECTION

Weighting factors for maps where wires are concentrated in one octant are determined by estimating the area of influence of the wire. This method was checked by computing can averages from the 32-can MARTY core as reported in BAW-1124.² The following computation was done for comparison: the can average for the wire pattern was computed by assigning weighting factors to the wire according to their location and computing the average from the extrapolated flux existing at the wire location. This number, when compared to the numerical average of the fuel pin data, gave an average difference of $+0.9\% \pm 4.1\%$.

In many of the maps measured, a maximum of eight wires was available to determine the average flux for a particular can, so an eight-wire pattern was established upon which an average could be based. A number of combinations of wires were tried in an effort to determine a set of weighting factors which could be independent of the rod positions around the can. The best agreement with the MARTY power maps described above came by using an average determined by

$$\bar{\phi} = \frac{\sum_{o=1}^4 9 \phi_o + \sum_{i=1}^4 32 \phi_i}{164}$$

where ϕ_o = each of four corner wires and
 ϕ_i = each of four specified inner wires
(9-9, 9-19, 19-9, 19-19).

Comparison with the MARTY maps gave an average difference of $-0.3\% \pm 3.0\%$ for 7 cases compared.

The extrapolation of the flux in the MARTY can to the flux in the corner wire, however, underestimated the flux in the corner wire as determined by activation of MARTY fuel pins, along with wires, in a special test insert in the Savannah core. Calculation of the average by this formula gives an average that is 1.09 ± 0.05 times the true average determined by the use of wires in each position in the can.

In general, the measurement of peak normalized flux is given an uncertainty of 6.3%. This error includes the maximum error due to positioning the wire (see Section 7.2), the uncertainty in activity of the point as a result of counting statistics, and the variation in wire composition.

Figures 41 through 64 show profiles of the axially averaged flux, and the data are tabulated in Volumes II and III of this report.

9.3 POWER PEAKING ANALYSIS

The transition from flux peaking factors to cold, power peaking factors is one involving several corrections, each having some associated uncertainty. The major corrections are as follows.

1. The higher flux seen by the corner wire due to its location
2. The spectral differences between wire activity and fuel activity
3. The effect on peaking of the boron plastic strips

Items 1 and 2 have been evaluated by the MARTY can maps described in Section 8.2. To evaluate these factors, the ratio of the normalized wire fluxes in each corner to the normalized fission product activity in the corner pins was determined. The average ratio for the data available was 1.21 ± 0.13 . Statistically, no dependence of this factor on borated plastic loading may be observed. This is further substantiated by an experiment to establish the flux gradients through fuel pins in the corners using manganese wire, as shown in Figure 39.

The effects of borated plastic were determined by two sets of runs, where two sets of similar MARTY can data were run with and without borated plastic. In one case (runs 426 and 430) the reactivity difference was taken up by adding more boron plastic to the remainder of the core. In the other case (runs 458 and 460), the reactivity difference was taken up by changing the water height. For 10 to 12 borated plastic strips per can, the average ratio of peak-to-average with borated plastic to peak-to-average without borated plastic was 1.08 ± 0.06 . The worst case observed was 1.17.

The second approach was to analyze three runs with eight wires per can for peaking factors discussed in Section 8.1. The average ratio of peak-to-average flux with 594 borated plastic strips to peak-to-average with no borated plastic was 1.04 ± 0.15 . The average ratio of peak-to-average flux with 256 borated plastic strips compared to the no borated plastic case was 1.10 ± 0.21 .

The conversion from wire peak-to-average flux to cold power peak-to-average may be broken down into three cases.

9.3.1 No Borated Plastic, Octant Symmetry

The correction factor is

$$0.9545 \times \frac{1}{1.21} = 0.7888,$$

where 0.9545 is the reduction resulting from the lower than average enrichment in the inner cans where the peak occurs, and $\frac{1}{1.21}$ is the pin power to wire flux ratio previously discussed.

The uncertainty on this case, calculated from combining the uncertainties of each factor, including the wire flux uncertainty, is $\pm 12.5\%$.

This factor applies to runs 418, 420, and 459.

9.3.2 With Borated Plastic, Octant Symmetry

The correction factor is

$$0.7888 \times \frac{1}{1.08} = 0.7304,$$

where $\frac{1}{1.08}$ is the borated plastic effect on peaking as previously discussed.

The combined uncertainties are $\pm 13.6\%$. This factor applies to runs 360, 363, 422, 425, 433, and 449.

9.3.3 With Borated Plastic, Using Eight-Wire Radial Averaging Method

The correction factor is

$$0.7304 \times 1.09 = 0.7961,$$

where 1.09 is the over-estimate of the can average due to the higher flux seen by the corner wires.

The uncertainties in this case are $\pm 14.3\%$.

This factor is applicable to runs 367, 370, 378, 383, 401, 404, 416, 422, and 445. It was applied partially to runs 432, 435, and 439 since a portion of the cans in each of these runs was averaged in this manner.

A slight correction, necessary due to renormalization of average power to 1.00, was not applied to the peak-to-average power in each of these cases since it is too small to be important with these

ranges of uncertainty. A systematic error of several percent also exists since the bottom 8.2 cm and the top 5 cm of the fuel region do not contribute to the average.

Figures 65 through 86 show averaged can fluxes and can powers for each of the flux maps, and Table XVII shows a summary of the peak flux factors and the peak power factors.

THIS PAGE
WAS INTENTIONALLY
LEFT BLANK

10. THREE DIMENSIONAL CALCULATION

10.1 INTRODUCTION

Three dimensional calculations were carried out to match two critical rod patterns as experimentally determined in this program.

Data from runs 418 and 420 were the basis of this work. The two cases are distinguished by control rod positions, as shown below.

POSITION OF BOTTOM OF ACTIVE CONTROL ROD

<u>Run</u>	<u>Rod Group</u>	<u>Referenced to Snubbers</u>	<u>Referenced to Active Fuel Bottom</u>
418	Group A	79 cm	86.24 cm
	Others	In	7.24 cm
420	Rod X	Out (150 cm)	157.24 cm
	Group C	108 cm	115.24 cm
	Others	In	

10.2 WESTINGHOUSE TKO PROGRAM FOR THE IBM 704 COMPUTER²

The TKO code solves few-group, time independent, neutron diffusion equations in x, y, z geometry. The number of lethargy groups may be one, two, three, or four, and the solution is obtained over a rectangular parallelepiped that is symmetrical with respect to the plane $x=y$, over one fourth of the core. A mesh of horizontal and vertical planes is imposed on this parallelepiped, and all region faces must occur on mesh planes. Input parameters are specified region-wise, and completely variable mesh spacings are permitted. The number of mesh

points on and to one side of the plane $x=y$ is limited to 2675 on 16,384-word computers and 4725 on 32,768-word computers. Either a zero flux or a zero current boundary condition may be applied at each boundary plane.

The equations solved are of the form

$$\left\{ -D_i \nabla^2 \phi_i + \left[\Sigma_i^a + \Sigma_i^R \right] \phi_i = \frac{X_i \psi_i}{\lambda} + \Sigma_{i-1}^R \phi_{i-1} \right\}_{i=1}^{i=K}$$

where $1 \leq K \leq 4$,

$$\Sigma_0^R = \Sigma_K^R \equiv 0,$$

$$\psi = \sum_{i=1}^K v_i \Sigma_i^f \phi_i,$$

$$X_i = 1 \text{ if } i = K-1, \Sigma_{i-1}^{K-1} X_i = 1, \text{ and}$$

$$X_K = 0 \text{ if } K > 1.$$

The physical interpretations of these symbols are as follows.

D = diffusion coefficient

Σ^a = absorption cross section

Σ^R = removal cross section

X_i = integral of the fission spectrum over the lethargy range represented by group i .

v_i = average number of neutrons produced by a fission in group i

Σ^f = fission cross section

ψ = fission source

ϕ = neutron flux

λ = eigenvalue.

Code input consists of a description of the mesh (intervals between successive mesh planes and composition placement) together with composition coefficients and a flux guess for each composition.

Output includes a complete edit of the input, a picture of each different x - y plane with all regions and interfaces indicated, the composition volumes, the composition integrated flux and source, and the point-wise flux and source values.

10.3 TKO INPUT PREPARATION

10.3.1 Composition Coefficients

All coefficients were generated by the B&W 40-group Spectral Code which gives spectrum weighted polygroup coefficients for the desired groups. The groups used in the TKO problems were as follows.

<u>Group</u>	<u>Energy Range</u>
1	10 Mev to 9.119 kev
2	9.119 kev to 50.3 ev
3	50.3 ev to 0.4 ev
4	Thermal (0.4 ev cutoff)

Data for the Spectral Code consist primarily of the atomic concentrations (Table XVIII), and the disadvantage factors (Table XIX) for each region. The leakage from one region can be used as a source in another (for example, from a fuel composition into steel). The coefficients are on page 1 of the TKO printout in Volume IV of this report.

10.3.2 Mesh Description and Overlay

The x-y mesh is identical in the two cases because only vertical rod position changes. Since a very limited number of points are available in the IBM-704 version of TKO, a certain amount of homogenization is required. Previous experience has established the strong influence of the steel cans on flux distribution, and for this reason the cans were shown as finite regions. The control rods were then homogenized with the adjacent water. A separate one-dimensional study showed a small increase in computed rod worth when using this method but it promised to give a better flux shape in the important areas (where flux peaks are expected) than if the can and water were combined. A diagram of the x-y mesh, including dimensions and composition position, is shown in Figure 87. Areas labeled "5, 6" are either control rods or followers at any given plane, depending on rod positions. The illustrated mesh applies to all vertical planes except those at the two reflectors, where the fuel in areas 2 and 3 is replaced with water.

A different z-mesh is required for each case. Lines defining necessary points such as region interfaces and rod tips were chosen first. Previous NMSR axial flux calculations were used to determine the optimum locations for the remaining planes. Figures 88 and 89 represent the two z meshes with dimensions and plane locations.

The detailed input for the two TKO cases is shown in Volume IV as part of the machine printout.

10.4 COMPARISON OF TKO AND EXPERIMENTAL RESULTS

Agreement between experiment and calculation might be expected in these four areas:

1. General flux shape
2. Location and magnitude of peaks
3. Excess reactivity of the core
4. Can averages of flux and power

10.4.1 General Flux Shape

The TKO code determines a point flux distribution, as does the experimental program, and a power, or source, distribution. Flux shapes are compared by normalizing the group four (thermal) flux to the average flux in the two fuel regions as determined by averaging the composition averages for group four in regions two and three as reported in Volume IV. This is compared to the manganese wire activity, also normalized to the average in the fuel region.

The general axial flux shapes agree well, as shown in Figures 90 through 99. In some cases, the wire location and the TKO line coincide exactly; in other cases they are several centimeters apart, but are in the same area of importance.

An examination of the traverses reveals a systematic difference between the axial location of the peaks as calculated and as measured. The source of this difference has not resolved; a recheck of experimental and calculational dimensions did not show a positioning error. This systematic position difference adds more uncertainty to the comparison of magnitudes since the peaks occur in regions of high gradients.

10.4.2 Location and Magnitude of Peaks

The location of both flux and power peaks given by TKO is different from that measured. This difference occurs because the curved can corner and the curved follower at the can corner cannot be accurately described with a limited x-y mesh. The highest peak in thermal flux, and power occurs in a position not directly measured with a wire; but as shown in Figures 39, 52, 53, 61 and 62, this position does not see this larger power or flux in physical reality. The highest normalized thermal flux and power are shown in Table XX.

10.4.3 Calculated Excess Reactivity

In the process of generating the mesh spacings, computer storage limitations required that the control rod and water gap be homogenized. A one-dimensional, four-group analysis established that this homogenization would increase control rod worth in the critical core by 2%. Thus, for the two experimental critical cases, a k_{eff} of about 0.98 would be expected, and TKO gives 0.9795 for run 418, and 0.9792 for run 420. Considering the very limited mesh, agreement is excellent.

10.4.4 Can Averages of Power

Can averages of power were computed by volume weighting each point within the cans. The normalized can powers are shown in Figures 100 and 101. The flux numbers shown on these figures are calculated by dividing by the ratio of the zone enrichment to the average enrichment, and then renormalizing the power to a quadrant average of unity.

10.5 CONCLUSIONS AND RECOMMENDATIONS

Comparison between experiment and calculation shows that in certain core positions reasonable agreement may be obtained with a limited mesh. The mesh planes can be placed to cover the most important locations, but a general lack of detail is inevitable. This becomes more and more serious as the complexity and size of the core increases.

TKO uses few-group neutron diffusion theory. Extensive experience with this model in one- and two-dimensional work establishes its validity

in production work. The four-group model, when properly used, gives good agreement with experimental data.

The primary shortcoming of TKO as presently used is the limited mesh. It is impossible to describe a NMSR-type core well enough with the limited storage of an IBM-704. TKO is being rewritten for the Philco 2000 (TRANSAC) machine which allows 100,000 interior points compared with only 4725 on the IBM-704. This new development will substantially increase the usefulness and value of this three-dimensional code.

The IBM-704 version of TKO is adequate for simple problems, but for a core as complex as the NMSR it is recommended that the Philco 2000 (TRANSAC) version or its equivalent be used.

11. APPENDIX

CONTROL ROD LOCATION IN SAVANNAH CORE

<u>Location in Reactor</u>	<u>Control Rod Number</u>
E1	1
C1	2
D1	3
D4	4
B4	5
<u>A1</u>	<u>19 Dimensioned Rod</u>
B1	7
E2	8
C4	9
A4	10
X	11
A2	12
C2	13
E4	14
B3	15
A3	16
B2	17
D2	18
D3	6
C3	20
E3	21

12. TABLES AND FIGURES

TABLE I
INSTRUMENT RESPONSE DURING FUEL LOADING

Run Number	Conditions		Ship BF ₃		Lab BF ₃ , c/sec (In Mockup)	Fission Counter, c/sec	Linear No. 1, μamp	Linear No. 2, μamp
	Added Bundles In Position	Total Number Bundles In Core	Ship's Meter, c/sec	Lab Scaler, c/sec				
338	7, 8, 9, 13, 14, 15, 19, 20, 21, 25, 26, 27	(Source In) 12	2.7	3.00	0.08	0.42	0.1	4.8
339	18 & 24	14	2.6	3.07	0.07	1.00	0.1	5.2
340	6 & 12	16	2.7	2.82	0.08	1.20	0.6	5.5
341	1 & 2	18	2.7	2.90	0.09	1.30	7.5	5.4
342	3 & 4	20	3.0	2.29	0.10	1.46	9.9	5.4
344	10 & 16	22	3.0	2.17	0.04	1.40	10.2	5.5
345	22 & 28	24	3.0	2.20	0.03	1.49	10.5	9.6
346	31 & 32	26	3.1	2.94	0.12	1.69	10.8	320
347	29 & 30	28	3.6	3.41	0.35	78.14	10.8	400
348	17 & 23	30	4.1	4.75	0.36	99.18	11.1	400
349	5 & 11	32	4.5 (1.8*)	4.60	0.50 0.42	108.08	23.0	410

* Corrected for background

TABLE II
APPROACH TO CRITICAL BY ROD WITHDRAWAL

Run Number	Rod Positions		Ship BF ₃			Fission Counter, c/sec	Linear No. 1, μamp	Linear No. 2, μamp
	Group D, in.	Group E, in.	Ships Meter, c/sec	Lab Scaler, c/sec	Lab BF ₃ , c/sec			
350	Full In	0	4.2	4.15	0.48	109	410	23
		9	4.3	4.45	0.41	113	420	32
		19	4.2	4.68	0.50	127	510	56
		29	5.4	6.25	0.90	198	960	99
		39	8.0	8.41	1.53	373	2040	165
		49	10.7	12.91	2.69	662	3800	250
		59	15.0	16.78	3.61	891	5200	320
351	Full Out	4	17.0	18.73	3.86	956	5500	350
		8	17.0	19.66	4.23	1063	6000	440
		12	24.0	28.82	6.70	1572	8700	730
		14	39.0	44.41	11.21	2450	12900	1080
		15	59.0	68.36	15.87	3785	19800	1980
		16	147.0	160.64	36.32	8813	46000	4900

Slightly Supercritical

TABLE II
ABSOLUTE FLUX MEASUREMENTS

<u>Can Number</u>	<u>Dy-Al Foil Number</u>	<u>Saturated Activity</u>	$A_{\text{sat}} \times 27.8, *$ <u>neut/cm²/sec</u>	$\bar{\phi}_{2200}$ <u>Per Can,</u> <u>neut/cm²/sec</u>	<u>Mn-Cu Wire</u> <u>Count Rate</u> <u>at 80 cm</u> <u>arbitrary</u> <u>units</u>	$\bar{\phi}_{2200}$ <u>Wire Count Rate</u>
10	4	5.59×10^5	1.56×10^7	1.58×10^7	274	0.576×10^5
	5	6.62×10^5	1.84×10^7			
	6	4.84×10^5	1.35×10^7			
	7	5.68×10^5	1.58×10^7			
14	8	4.98×10^5	1.39×10^7	1.40×10^7	249	0.562×10^5
	9	5.12×10^5	1.42×10^7			
	10	4.97×10^5	1.38×10^7			
	11	5.13×10^5	1.43×10^7			
15	12	6.82×10^5	1.90×10^7	1.90×10^7	331	0.574×10^5
	13	7.07×10^5	1.97×10^7			
	14	6.47×10^5	1.80×10^7			
	15	6.97×10^5	1.94×10^7			
					Average	0.571×10^5

* The conversion factor of 27.8 was determined for the Dy-Al foils from an intercalibration with the National Bureau of Standards absolute neutron flux.

TABLE IV
POWER CALCULATIONS

Can Number	Mn-Cu Wire Count Rate at 80 cm	$(\phi_{2200})_{80 \text{ cm}}$ Wire Count Rate x 0.571×10^5	f_v^*	f_R^*	$\bar{\phi}_{2200}$ per Can, neut/cm ² /sec	Power Factor	Power/Can, watts
5	165	0.94×10^7	0.80	1.00	0.75×10^7	4.15×10^{-7}	3.1
6	366	2.09×10^7	0.74	1.00	1.55×10^7	$1/2 \times 3.88 \times 10^{-7} \star$	3.0
9	359	2.05×10^7	0.735	1.00	1.51×10^7	$1/2 \times 3.88 \times 10^{-7} \star$	2.9
10	274	1.58×10^7	0.705	1.00	1.11×10^7	4.15×10^{-7}	4.6
11	199	1.14×10^7	0.775	0.95	0.84×10^7	4.15×10^{-7}	3.5
12	267	1.52×10^7	0.768	0.85	0.99×10^7	3.88×10^{-7}	3.8
13	257	1.47×10^7	0.705	0.85	0.88×10^7	$1/2 \times 3.88 \times 10^{-7} \star$	1.7
14	249	1.40×10^7	0.723	0.85	0.86×10^7	$1/2 \times 3.88 \times 10^{-7} \star$	1.7
15	331	1.90×10^7	0.716	0.85	1.16×10^7	3.88×10^{-7}	4.5
16	296	1.69×10^7	0.746	0.95	1.20×10^7	4.15×10^{-7}	5.0

Total Power/Quadrant = 33.8 watts

Power of Total Core = $33.8 \times 4 = 135$ watts

* f_v = Vertical Correction Factor

f_R = Radial Correction Factor

★ The factor 1/2 was used since only one-half the can was in the measured quadrant.

TABLE V
SHIP INSTRUMENT CALIBRATION AT CEL

<u>Instrument</u>	<u>Instrument Count Rate, c/sec</u>	<u>Reactor Power, watts</u>	<u>Counts/sec/watt</u>
Ship BF ₃	1.7 x 10 ³	135	12.5
Ship Fission Chamber	11.2	135	0.083

TABLE VI
ESTIMATE OF POWER CALIBRATION ERRORS

<u>Factor</u>	<u>Estimated Error, %</u>	<u>Comments</u>
N ₂₅	± 1	Estimated from fuel manufacturing data
(σ _f) ₂₂₀₀	± 1	Reference 10
$\bar{\phi}_{2200}$	± 20	Includes errors in f _v , f _r , and absolute flux calibration
V	± 1	
F	± 5	Includes both calculational and experimental errors
R	± 3	Experimental error
E	± 2	Experimental error

$$\text{Total error} = \sqrt{(1)^2 + (2)^2 + (20)^2 + (1)^2 + (5)^2 + (3)^2 + (2)^2} \% = \pm 21\%$$

Total power = 135 ± 28 watts for run 352

TABLE VII
INTEGRAL COUNTS OF NICKEL FOILS

<u>Nickel Foil Number</u>	<u>Net Counts Per Minute</u>	<u>Weight, gm</u>	<u>Net Counts Per Minute/gm</u>
1	384	2.56	150
2	241	2.64	91.3
3	155	2.68	57.7
4	82	2.60	31.5
5	70.3	2.55	27.6
6	399	2.58	155
7	563	2.52	223
8	20,765	0.682	30,507

TABLE VIII
SUMMARY OF "STUCK ROD GROUP" MEASUREMENTS

<u>Rod Group Withdrawn (All Others Inserted)</u>	<u>Conditions</u>	<u>Comments</u>
X	Subcritical	
A	Critical	A-1 150 cm A-2 150 cm A-3 66.4 cm A-4 2.5 cm
B	Critical	B-1 150 cm B-2 150 cm B-3 69.8 cm B-4 150 cm
C	Subcritical	
D	Subcritical	
E	Subcritical	

TABLE IX
BORATED PLASTIC SAMPLE WEIGHTS

<u>Sample Number</u> 10 cm Long	<u>Weight,</u> gm	<u>Sample Number</u> 10 cm Long	<u>Weight,</u> gm
1	3.3156	18	3.2240
2	3.3147	19	3.3662
3	3.2579	20	3.3025
4	3.3747	21	3.4131
5	3.3870	22	3.4003
6	3.4109	23	3.2858
7	3.2748	24	3.3565
8	3.2553	25	3.3818
9	3.3330	26	3.3349
10	3.3347	27	3.3319
11	3.2458	28	3.3980
12	3.3284	29	3.3832
13	3.4078	30	3.3209
14	3.550	31	3.3104
15	3.3116	32	3.3148
16	3.3994	33	3.2986
17	3.4414	34	3.3737

Average 3.3395±0.057

TABLE X
FLUX MAP EXPOSURES

Reactor Run Number	Log CRM	Log N, μ amp	Linear No. 1	Linear No. 2	Monitron, R/hr	Safety No. 1 amp	Safety No. 2 amp	Shield Tank Chamber, amp	Core Tank Temperature, C	Water Height, cm	Exposure Time
352	65000	0.023	40% K	37% N	0.023	$17\% \times 10^{-8}$	$5\% \times 10^{-7}$	-	19.2	Full	20 min
360	Off Scale	9	37% N*	33% O	1.0	$35\% \times 10^{-8}$	$20\% \times 10^{-8}$	-	18.8	Full	10 min
363	Off Scale	6	50% O	66% Q	7.0	$20\% \times 10^{-7}$	$8\% \times 10^{-7}$	-	19.1	Full	60 sec DT
367	Off Scale	2	49% O	29% Q	7.0	$15\% \times 10^{-7}$	$55\% \times 10^{-8}$	-	18.3	Full	59 sec DT
370	Off Scale	2	46% O	29% Q	7.0	$15\% \times 10^{-7}$	$50\% \times 10^{-8}$	-	17.8	Full	62 sec DT
378	Off Scale	8	80% O	85% P	7.0	$35\% \times 10^{-7}$	$18\% \times 10^{-7}$	-	17.5	Full	56 sec DT
383 **					7.0			-		Full	56 sec DT
401	Off Scale	6	45% O	24% Q	7.0	$34\% \times 10^{-7}$	$22\% \times 10^{-7}$	-	20.8	Full	60 sec DT
404	Off Scale	4	41% O	30% O	11.0	$80\% \times 10^{-7}$	$120\% \times 10^{-7}$	-	20.0	51.74	73 sec DT
405	Off Scale	3	37% O	26% O	10.0	$135\% \times 10^{-7}$	$70\% \times 10^{-7}$	-	20.0	35.65	115 sec DT
416	Off Scale	8.5	89% O	32% Q	7.0	$84\% \times 10^{-8}$	$73\% \times 10^{-8}$	-	20.2	Full	66 sec DT
418	Off Scale	7	32% P	66% P	7.0	$45\% \times 10^{-8}$	$55\% \times 10^{-8}$	-	19.5	Full	60 sec DT
420	Off Scale	8	68% O	70% P	6.0	$65\% \times 10^{-8}$	$70\% \times 10^{-8}$	-	18.9	Full	67 sec DT
422	Off Scale	8	30% P	25% Q	7.0	$45\% \times 10^{-8}$	$55\% \times 10^{-8}$	-	-	Full	62 sec DT
425	Off Scale	8	34% P	23% Q	5.0	$45\% \times 10^{-8}$	$55\% \times 10^{-8}$	-	18.5	Full	58 sec DT
426	Inoperative	2	35% O	29% P	1.5	$12\% \times 10^{-8}$	$15\% \times 10^{-8}$	$70\% \times 10 \times 10^{-11}$	19.0	Full	63 sec DT
430	Inoperative	0.8	42% N	63% O	1.0	$45\% \times 10^{-9}$	$45\% \times 10^{-9}$	-	18.0	Full	61 sec DT
432	Inoperative	8	30% P	75% P	7.0	$45\% \times 10^{-8}$	$50\% \times 10^{-8}$	$88\% \times 3 \times 10^{-9}$	18.0	Full	50 sec DT
433	Inoperative	8	30% P	24% Q	7.0	$45\% \times 10^{-8}$	$50\% \times 10^{-8}$	$28\% \times 10 \times 10^{-9}$	18.1	Full	50 sec DT
435	Off Scale	9	93% O	89% P	7.0	$74\% \times 10^{-8}$	$75\% \times 10^{-8}$	$100\% \times 3 \times 10^{-9}$	17.9	Full	57 sec DT
439	Off Scale	9	35% P	24% Q	7.0	$60\% \times 10^{-8}$	$70\% \times 10^{-8}$	$92\% \times 3 \times 10^{-9}$	18.0	Full	57 sec DT
442	Off Scale	5	70% O	80% P	7.0	$55\% \times 10^{-8}$	$55\% \times 10^{-8}$	$35\% \times 10 \times 10^{-12}$	19.9	Full	61 sec DT
445	Off Scale	7	87% O	100% P	7.0	$80\% \times 10^{-8}$	$70\% \times 10^{-8}$	-	19.5	Full	65 sec DT
449	Off Scale	8	55% P	84% P	7.0	$45\% \times 10^{-8}$	$55\% \times 10^{-8}$	-	18.0	Full	55 sec DT
456	Off Scale	3.5	24% P	45% P	2.5	$30\% \times 10^{-8}$	$30\% \times 10^{-8}$	$38\% \times 3 \times 10^{-9}$	19.5	Full	48 sec DT
458	Off Scale	2.0	95% N	70% N	6.5	$70\% \times 10^{-7}$	$38\% \times 10^{-7}$	$51\% \times 3 \times 10^{-8}$	20.5	47.2	59 sec DT
459	Off Scale	10.0	43% P	60% P	7.0	$15\% \times 10^{-7}$	$15\% \times 10^{-7}$	-	20.0	Full	43 sec DT
460	Off Scale	4.0	93% N	85% O	6.0	$43\% \times 10^{-7}$	$25\% \times 10^{-7}$	$20\% \times 3 \times 10^{-8}$	19.9	114.53	63 sec DT

* N: 3×10^{-6} amperes full scale
 O: 10×10^{-6} amperes full scale
 P: 3×10^{-5} amperes full scale
 Q: 10×10^{-5} amperes full scale

** All Instruments Not Read

DT: Doubling Time

TABLE XI
ROD POSITIONS FOR FLUX MAP EXPOSURES

Reactor Run Number	X	Rod Position, cm Withdrawn					Number of Boron Strips	Comments
		Group A	Group B	Group C	Group D	Group E		
352	0	0	0	0	42.25	151	0	
360	0	0	88.6	150	150	150	336	
363	0	89.0	0	150	150	150	320	
367	0	80.0	30.0	C1-0 C2,3,4,-150	150	150	320	
370	0	25.0	79.8	C1-0 C2,3,4,-150	150	150	320	
378	0	A3-0 A1,2,4,-150	91.0	150	150	150	448	
383	150	A3-0 A1,2,4,-150	82.8	150	150	150	488	
401	150	150	150	150	150	150	594	
404	150	150	B1,2,-150 B3,4,-70	150	150	150	256	
405	150	150	B1,2,-150 B3,4,-50	150	D1,2,3,-150 D4-60	E1,2,3,-150 E4-60	0	
416	0	101.0	0	150	D1-0 D2,3,4,-150	150	320	
418	0	79.0	0	0	0	0	0	
420	150	0	0	108.0	0	0	0	
422	0	100.0	0	101.7	150	150	320	
425	0	89.6	45.0	150	150	150	384	
426	0	82.5	45.0	150	150	150	384	MARTY can in Position 27
430	0	88.1	45.0	150	150	150	419	MARTY can in Position 27
432	0	90.0	B2,4,-150 B1,3,-75.0	150	150	150	458	
433	0	90.0	90.0	150	150	150	458	
435	0	90.0	B1,3,-102 B2,4,-180.0	180	180	180	458	
439	90	90.0	B2,4,-150 B1,3,-39.0	150	150	150	458	
442	0	A1-150 A2,3,4,-101.3	B2,3,-150 B1,4,-55.0	150	150	150	458	
445	0	A1-150 A2,3,4,-104.0	150	C1-0 C2,3,4,-150.0	150	150	496	
449	0	88.5	0	50.0	150	150	240	
456	0	75.2	0	0	0	0	0	MARTY can in Position 20
458	0	A2,3,4,-150.0 A1-75.0	0	75.0	150	150	0	MARTY can in Position 20
459	0	79.0	0	0	0	0	0	
460	0	140.0	0	150	150	150	320	MARTY can in Position 20

TABLE XII
STANDARD DEVIATION OF COLOR GROUPS

<u>Color Group</u>	<u>Reactor Runs</u>	<u>Nominal Composition, % Mn</u>	<u>Standard Deviation, %</u>
Red	413, 416	20	1.0
Blue	416	20	1.8
Red and Blue	416	20	1.6
Brown	433	20	2.4
Green	456	80	1.8

Over-all Standard Deviation in wire composition within composition group: 1.5%.

TABLE XIII
MARTY ELEMENT MEASUREMENTS

<u>Run Number</u>	<u>Marty Element In Can Number</u>	<u>Refer to Figure</u>	<u>Number of Borated Polyethylene Strips in Marty Can</u>	<u>Water Height, cm</u>	<u>Rod Positions, cm</u>	<u>Comments</u>
426	27	52	12	full	X: in A: 82.5 B: 45.0 C, D, E: out	For comparison to Run 430 to evaluate boron plastic effects
430	27	53	0	full	X: in A: 88.1 B: 45.0 C, D, E: out	For comparison to Run 426
456	20	61	0	full	X: in A: 75.2 B, C, D, E: in	For evaluation of flux to power conversion in case to be calculated on the IBM 704
457	20	62	0	47.2	X: in A: out B: in C, D, E: out	For comparison to Run 460 for boron plastic effects and flux to power conversion
460	20	64	10	114.53	X: in A: out B: in C, D, E: out	For comparison to Run 457

TABLE XIV
SUMMARY OF CADMIUM FRACTION MEASUREMENTS

Run Number	Can and Position	Manganese-Copper	
		Cadmium Ratio at 49.4 cm	Cadmium Fraction
420	14-09-19	4.55	0.7787
	14-19-09		
422	14-09-19	4.29	0.7670
	14-19-09		
425	14-09-19	3.89	0.7427
	14-19-09		
426	27-03-03	26.6	0.9624
	27-25-25		
430	27-03-03	28.2	0.9644
	27-25-25		
433	14-05-23	4.21	0.7690
	14-23-05		
439	14-23-05	3.907	0.7440
	14-05-23		
442	14-09-19	3.796	0.7366
	13-19-19		
445	10-05-05	5.593	0.8212
	05-23-05		
449	08-05-23	4.020	0.7512
	07-23-23		
459	14-09-19	4.245	0.7641
	14-19-09		

Run Number	Can and Position	Uranium	
		Cadmium Ratio at 49.4 cm	Cadmium Fraction
434	14-05-23	8.023	0.8754
	14-23-05		
434	20-09-09	6.498	0.8461
	20-19-19		

TABLE XV
COCKED ROD MEASUREMENTS

RUN 456

ROD A-4 COCKED

<u>Can 12</u>			<u>Can 18</u>	
<u>Wire Position</u>	<u>Average Axial Activity, Counts</u>	<u>Ratio*</u>	<u>Wire Position</u>	<u>Average Axial Activity, Counts</u>
12-23-03	13378	1.046	18-23-25	13995
12-25-03	18559	1.010	18-25-25	18751
12-25-05	13778	1.010	18-25-23	13921

<u>Can 13</u>			<u>Can 19</u>	
<u>Wire Position</u>	<u>Average Axial Activity, Counts</u>	<u>Ratio**</u>	<u>Wire Position</u>	<u>Average Axial Activity, Counts</u>
13-03-03	22632	1.11	19-03-25	25061
13-03-05	16030	0.953	19-03-23	15275
13-05-03	16089	0.980	19-03-25	15764

* The ratio of wire activities of symmetrically located wires in Can 18 to wires in Can 12.

** The ratio of wire activities of symmetrically located wires in Can 19 to wires in Can 13.

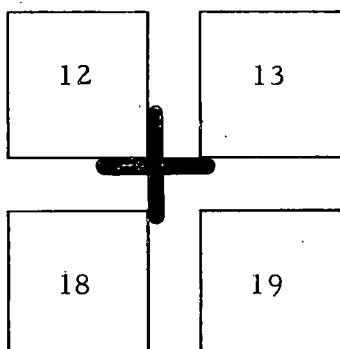


TABLE XVI
COCKED ROD MEASUREMENTS

RUN 458

MARTY CAN 20

RODS A-2 & A-3 COCKED

<u>Fuel Position</u>	<u>Average Axial Activity, Counts</u>	<u>Ratio*</u>	<u>Fuel Position</u>	<u>Average Axial Activity, Counts</u>
20-02-04	13163	1.05	20-26-24	13851
20-02-06	11705	0.950	20-26-22	11114
20-04-02	14242	0.968	20-24-26	13786
20-04-04	10810	1.01	20-24-24	10969
20-04-06	9493	1.04	20-24-22	9904
20-06-02	11390	1.02	20-22-26	11563

* Ratio of fuel activities in symmetrical corners of the can away from the rod to activity in corners against the rod.

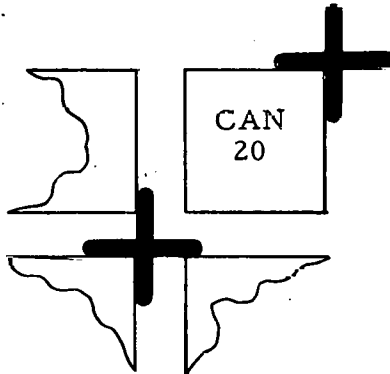


TABLE XVII
PEAK FLUX AND PEAK POWER FACTORS

<u>Run Number</u>	<u>Position, Can #, x, y</u>	<u>Axial Position, cm from Bottom of Active Fuel</u>	<u>Highest Normalized Flux (as measured) Av = 1.000</u>	<u>Highest Normalized Power Av = 1.000</u>
360	14-25-25	70.0	4.36 ± 0.27	3.18 ± 0.43
363	08-03-25	80.3	3.91 ± 0.25	2.86 ± 0.39
367	26-03-25	49.5	5.09 ± 0.32	4.05 ± 0.58
370	26-25-03	49.5	5.42 ± 0.34	4.31 ± 0.62
378	14-03-25	59.8	5.20 ± 0.33	4.14 ± 0.59
383	14-03-03	59.8	5.43 ± 0.34	4.32 ± 0.62
401	14-03-03	90.7	5.50 ± 0.35	4.38 ± 0.63
404	13-25-03	34.2	4.49 ± 0.28	3.57 ± 0.51
405	20-03-25	22.2	3.93 ± 0.25	3.38 ± 0.45
416	25-25-25	70.0	4.91 ± 0.31	3.91 ± 0.56
418	14-03-25	48.4	7.53 ± 0.47	5.94 ± 0.74
420	19-25-25	69.0	5.77 ± 0.36	4.55 ± 0.57
422	08-03-03	69.0	4.66 ± 0.29	3.40 ± 0.49
425	21-03-25	48.4	4.91 ± 0.31	3.59 ± 0.49
432	21-03-03	59.7	4.87 ± 0.31	3.72 ± 0.53
433	14-25-25	59.7	5.90 ± 0.37	4.31 ± 0.59
435	20-25-25	70.0	5.15 ± 0.32	3.93 ± 0.56
439	20-25-25	59.7	5.82 ± 0.37	4.44 ± 0.63
442	20-25-03	70.0	5.34 ± 0.34	4.25 ± 0.60
445	21-03-03	49.4	4.97 ± 0.31	3.96 ± 0.56
449	07-25-03	49.4	5.53 ± 0.35	4.04 ± 0.55
459	14-03-25	59.7	7.41 ± 0.47	5.85 ± 0.73

- 75 -

TABLE XVIII
ATOM CONCENTRATIONS

<u>Composition</u>	<u>Element</u>	<u>N X 10⁻²⁴</u>
1, Moderator	Hydrogen	0.0668
	Oxygen	0.0334
2, Inner zone fuel	Hydrogen	0.03636
	Oxygen	0.0325
	Stainless Steel	0.01061
	U-235	0.0002937
	U-238	0.00653
3, Outer zone fuel	Hydrogen	0.03636
	Oxygen	0.0325
	Stainless Steel	0.01061
	U-235	0.0003217
	U-238	0.00655
4, Flow block area	Hydrogen	0.03908
	Oxygen	0.01954
	Zircaloy II	0.017
5, Control rod and moderator	Hydrogen	0.0319
	B-10	0.003761
	Oxygen	0.0159
	Stainless Steel	0.04155
6, Follower and moderator	Hydrogen	0.02238
	Oxygen	0.02286
	Aluminum	0.00778
	Zircaloy	0.02119
7, Can	Stainless Steel	0.0847

TABLE XIX
DISADVANTAGE FACTORS
(In Fuel Regions as Determined by P₃ Approximation)

<u>Composition</u>	<u>Element</u>	<u>ϕ/ϕ_{cell}</u>
2	H	1.1356
	O	1.0000
	SS	0.9160
	U-235	0.7751
	U-238	0.7915
3	H	1.1446
	O	1.0000
	SS	0.9140
	U-235	0.7608
	U-238	0.7769

TABLE XX
EXPERIMENTAL AND CALCULATED FLUX AND POWER PEAKS

Run	Position		Experimental Magnitude		Calculated Magnitude	
	TKO Mesh	Mn-Cu Wire	Flux	Power*	Flux	Power*
418	4-7 ; plane 4 7-4 ; plane 4	14-03-25; 48.4 cm	7.53 ± 0.47	5.94 ± 0.74	7.67	7.36
418	7-3 ; plane 4 3-7 ; plane 4	- - -	- - -	- - -	10.3	9.31
420	4-4 ; plane 5	19-25-25; 69.0 cm	5.77 ± 0.36	4.55 ± 0.57	3.86	3.59
420	4-3 ; plane 5 3-4 ; plane 5	- - -	- - -	- - -	5.14	4.58

* Note that normalized power peak in the experiment is determined for the nearest fuel pin to the corner and does not lie on the point of measured flux; calculated normalized power peak is determined as if homogenized fuel existed at the mesh point.

FIG. 1: ELEVATION DIAGRAM OF SAVANNAH CONTROL RODS AND FUEL ELEMENTS IN TEST FACILITY

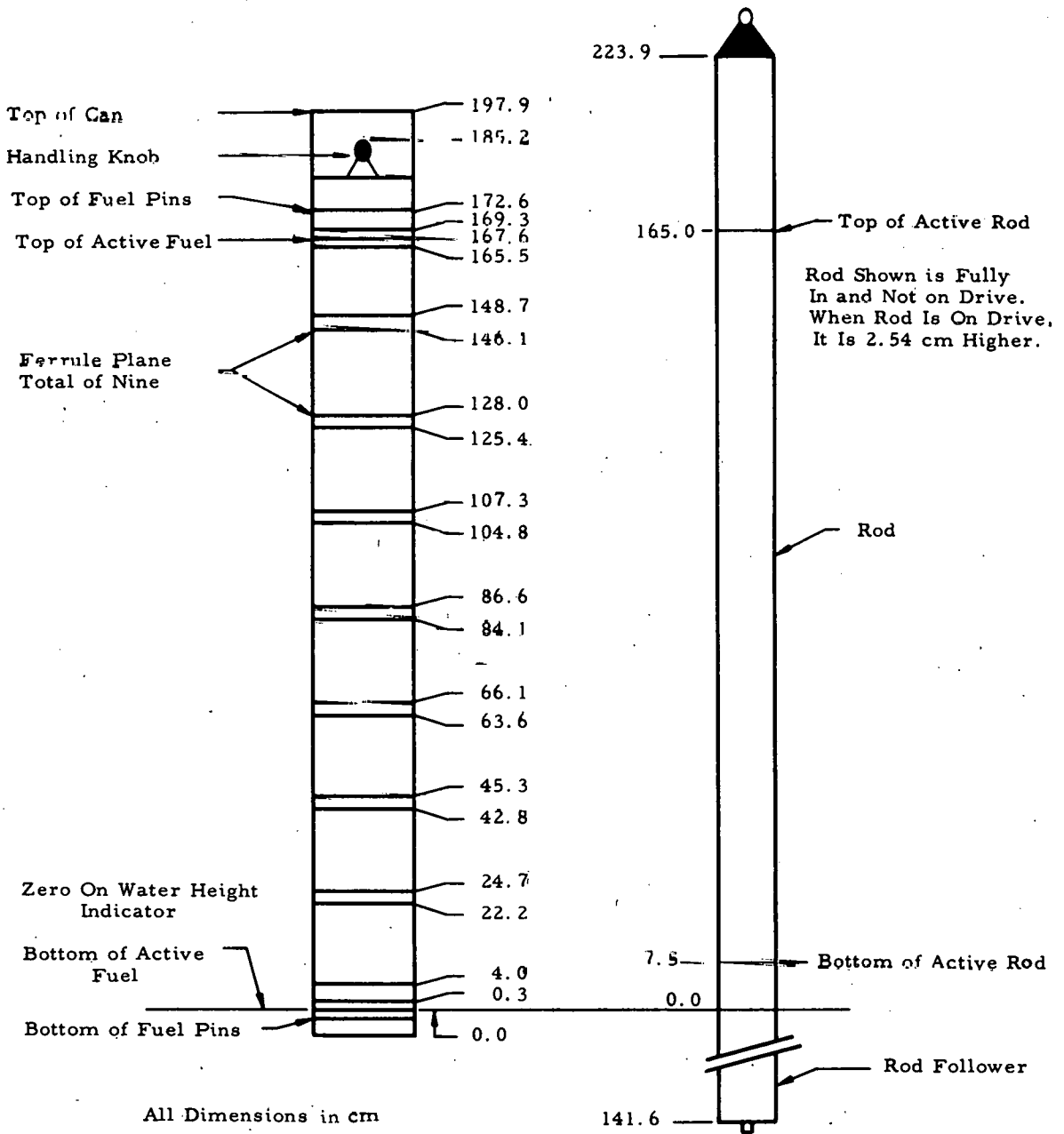


FIG. 2: NORMAL INSTRUMENT LOCATION AROUND CRITICAL FACILITY

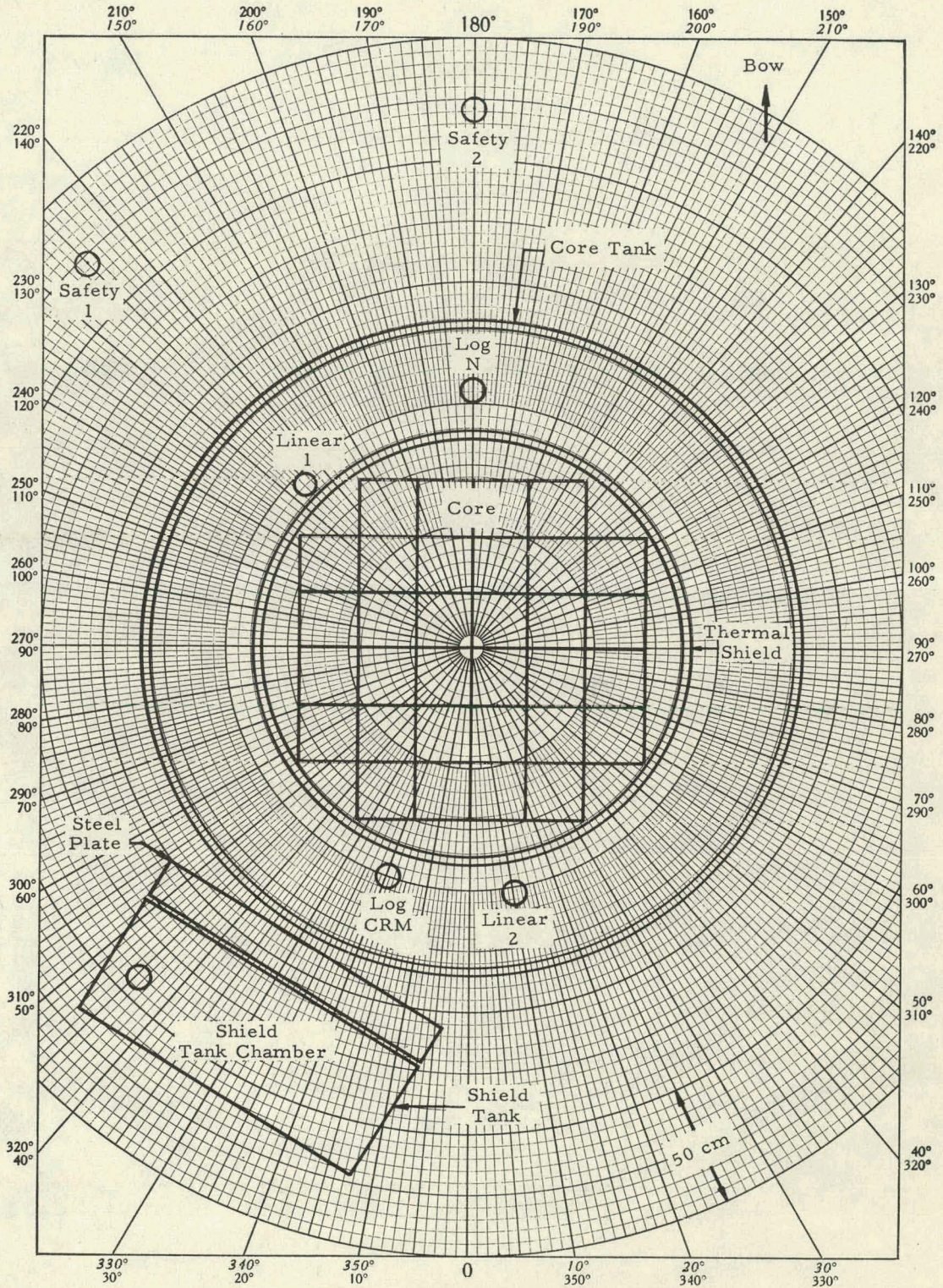


FIG. 3: PHOTOGRAPH OF SAVANNAH CORE

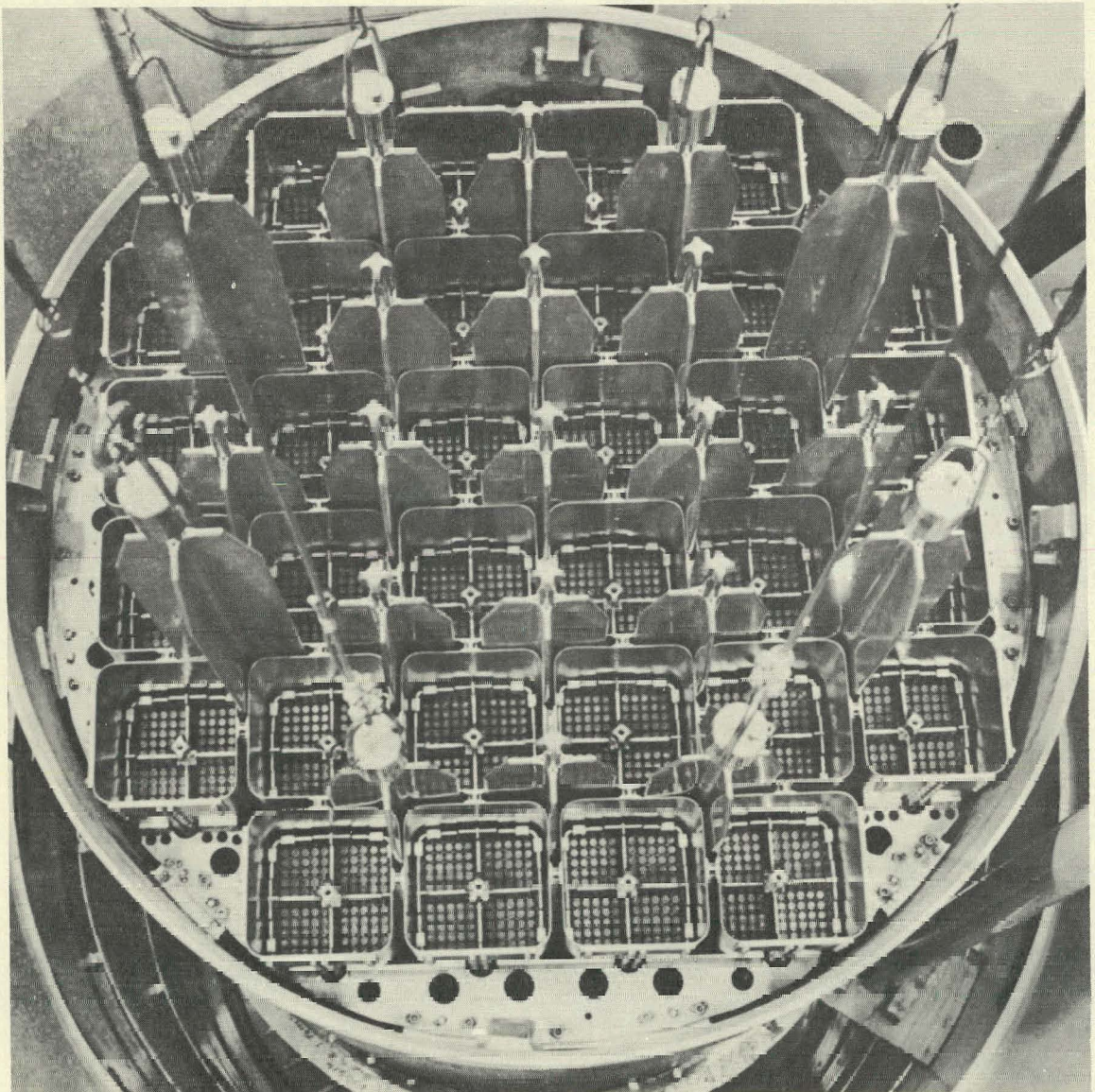


FIG. 4: BLOCK DIAGRAM OF INSTRUMENTATION FOR ZERO POWER
EXTENSION TESTS ON CORE I

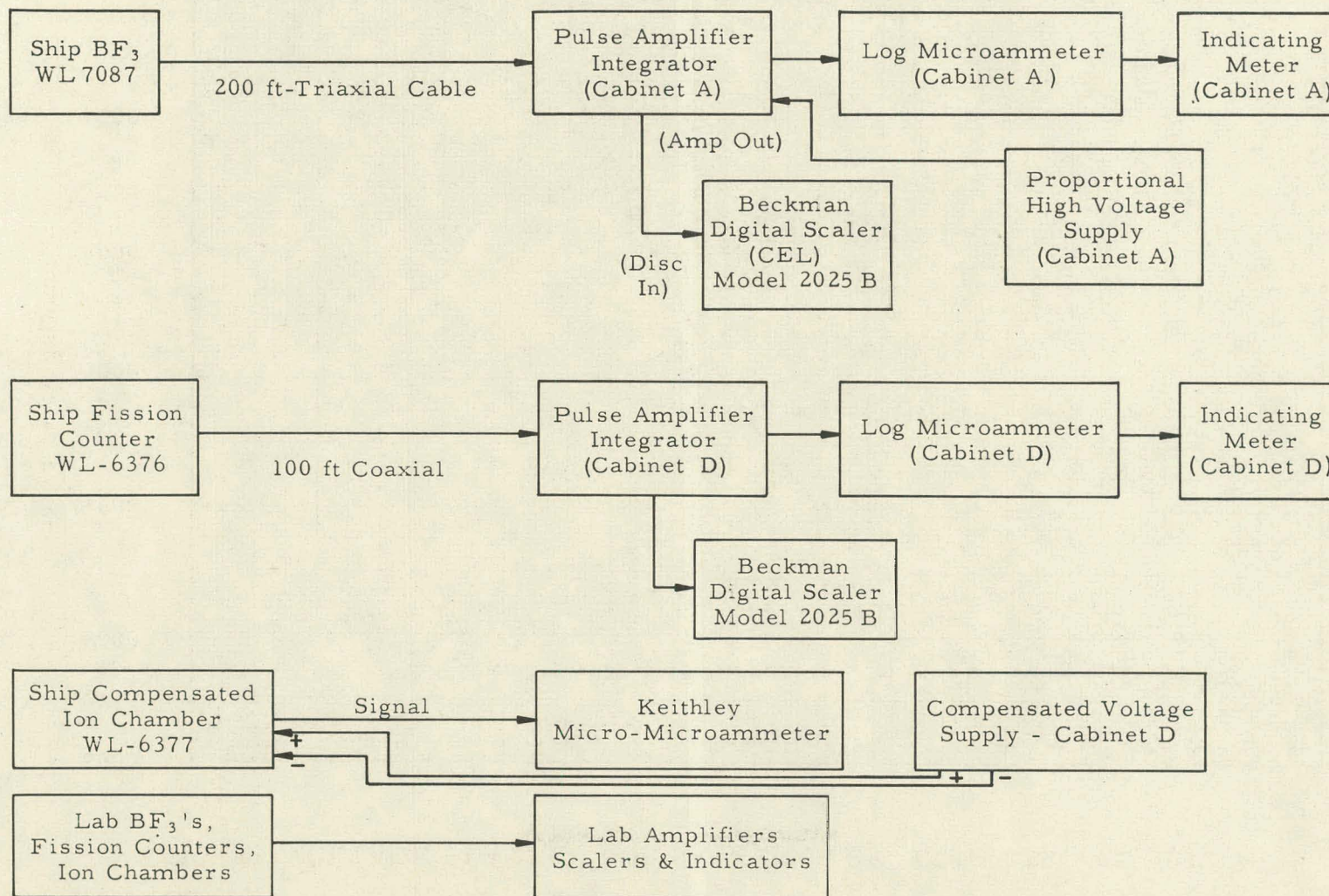


FIG. 5: VOLTAGE PLATEAU FOR SAVANNAH BF₃ COUNTER, WL-7087

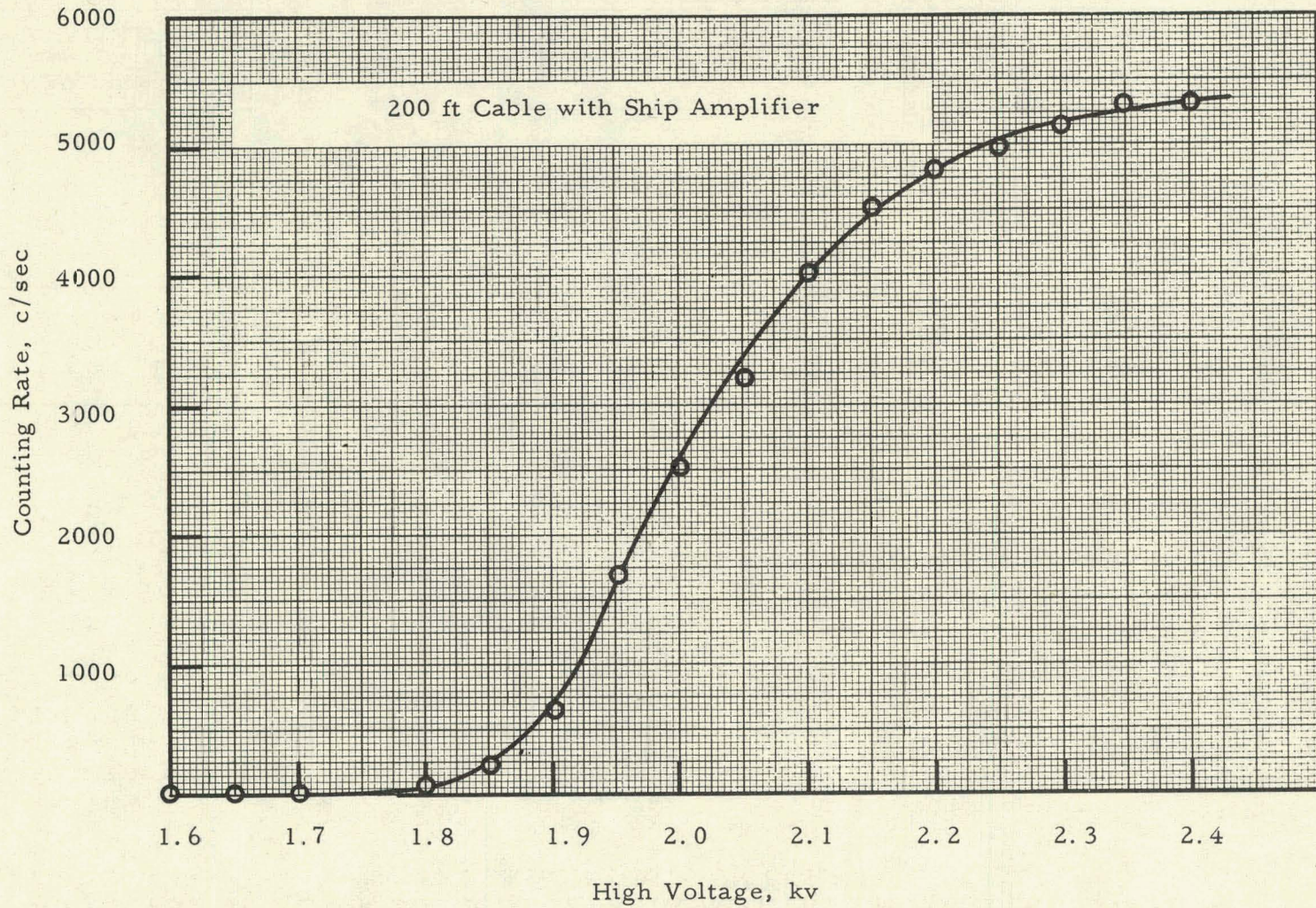


FIG. 6: BIAS CURVE WITH REACTOR FOR SAVANNAH FISSION COUNTER, WL-6376

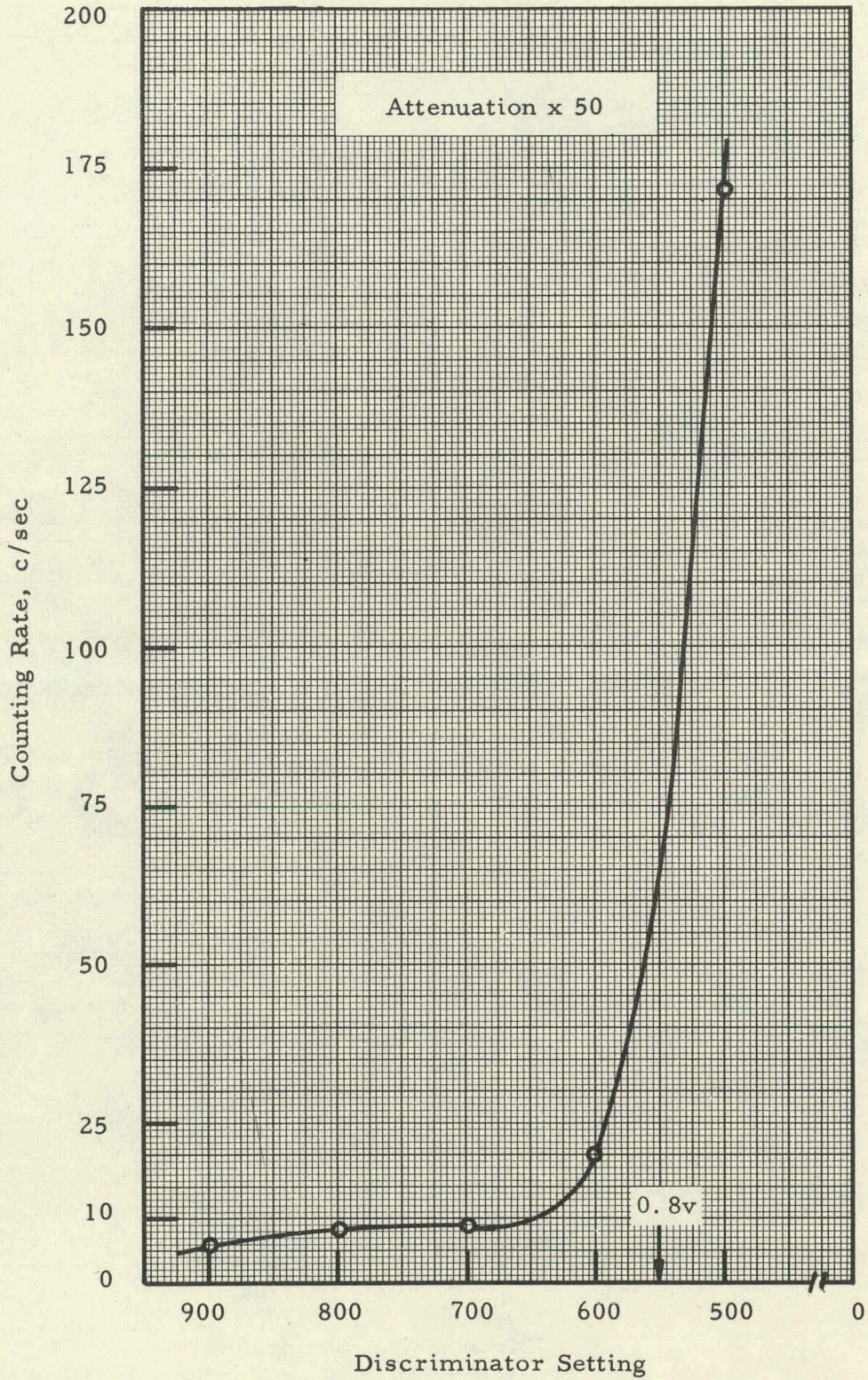


FIG. 7: BIAS CURVE WITH Po-Be SOURCE FOR SAVANNAH FISSION COUNTER, WL-6376

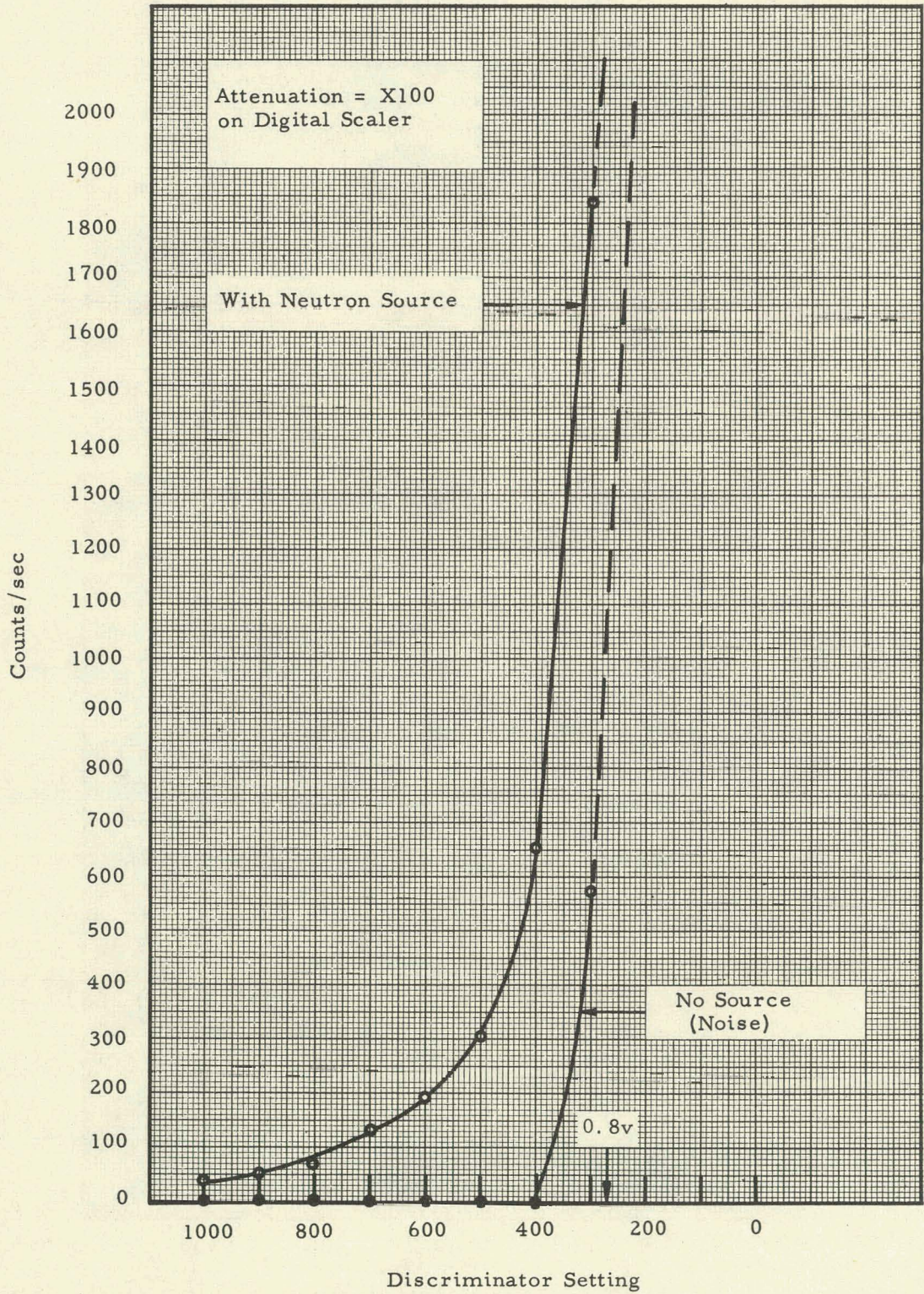


FIG. 8: SIMULTANEOUS RESPONSE OF THREE SHIP DETECTORS

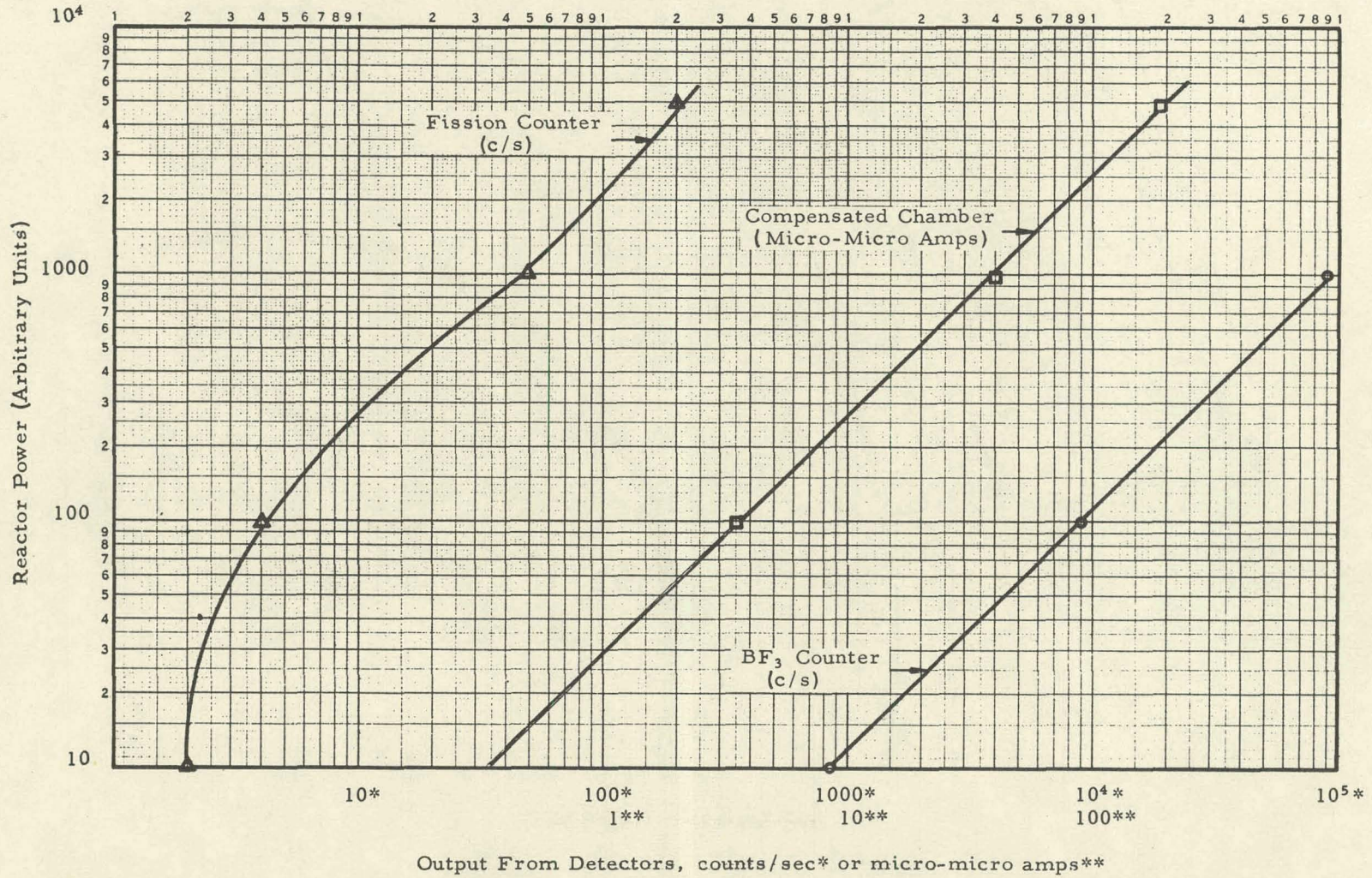


FIG. 9: LOCATION OF INSTRUMENTS IN SHIELD MOCKUP AT
CEL - TOP VIEW

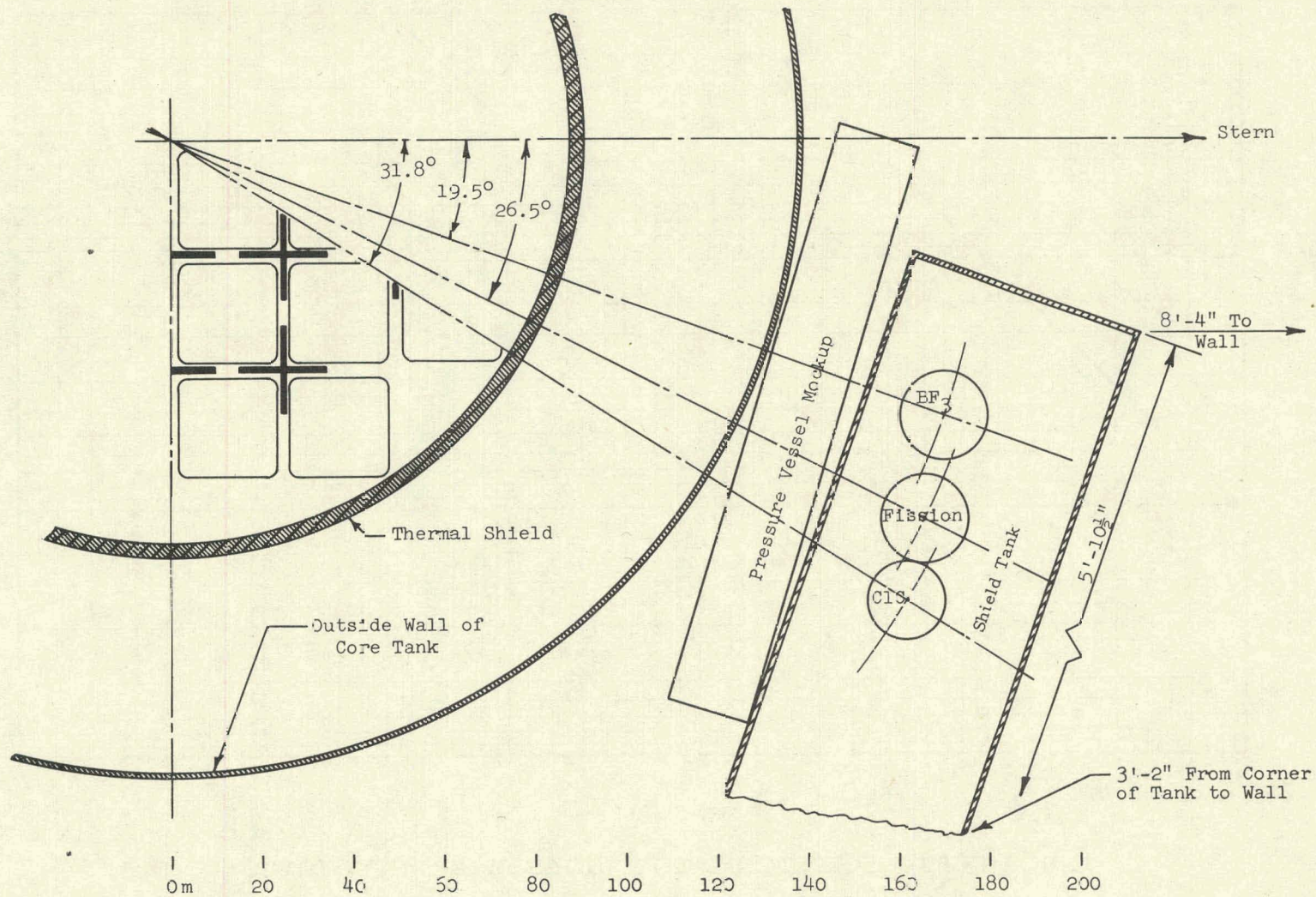
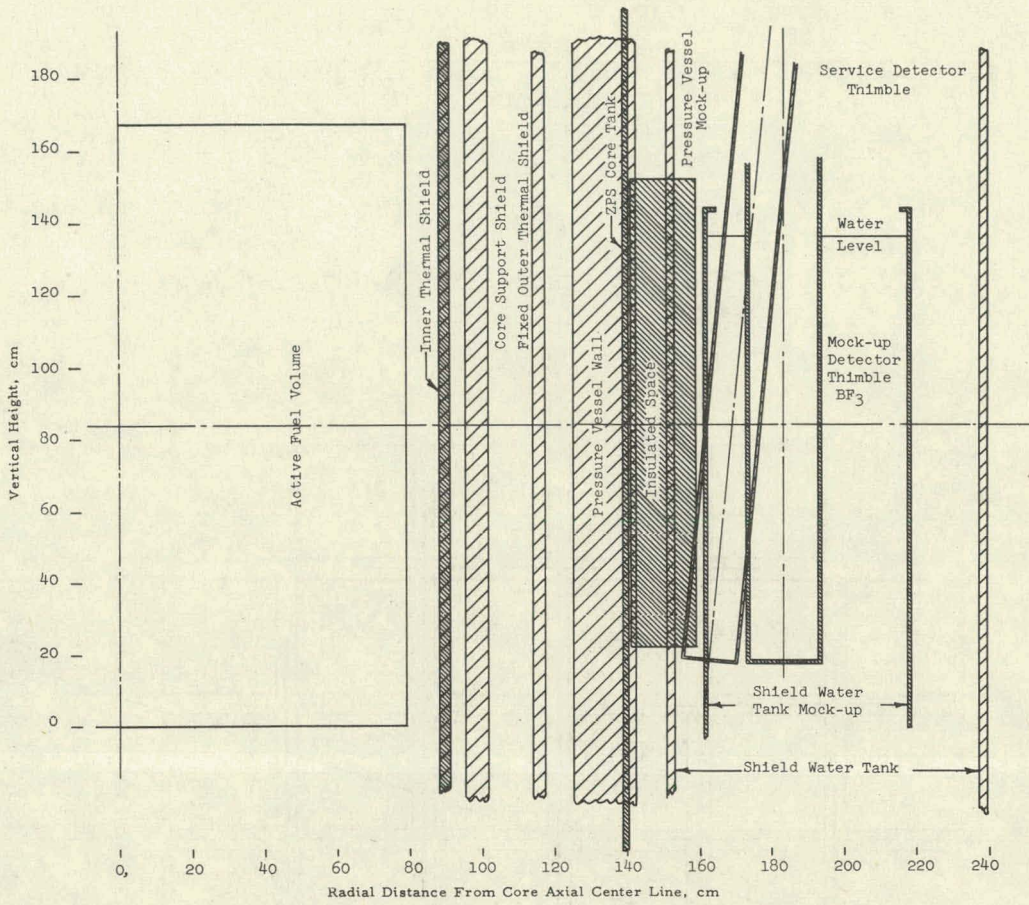


FIG. 10: RELATIVE DISTANCES OF INSTRUMENTS FROM REACTOR - SIDE VIEW



NS Savannah
 CEL Experiment and NS Savannah
 CEL Experiment

Thimble Shielding Difference cm Radial				
	NMSR	BF ₃	Fission	CIC
Steel	25.7	19.4	19.5	19.8
H ₂ O	33.7	57.8	61.3	63.8
Void	8.5	3.1	4.8	7.0
Total	67.9	80.3	85.6	90.6

Difference From NMSR Δcm Radial			
	BF ₃	Fission	CIC
Steel	-6.3	-6.2	-5.9
H ₂ O	+24.1	+27.6	+30.1
Void	-5.4	-3.7	-1.5
Net	+12.4	+17.7	+22.7

	Mockup Radial Distances, cm					
	BF ₃		Fission		CIC	
	Δ	Σ	Δ	Σ	Δ	Σ
Thermal Shield OD	91.5	91.5	91.5	91.5	91.5	91.5
H ₂ O	46.3	46.3	46.3	46.3	46.3	46.3
Core Tank ID	137.8	137.8	137.8	137.8	137.8	137.8
Steel	1.1	1.1	1.1	1.1	1.1	1.1
Core Tank OD	138.9	138.9	138.9	138.9	138.9	138.9
Void	0.8	0.8	2.8	2.8	5.5	5.5
Plate "ID"	139.7	139.7	141.7	141.7	144.4	144.4
Steel	18.0	18.0	18.1	18.1	18.4	18.4
Plate "OD"	157.7	157.7	159.8	159.8	162.8	162.8
Void	2.3	2.3	2.0	2.0	1.5	1.5
Tank "ID"	160.0	160.0	161.8	161.8	164.3	164.3
Steel	0.3	0.3	0.3	0.3	0.3	0.3
Tank "OD"	160.3	160.3	162.1	162.1	164.6	164.6
H ₂ O	11.5	11.5	15.0	15.0	17.5	17.5
Thimble Outer Edge	171.8	171.8	177.1	177.1	182.1	182.1
Thimble Wall	0.8	0.8	0.8	0.8	0.8	0.8
Thimble Inner Edge	172.6	172.6	177.9	177.9	182.9	182.9
Void	7.7	7.7	7.7	7.7	7.7	7.7
Thimble Center Line	180.3	180.3	185.6	185.6	190.6	190.6

NOTE: Δ = Difference
Σ = Sum

FIG. 11: PLACEMENT OF DETECTORS AROUND CORE ABOARD NS SAVANNAH

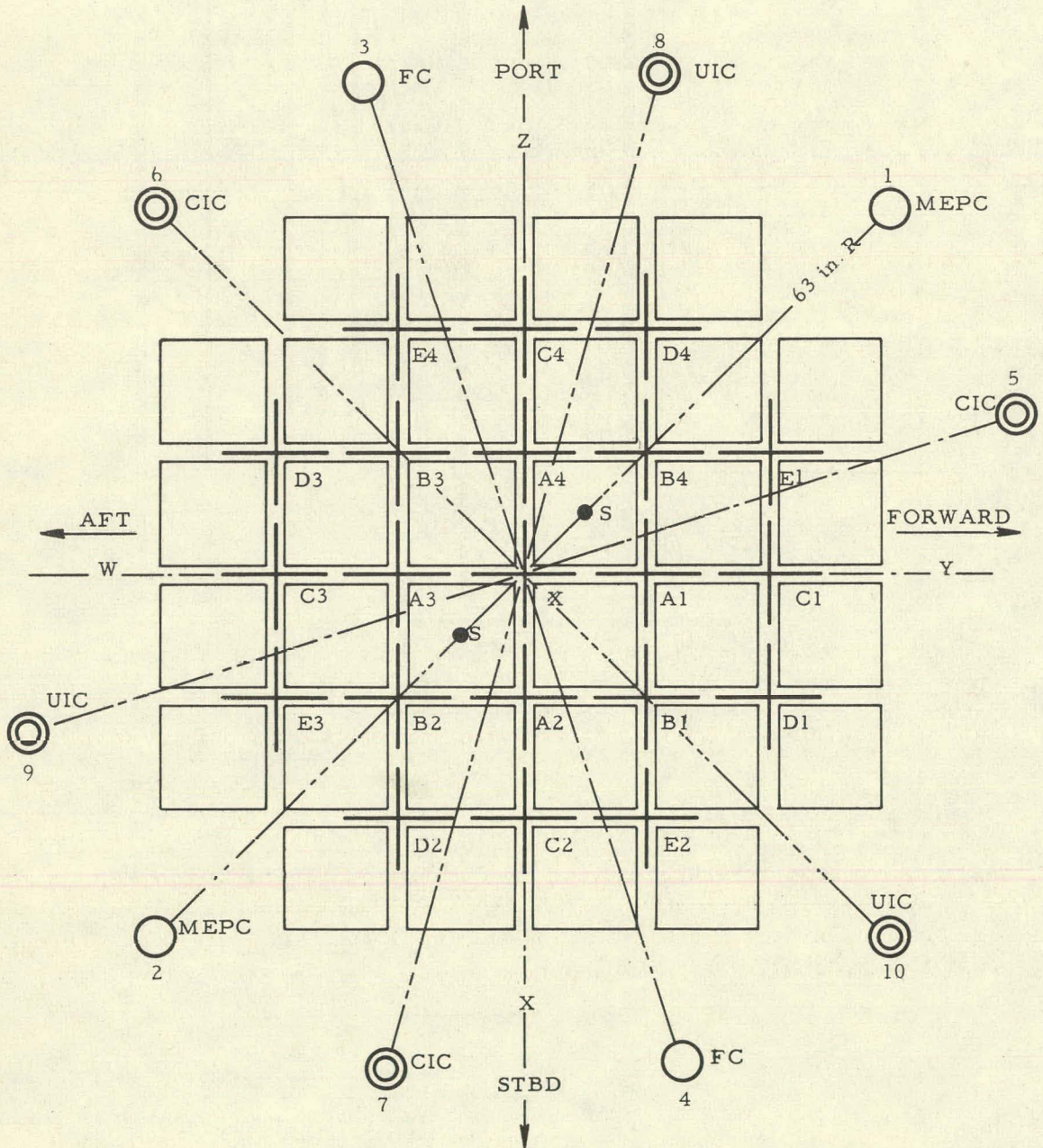


FIG. 12: FLUX DISTRIBUTION V_s DISTANCE FROM THERMAL SHIELD AT CEL

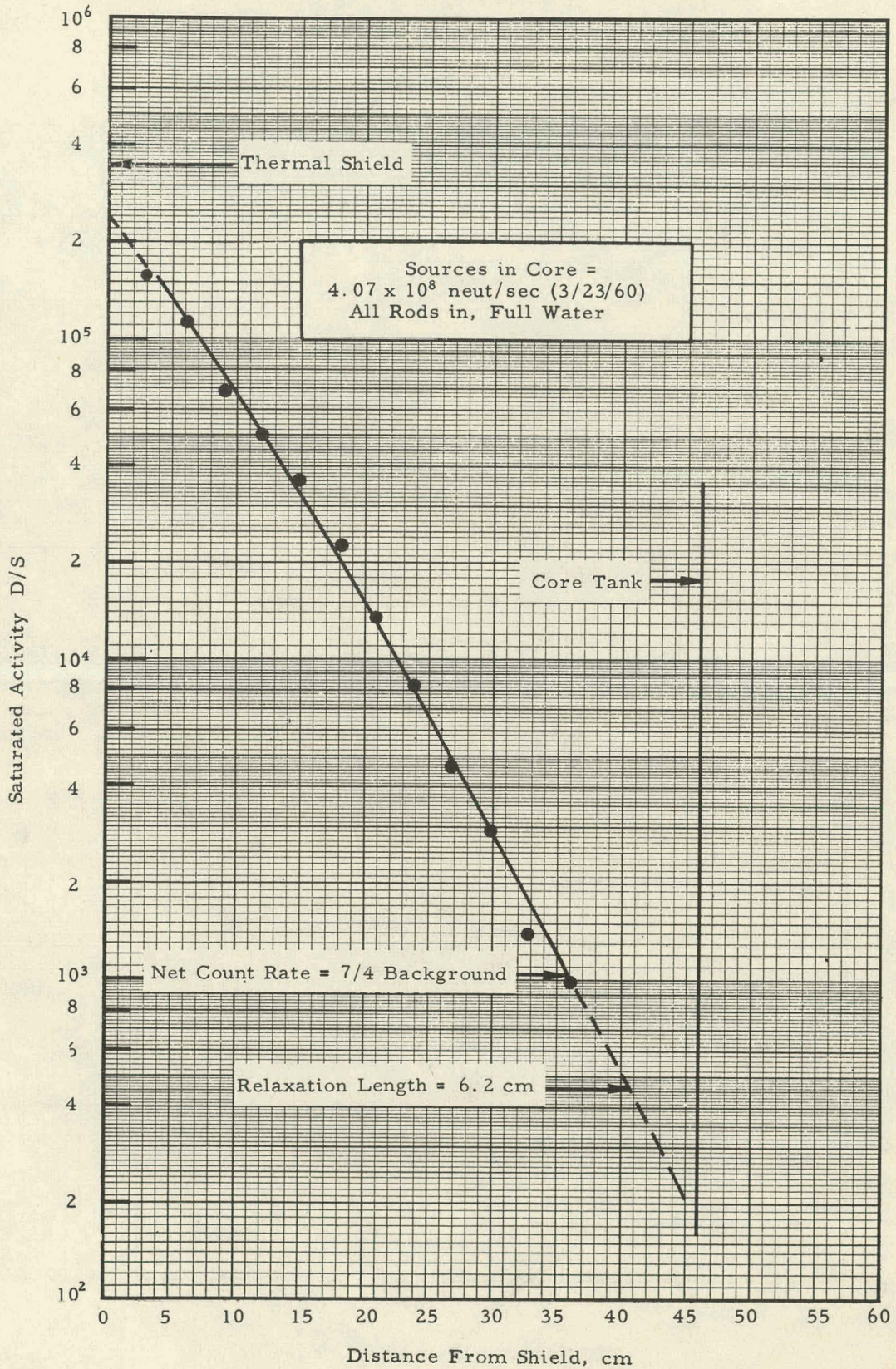


FIG. 13: SHIP DETECTOR RESPONSE Vs FUEL ELEMENTS LOADED

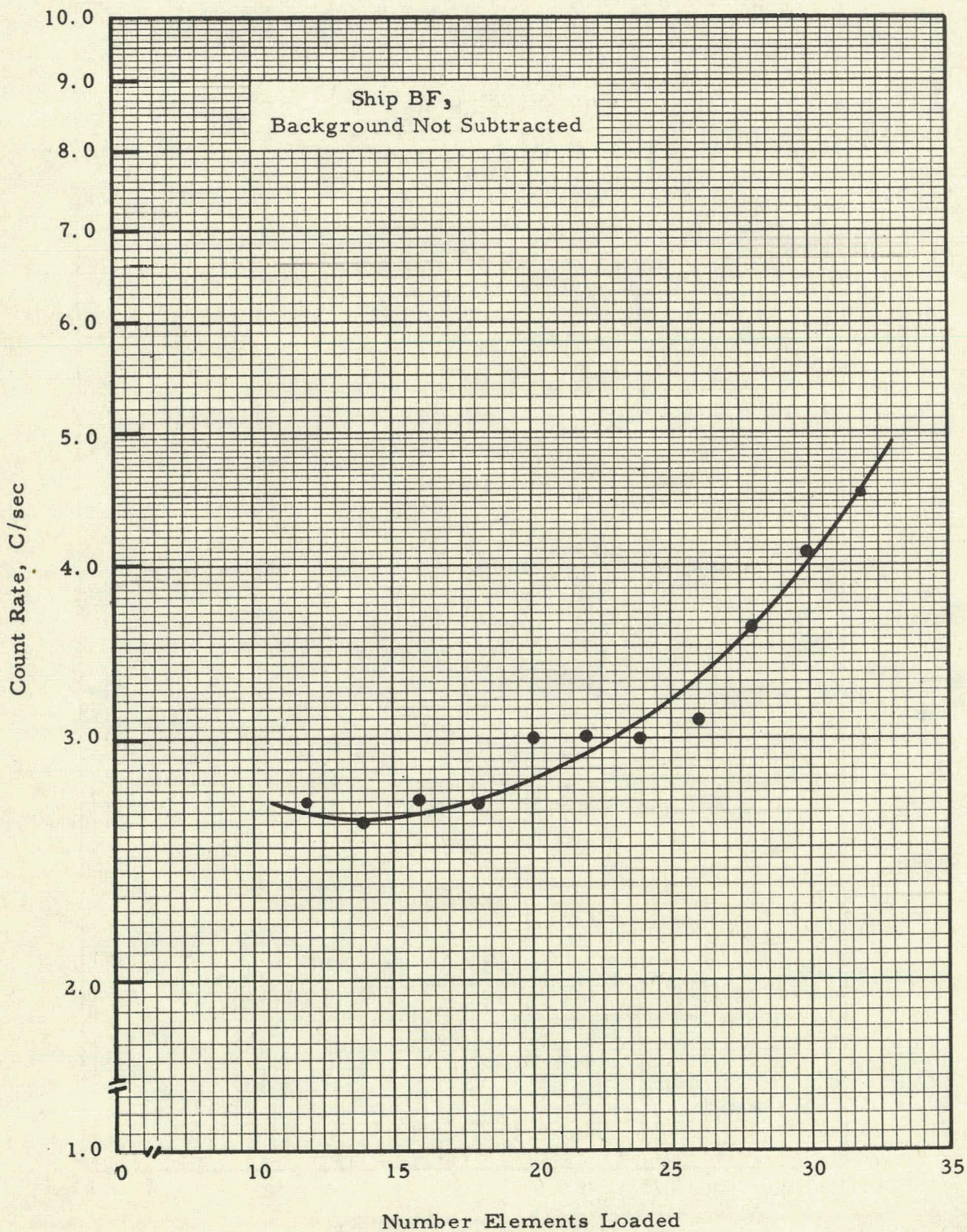


FIG. 14: NORMALIZED INVERSE COUNT RATE OF SHIP BF₃ IN
CEL MOCKUP - NS SAVANNAH CORE I

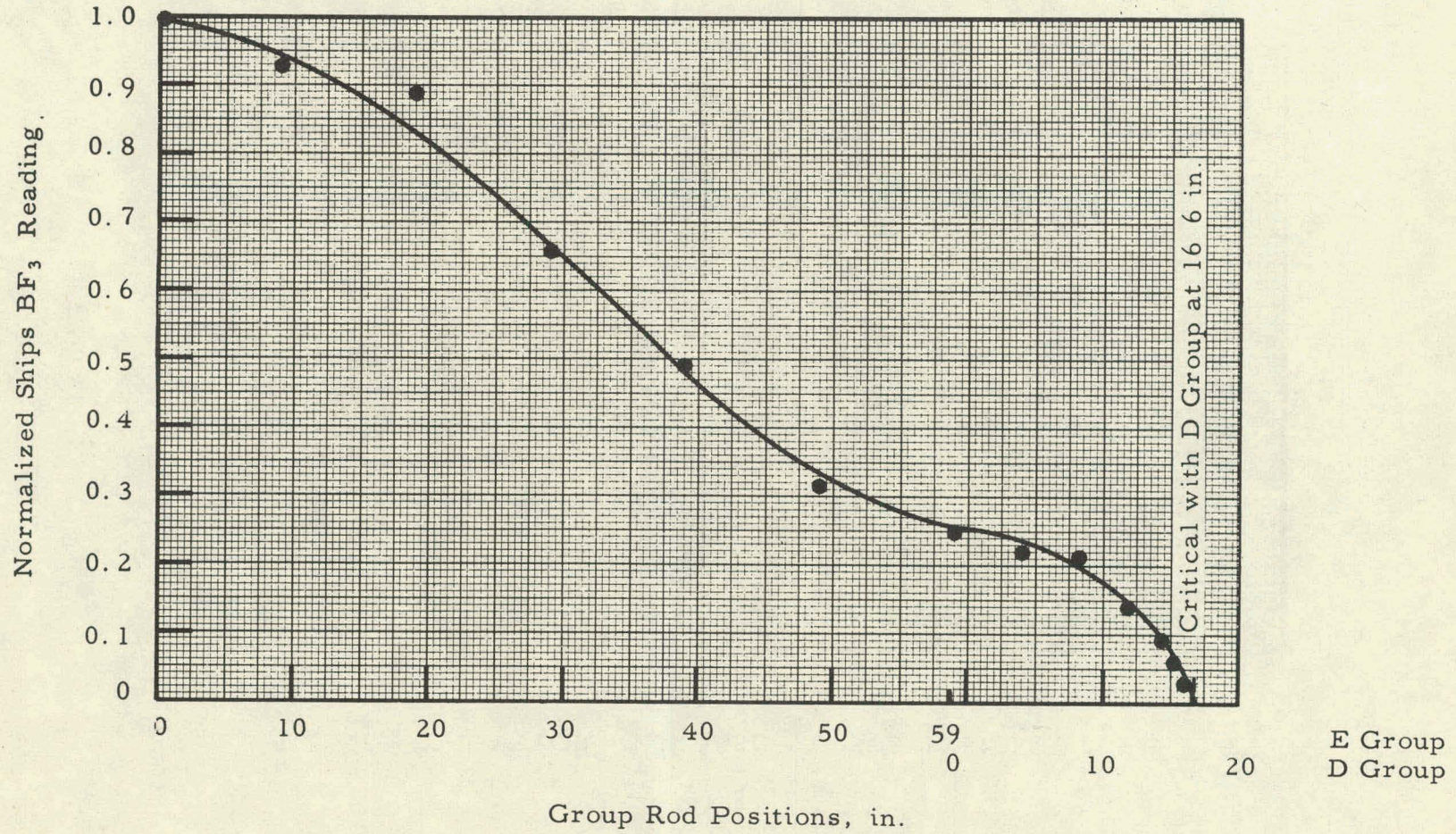


FIG. 15: DETECTOR RESPONSE VERSUS TEMPERATURE

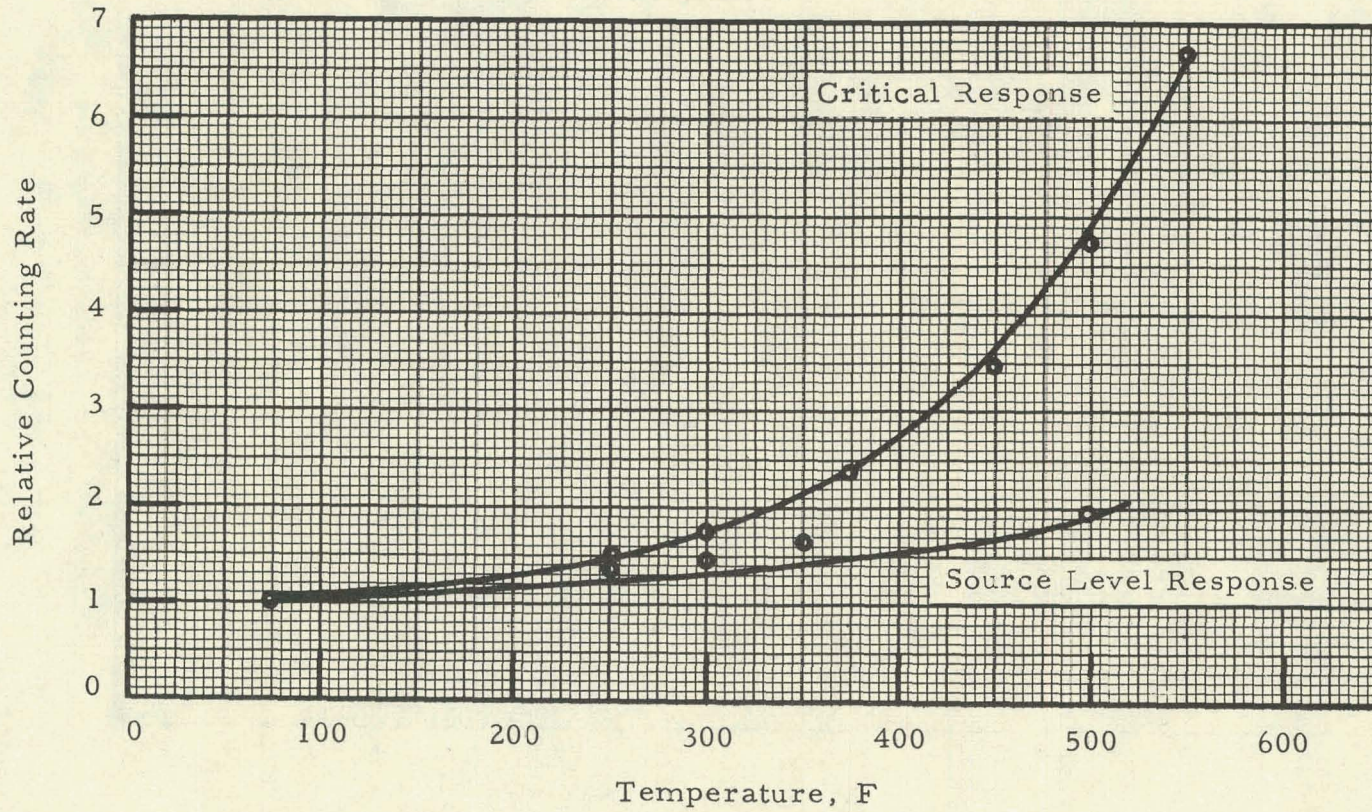


FIG. 16: WIRE AND FOIL LOCATION FOR POWER CALIBRATION

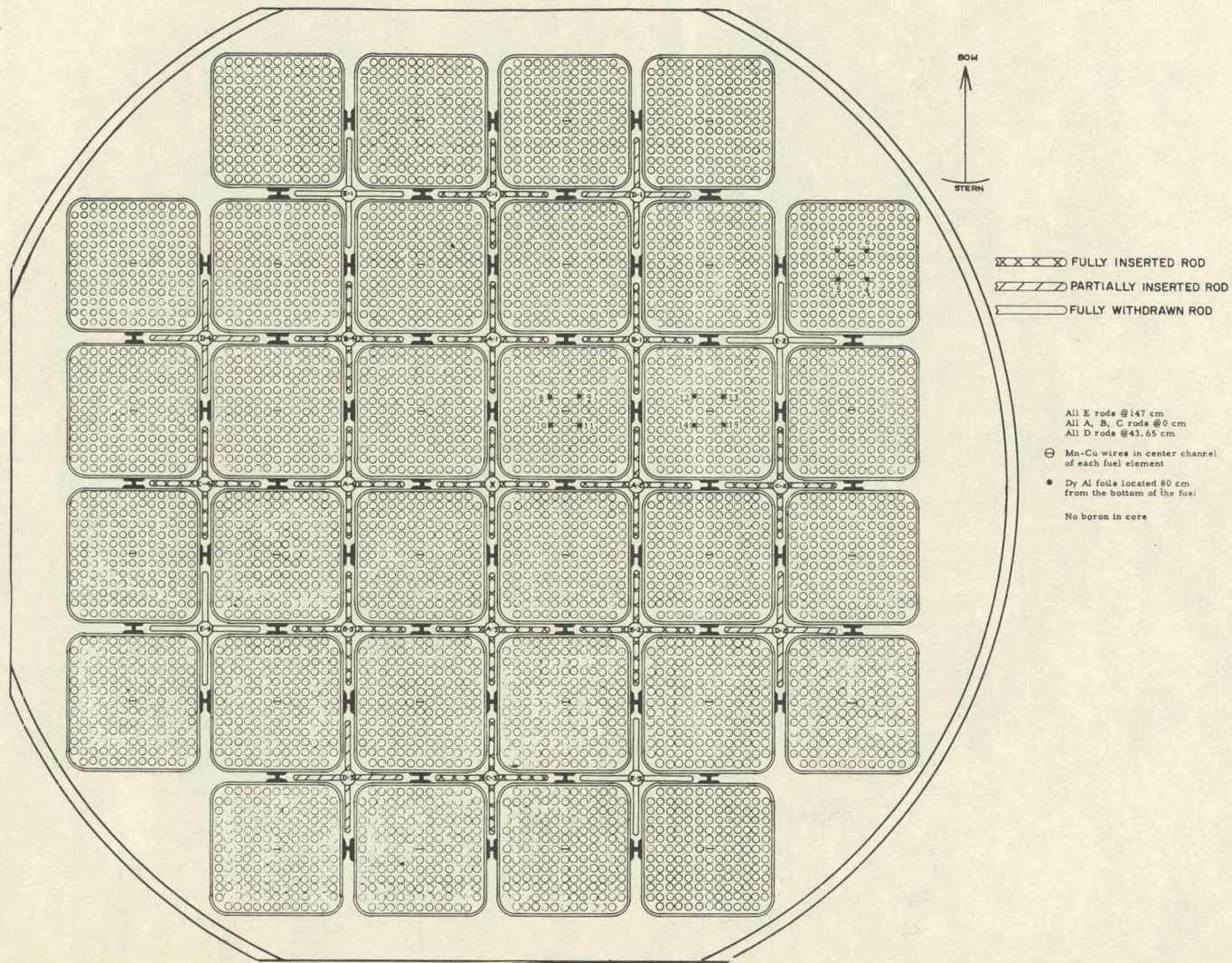
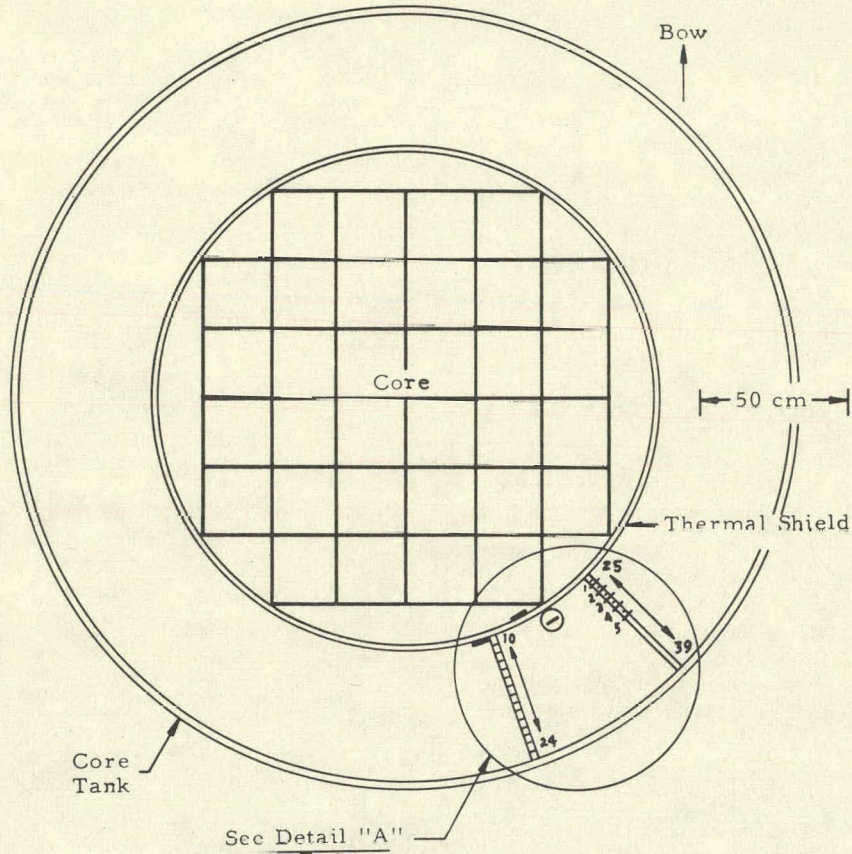


FIG. 17: NICKEL AND GOLD FOIL LOCATION IN CORE FOR FAST FLUX MEASUREMENT



Note: All foils located 84 cm below top of fuel pins

DETAIL "A"

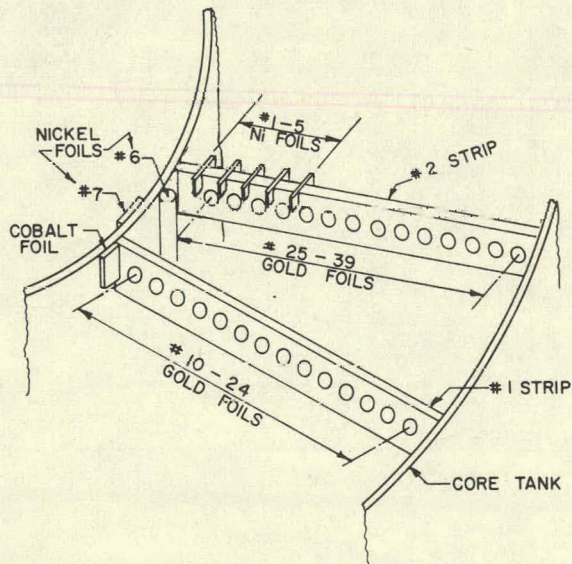


FIG. 18: GOLD FOIL TRAVERSE AT CORE CENTERLINE FROM CORE TANK TO THERMAL SHIELD

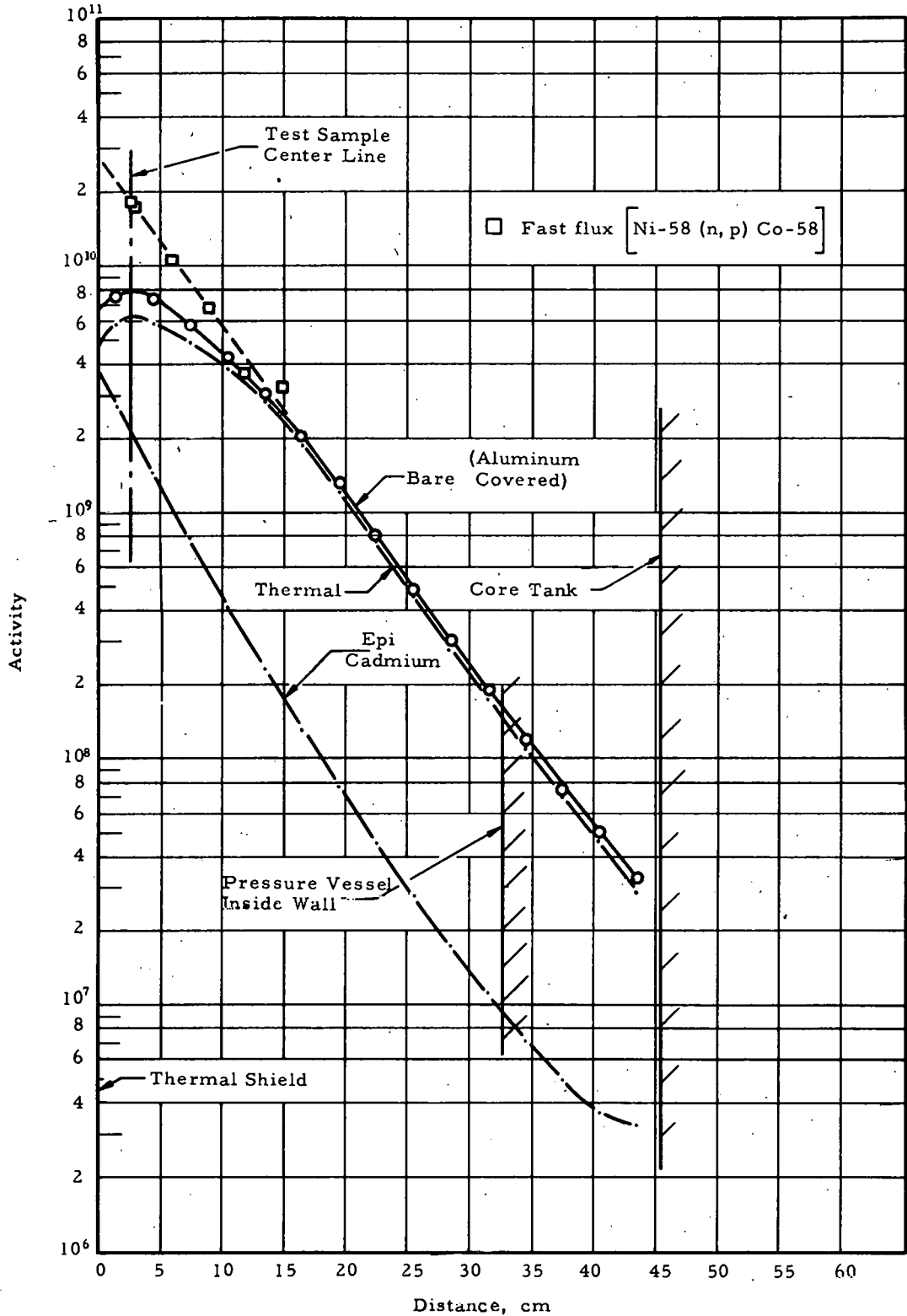


FIG. 19: GOLD FOIL TRAVERSE AT TOP OF FUEL FROM CORE TANK TO THERMAL SHIELD

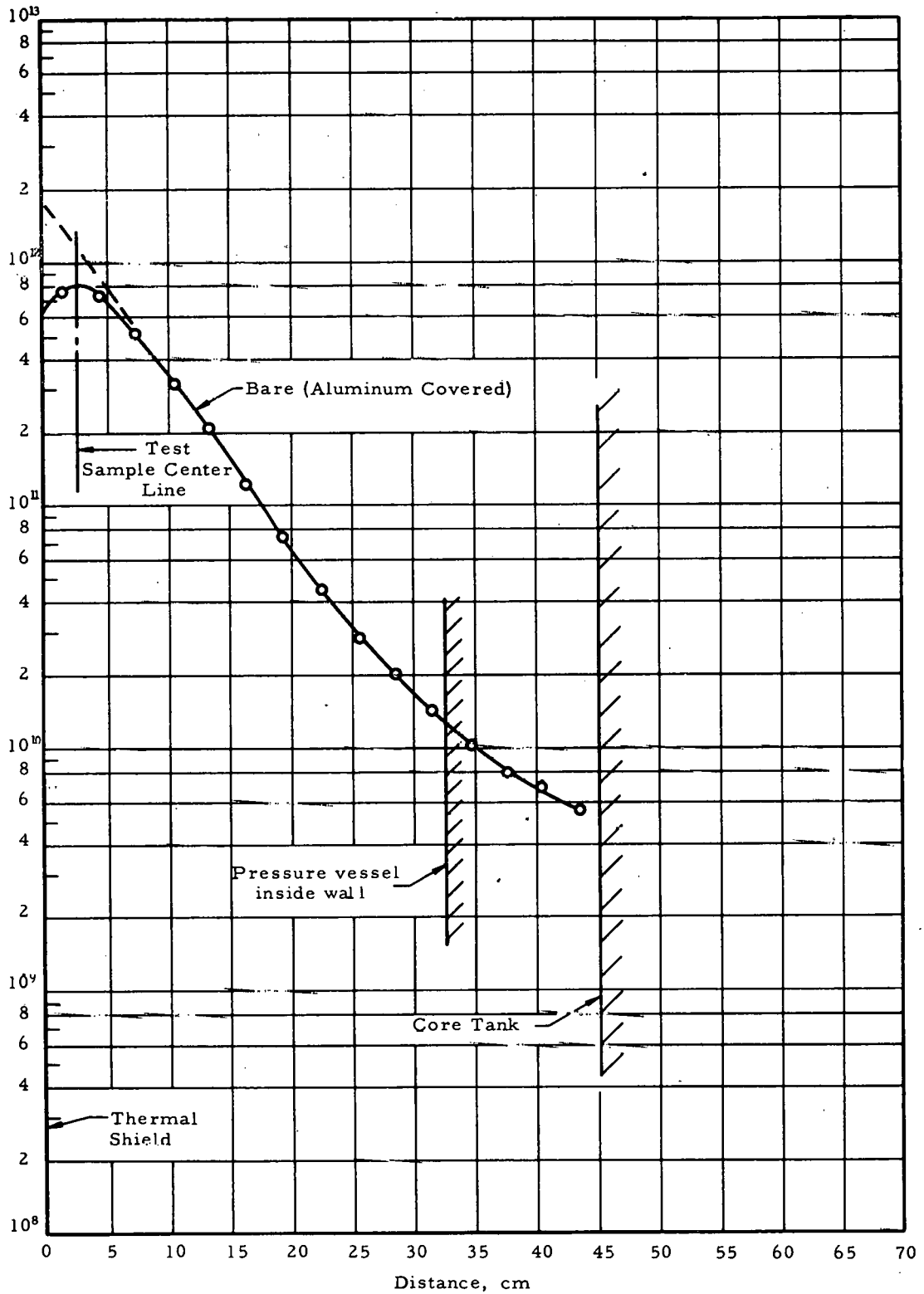


FIG. 20: SPATIAL RESOLUTION OF WIRE SCANNER

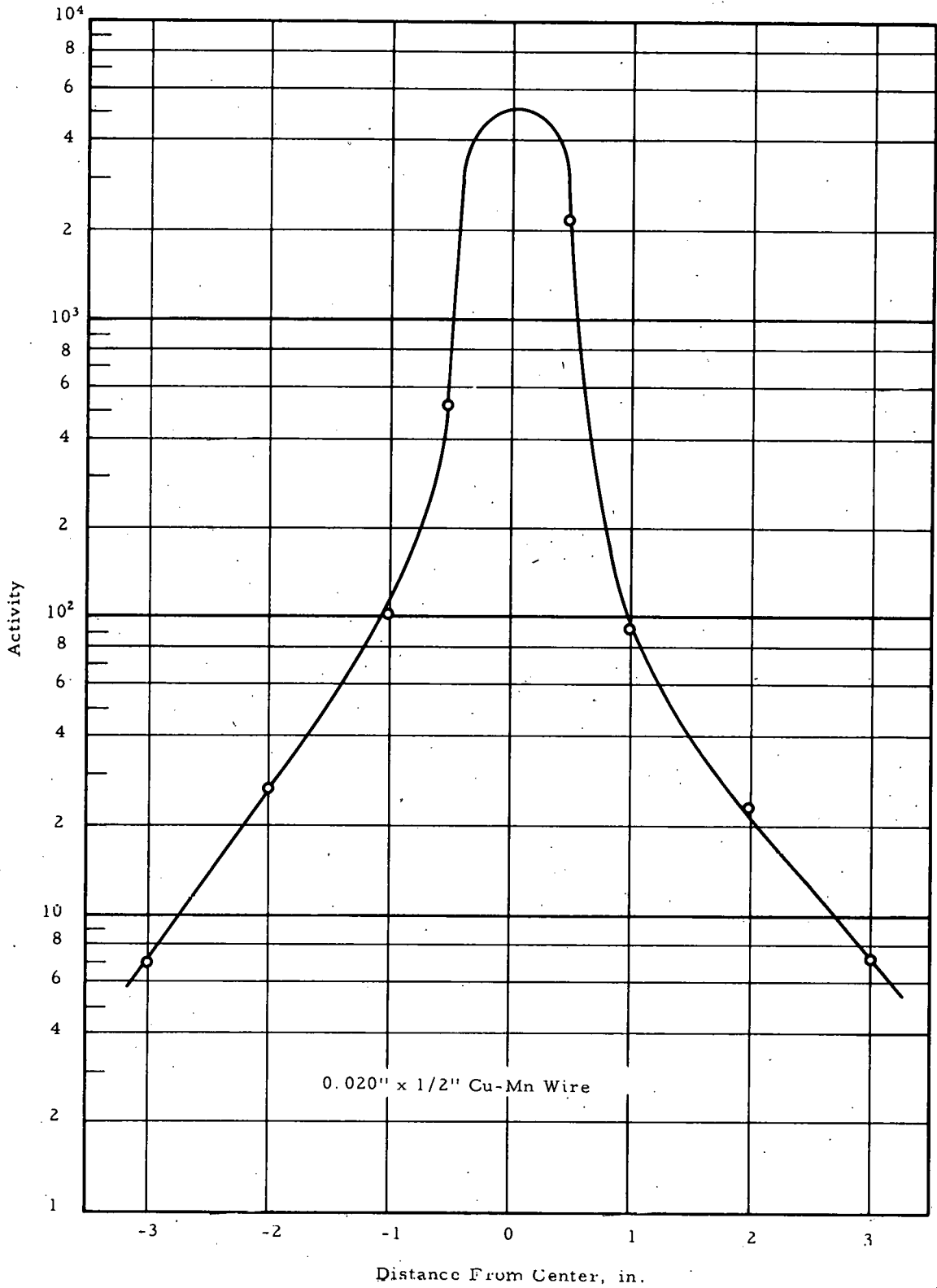


FIG. 21: BLOCK DIAGRAM OF WIRE SCANNER

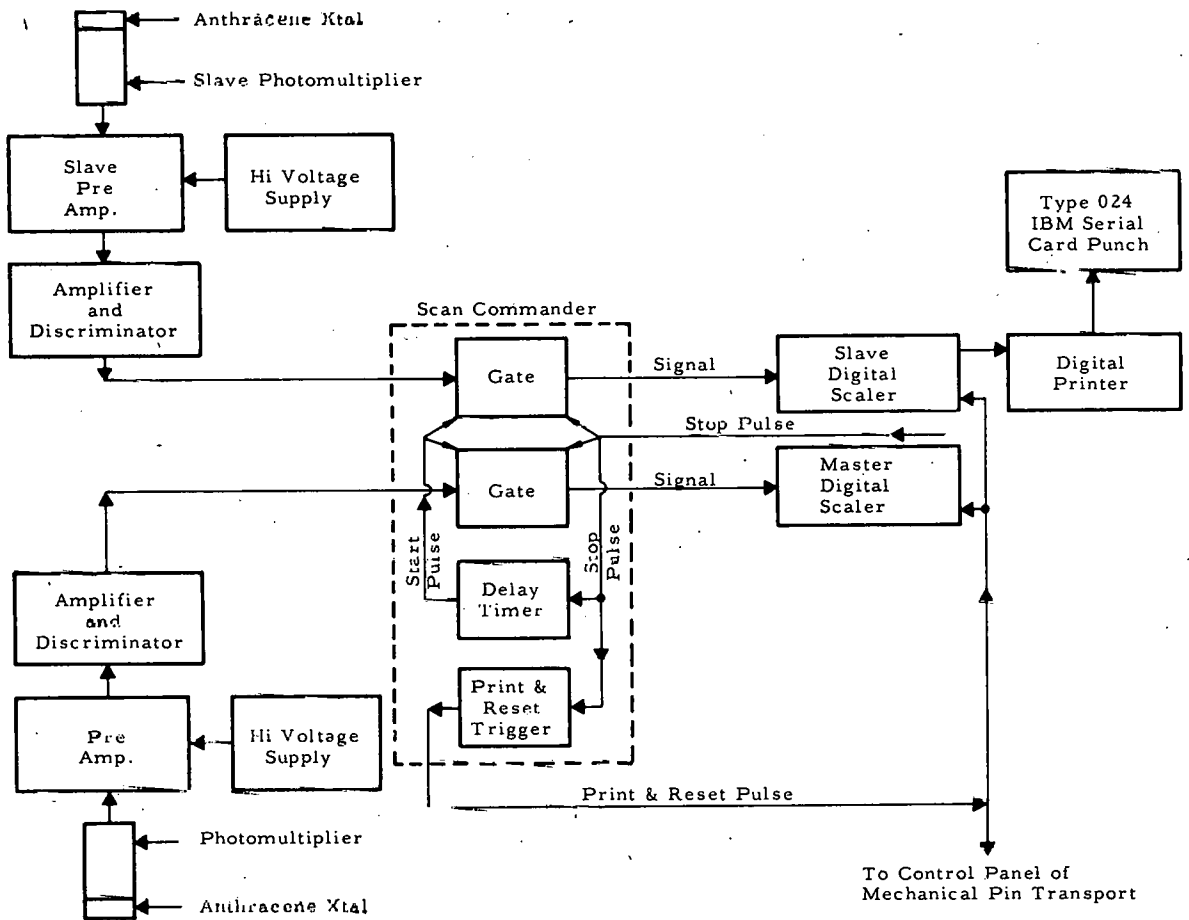


FIG. 22: RESOLUTION LOSS OF WIRE SCANNER WITH Mn-Cu WIRE

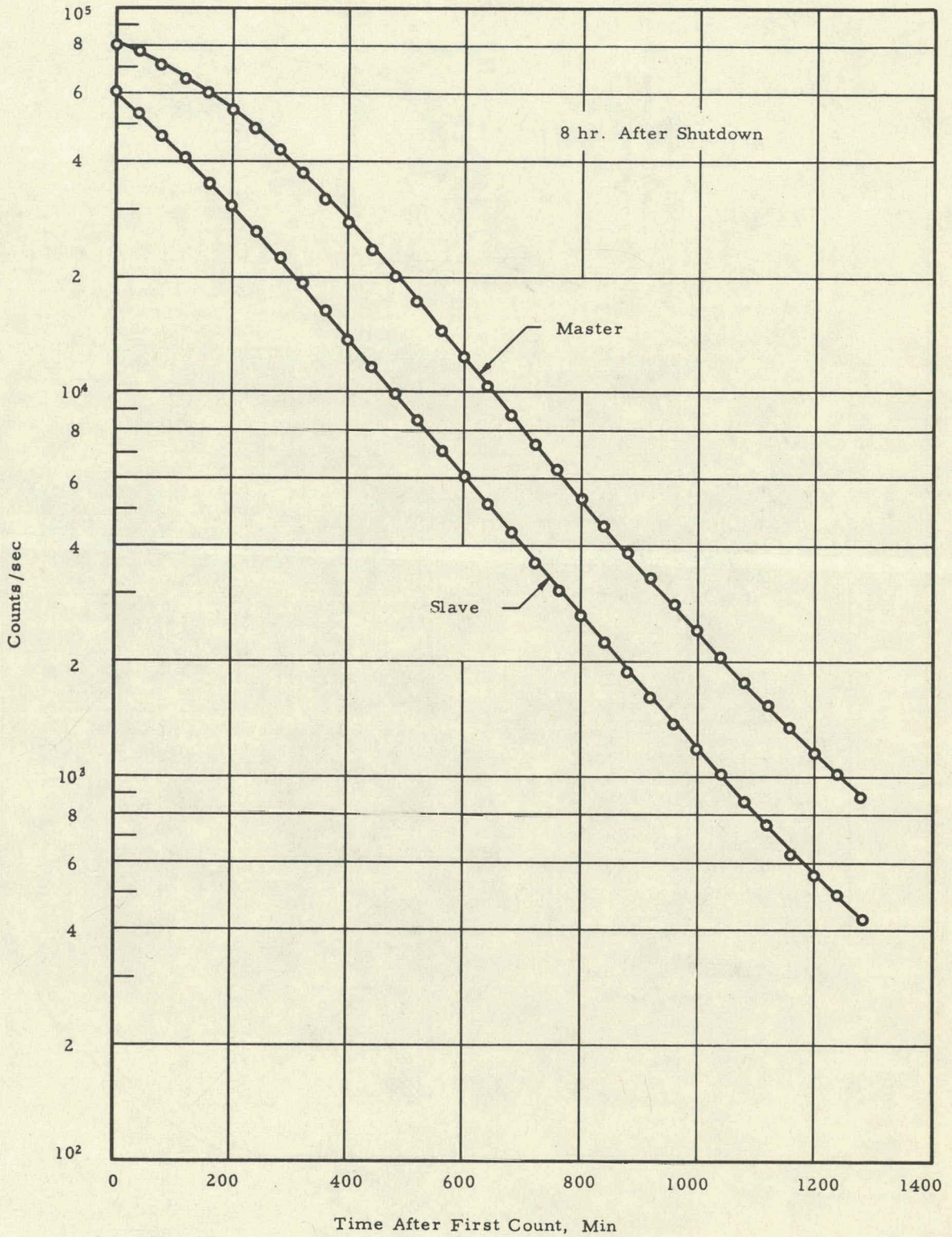


FIG. 23: RADIAL PROFILE OF AXIALLY AVERAGED FLUX

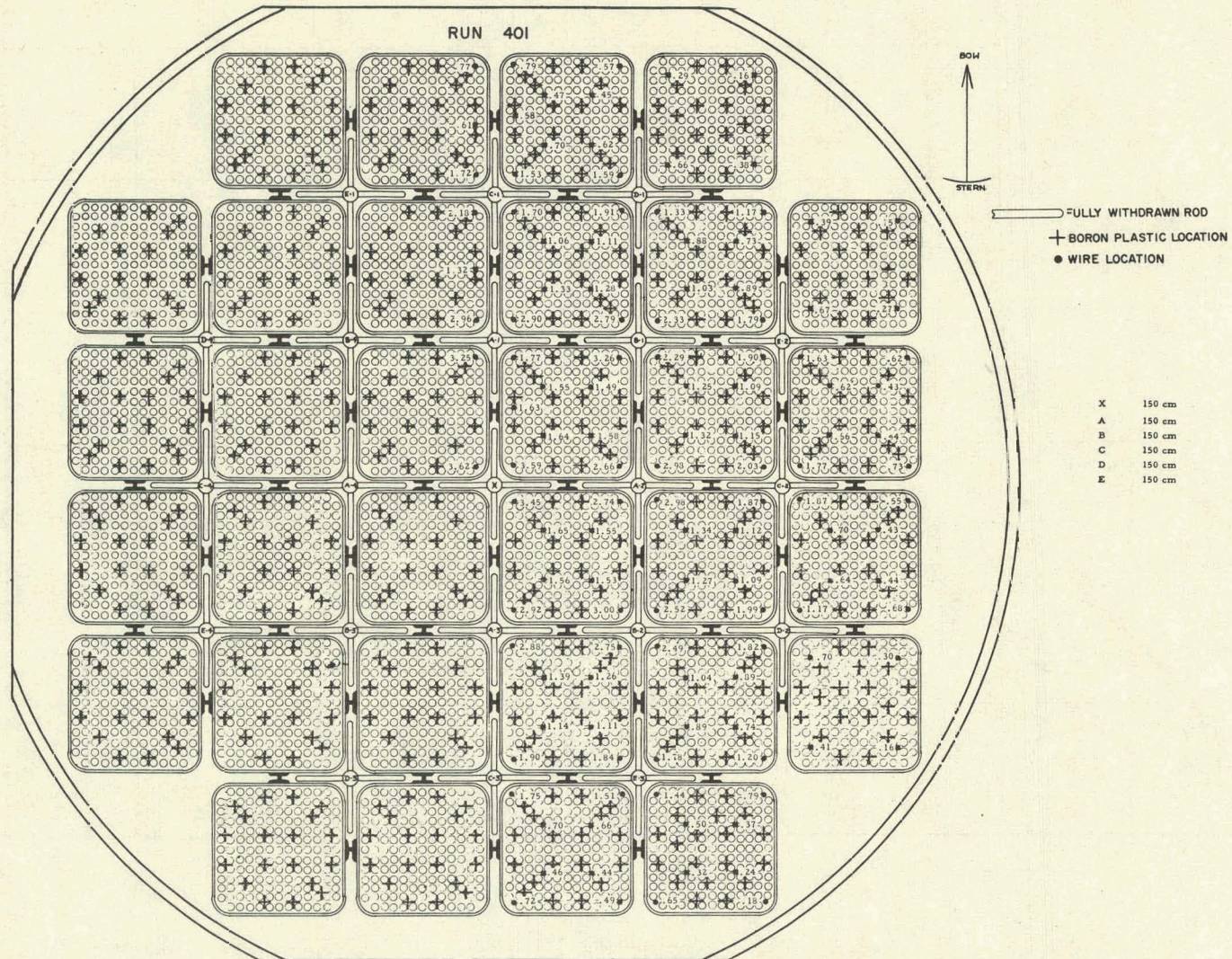


FIG. 24: RADIAL PROFILE OF AXIALLY AVERAGED FLUX

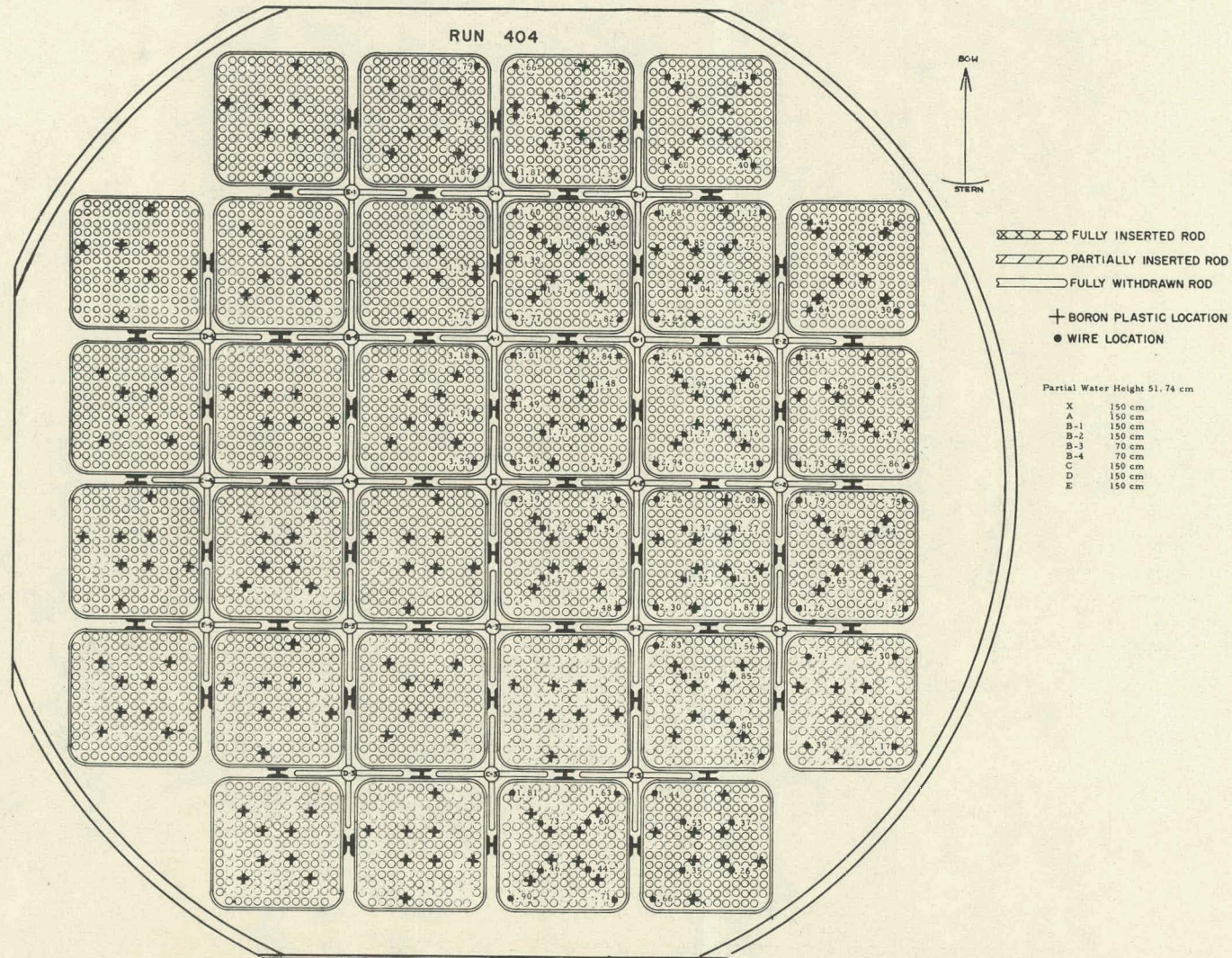


FIG. 25: RADIAL PROFILE OF AXIALLY AVERAGED FLUX

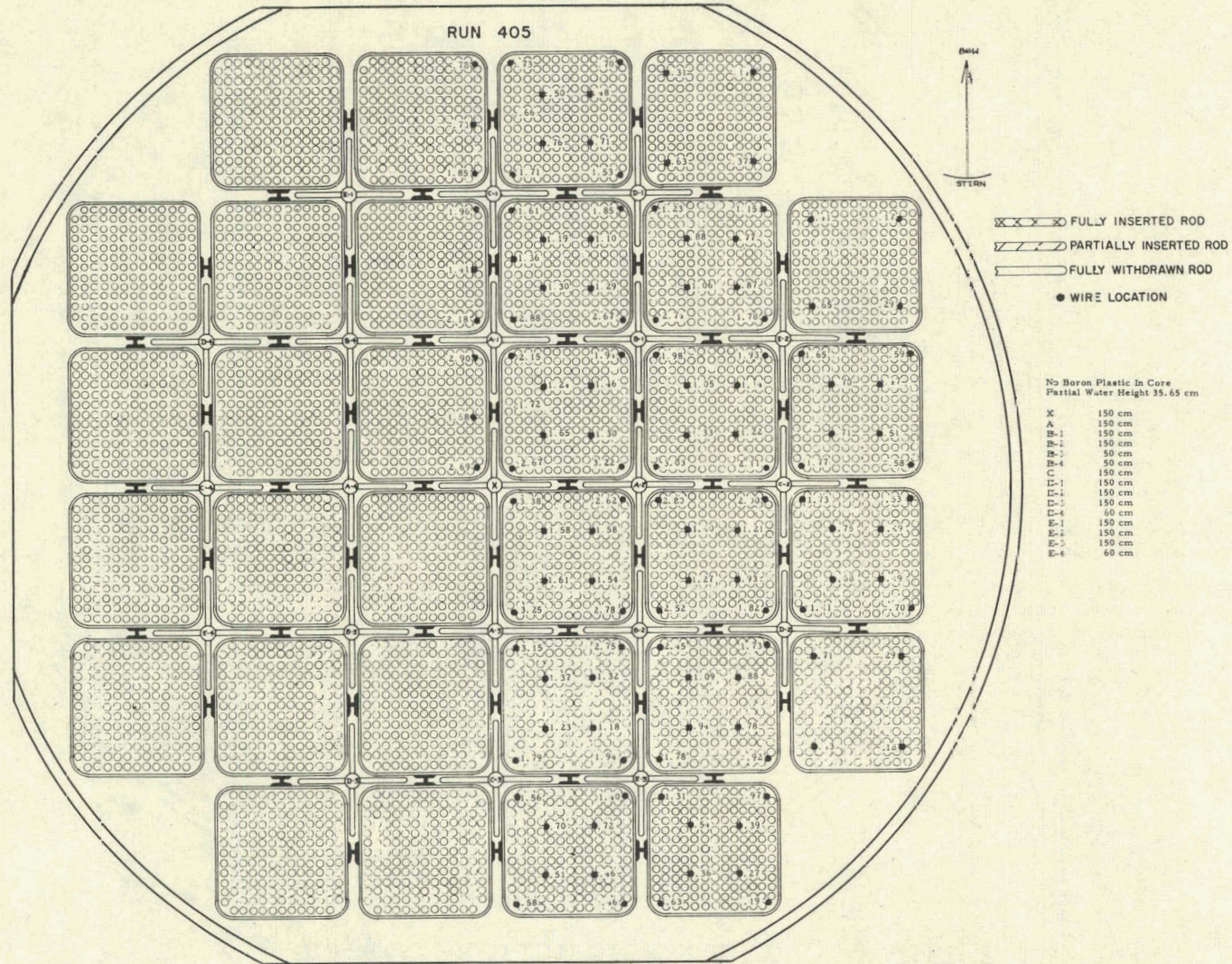


FIG. 26: CADMIUM FRACTION Vs AXIAL POSITION

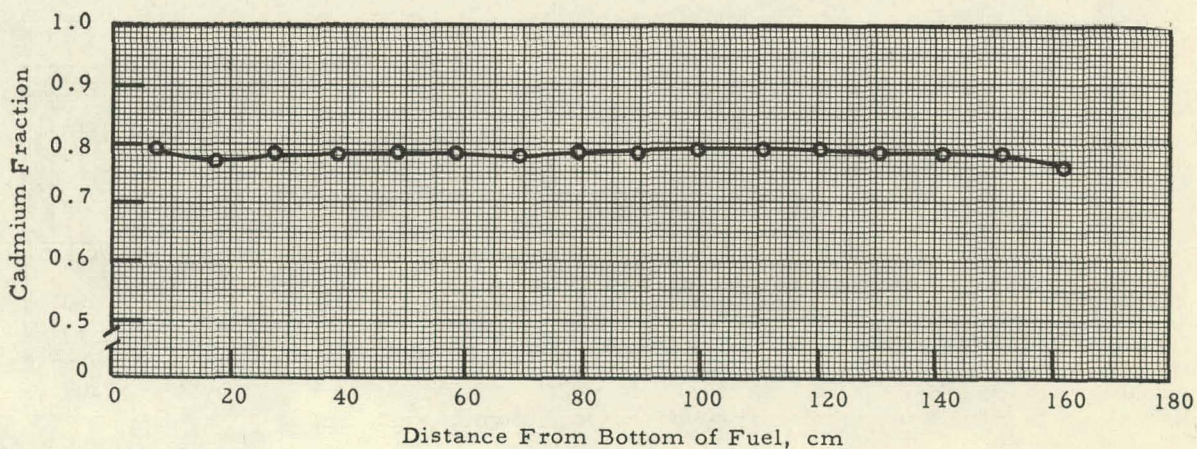
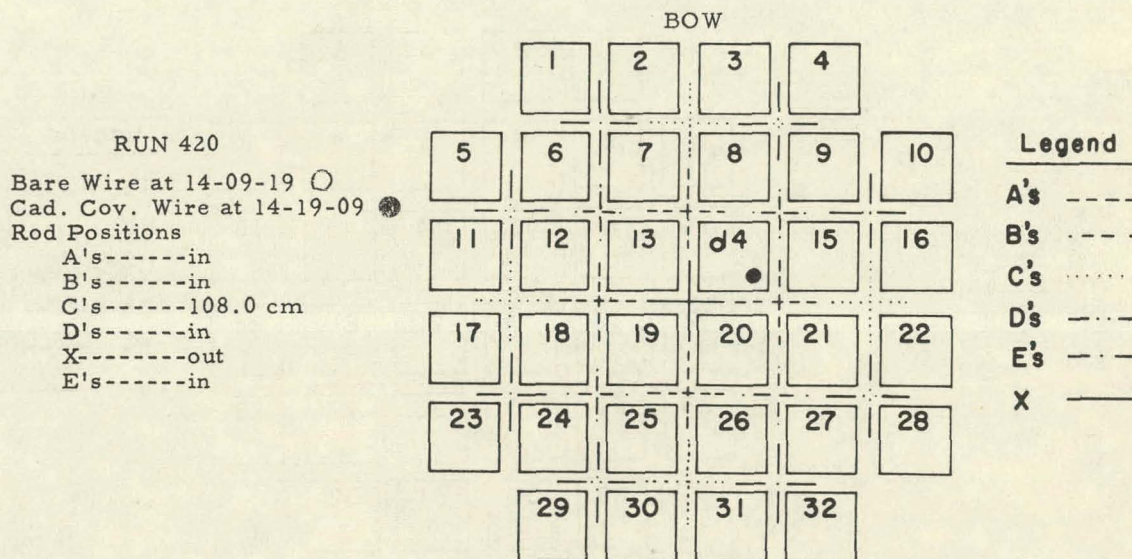


FIG. 27: CADMIUM FRACTION VS AXIAL POSITION

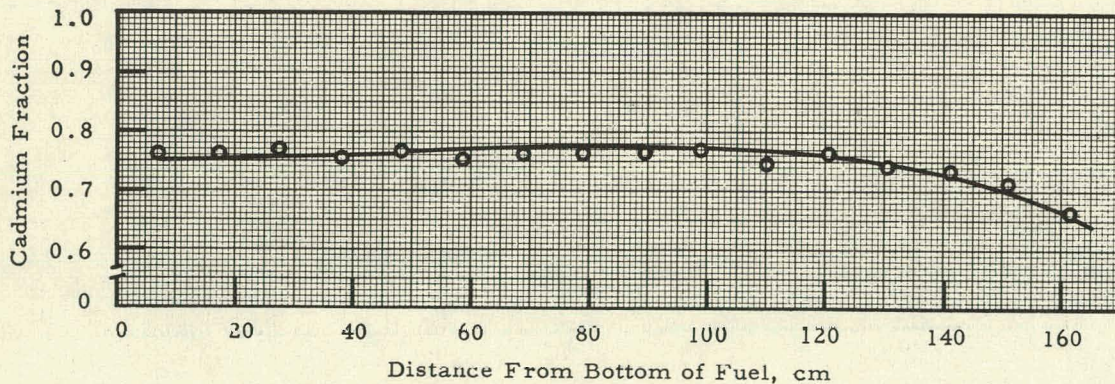
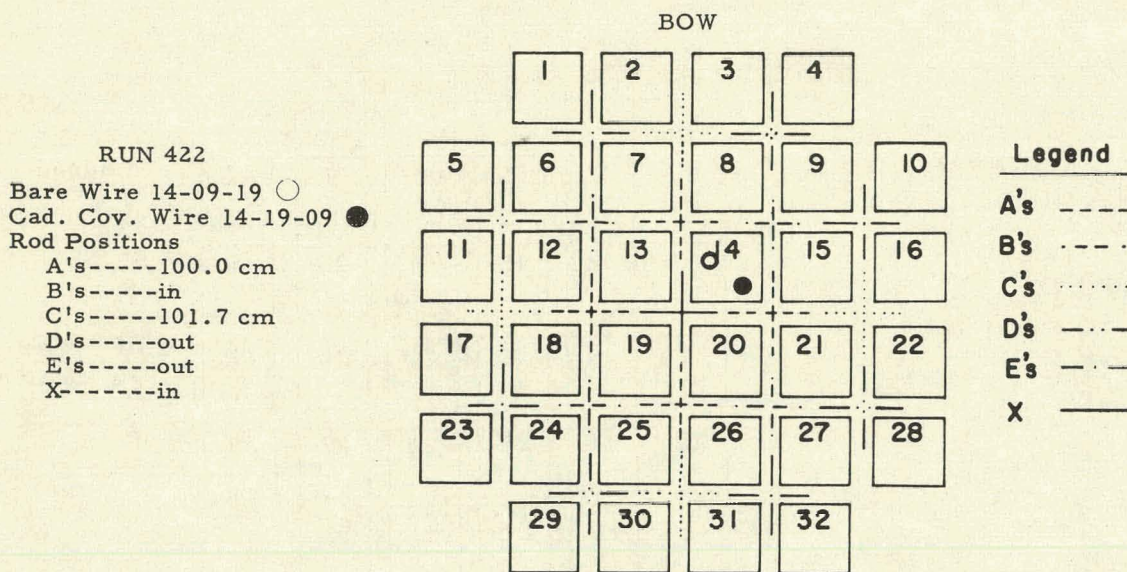


FIG. 28: CADMIUM FRACTION Vs AXIAL POSITION

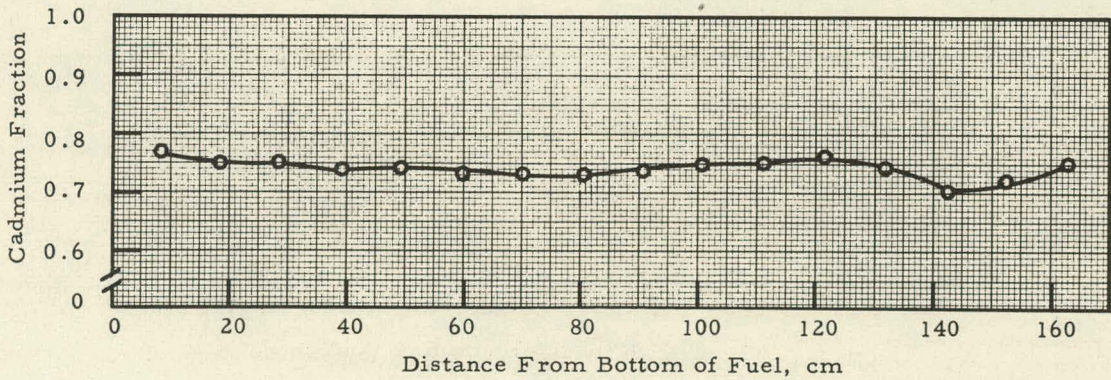
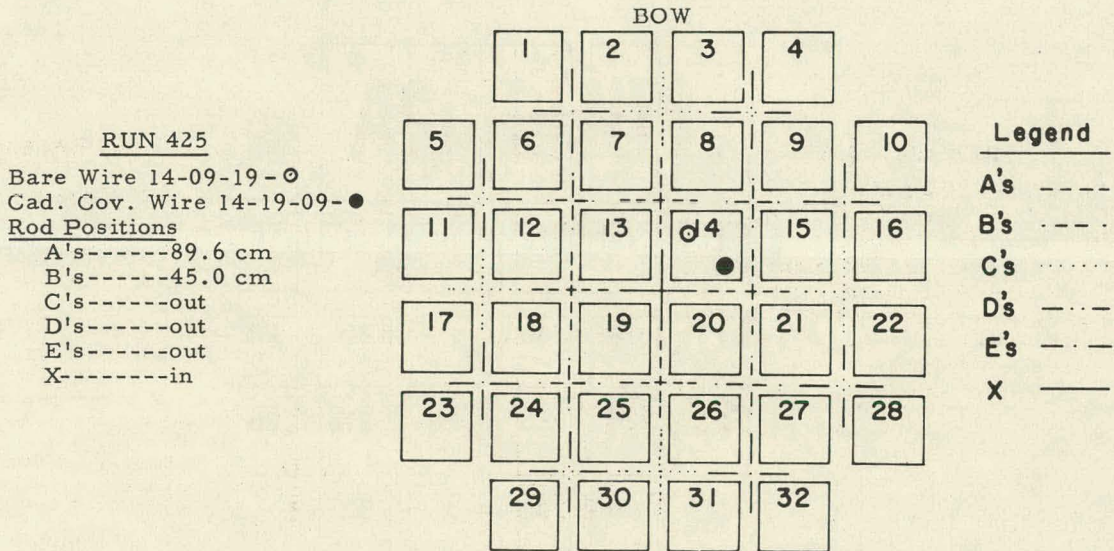


FIG. 29: CADMIUM FRACTION VS AXIAL POSITION

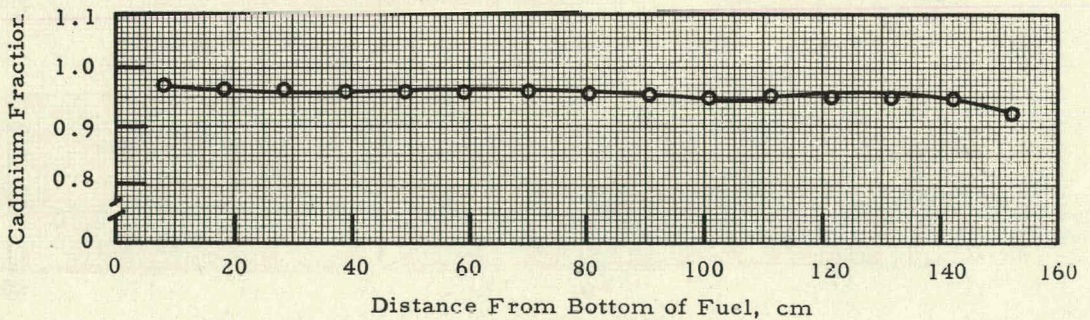
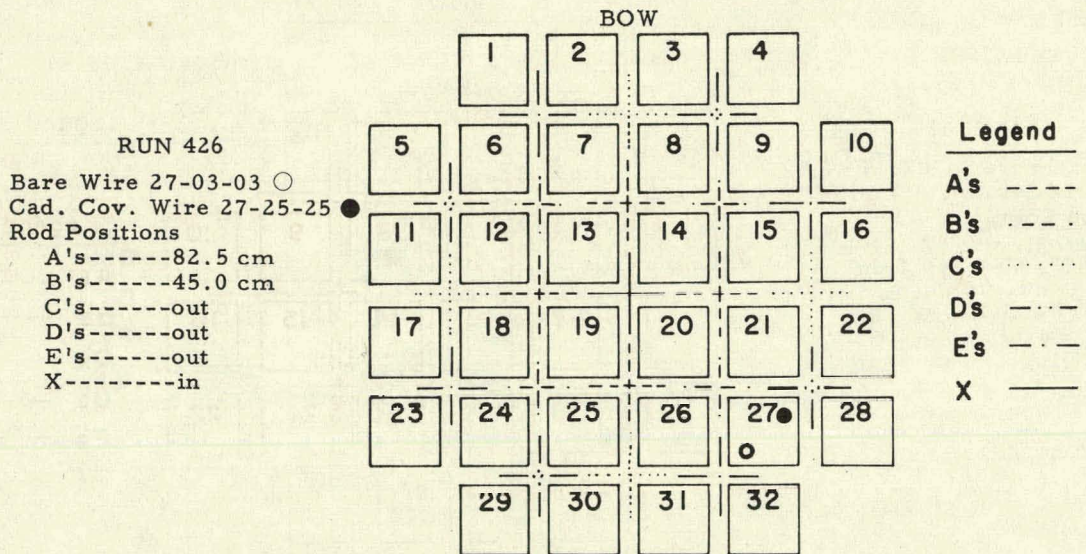


FIG. 30: CADMIUM FRACTION Vs AXIAL POSITION

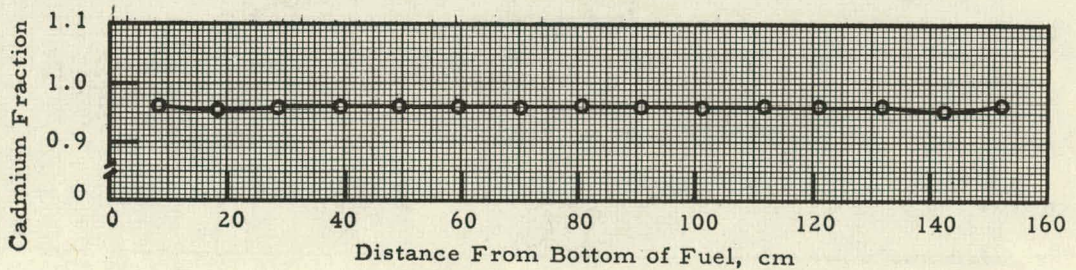
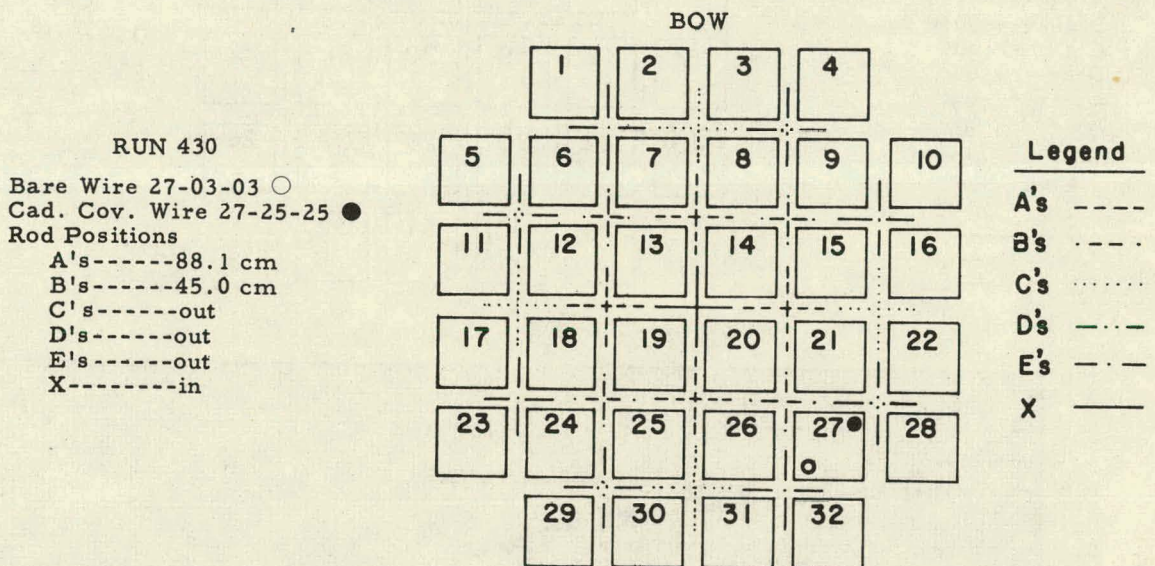


FIG. 31: CADMIUM FRACTION Vs AXIAL POSITION

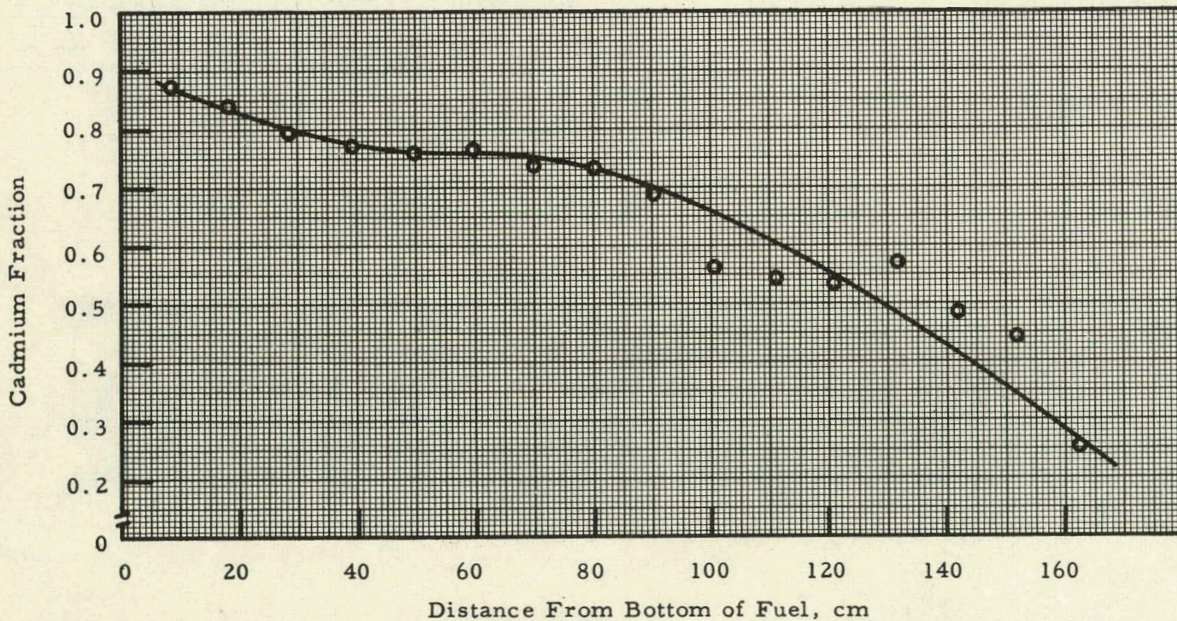
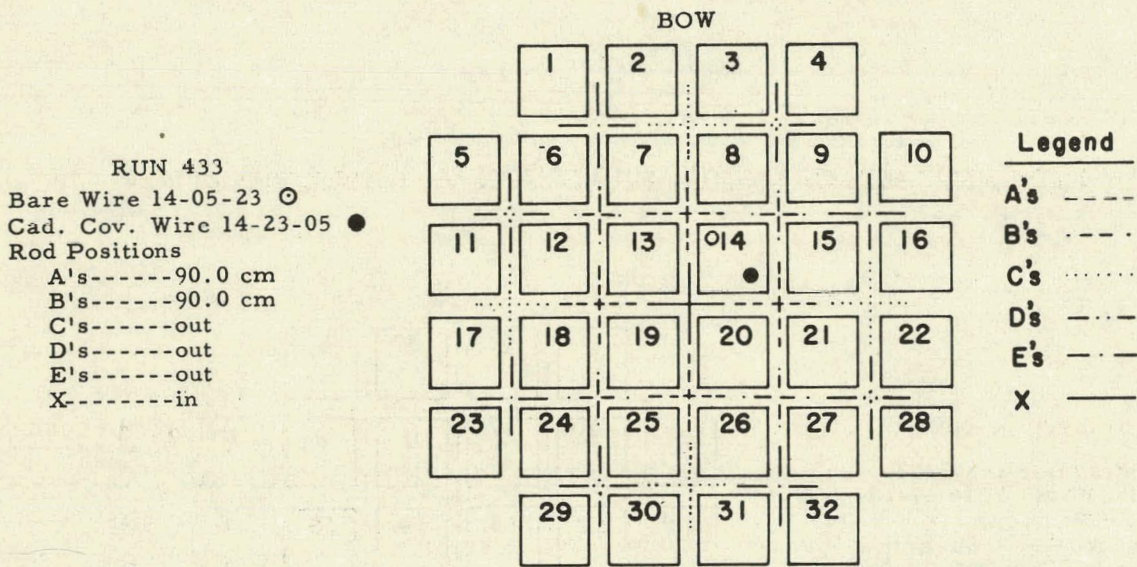


FIG. 32: CADMIUM FRACTION Vs AXIAL POSITION

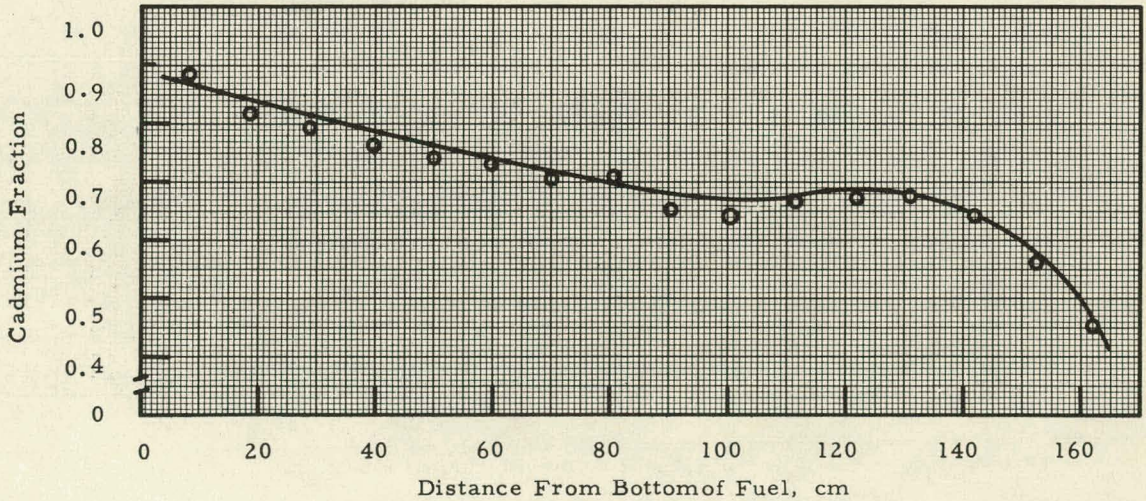
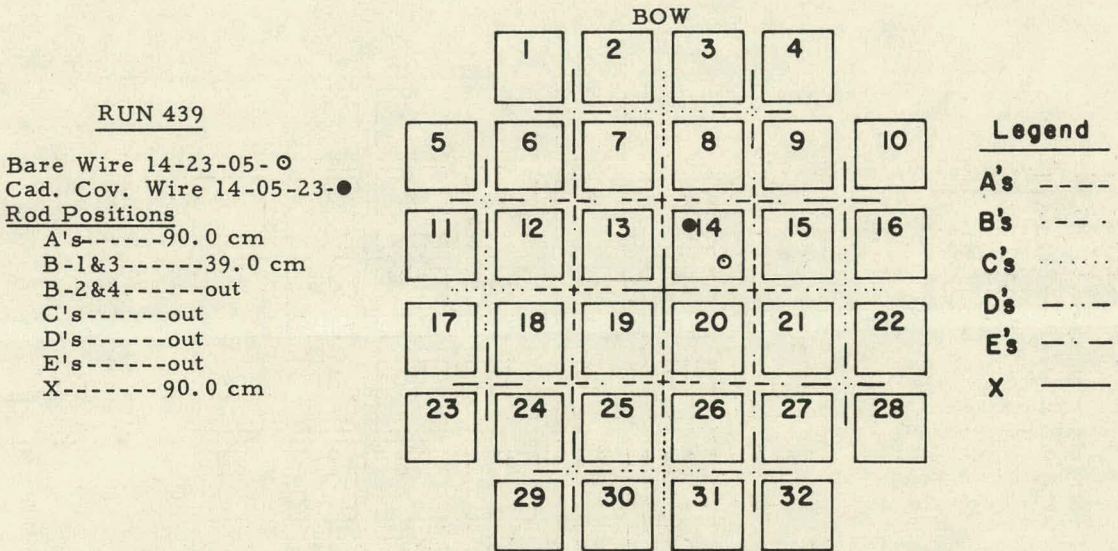


FIG. 33: CADMIUM FRACTION Vs AXIAL POSITION

RUN 442
 Bare Wire 14-09-19-○
 Cad. Cov. Wire 13-19-19-●

Rod Positions

- A-1-----out
- A-2, 3&4 ---101.3 cm
- B-1 ----- 55.0 cm
- B-2&3 -----out
- B-4 ----- 55.0 cm
- C's-----out
- D's-----out
- E's-----out
- X -----In

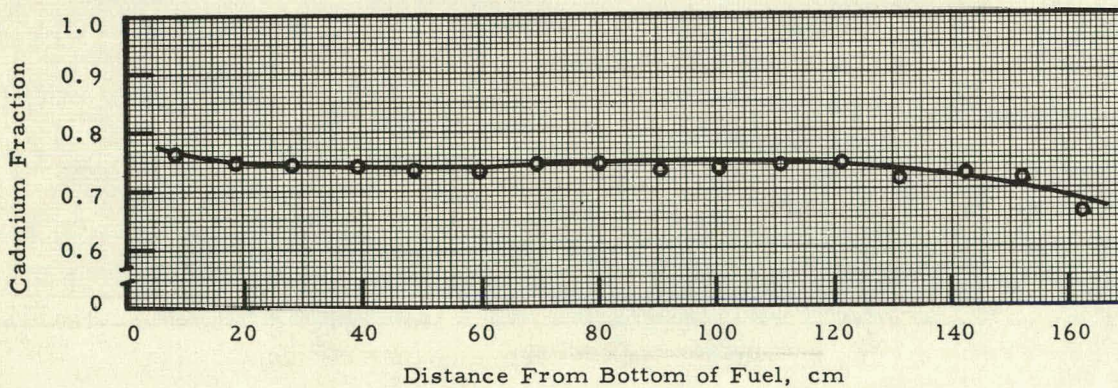
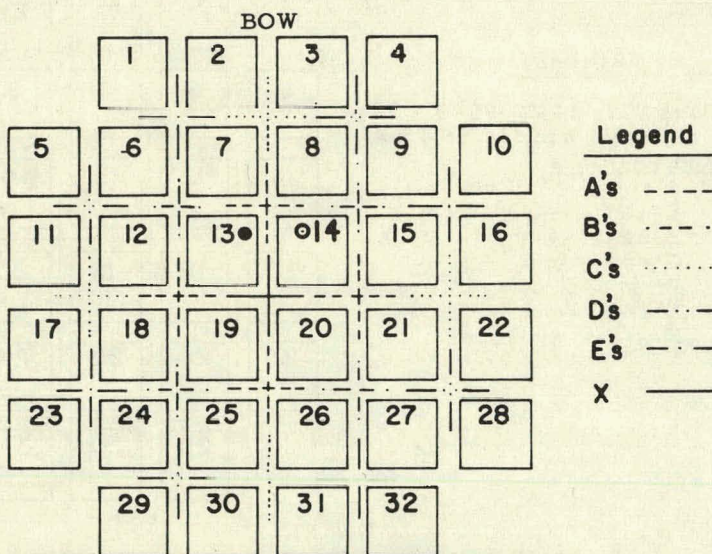


FIG. 34: CADMIUM FRACTION Vs AXIAL POSITION

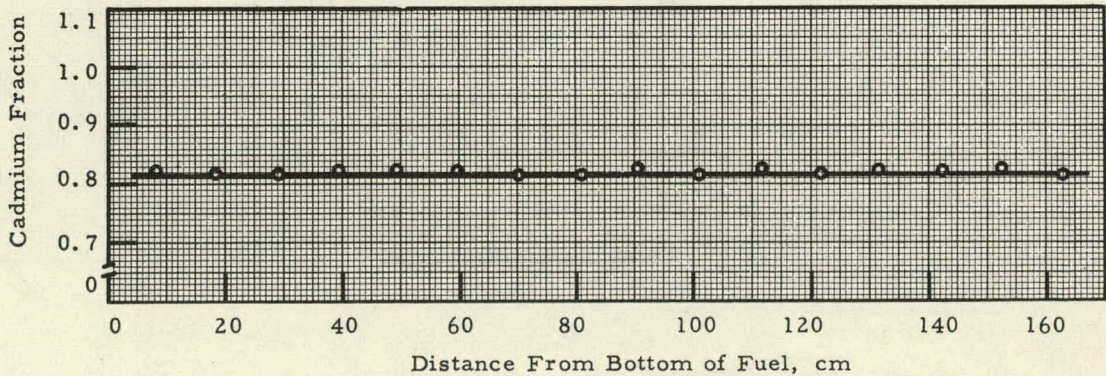
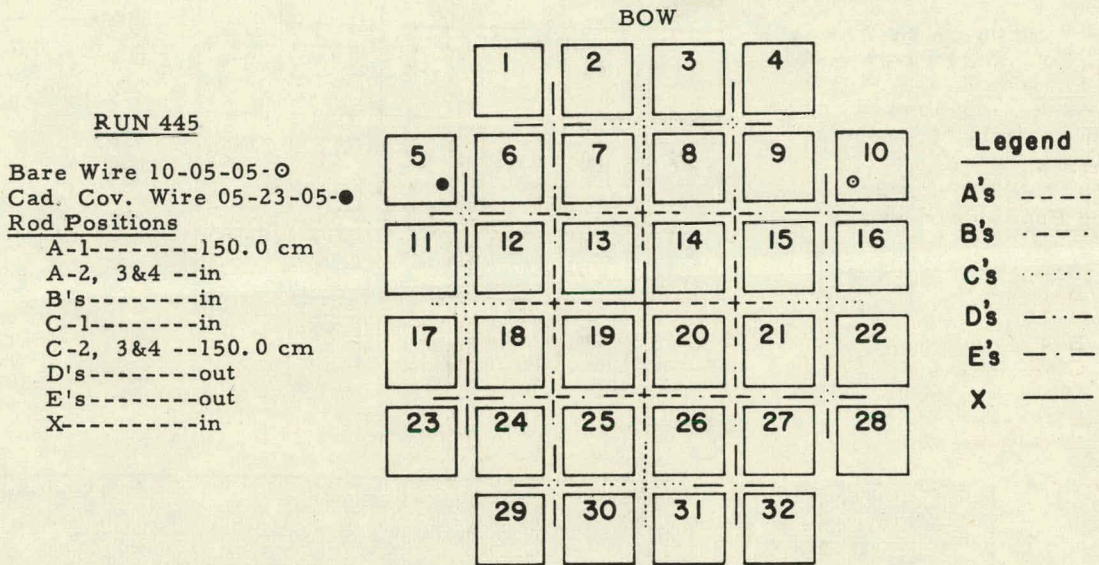


FIG. 35: CADMIUM FRACTION Vs AXIAL POSITION

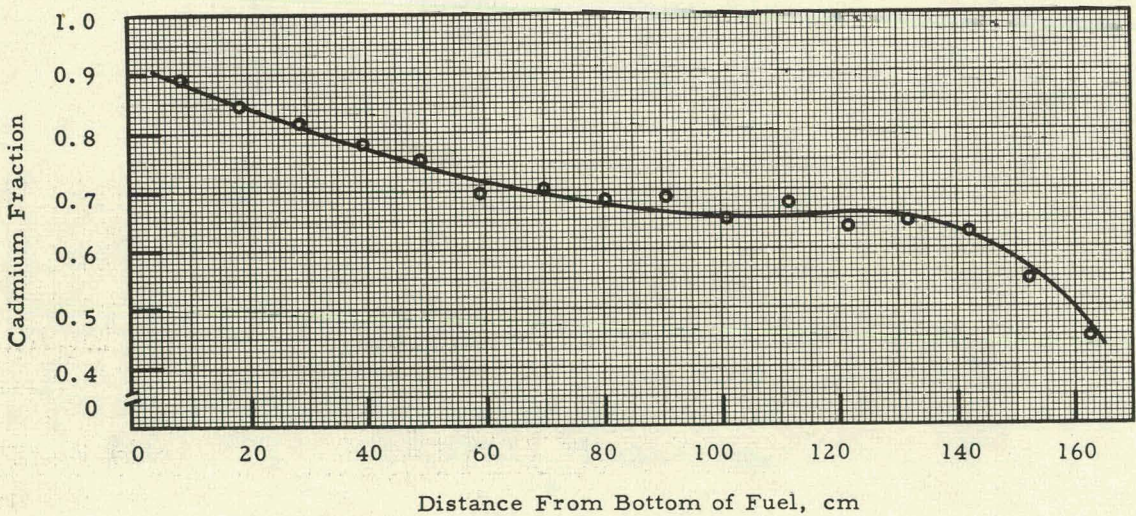
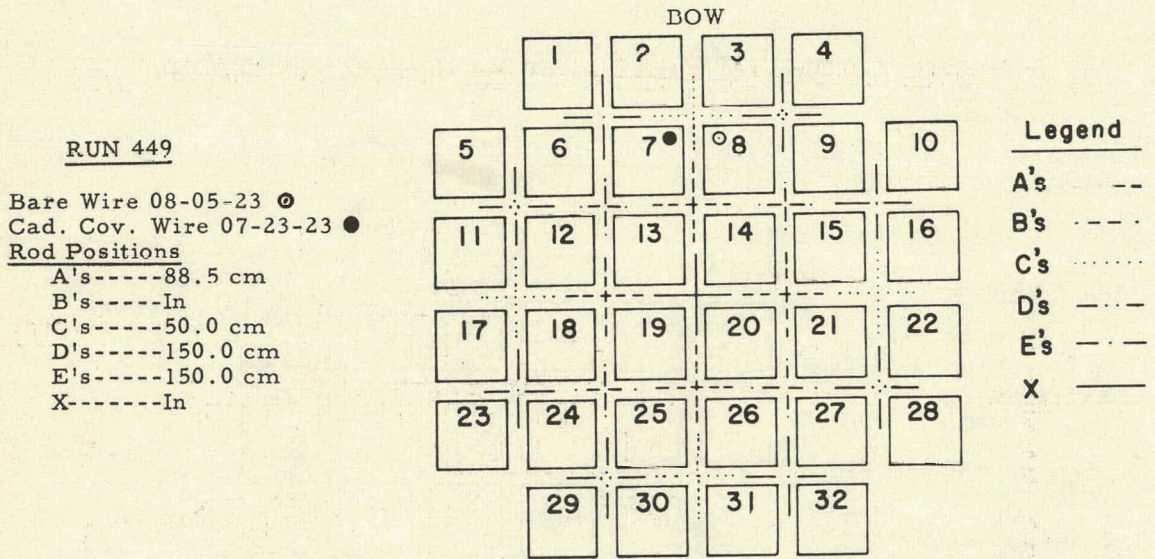


FIG. 36: CADMIUM FRACTION Vs AXIAL POSITION

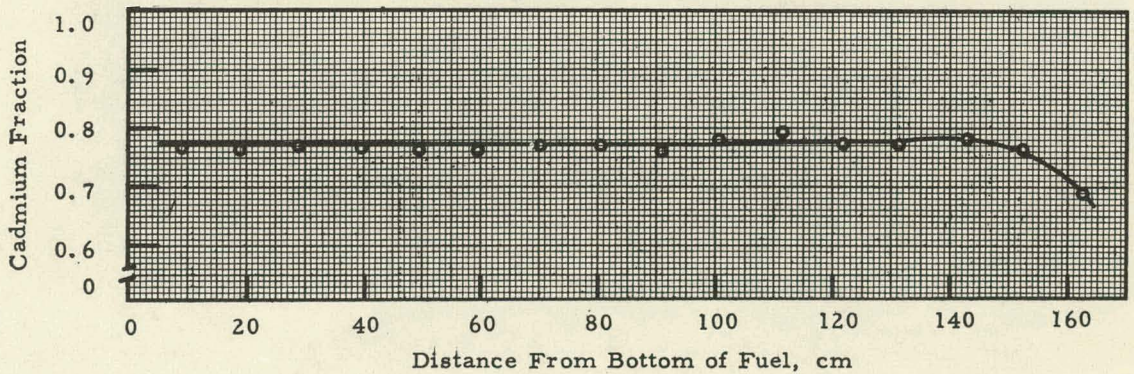
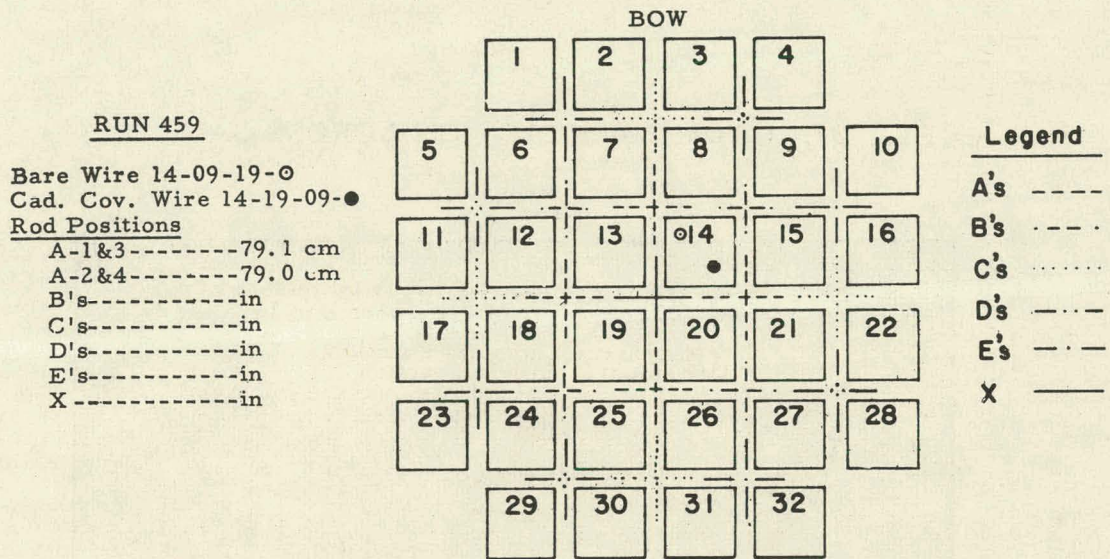


FIG. 37: CADMIUM FRACTION ACROSS CAN

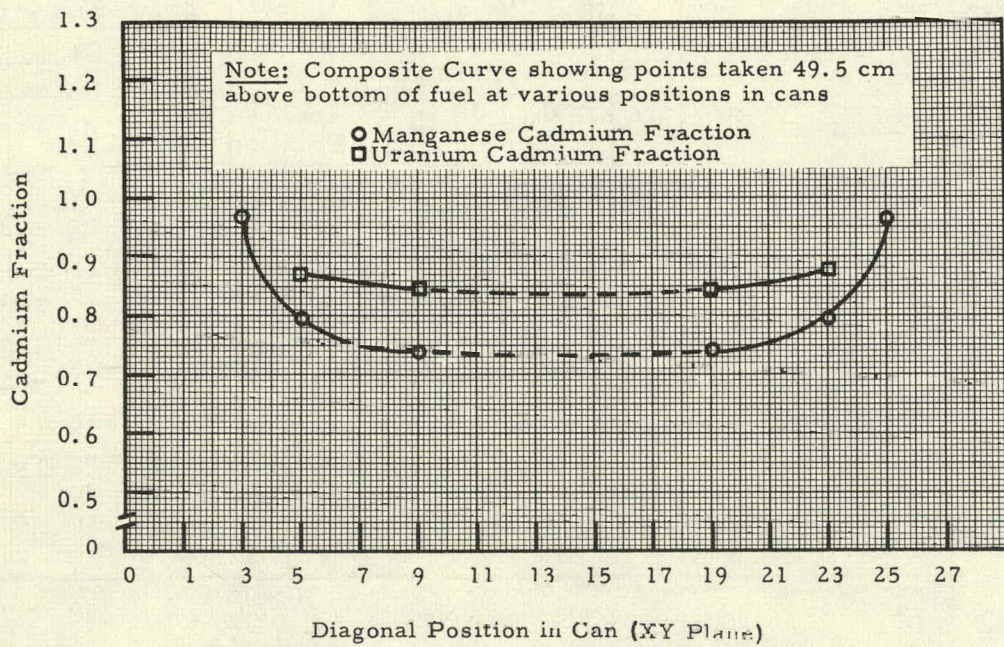


FIG. 38: FINE STRUCTURE THROUGH CORNER OF SAVANNAH FUEL BUNDLE

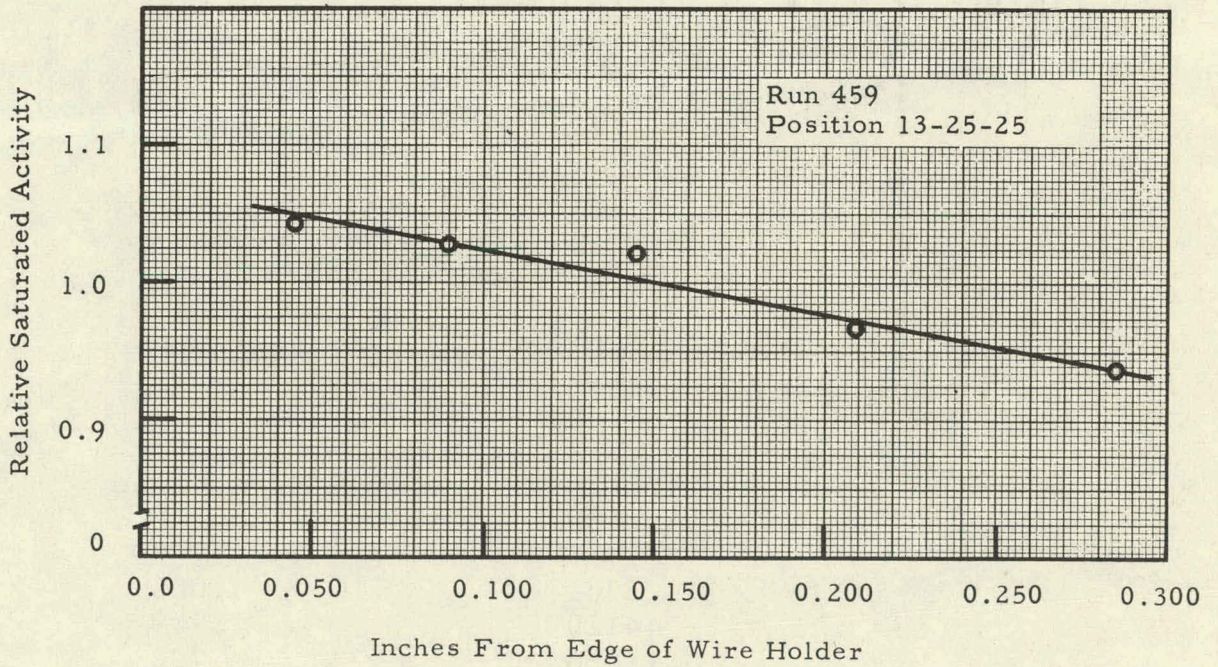
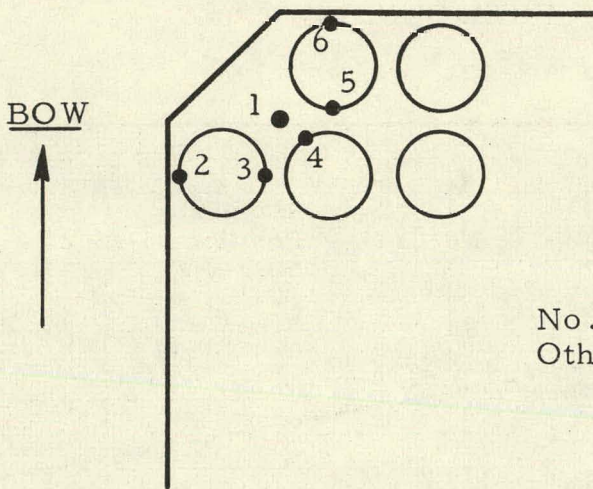


FIG. 39: WIRE ACTIVITIES ADJACENT TO CORNER FUEL PINS

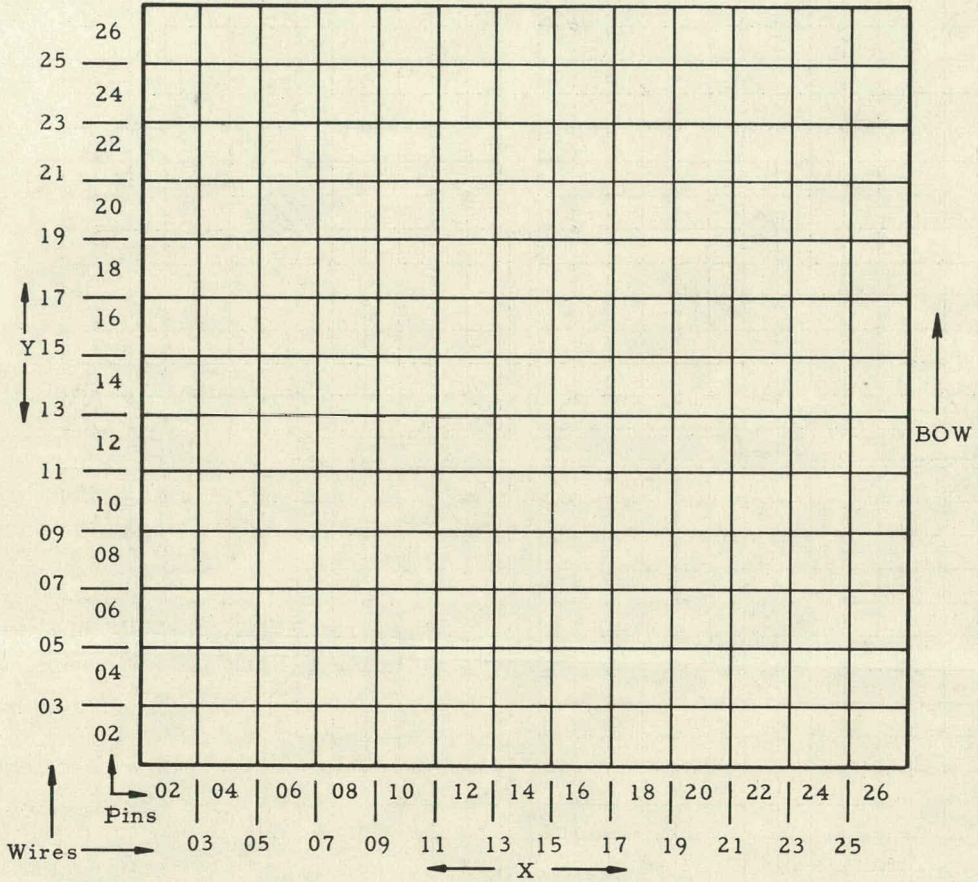
Run 422 Can 31
 Axial Position - 49.4 cm Above Active Fuel



No. 1 Position -31-03-25
 Other wires taped to pins
 as shown

<u>Wire</u>	<u>Relative Activity</u>	<u>Normalized Activity</u>
1	15361	1.000
2	14120	.919
3	11856	.772
4	11890	.774
5	12164	.792
6	15156	.987

FIG. 40: LOCATION MATRIX FOR PIN AND WIRE POSITIONS



BOW

	1	2	3	4	
5	6	7	8	9	10
11	12	13	14	15	16
17	18	19	20	21	22
23	24	25	26	27	28
	29	30	31	32	

FIG. 41: RADIAL PROFILE OF AXIALLY AVERAGED FLUX

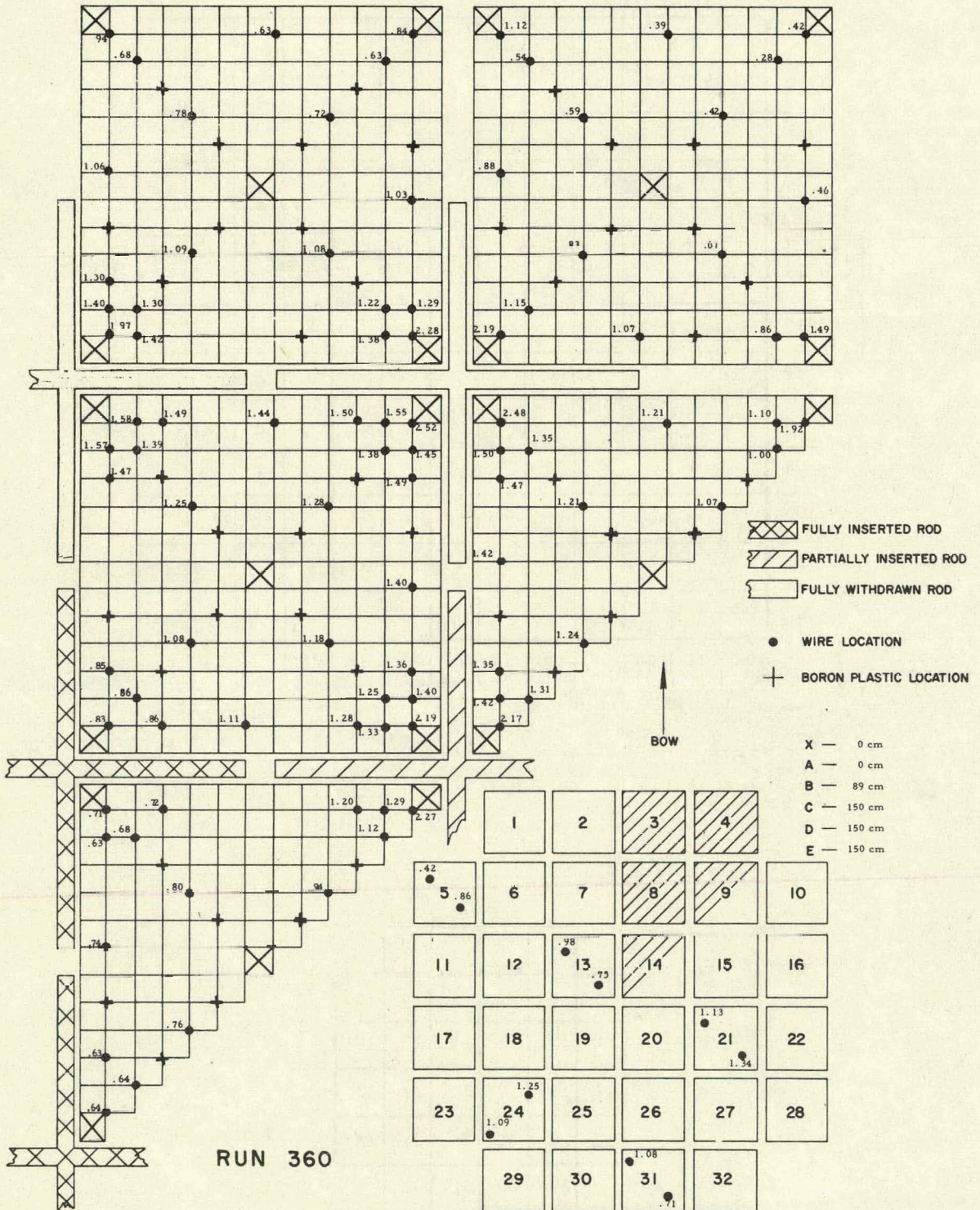


FIG. 42: RADIAL PROFILE OF AXIALLY AVERAGED FLUX

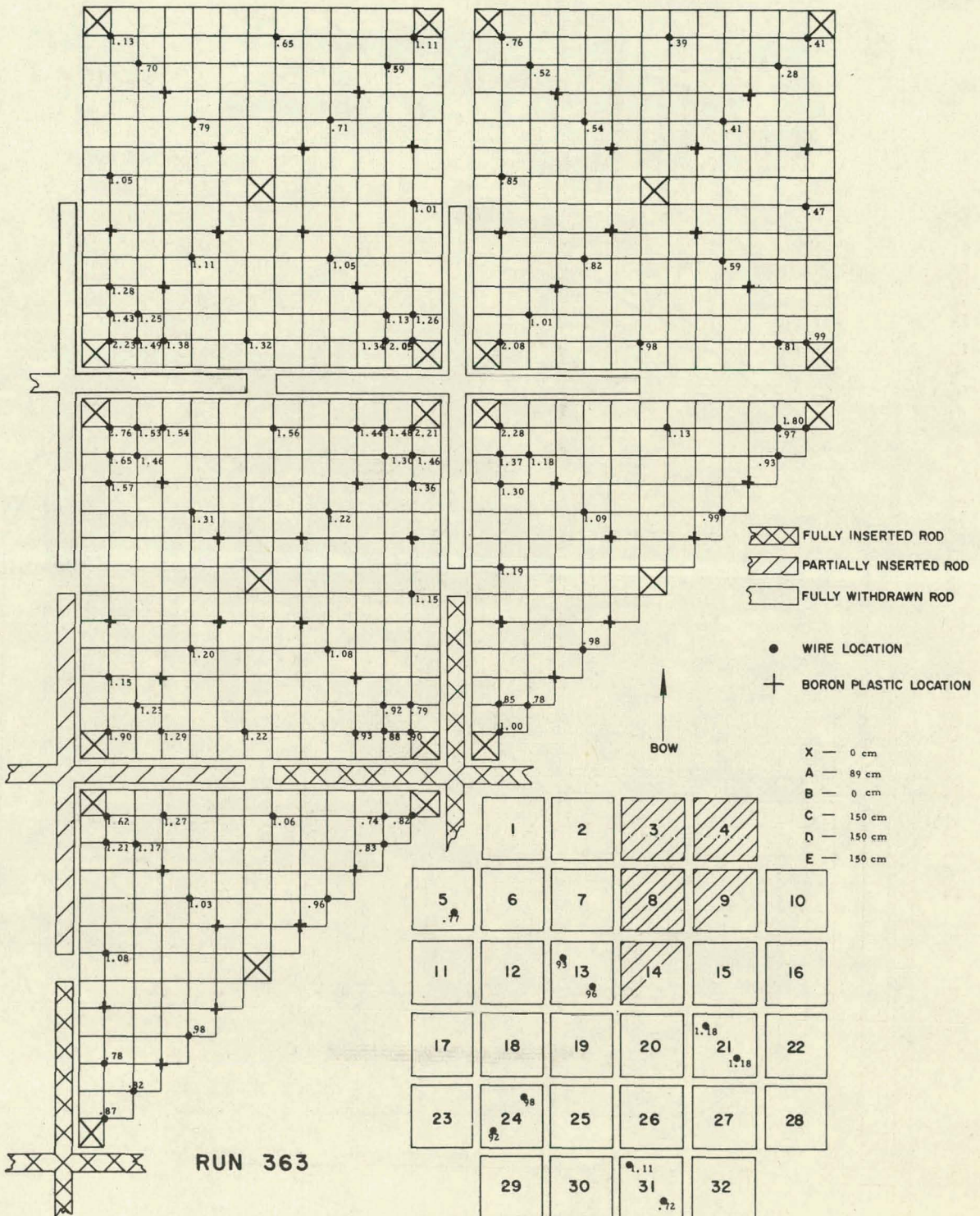


FIG. 43: RADIAL PROFILE OF AXIALLY AVERAGED FLUX

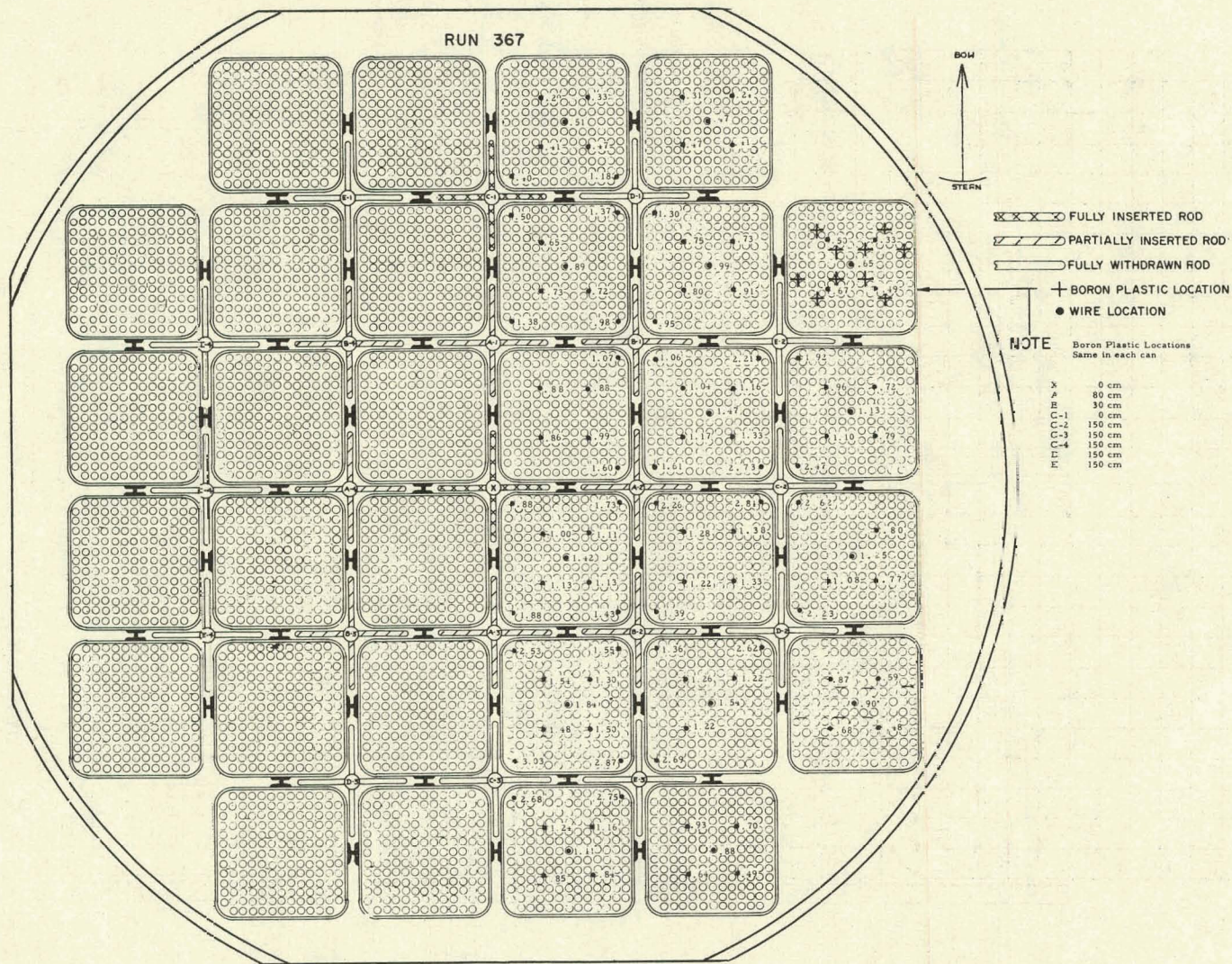


FIG. 44: RADIAL PROFILE OF AXIALLY AVERAGED FLUX

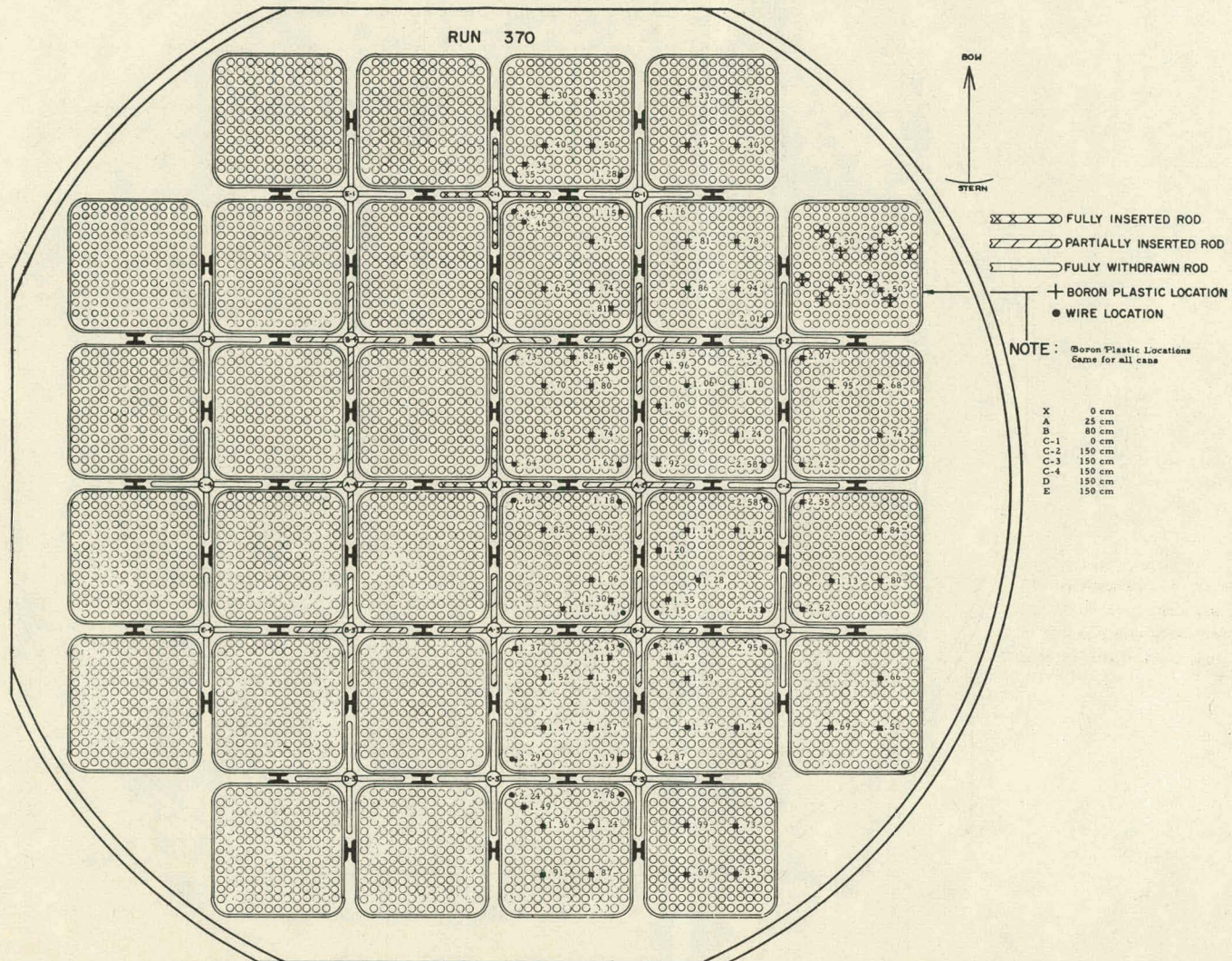


FIG. 45: RADIAL PROFILE OF AXIALLY AVERAGED FLUX

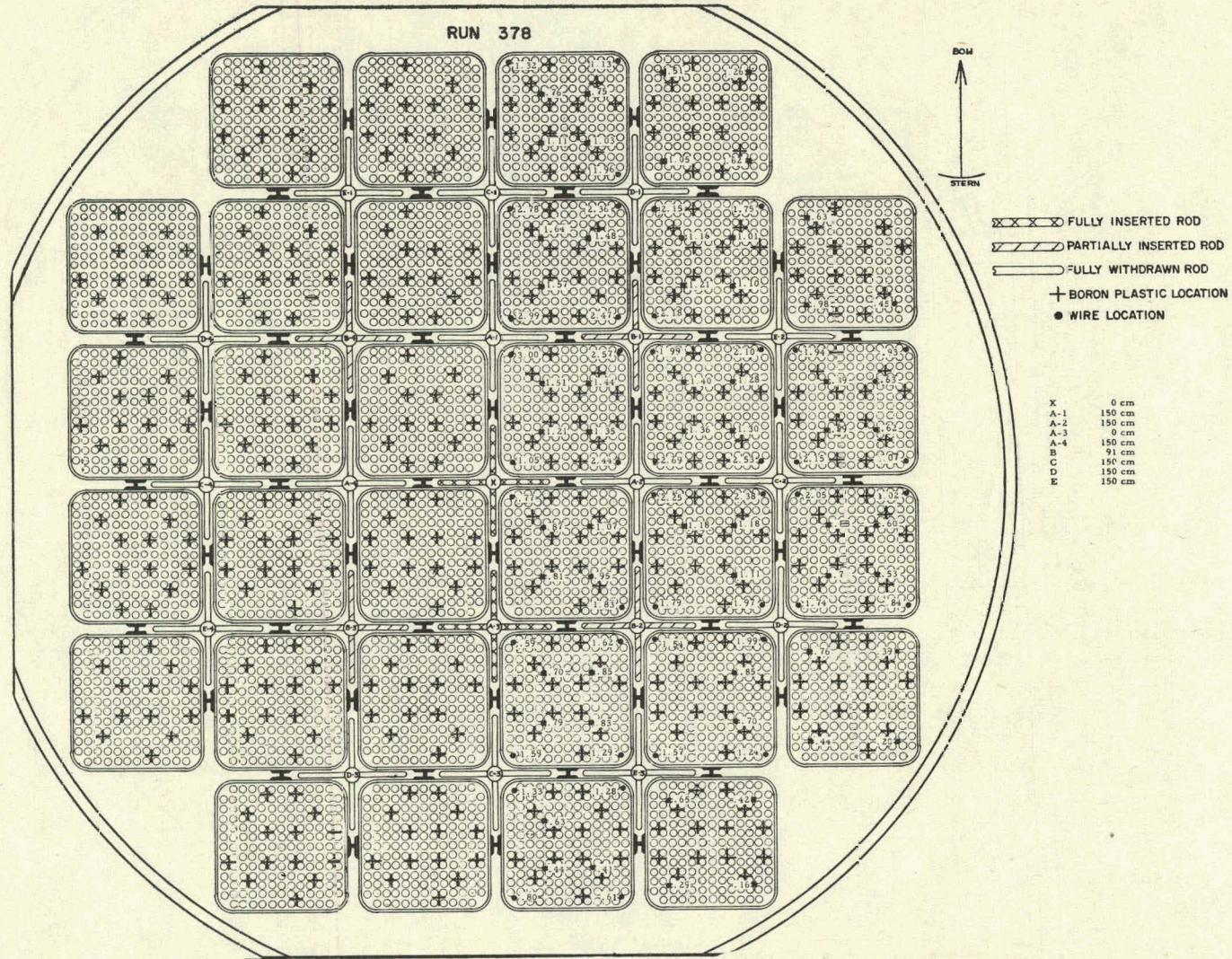


FIG. 46: RADIAL PROFILE OF AXIALLY AVERAGED FLUX

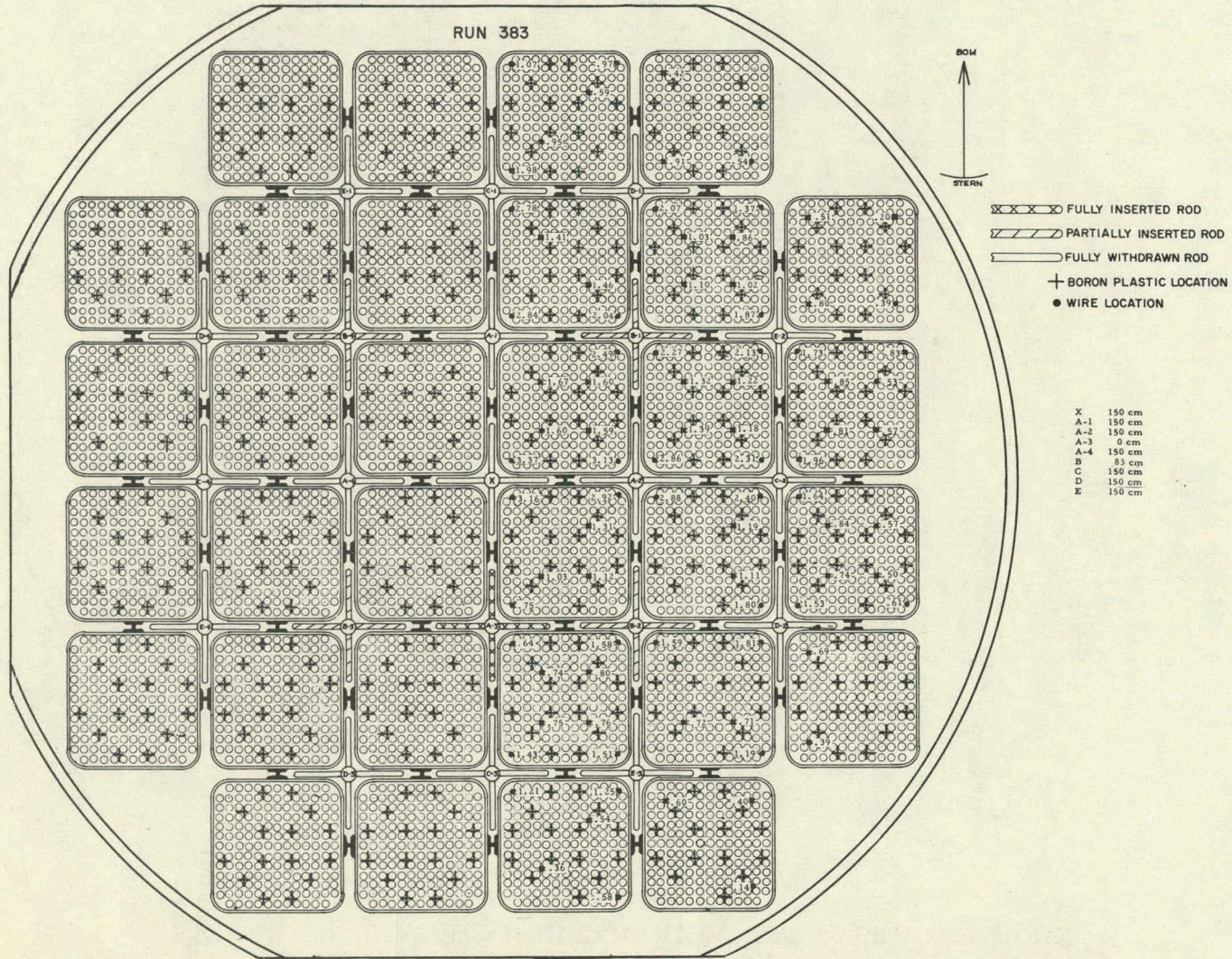


FIG. 47: RADIAL PROFILE OF AXIALLY AVERAGED FLUX

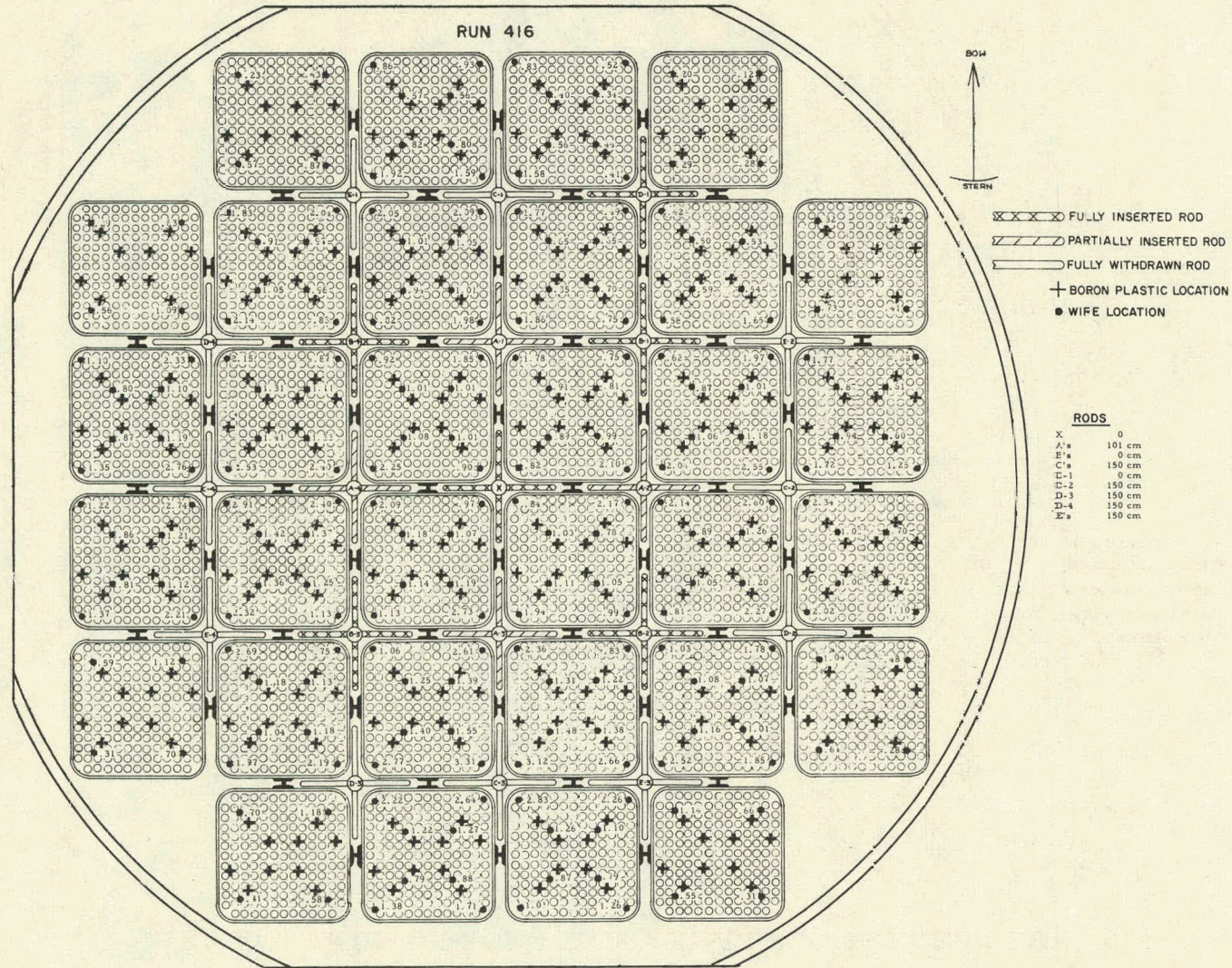


FIG. 48: RADIAL PROFILE OF AXIALLY AVERAGED FLUX

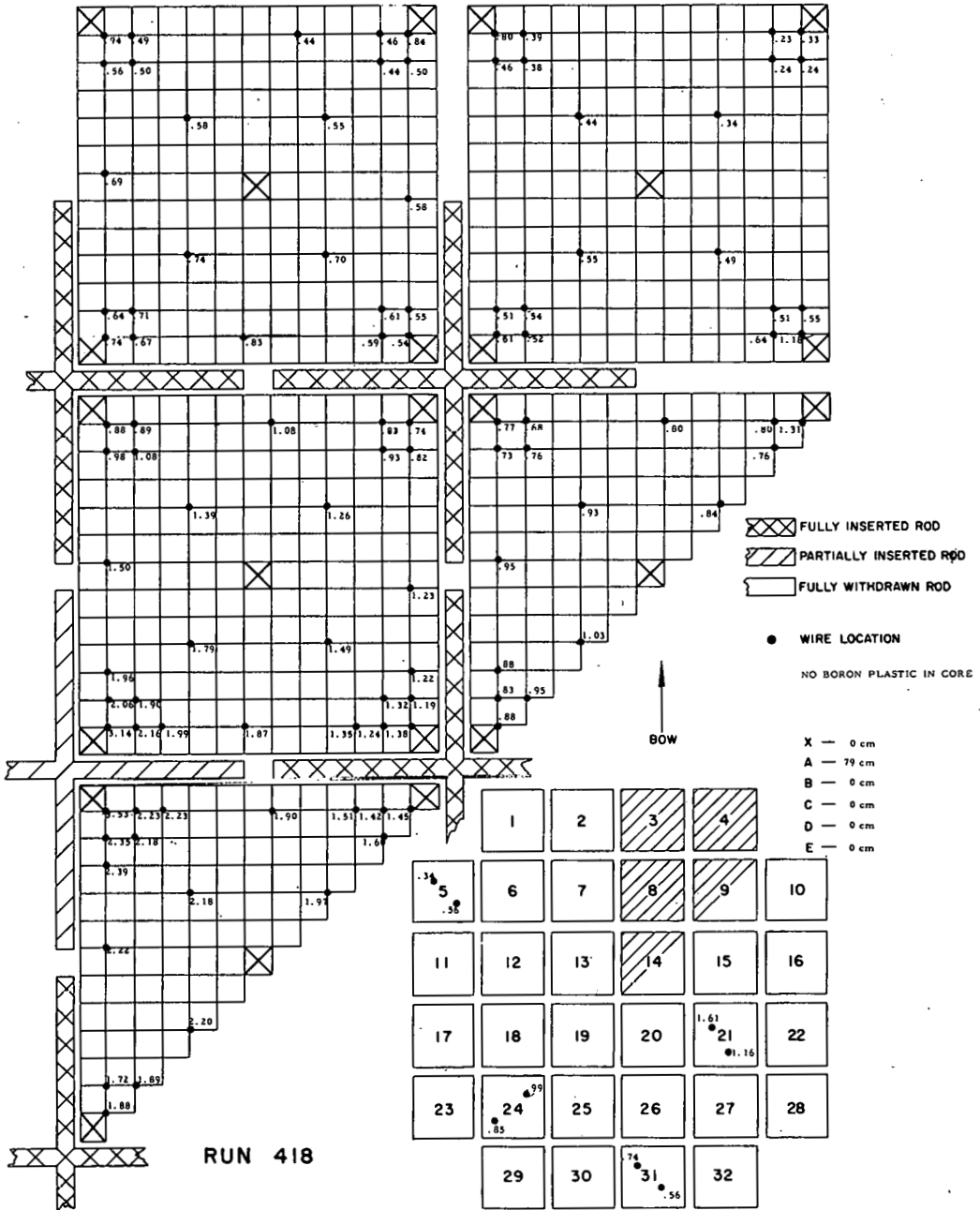


FIG. 49: RADIAL PROFILE OF AXIALLY AVERAGED FLUX

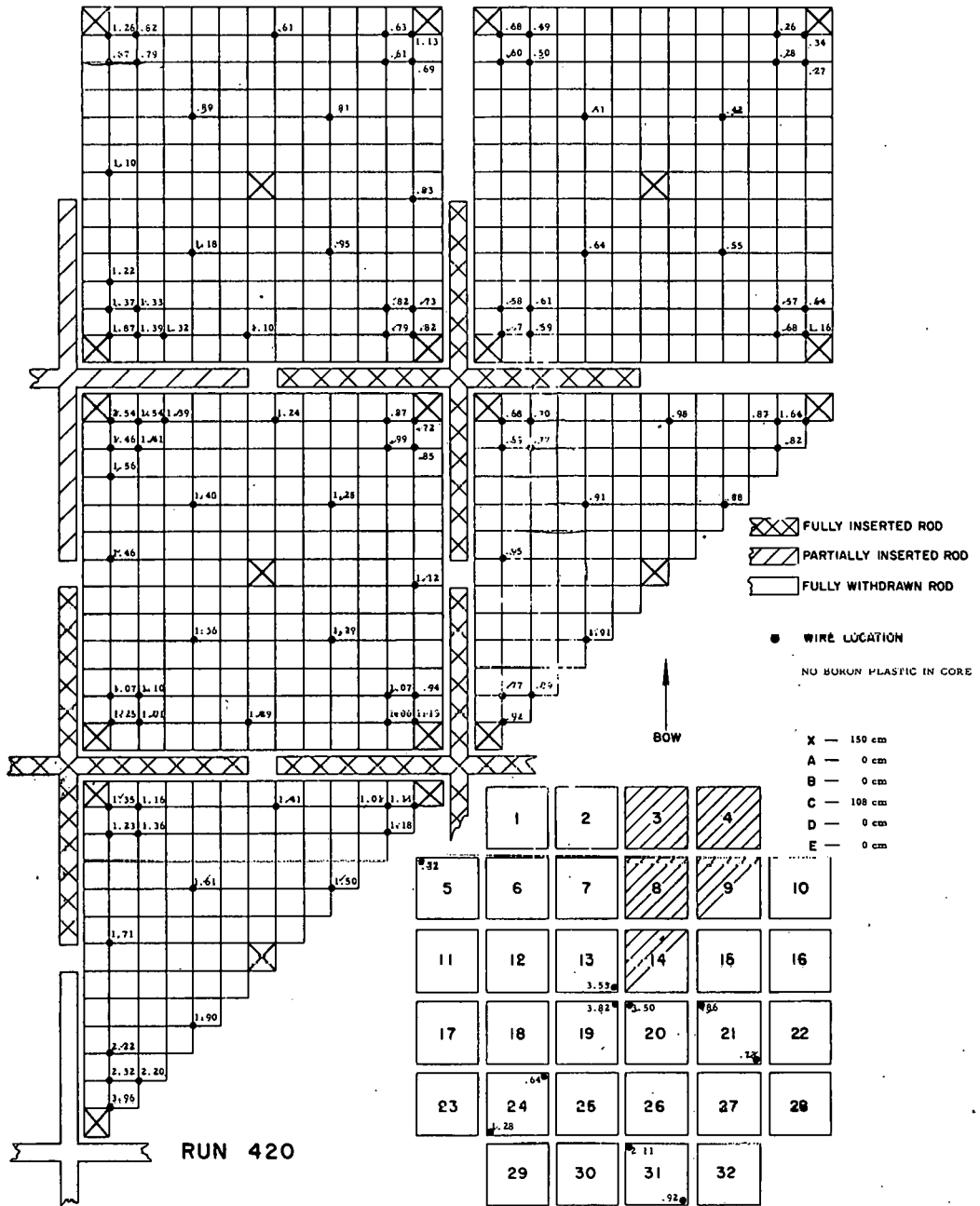


FIG. 50: RADIAL PROFILE OF AXIALLY AVERAGED FLUX

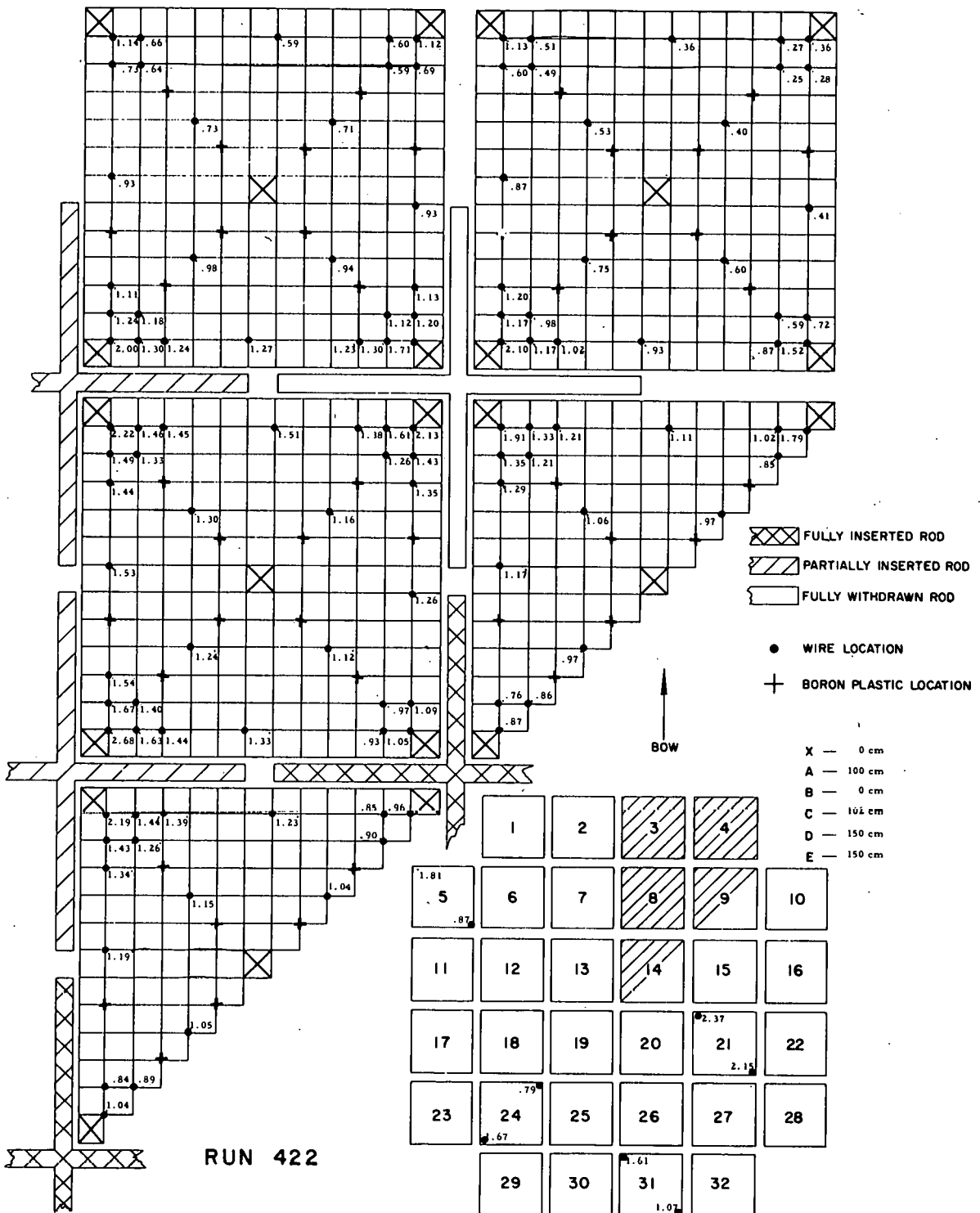


FIG. 51: RADIAL PROFILE OF AXIALLY AVERAGED FLUX

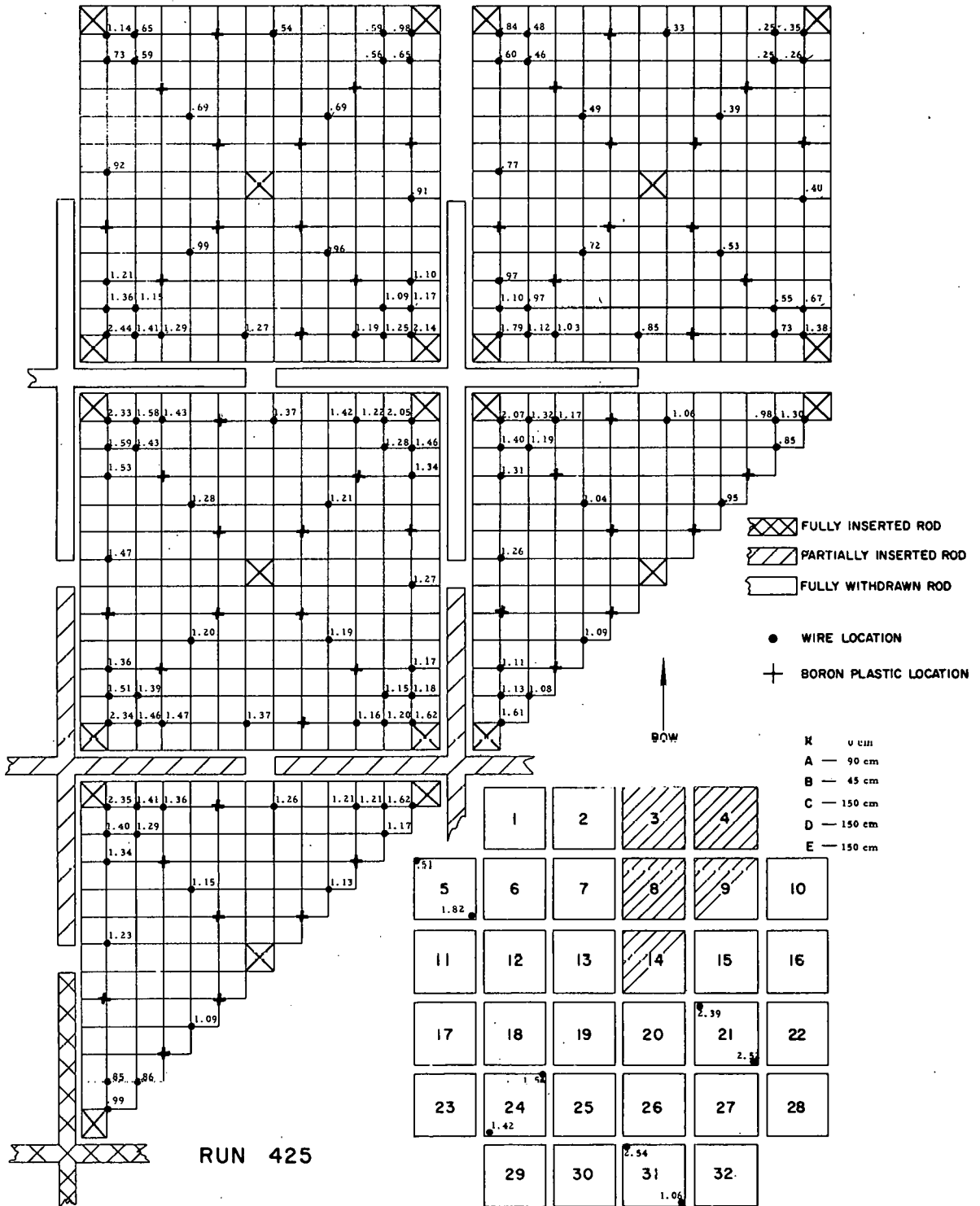
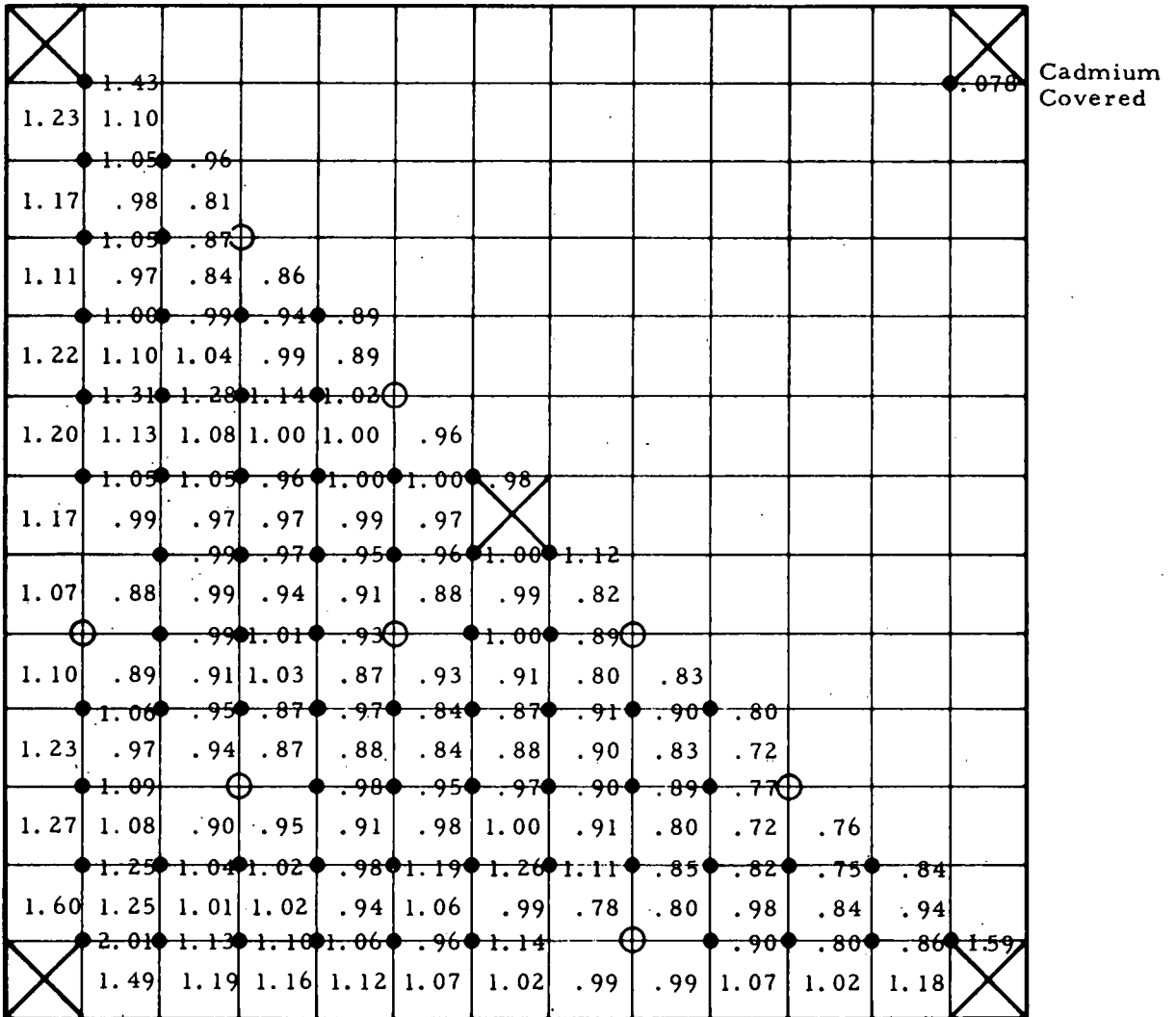


FIG. 52: RADIAL PROFILE OF AXIALLY AVERAGED FLUX

Run 426
Marty Can in Position 27



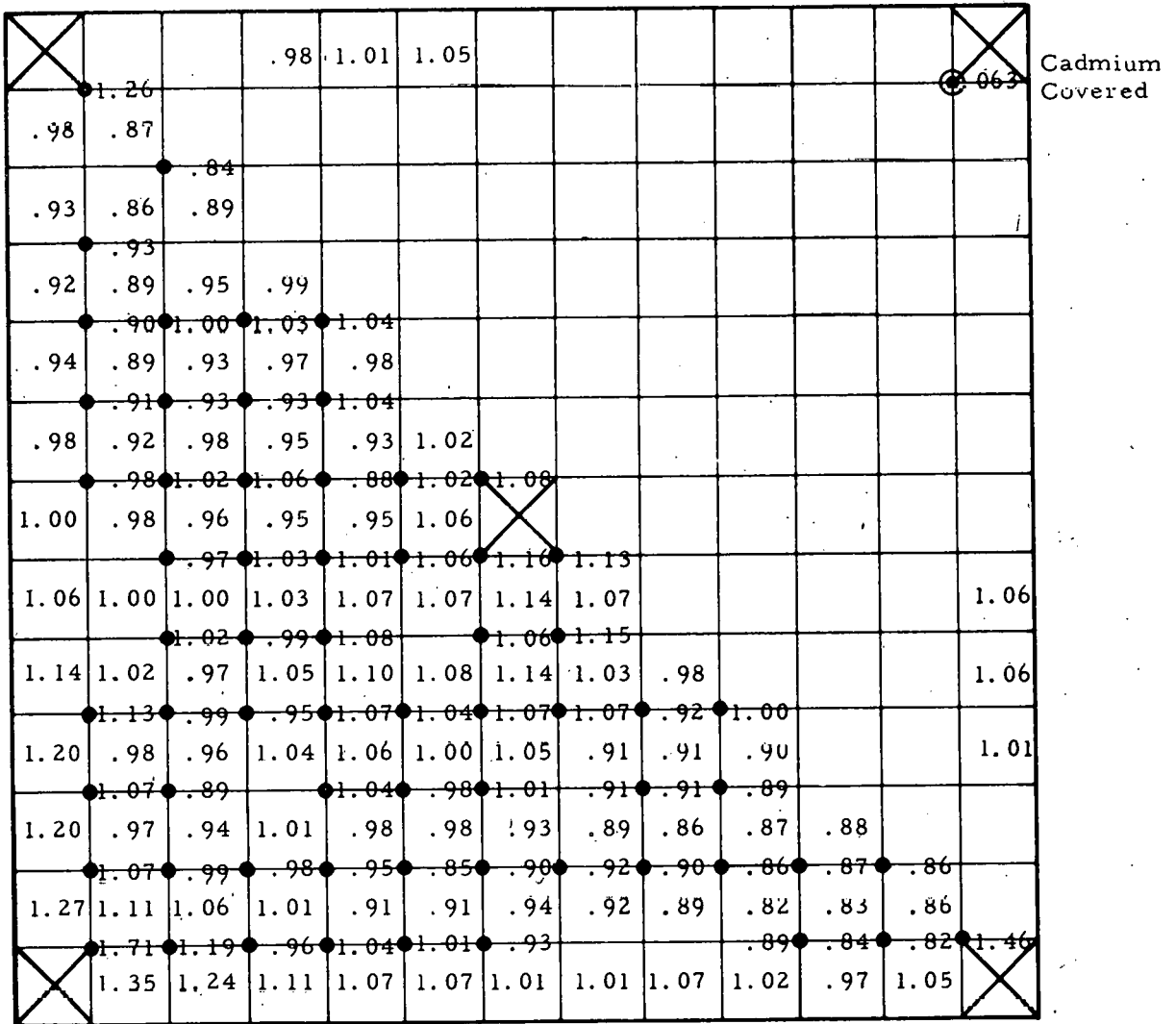
- Boron Plastic
- ⊕ 1.00 Wire Normalized to Core Avg = 1.0
- 1.00 Pins Normal to Core Avg = 1.0

- Rod Positions
- X — 0 cm
 - A — 82.5 cm
 - B — 45 cm
 - C — 150 cm
 - D — 150 cm
 - E — 150 cm

FIG. 53: RADIAL PROFILE OF AXIALLY AVERAGED FLUX

Run 430

Martyr Can in Position 27



1.00 Wire

1.00 Pins

Cadmium Covered Wire
No Boron Plastic in Core

Rod Positions

- X — 0
- A — 88.1
- B — 45
- C — 150
- D — 150
- E — 150

FIG. 54: RADIAL PROFILE OF AXIALLY AVERAGED FLUX

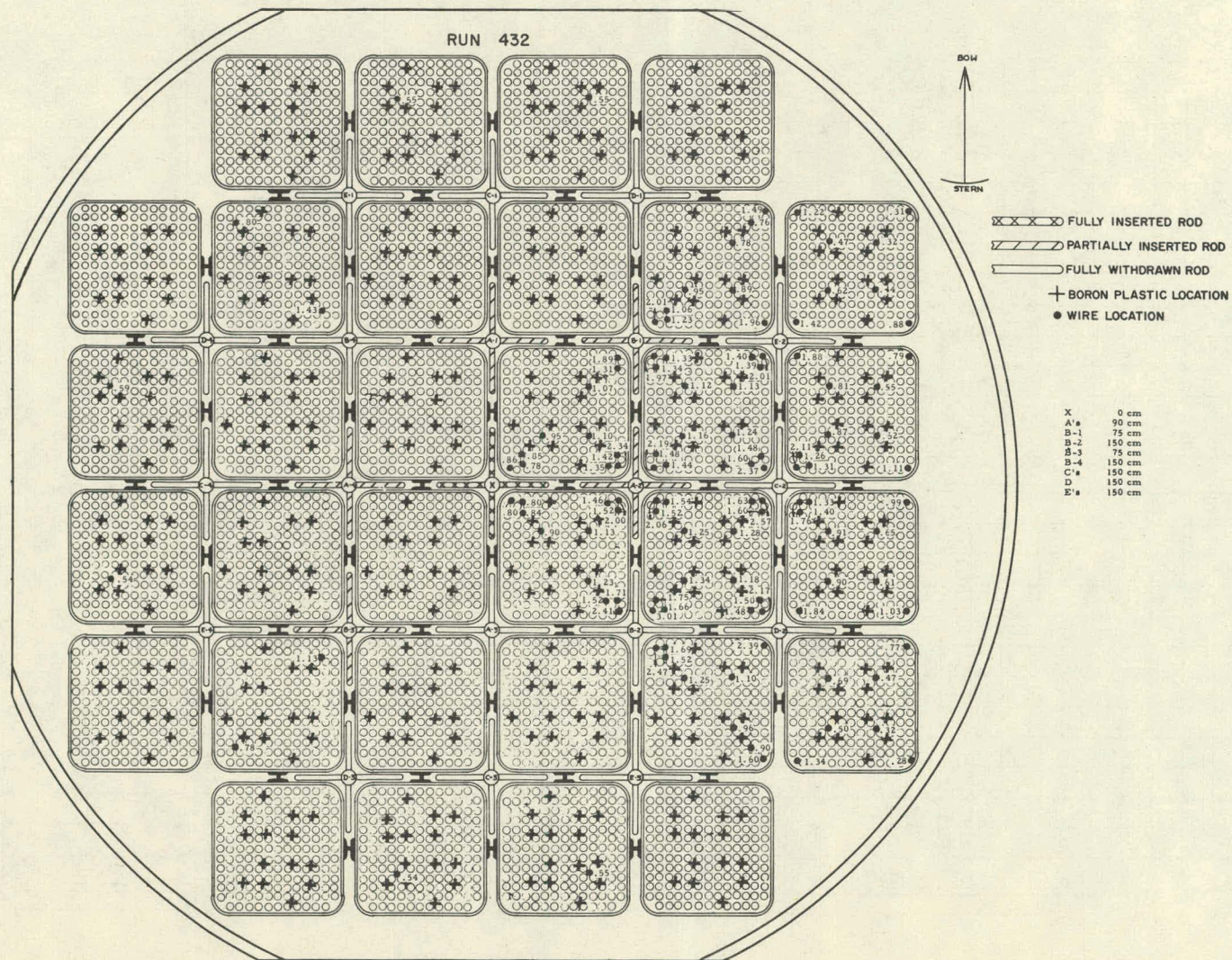


FIG. 56: RADIAL PROFILE OF AXIALLY AVERAGED FLUX

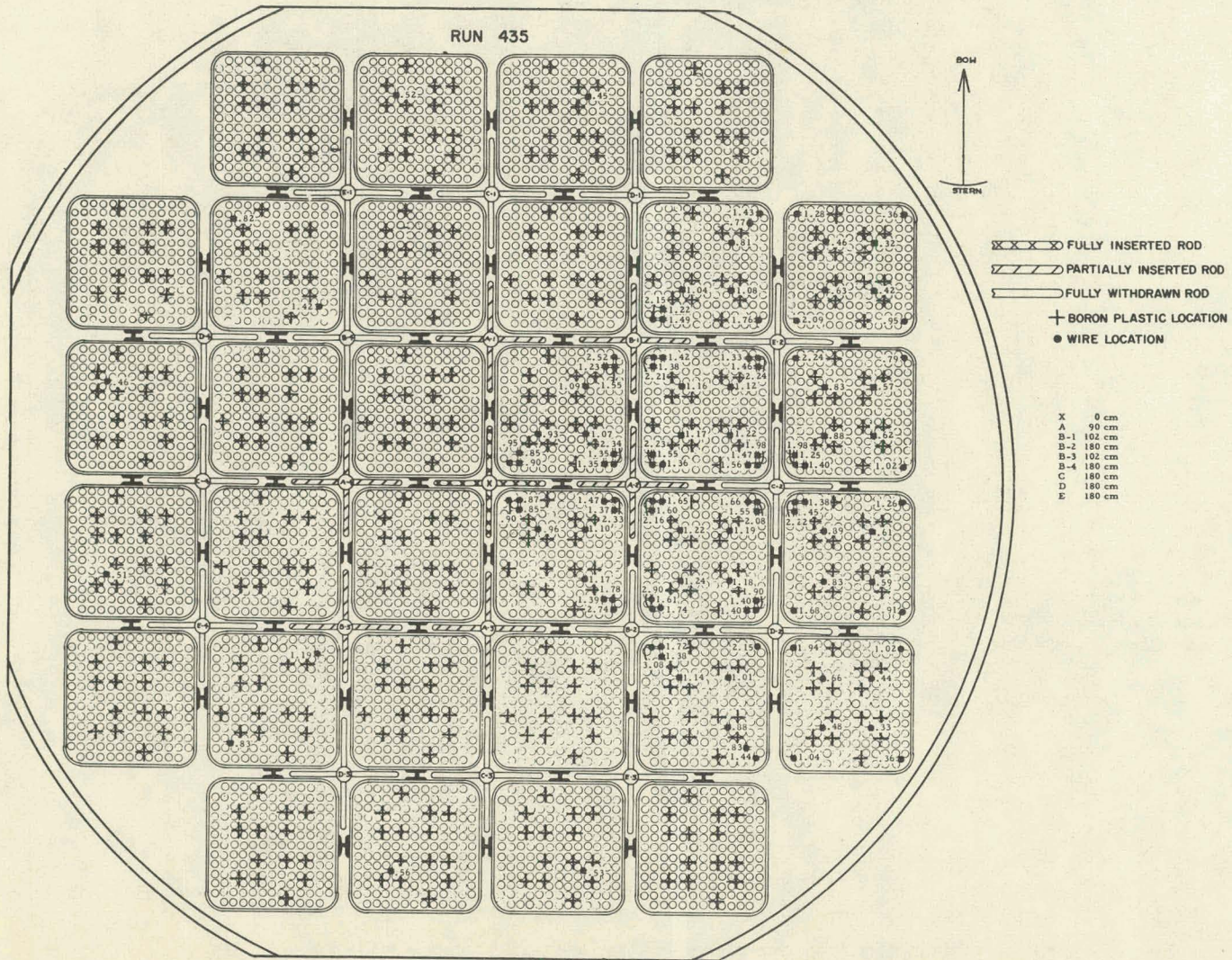


FIG. 57: RADIAL PROFILE OF AXIALLY AVERAGED FLUX

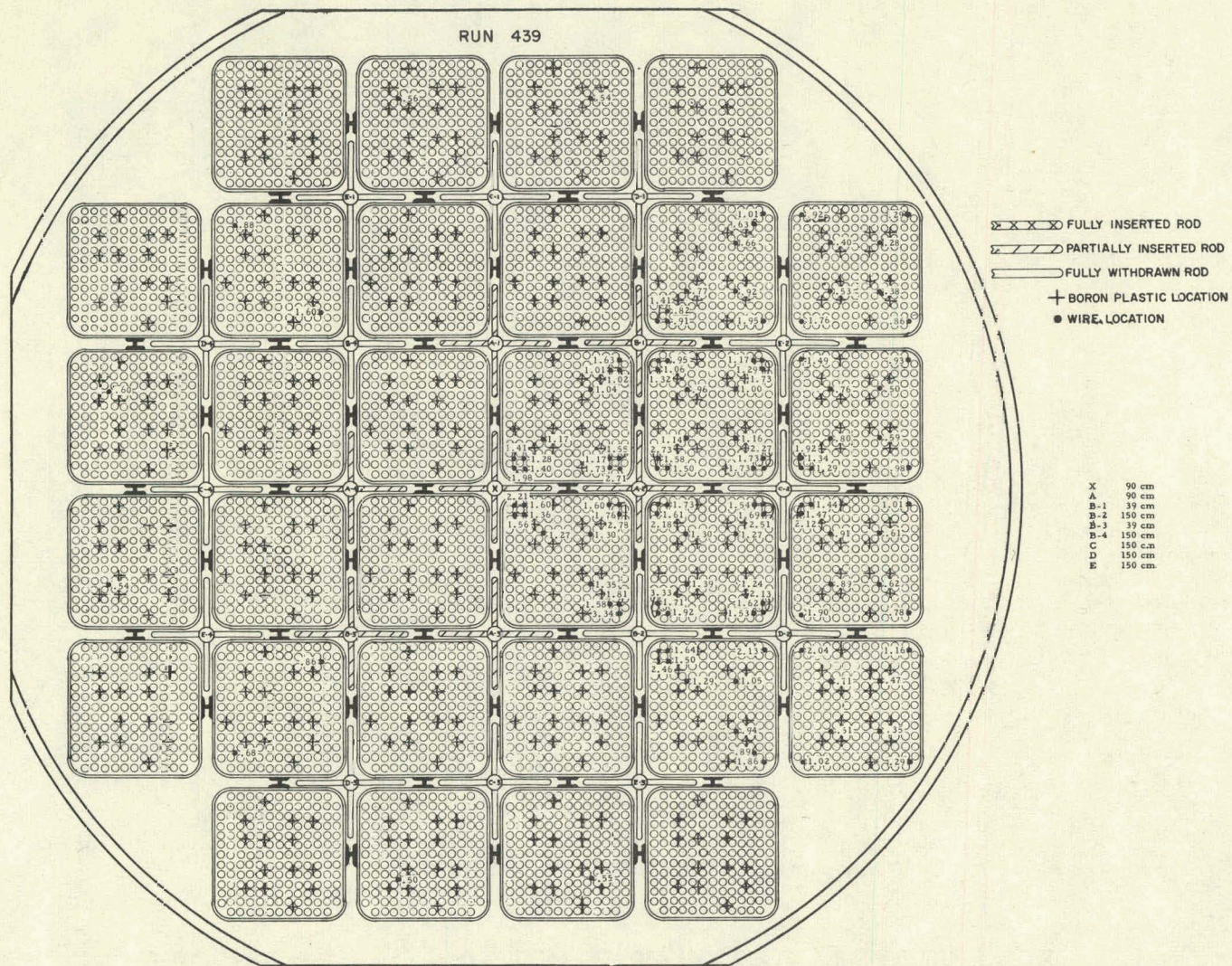


FIG. 58: RADIAL PROFILE OF AXIALLY AVERAGED FLUX

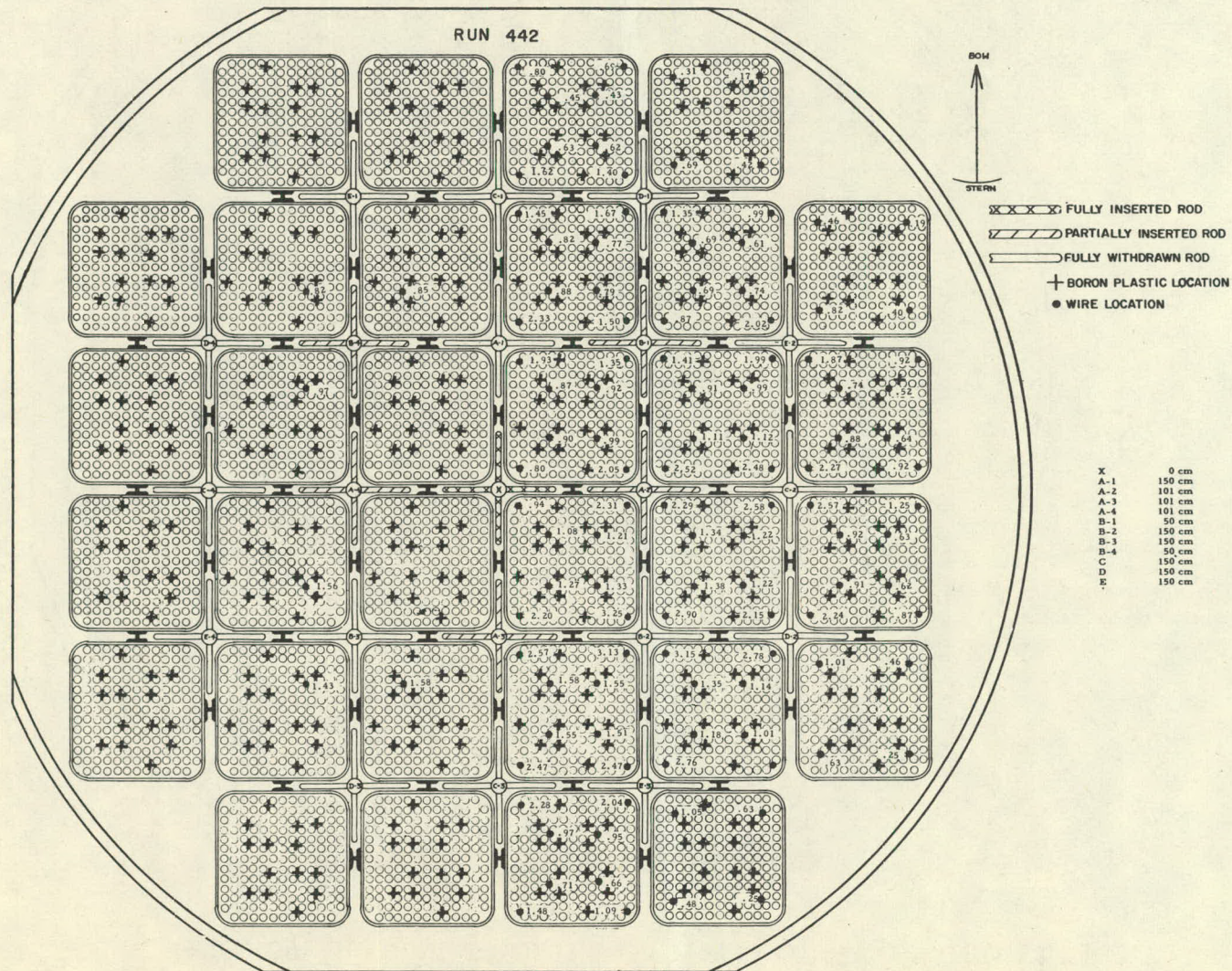


FIG. 59: RADIAL PROFILE OF AXIALLY AVERAGED FLUX

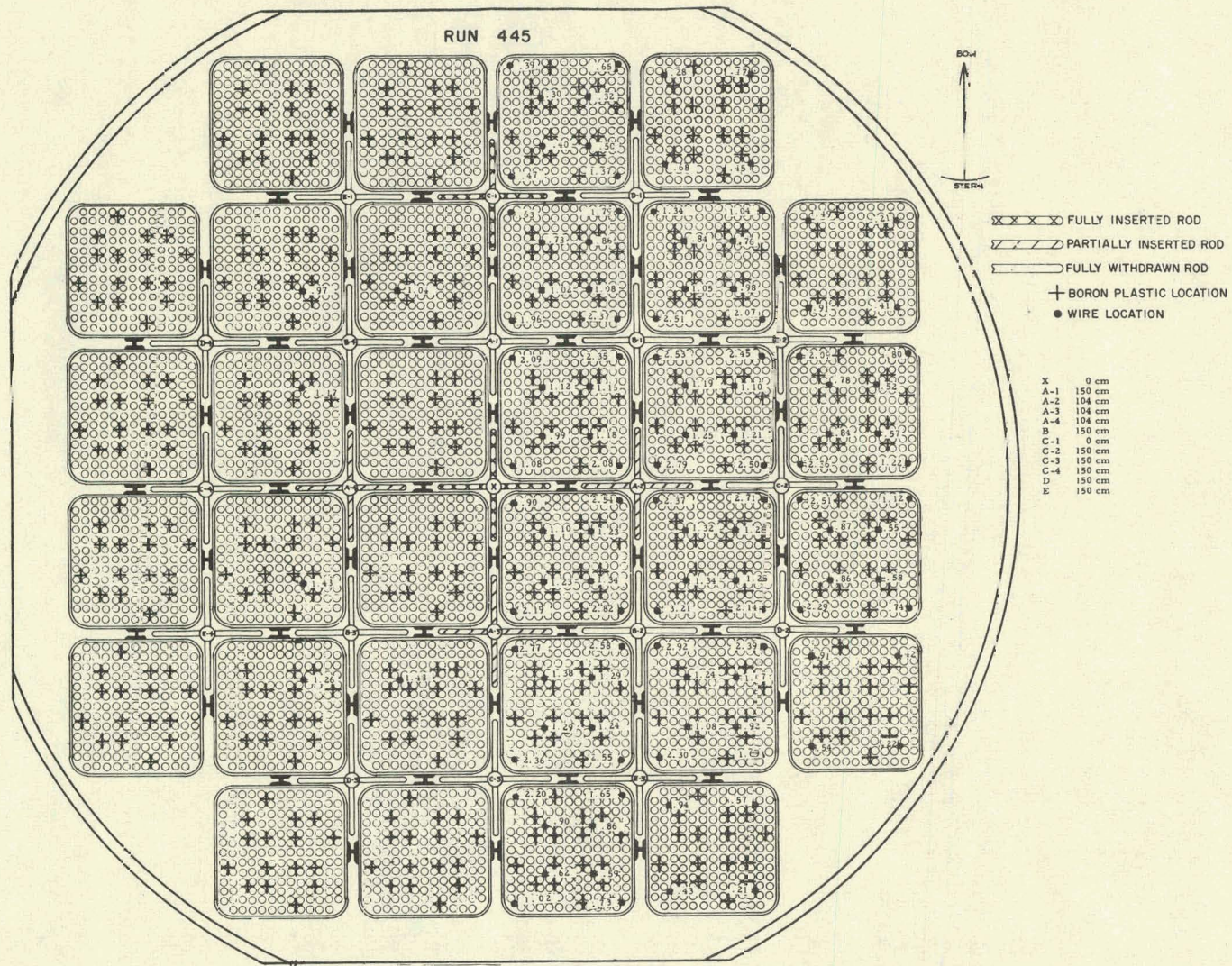


FIG. 60: RADIAL PROFILE OF AXIALLY AVERAGED FLUX

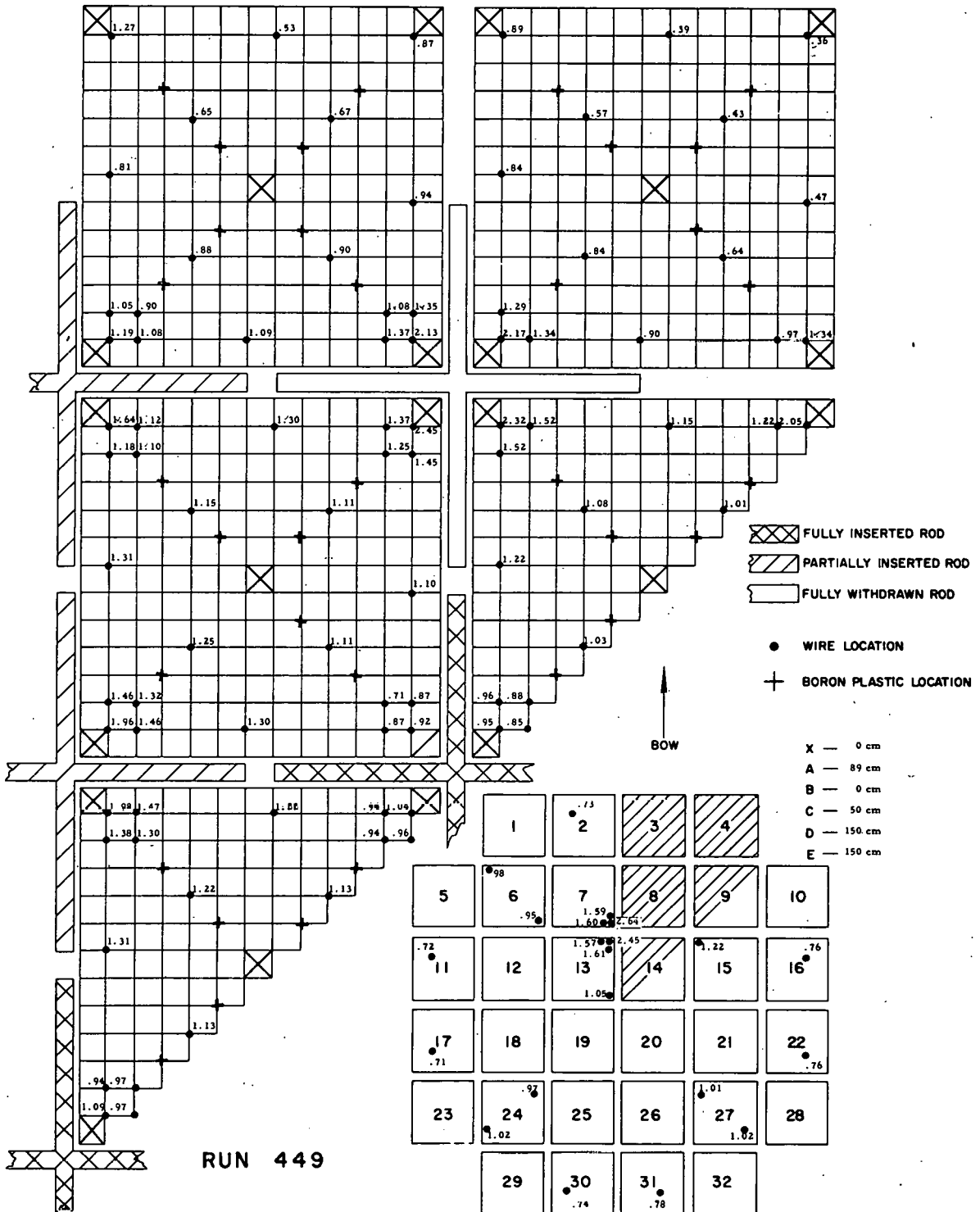
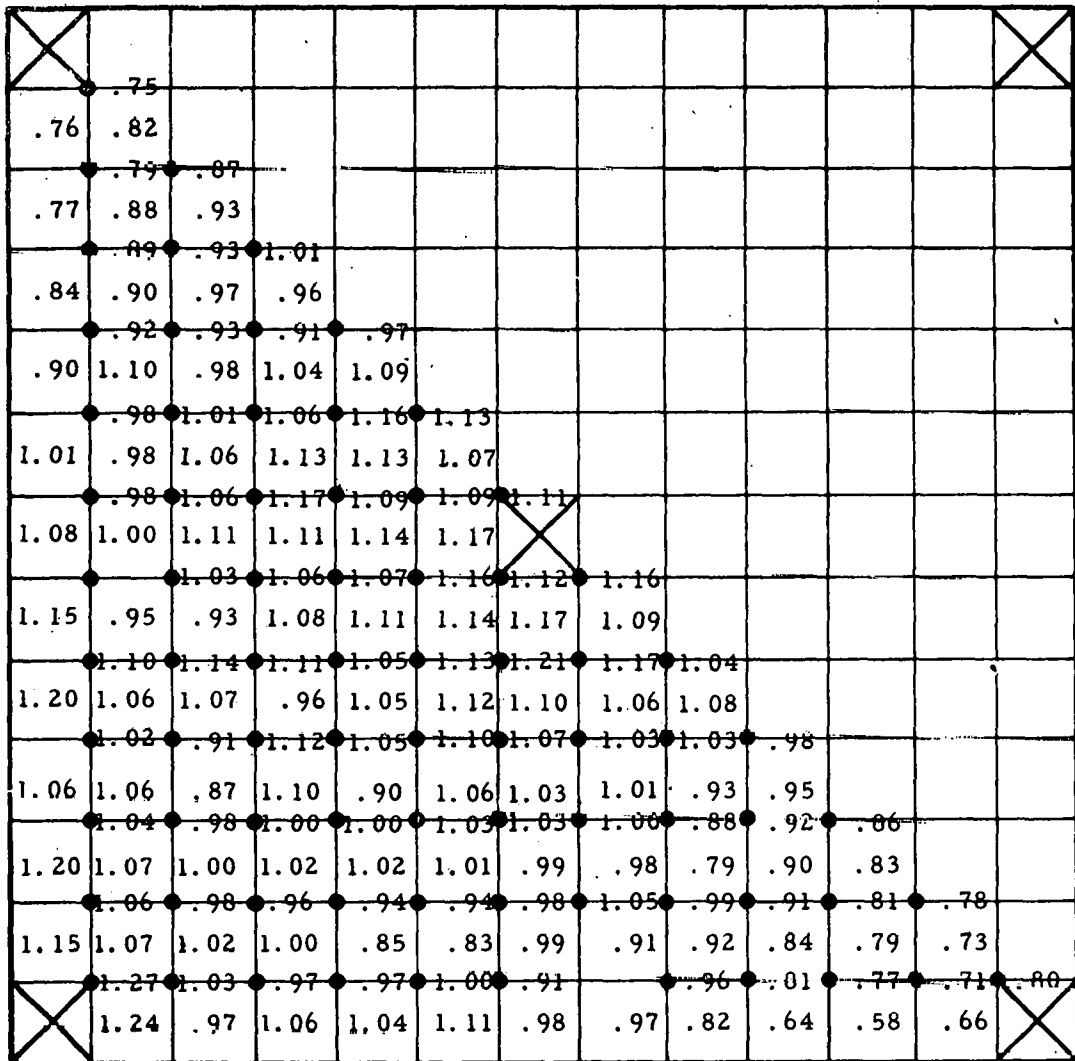


FIG. 61: RADIAL PROFILE OF AXIALLY AVERAGED FLUX

Run 456

Marty Can in Position 20



(75 cm)



Wire Location

Pin Location

Rod Positions

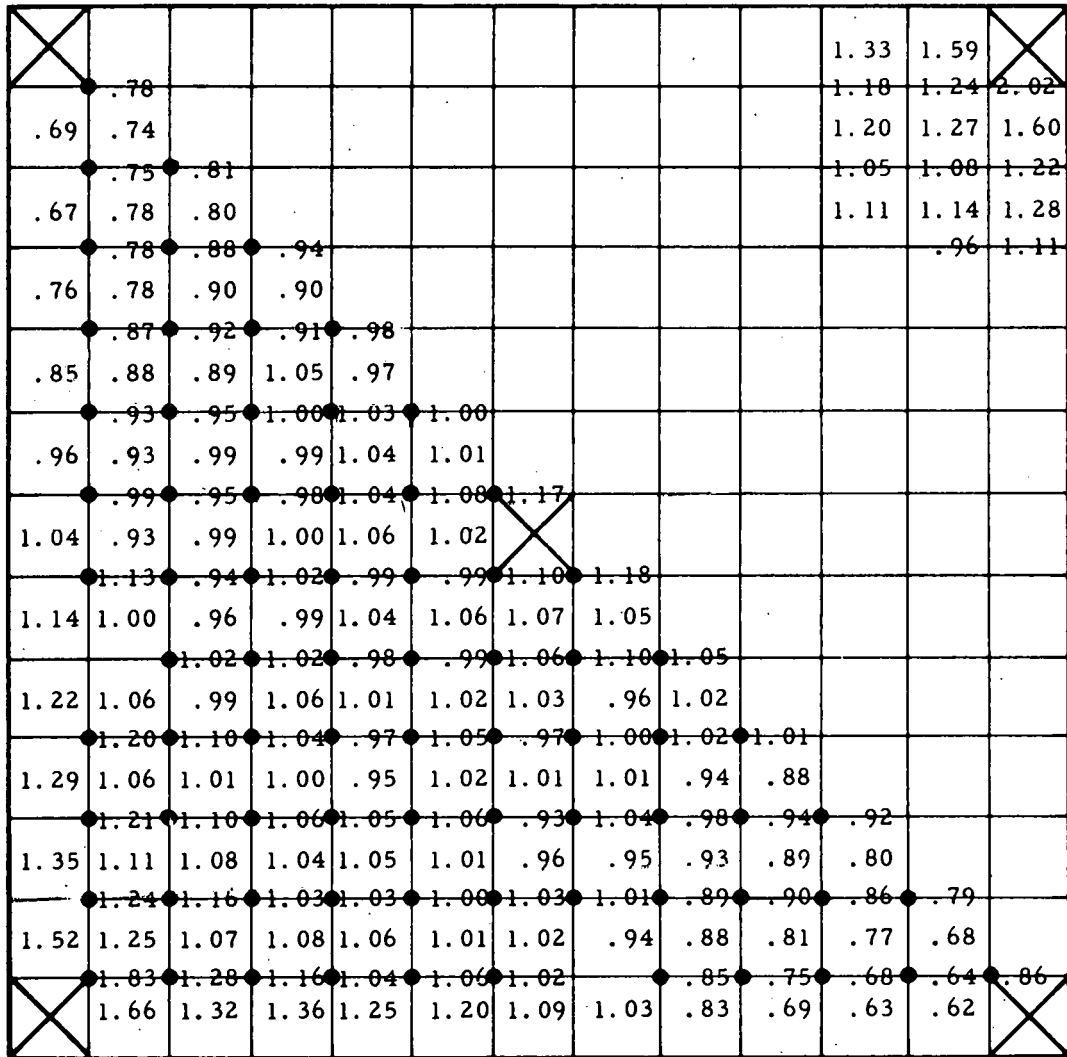
- X 0 cm
- A 75.2 cm
- B 0 cm
- C 0 cm
- D 0 cm
- E 0 cm

No Boron Plastic In Core

FIG. 62: RADIAL PROFILE OF AXIALLY AVERAGED FLUX

Run 458

Martyr Can in Position 20



Wire Location



Pin Location

Partial Water Ht 47.2 cm
No Boron Plastic

Rod Positions

- X 0 cm
- A-1 75 cm (out)
- A-2 150
- A-3 150
- A-4 150
- B 0 cm
- C 75 cm (out)
- D 150
- E 150

FIG. 63: RADIAL PROFILE OF AXIALLY AVERAGED FLUX

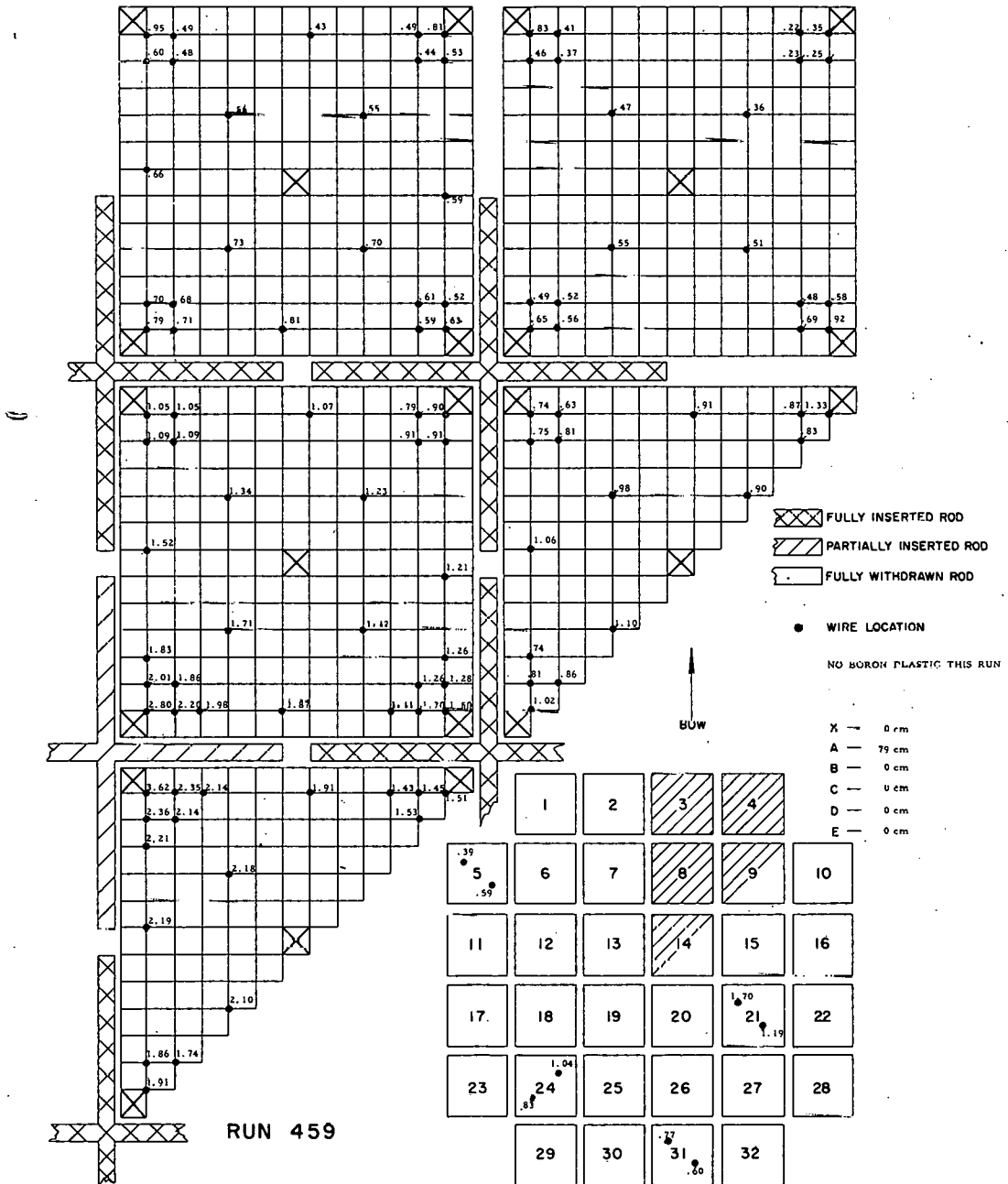
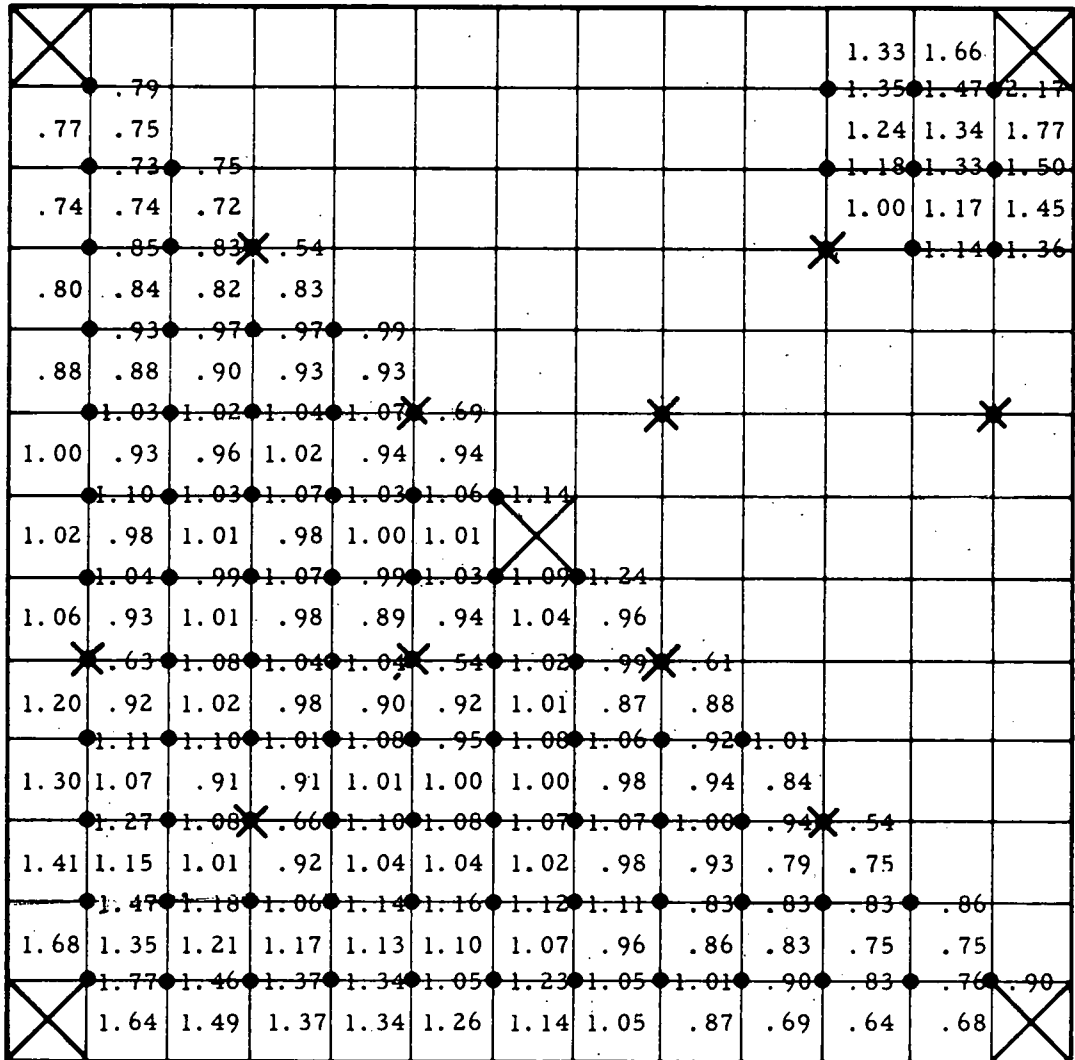


FIG. 64: RADIAL PROFILE OF AXIALLY AVERAGED FLUX

Run 460

Martyr Can in Position 20



Wire Locations



Pin Locations

Partial Water Ht 114.5 cm

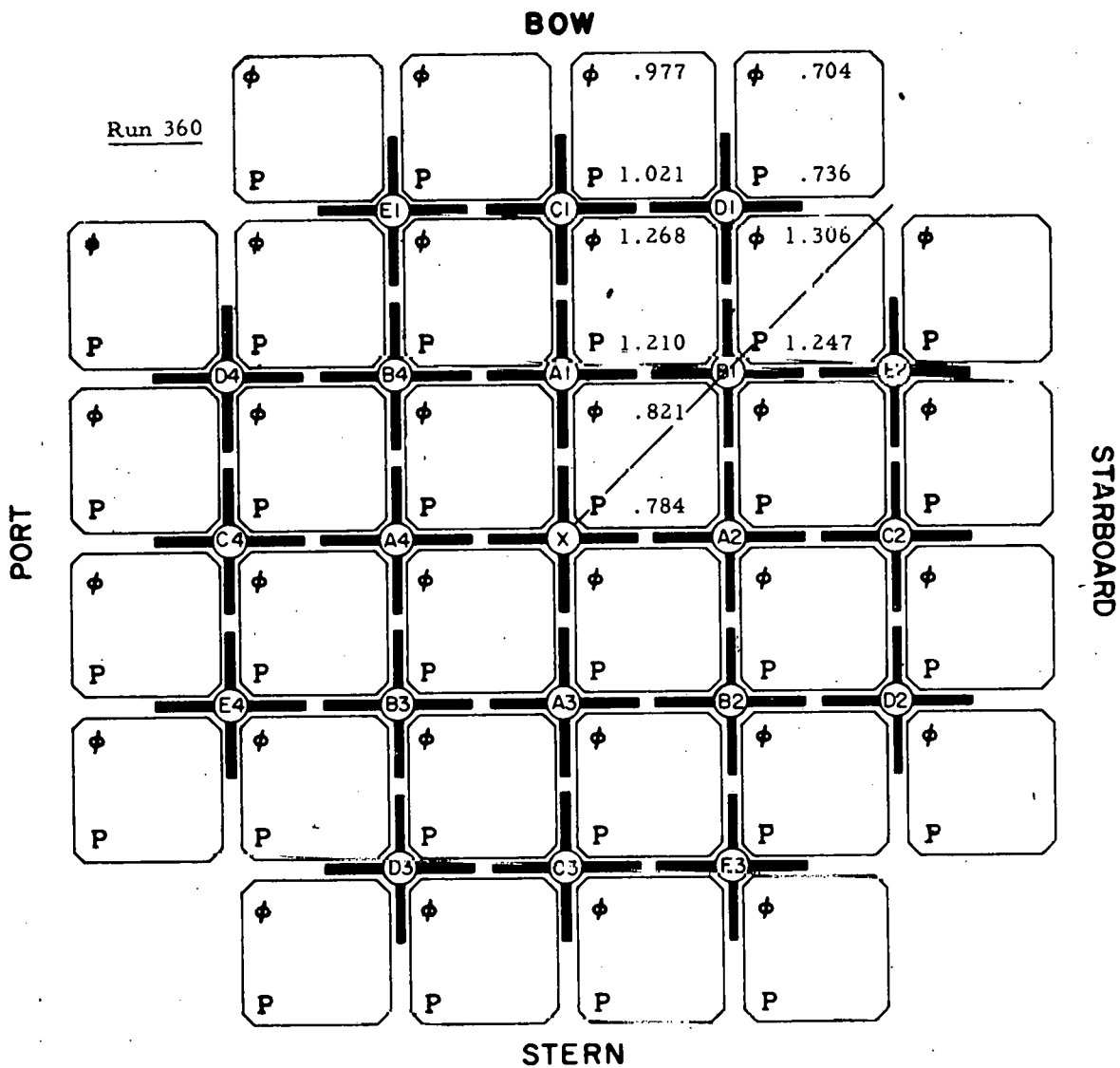


Boron Plastic Locations

Rod Positions

X	0
A	140 (out)
B	0
C	150
D	150
E	150

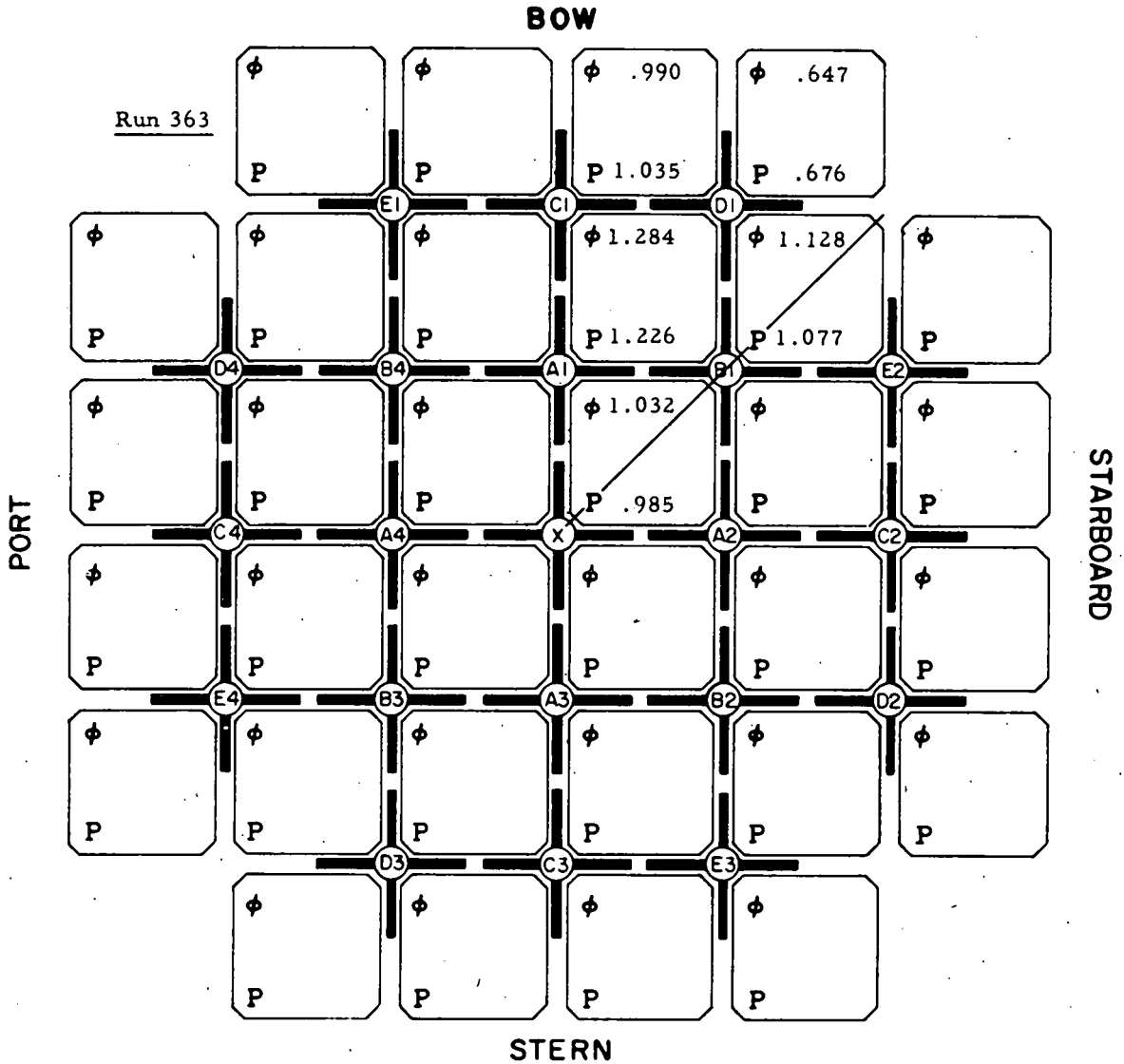
FIG. 65: CAN FLUX AND POWER AVERAGES



Rod Positions
(cm)

A1	0	B1	88.6	C1	150	D1	150	E1	150
A2	0	B2	88.6	C2	150	D2	150	E2	150
A3	0	B3	88.6	C3	150	D3	150	E3	150
A4	0	B4	88.6	C4	150	D4	150	E4	150
		X	0						

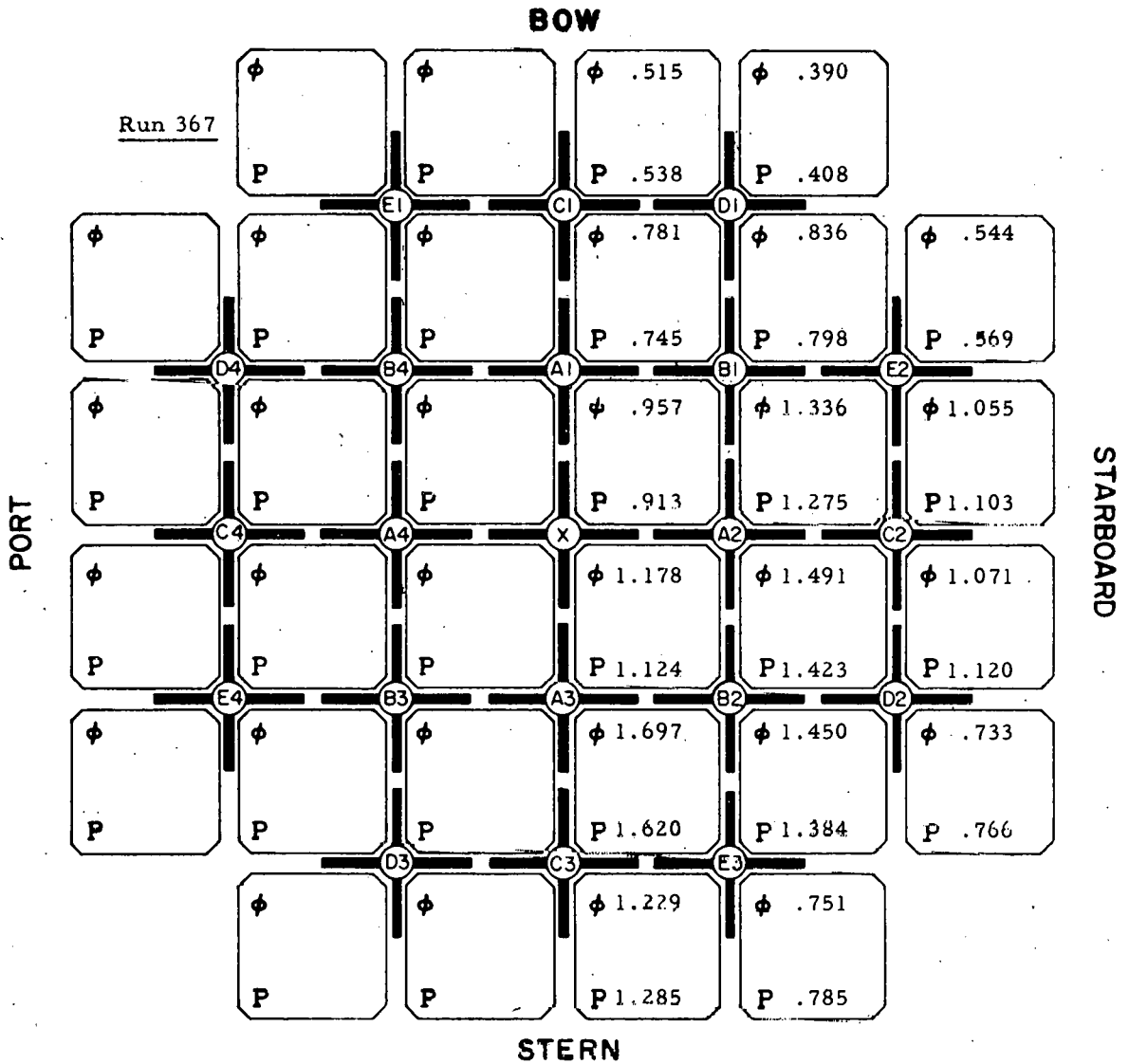
FIG. 66: CAN FLUX AND POWER AVERAGES



Rod Positions
(cm)

A1 89.0	B1 0	C1 150	D1 150	E1 150
A2 89.0	B2 0	C2 150	D2 150	E2 150
A3 89.0	B3 0	C3 150	D3 150	E3 150
A4 89.0	B4 0	C4 150	D4 150	E4 150
X 0				

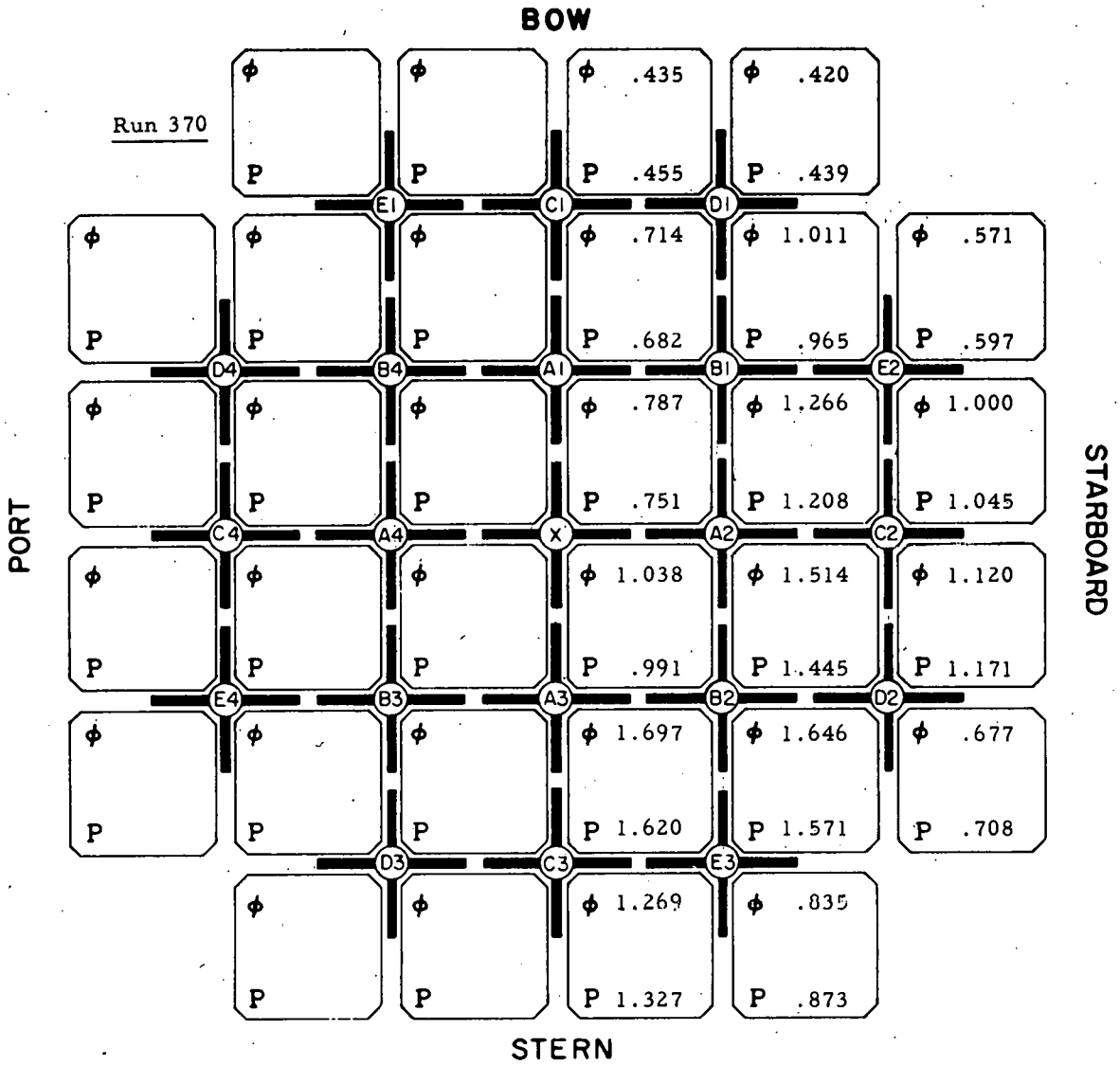
FIG. 67: CAN FLUX AND POWER AVERAGES



Rod Positions
(cm)

A1	80.0	B1	30.0	C1	0	D1	150	E1	150
A2	80.0	B2	30.0	C2	150	D2	150	E2	150
A3	80.0	B3	30.0	C3	150	D3	150	E3	150
A4	80.0	B4	30.0	C4	150	D4	150	E4	150
X	0								

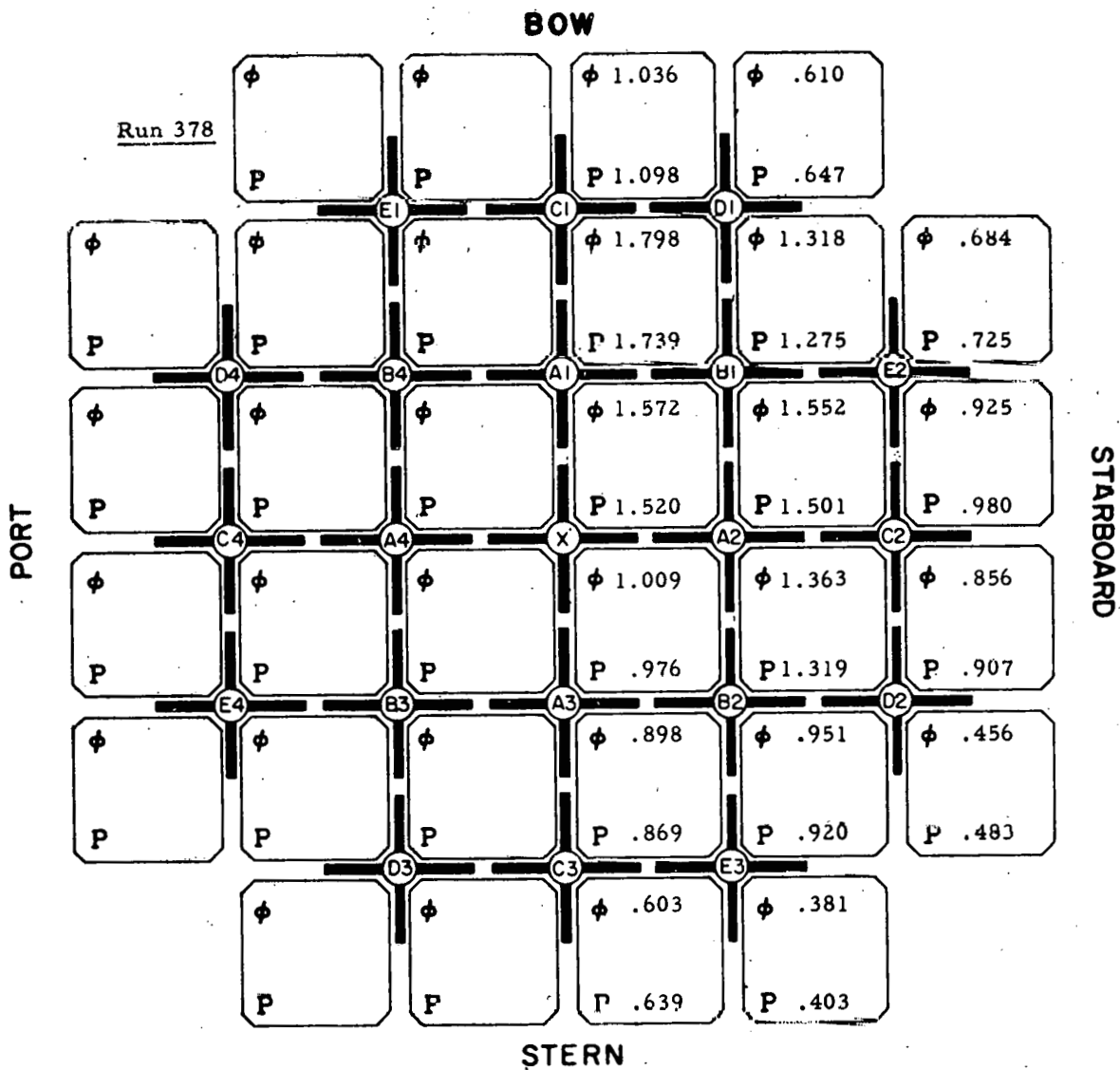
FIG. 68: CAN FLUX AND POWER AVERAGES



Rod Positions
(cm)

A1 25.0	B1 79.8	C1 0	D1 150	E1 150
A2 25.0	B2 79.8	C2 150	D2 150	E2 150
A3 25.0	B3 79.8	C3 150	D3 150	E3 150
A4 25.0	B4 79.8	C4 150	D4 150	E4 150
X 0				

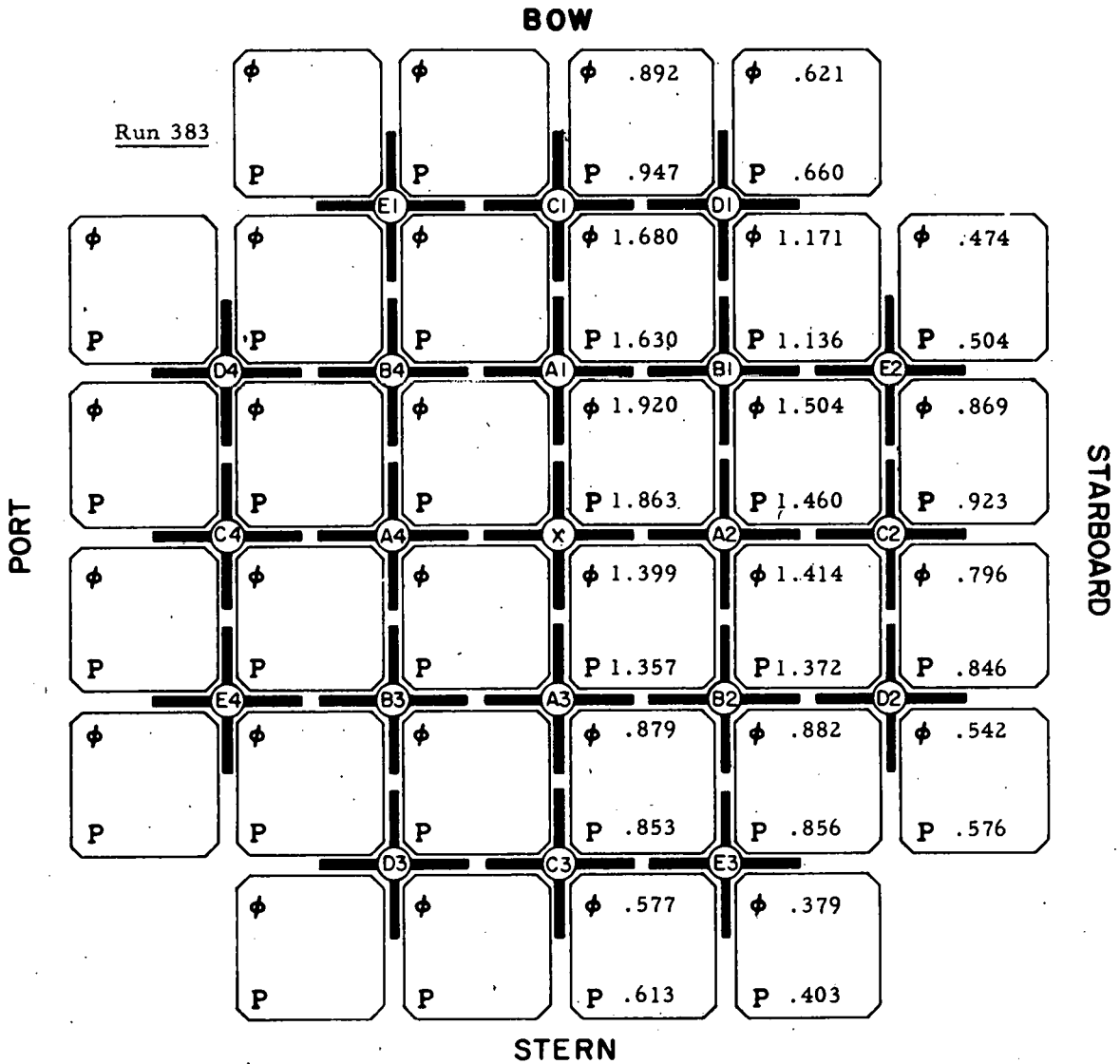
FIG. 69: CAN FLUX AND POWER AVERAGES



Rod Positions
(cm)

A1	150	B1	91.0	C1	150	D1	150	E1	150
A2	150	B2	91.0	C2	150	D2	150	E2	150
A3	0	B3	91.0	C3	150	D3	150	E3	150
A4	150	B4	91.0	C4	150	D4	150	E4	150
		X	0						

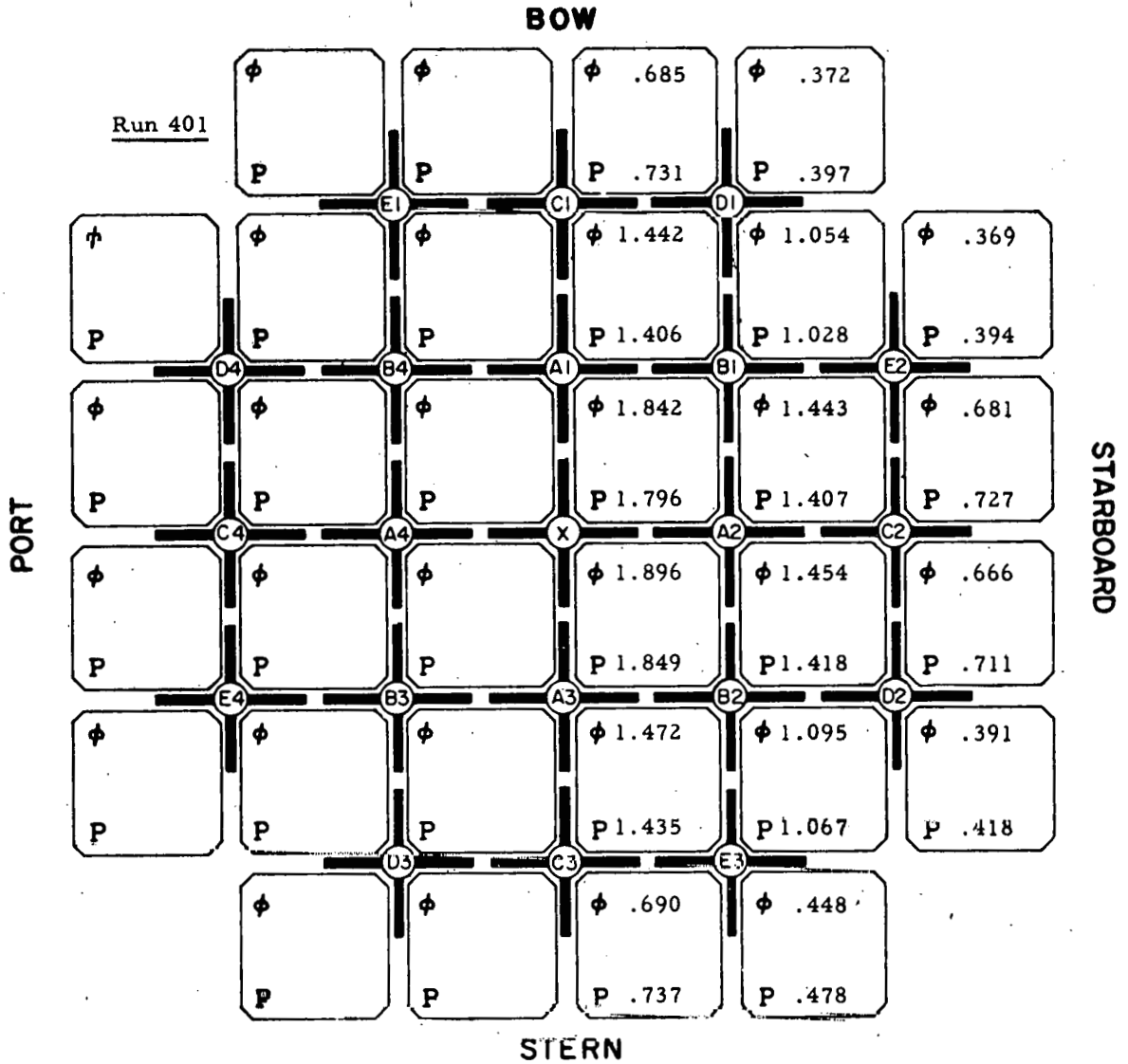
FIG. 70: CAN FLUX AND POWER AVERAGES



Rod Positions
(cm)

A1	150	B1	82.8	C1	150	D1	150	E1	150
A2	150	B2	82.8	C2	150	D2	150	E2	150
A3	0	B3	82.8	C3	150	D3	150	E3	150
A4	150	B4	82.8	C4	150	D4	150	E4	150
		X	150						

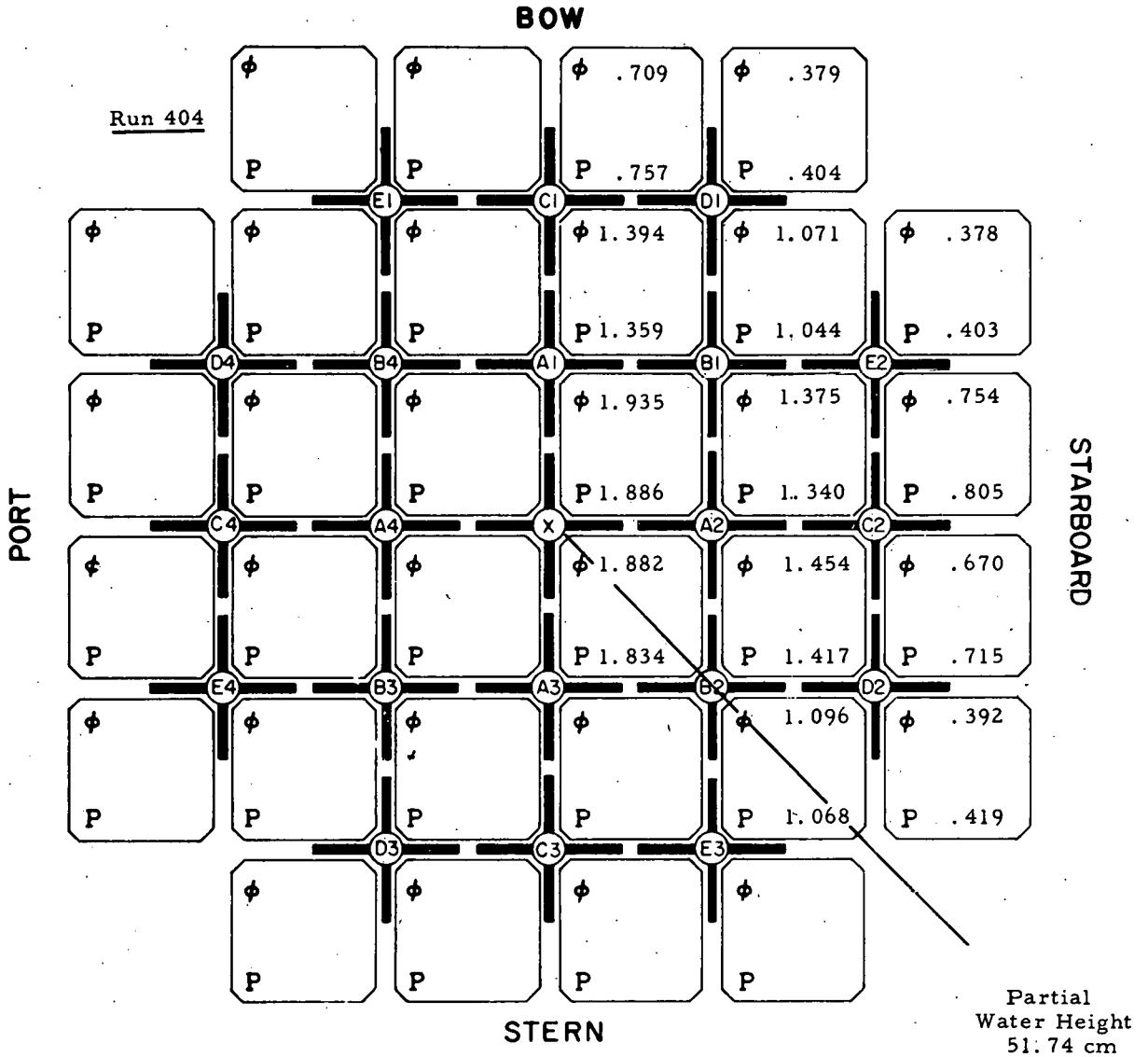
FIG. 71: CAN FLUX AND POWER AVERAGES



Rod Positions
(cm)

A1	150	B1	150	C1	150	D1	150	E1	150
A2	150	B2	150	C2	150	D2	150	E2	150
A3	150	B3	150	C3	150	D3	150	E3	150
A4	150	B4	150	C4	150	D4	150	E4	150
				X	150				

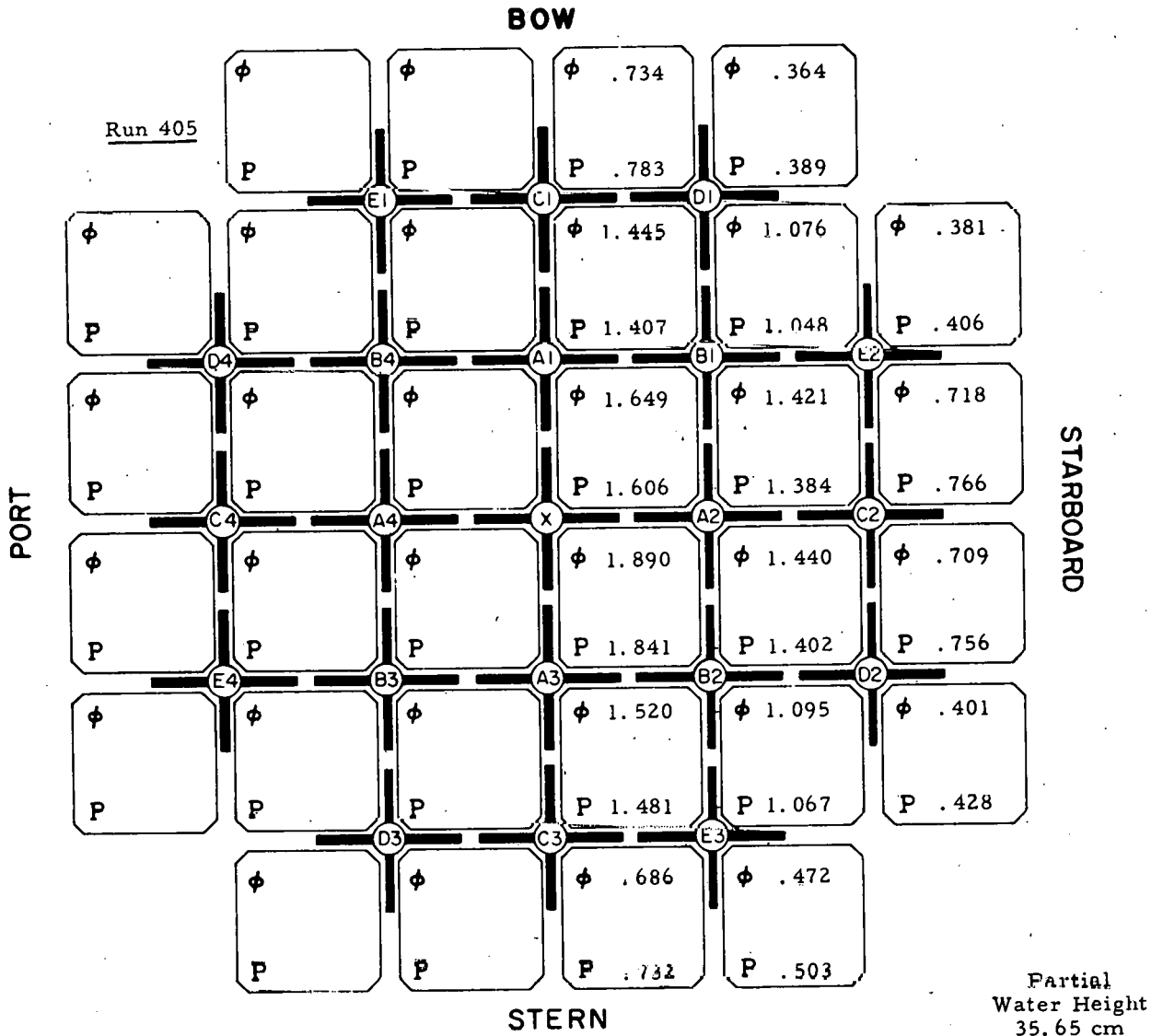
FIG. 72: CAN FLUX AND POWER AVERAGES



Rod Positions
(cm)

A1	150	B1	150	C1	150	D1	150	E1	150
A2	150	B2	150	C2	150	D2	150	E2	150
A3	150	B3	70	C3	150	D3	150	E3	150
A4	150	B4	70	C4	150	D4	150	E4	150
X	150								

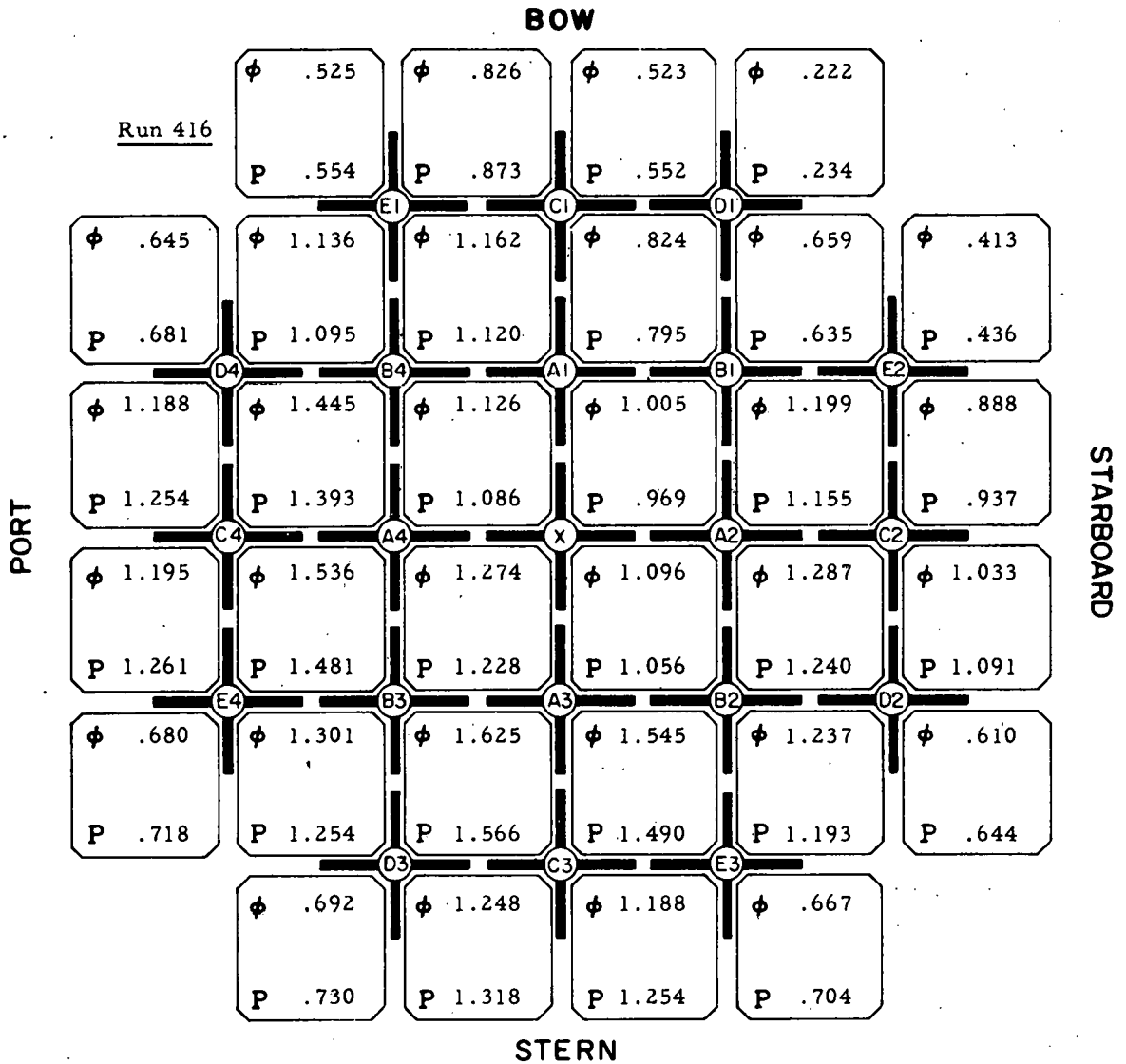
FIG. 73: CAN FLUX AND POWER AVERAGES



Rod Positions
(cm)

A1	150	B1	150	C1	150	D1	150	E1	150
A2	150	B2	150	C2	150	D2	150	E2	150
A3	150	B3	50	C3	150	D3	150	E3	150
A4	150	B4	50	C4	150	D4	60	E4	60
		X	150						

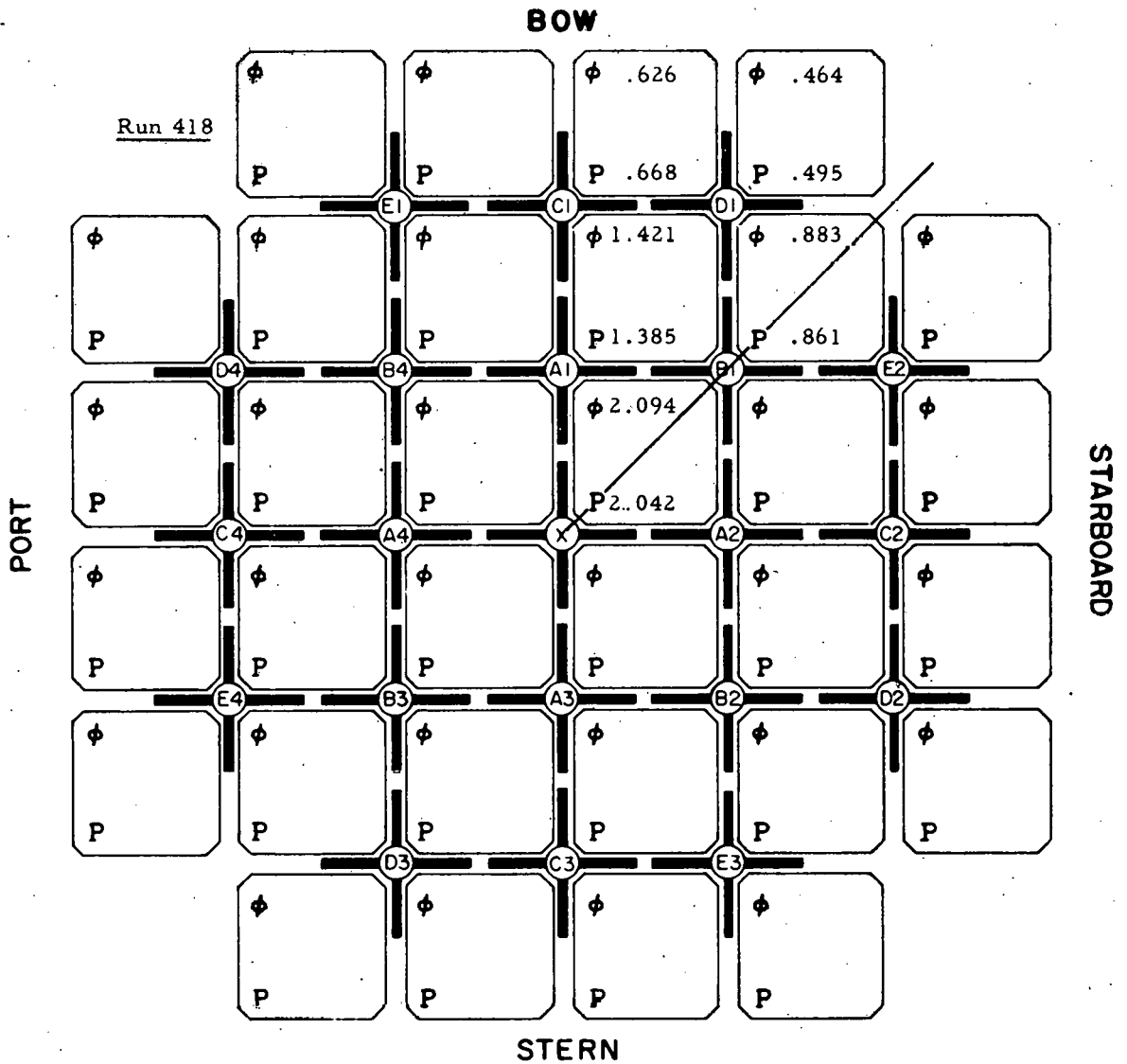
FIG. 74: CAN FLUX AND POWER AVERAGES



Rod Positions
(cm)

A1	101	B1	0	C1	150	D1	0	E1	150
A2	101	B2	0	C2	150	D2	150	E2	150
A3	101	B3	0	C3	150	D3	150	E3	150
A4	101	B4	0	C4	150	D4	150	E4	150
		X	0						

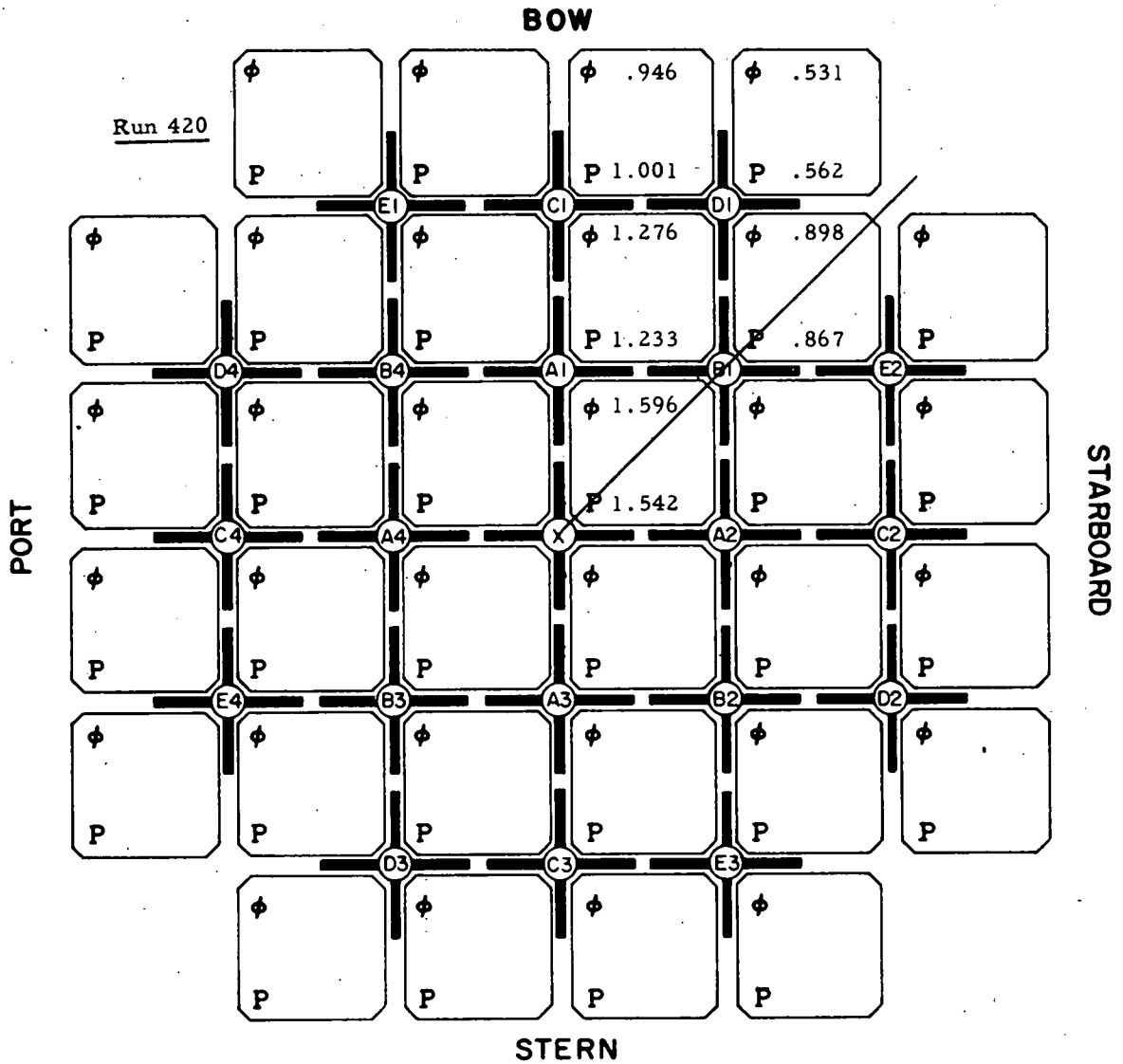
FIG. 75: CAN FLUX AND POWER AVERAGES



Rod Positions
(cm)

A1	79.0	B1	0	C1	0	D1	0	E1	0
A2	79.0	B2	0	C2	0	D2	0	E2	0
A3	79.0	B3	0	C3	0	D3	0	E3	0
A4	79.0	B4	0	C4	0	D4	0	E4	0
		X							

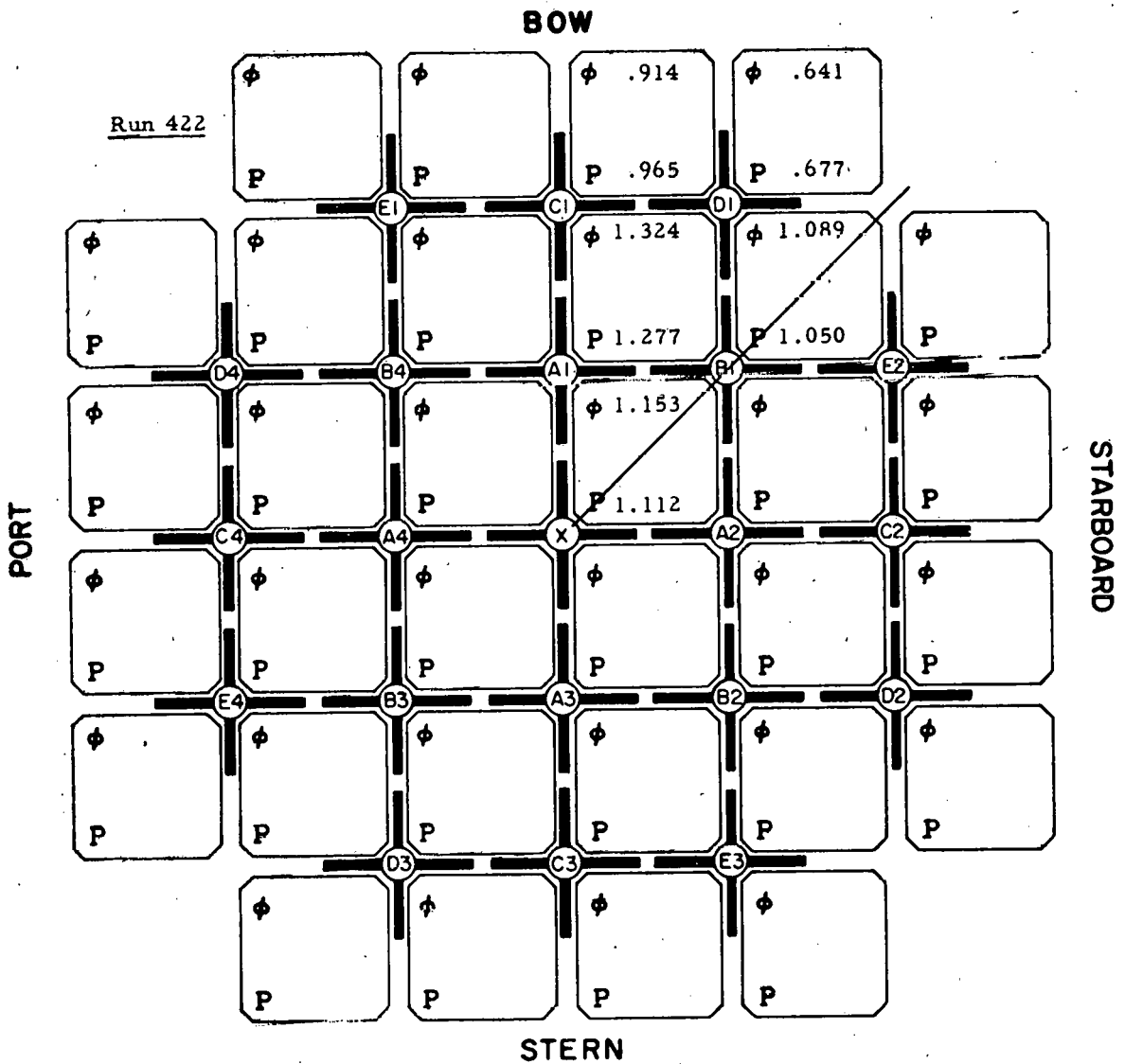
FIG. 76: CAN FLUX AND POWER AVERAGES



Rod Positions
(cm)

A1 <u> 0 </u>	B1 <u> 0 </u>	C1 <u>108 </u>	D1 <u> 0 </u>	E1 <u> 0 </u>
A2 <u> 0 </u>	B2 <u> 0 </u>	C2 <u>108 </u>	D2 <u> 0 </u>	E2 <u> 0 </u>
A3 <u> 0 </u>	B3 <u> 0 </u>	C3 <u>108 </u>	D3 <u> 0 </u>	E3 <u> 0 </u>
A4 <u> 0 </u>	B4 <u> 0 </u>	C4 <u>108 </u>	D4 <u> 0 </u>	E4 <u> 0 </u>
X <u>150 </u>				

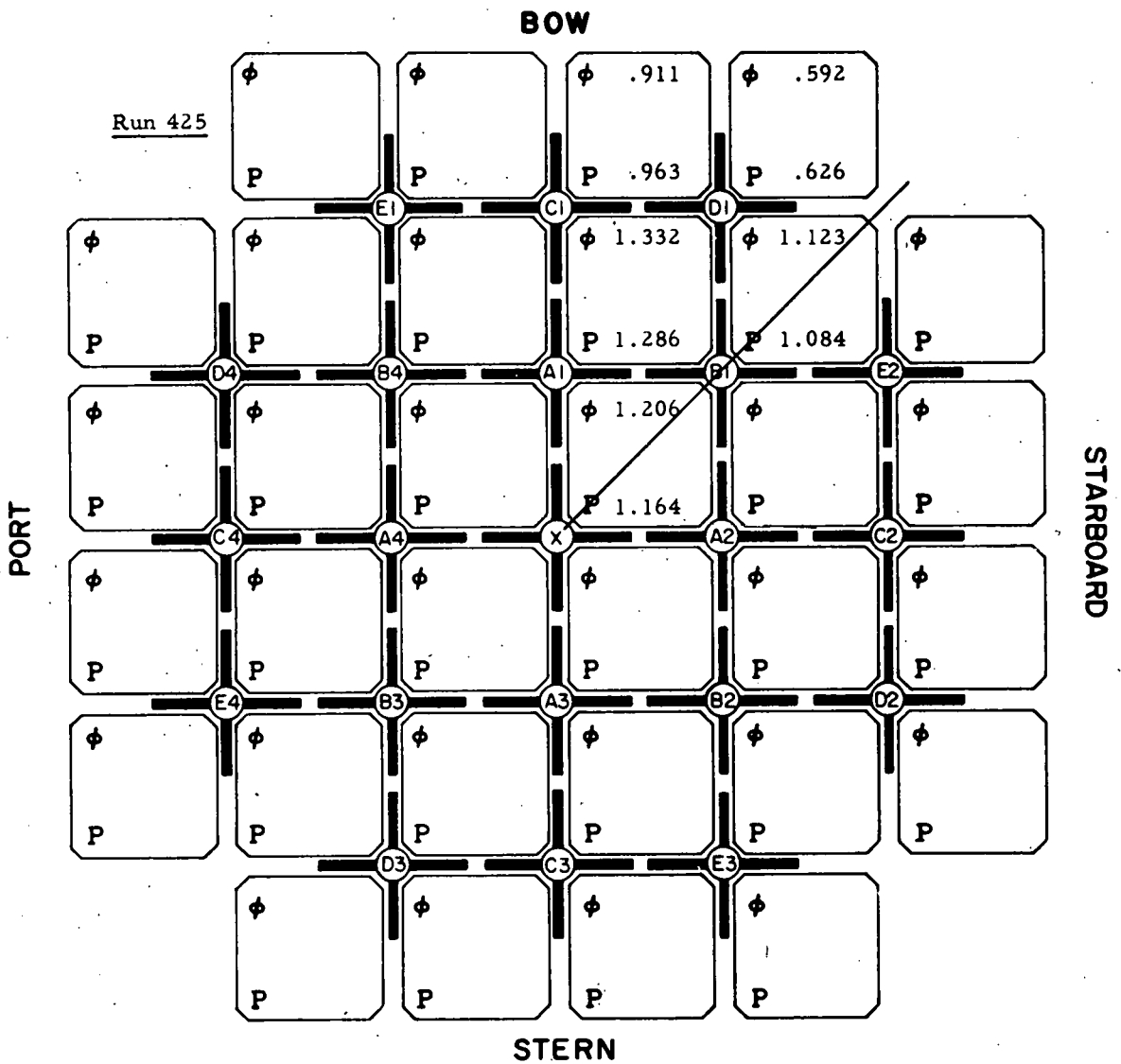
FIG. 77: CAN FLUX AND POWER AVERAGES



Rod Positions
(cm)

A1	100	B1	0	C1	101.7	D1	150	E1	150
A2	100	B2	0	C2	101.7	D2	150	E2	150
A3	100	B3	0	C3	101.7	D3	150	E3	150
A4	100	B4	0	C4	101.7	D4	150	E4	150
X	0								

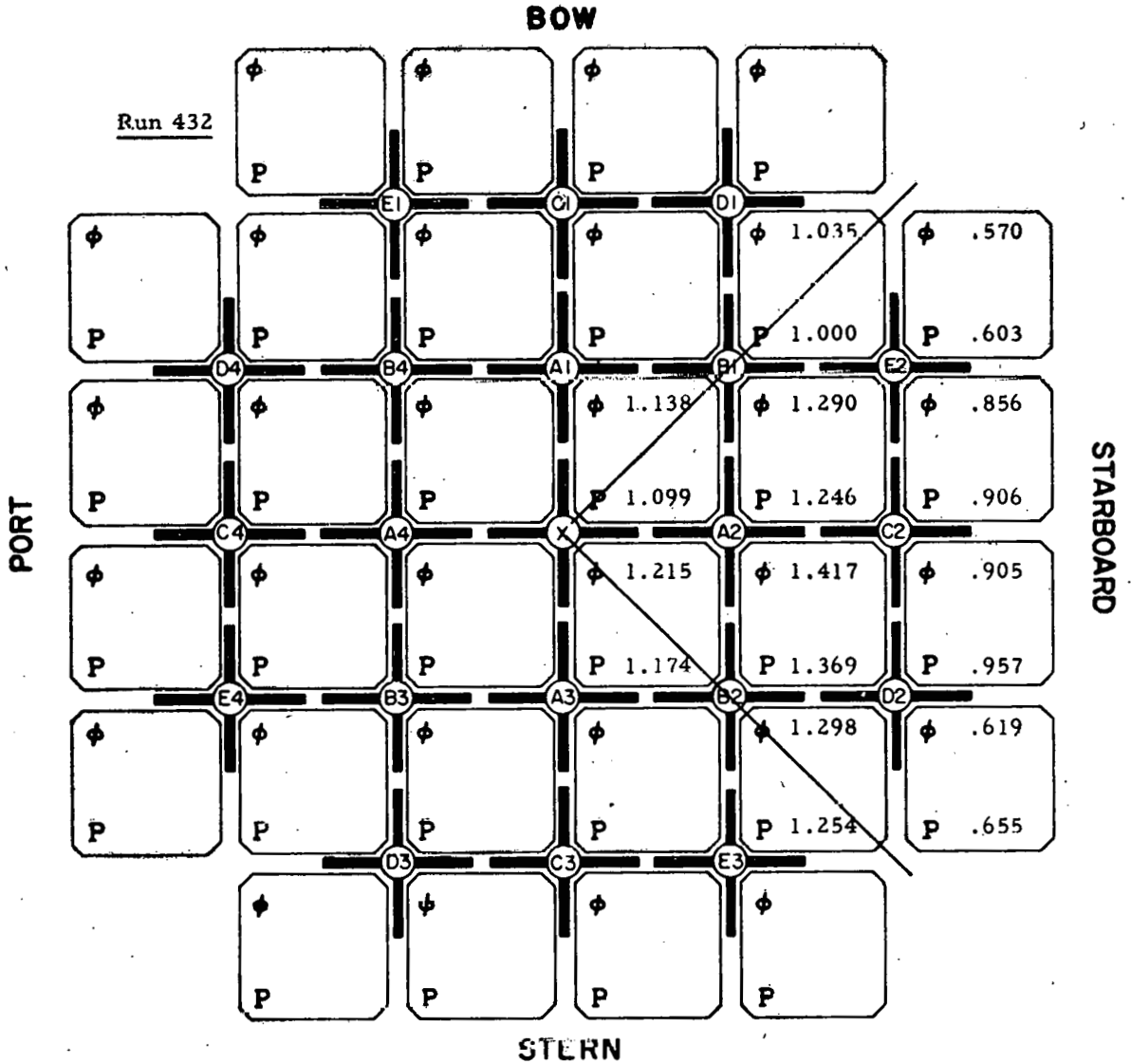
FIG. 78: CAN FLUX AND POWER AVERAGES



Rod Positions
(cm)

A1	89.6	B1	45.0	C1	150	D1	150	E1	150
A2	89.6	B2	45.0	C2	150	D2	150	E2	150
A3	89.6	B3	45.0	C3	150	D3	150	E3	150
A4	89.6	B4	45.0	C4	150	D4	150	E4	150
X	0								

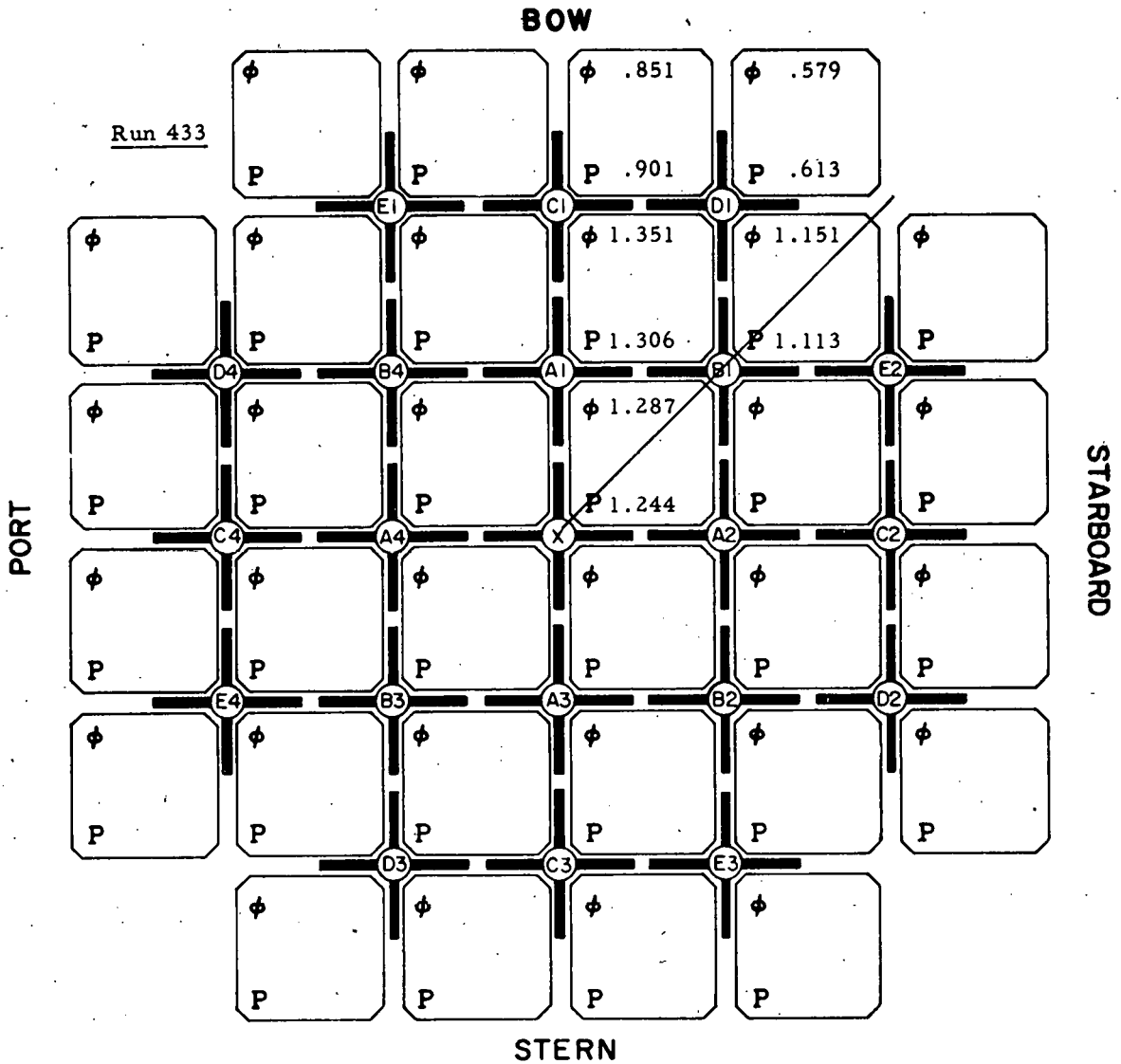
FIG. 79: CAN FLUX AND POWER AVERAGES



Rod Positions
(cm)

A1	90.0	B1	75.0	C1	150	D1	150	E1	150
A2	90.0	B2	150	C2	150	D2	150	E2	150
A3	90.0	B3	75.0	C3	150	D3	150	E3	150
A4	90.0	B4	150	C4	150	D4	150	E4	150
X	0								

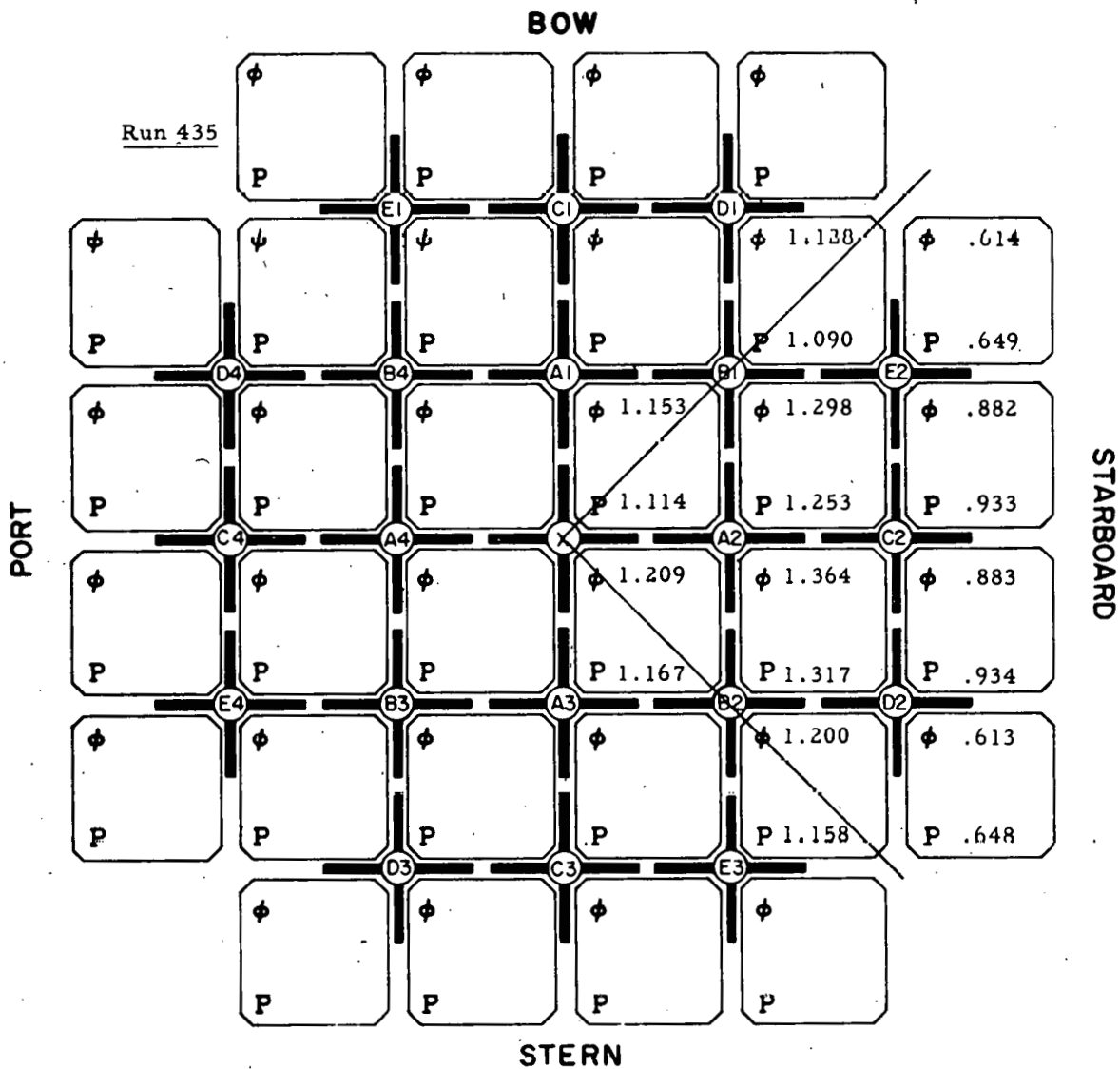
FIG. 80: CAN FLUX AND POWER AVERAGES



Rod Positions
(cm)

A1	90	B1	90	C1	150	D1	150	E1	150
A2	90	B2	90	C2	150	D2	150	E2	150
A3	90	B3	90	C3	150	D3	150	E3	150
A4	90	B4	90	C4	150	D4	150	E4	150
X	0								

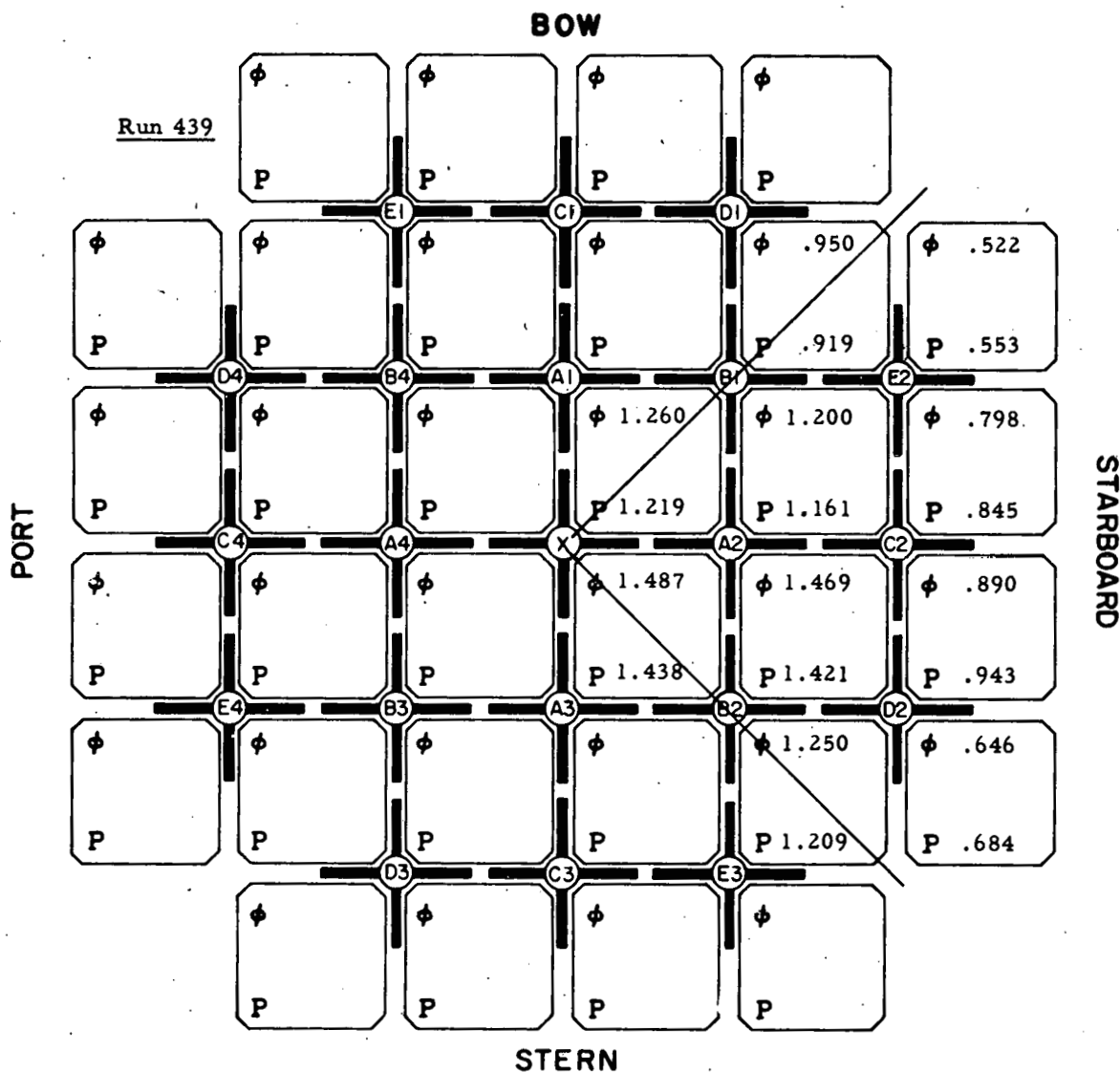
FIG. 81: CAN FLUX AND POWER AVERAGES



Rod Positions
(cm)

A1	90	B1	102	C1	180	D1	180	E1	180
A2	90	B2	180	C2	180	D2	180	E2	180
A3	90	B3	102	C3	180	D3	180	E3	180
A4	90	B4	180	C4	180	D4	180	E4	180
X	0								

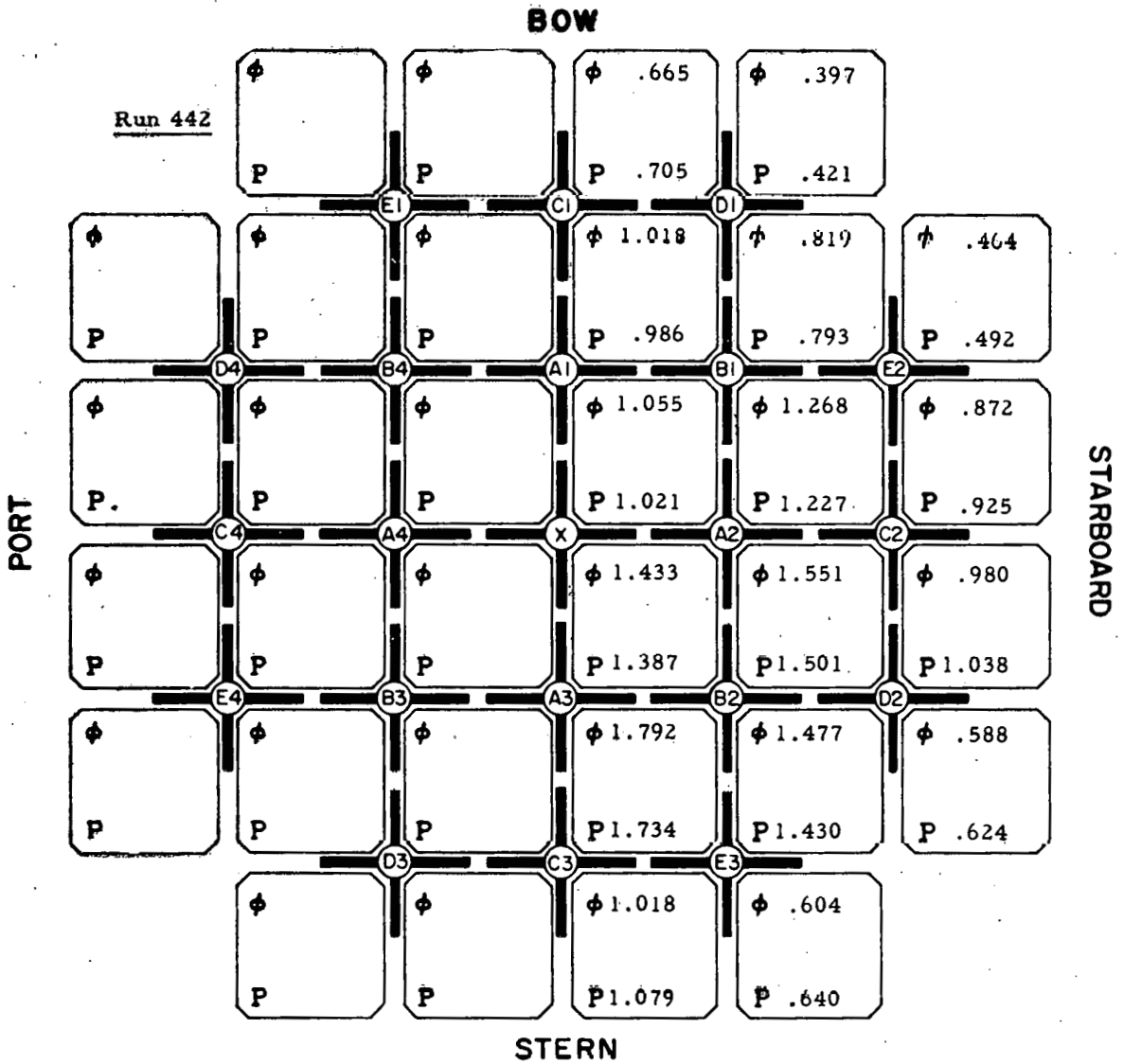
FIG. 82: CAN FLUX AND POWER AVERAGES



Rod Positions
(cm)

A1	90	B1	39.0	C1	150	D1	150	E1	150
A2	90	B2	150	C2	150	D2	150	E2	150
A3	90	B3	39.0	C3	150	D3	150	E3	150
A4	90	B4	150	C4	150	D4	150	E4	150
X	90								

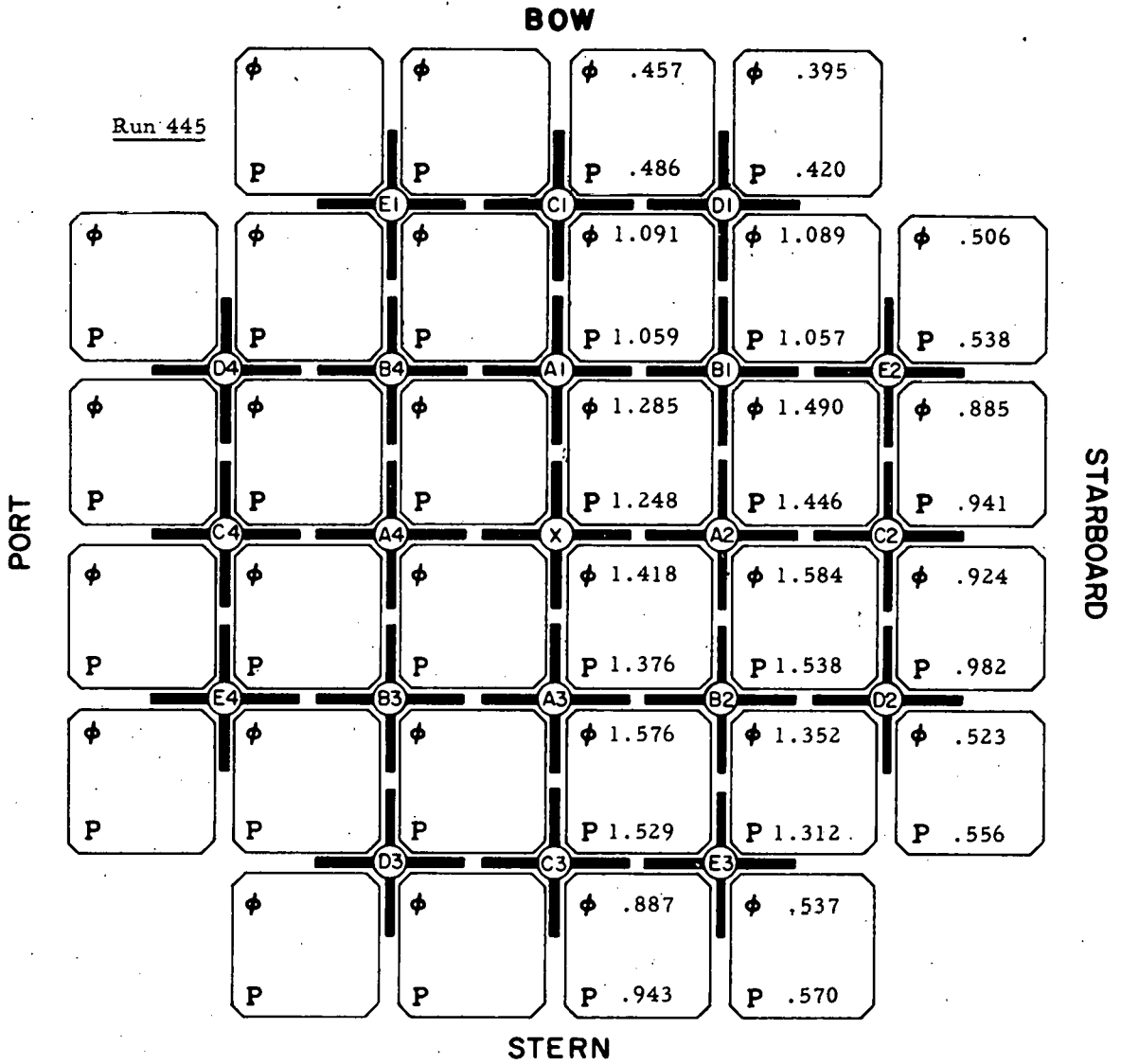
FIG. 83: CAN FLUX AND POWER AVERAGES



Rod Positions
(cm)

A1	150	B1	55.0	C1	150	D1	150	E1	150
A2	101.3	B2	150	C2	150	D2	150	E2	150
A3	101.3	B3	150	C3	150	D3	150	E3	150
A4	101.3	B4	55.0	C4	150	D4	150	E4	150
		X	0						

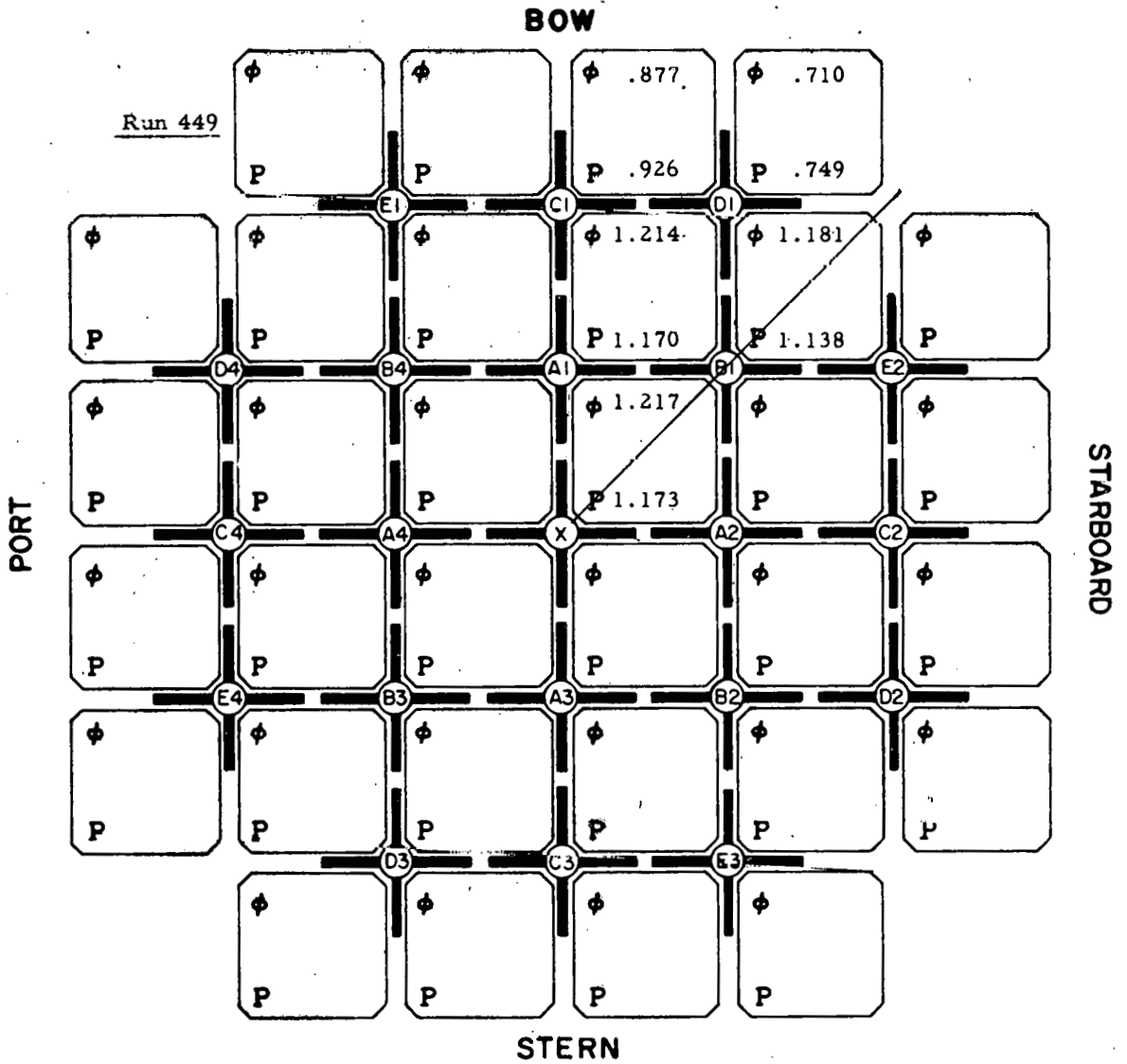
FIG. 84: CAN FLUX AND POWER AVERAGES



Rod Positions
(cm)

A1	150	B1	150	C1	0	D1	150	E1	150
A2	104	B2	150	C2	150	D2	150	E2	150
A3	104	B3	150	C3	150	D3	150	E3	150
A4	104	B4	150	C4	150	D4	150	E4	150
				X	0				

FIG. 85: CAN FLUX AND POWER AVERAGES



Rod Positions
(cm)

A1	88.5	B1	0	C1	50.0	D1	150	E1	150
A2	88.5	B2	0	C2	50.0	D2	150	E2	150
A3	88.5	B3	0	C3	50.0	D3	150	E3	150
A4	88.5	B4	0	C4	50.0	D4	150	E4	150
		X	0						

FIG. 87: XY MESH FOR TKO CODE

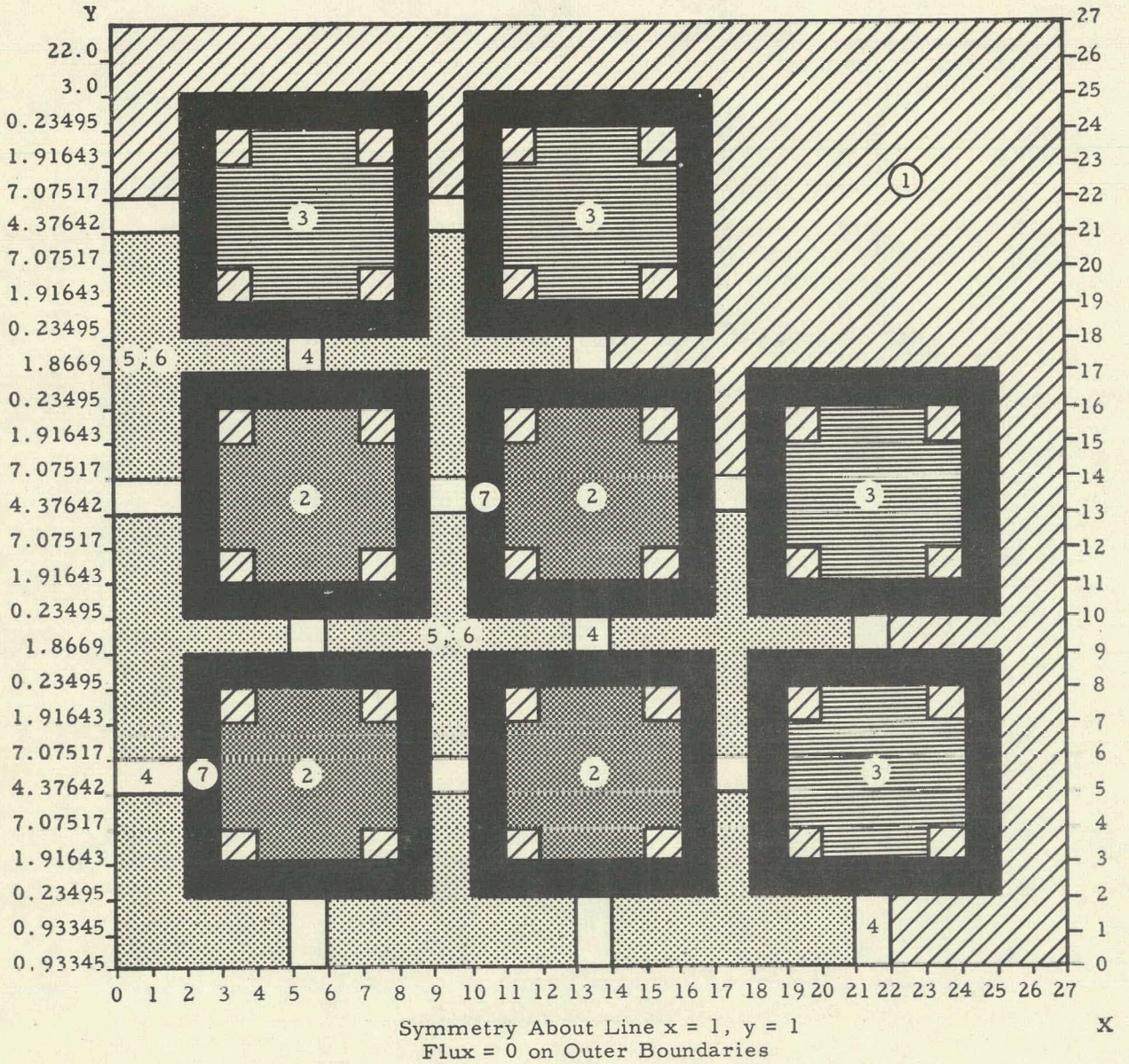
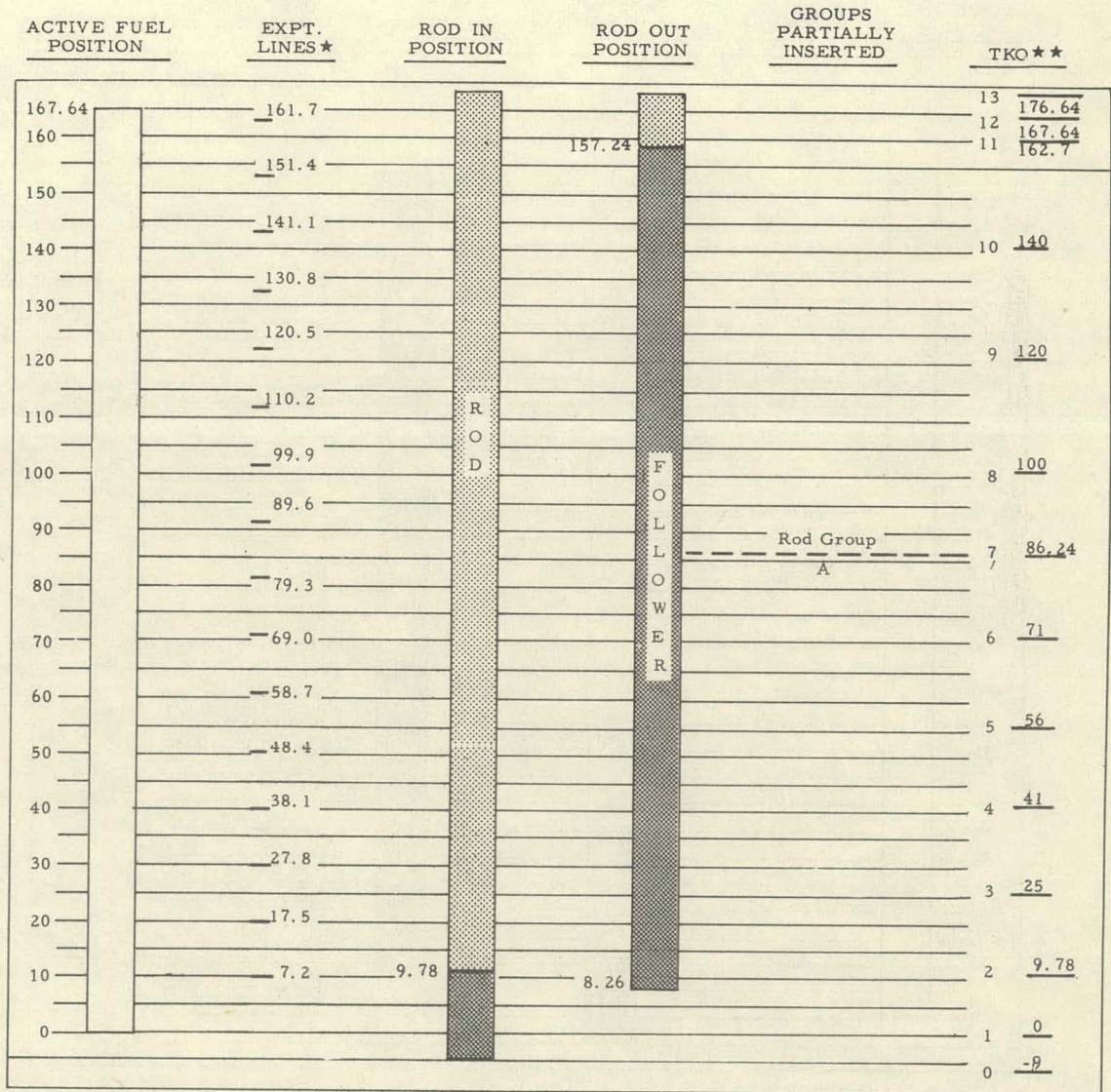
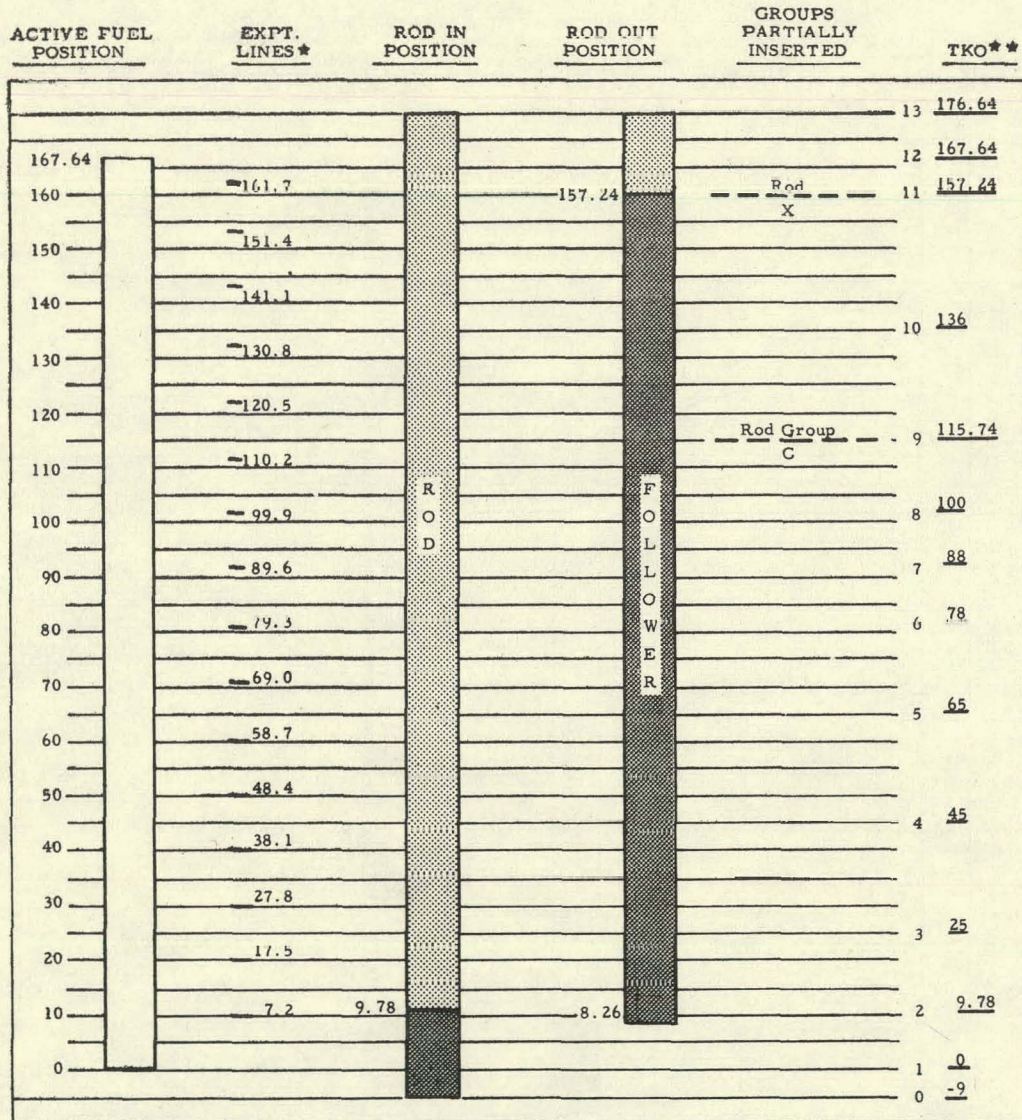


FIG. 88: Z MESH FOR TKO CODE - RUN 418



★ Points where experimental wires were counted
 ★★ Location of mesh planes

FIG. 89: Z MESH FOR TKO CODE - RUN 420



★★ Location of mesh planes.

★ Points where experimental wires were counted.

FIG. 90: AXIAL FLUX TRAVERSE

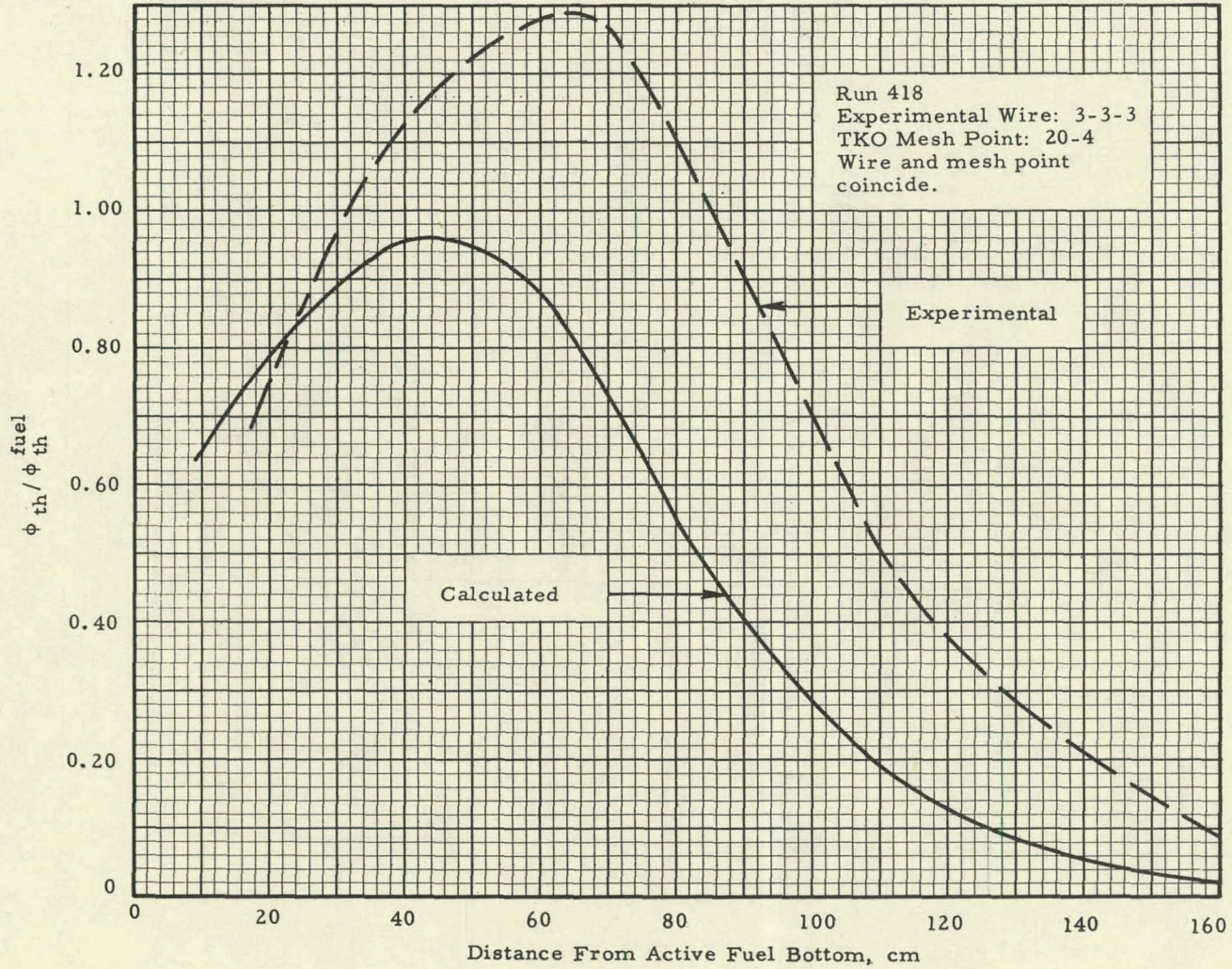


FIG. 91: AXIAL FLUX TRAVERSE

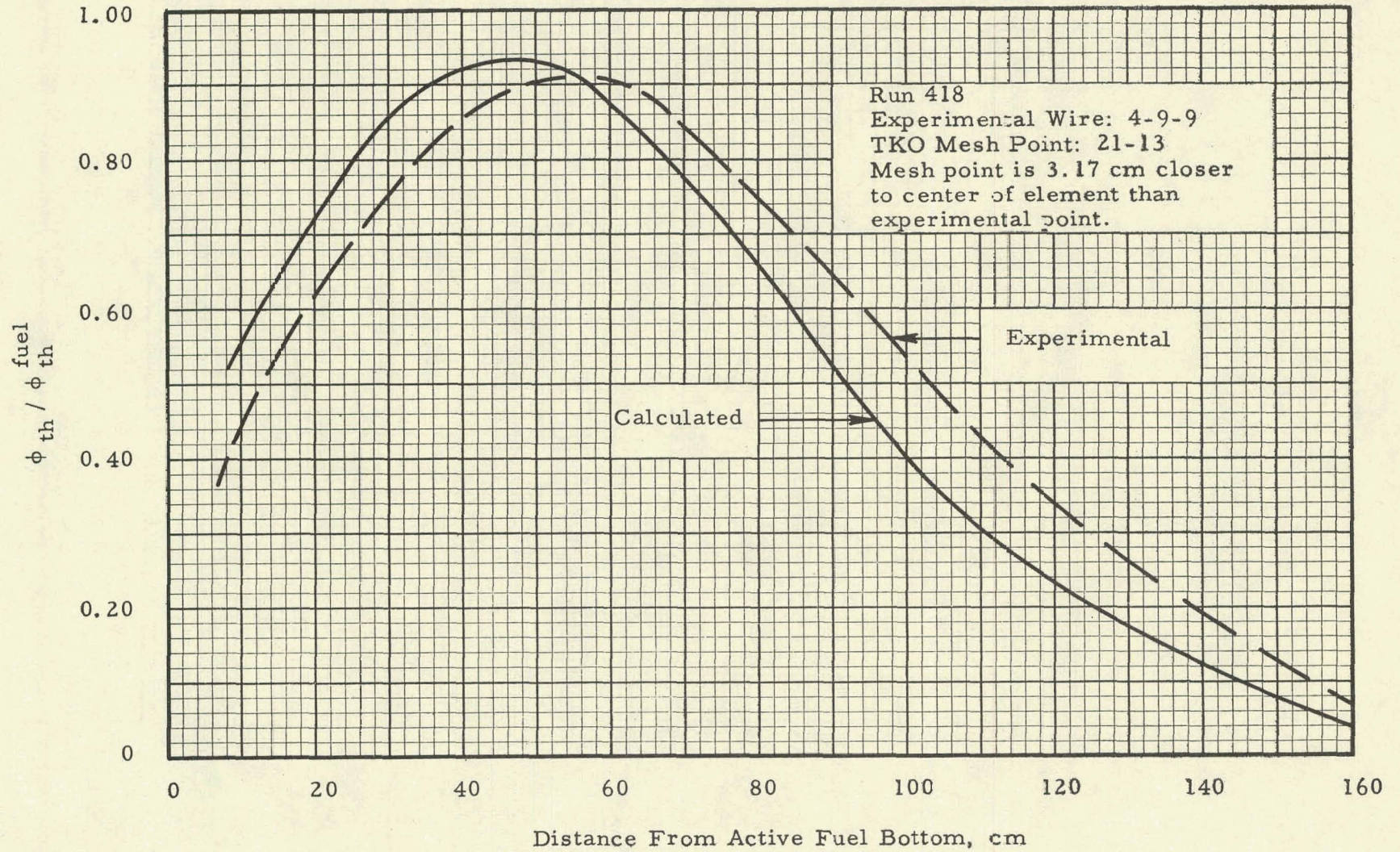


FIG. 92: AXIAL FLUX TRAVERSE

- 69I -

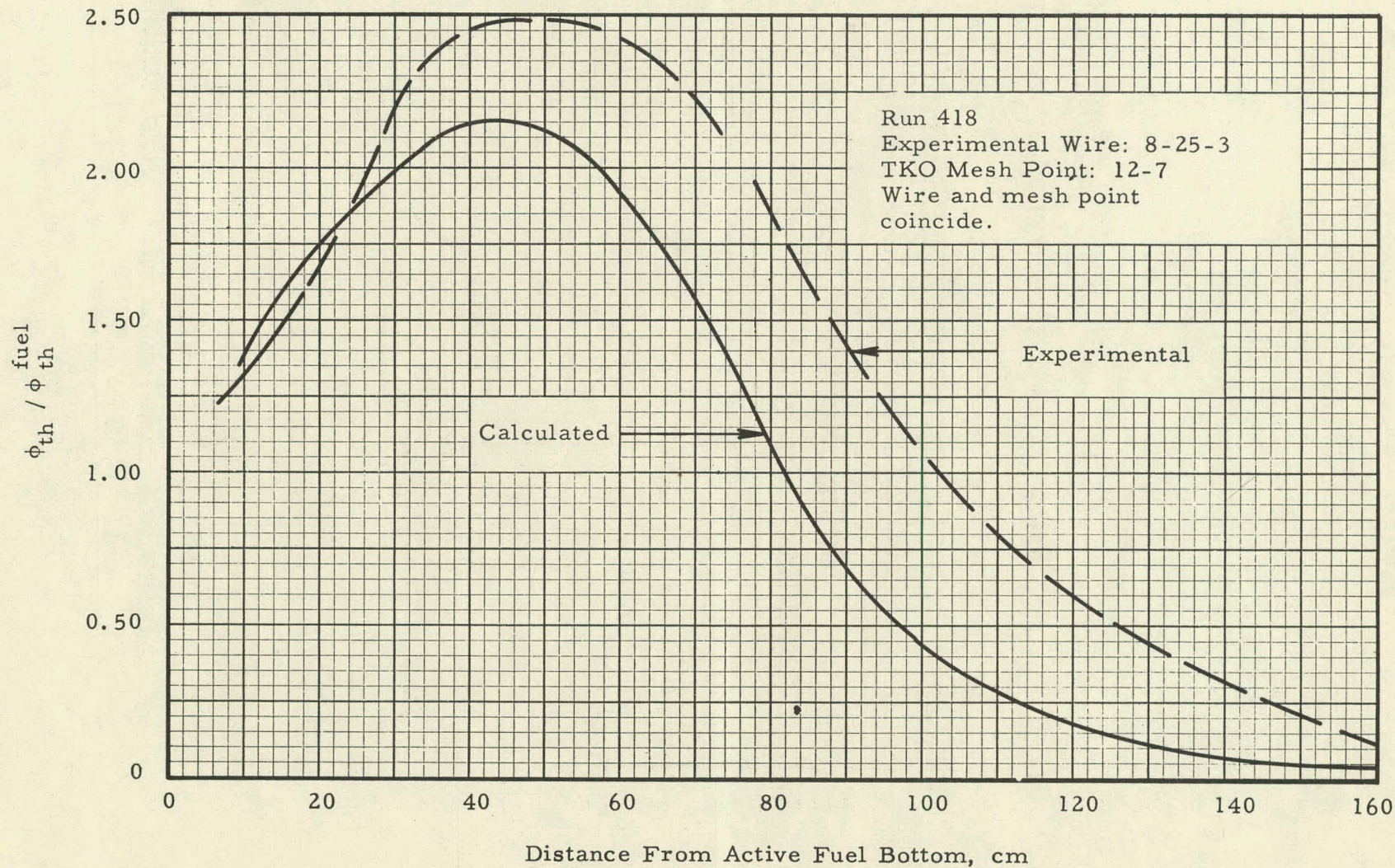


FIG. 93: AXIAL FLUX TRAVERSE

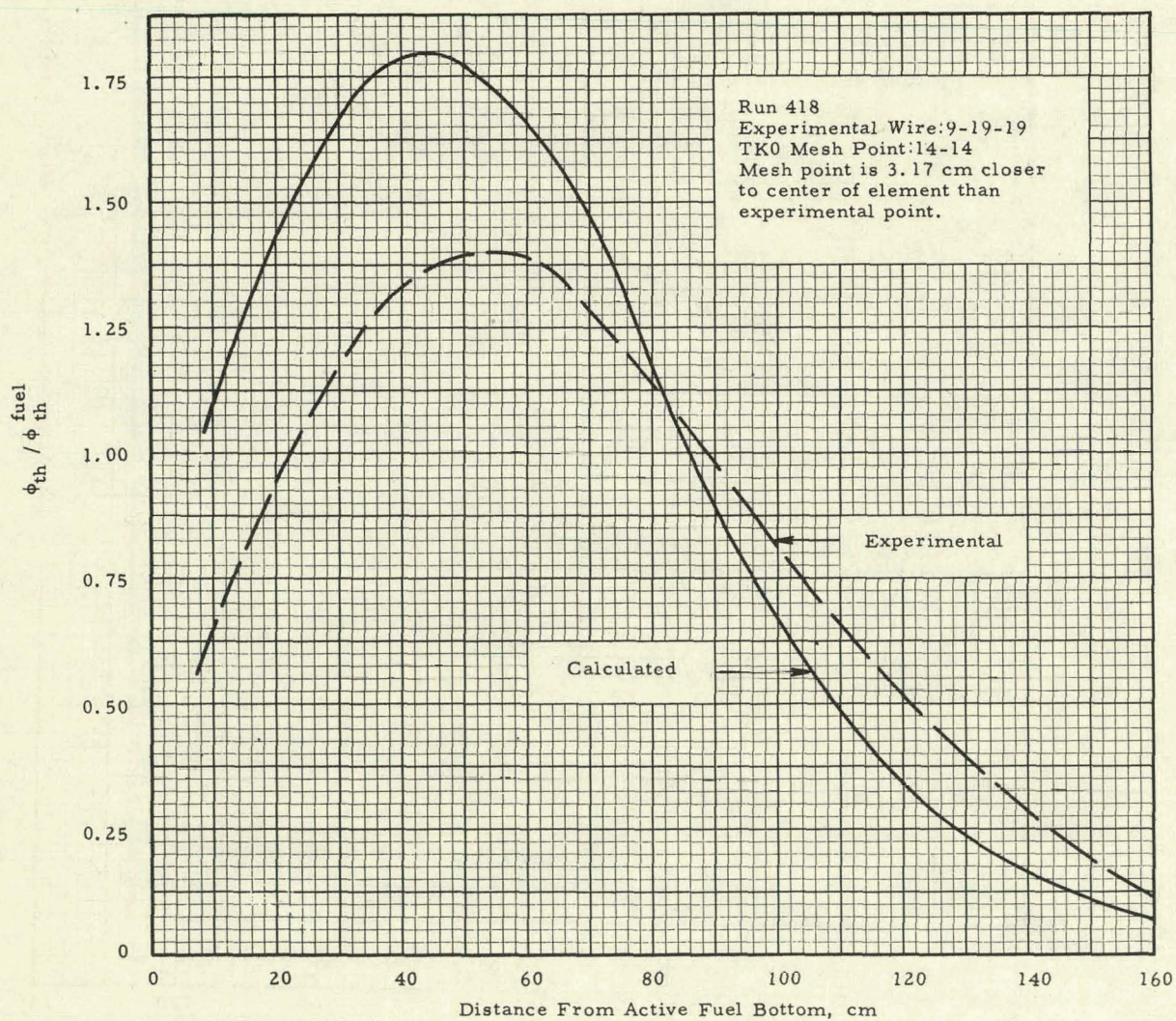


FIG. 94: AXIAL FLUX TRAVERSE

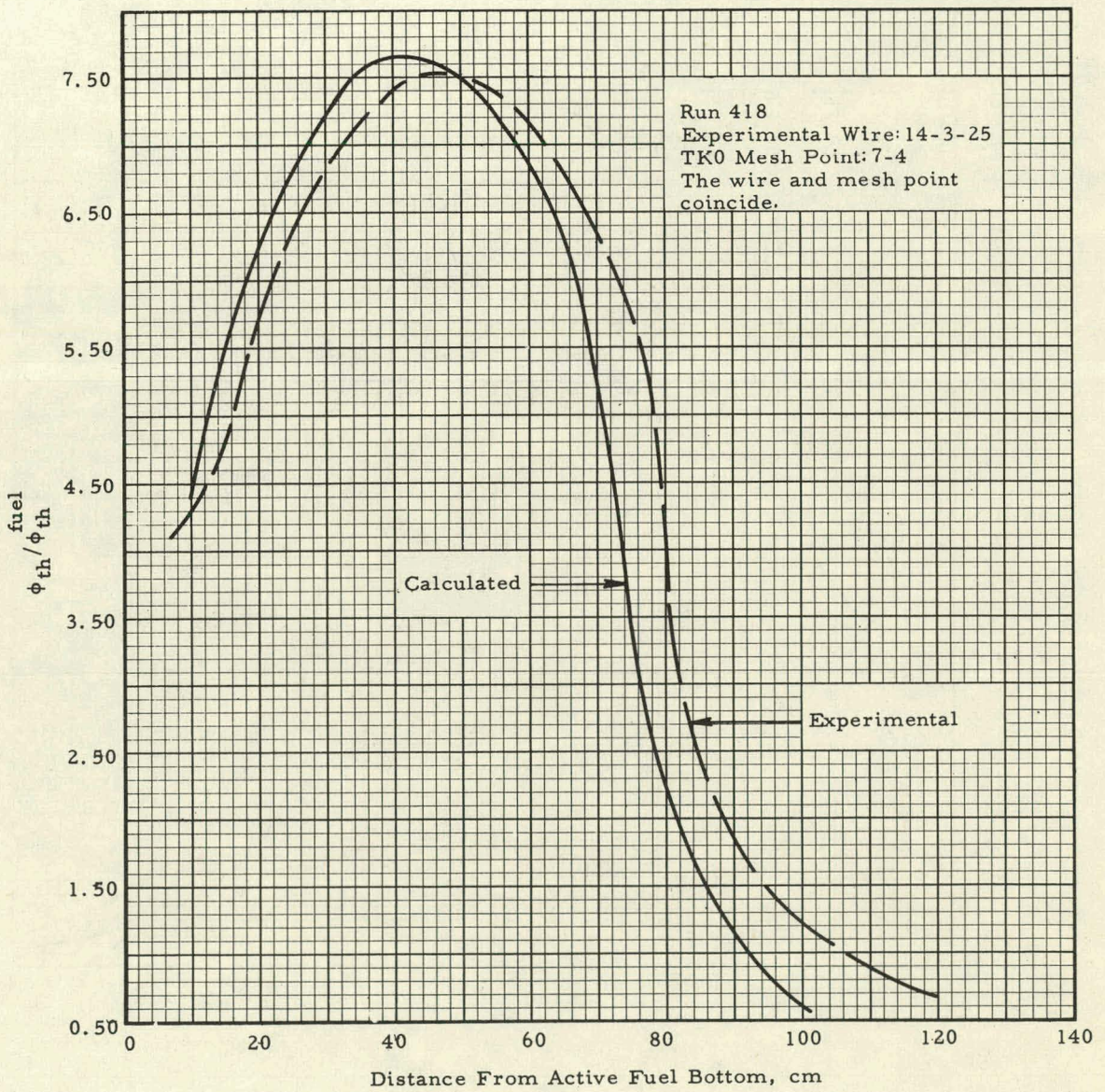


FIG. 95: AXIAL FLUX TRAVERSE

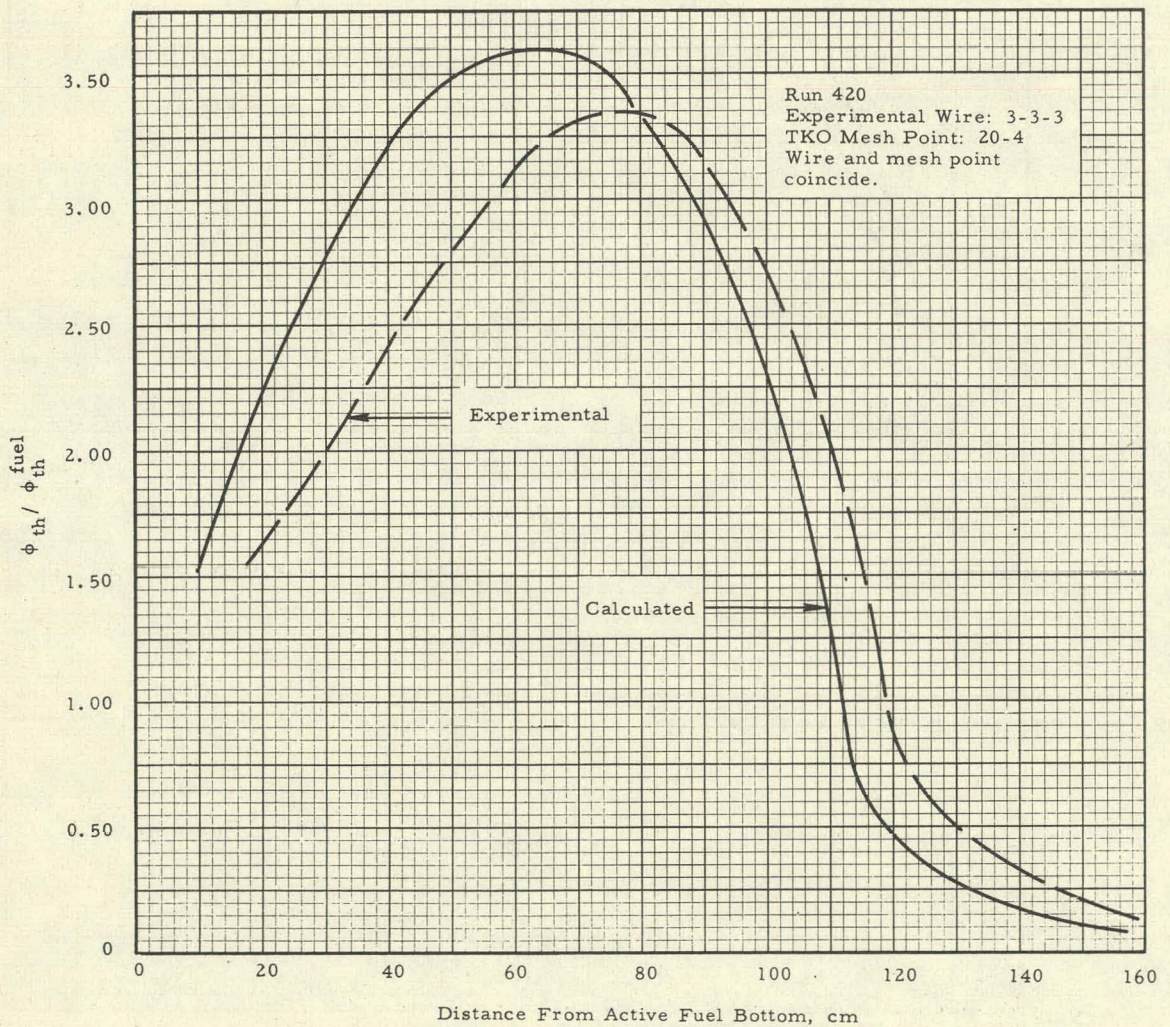


FIG. 96: AXIAL FLUX TRAVERSE

- 173 -

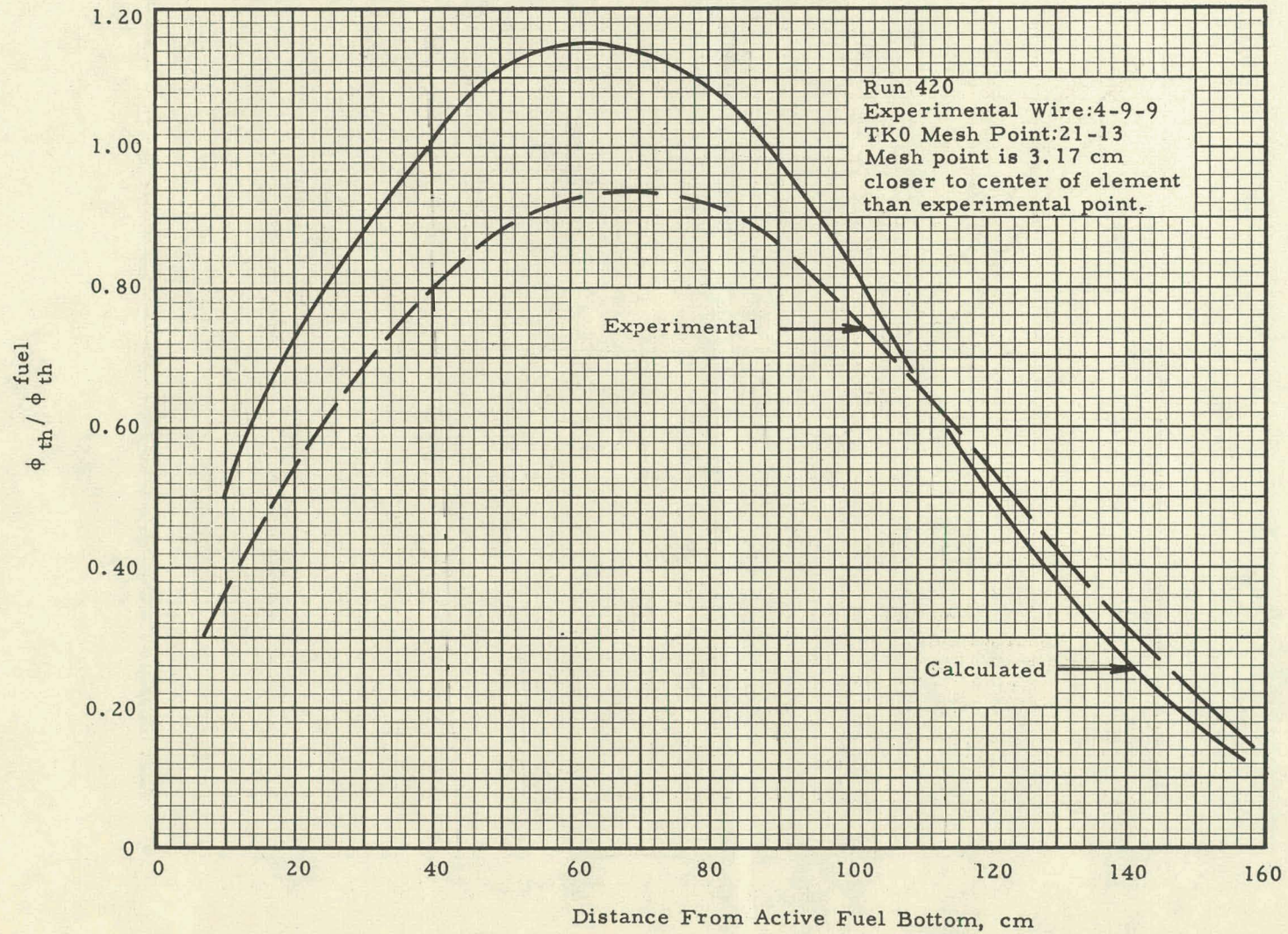


FIG. 97: AXIAL FLUX TRAVERSE

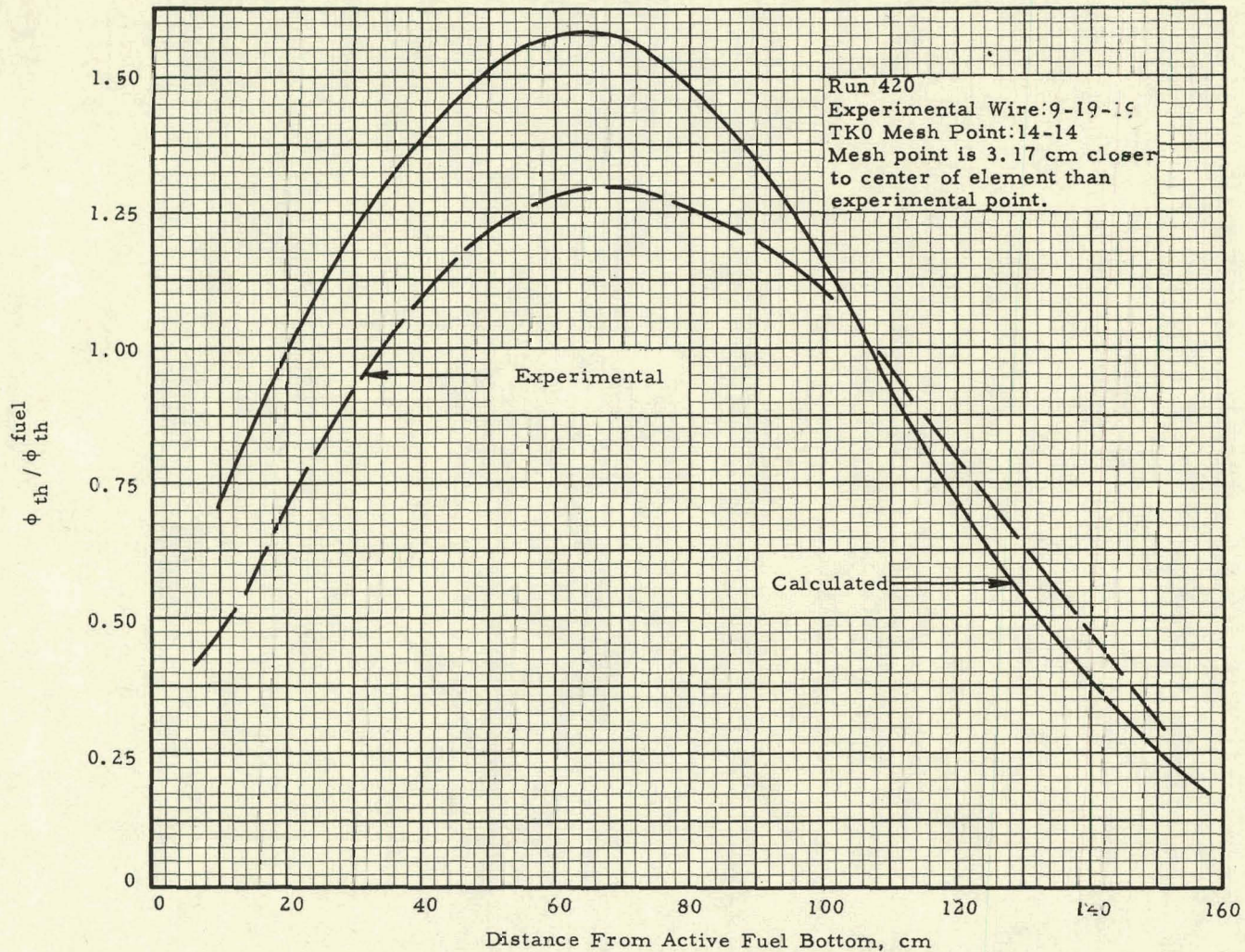


FIG. 98: AXIAL FLUX TRAVERSE

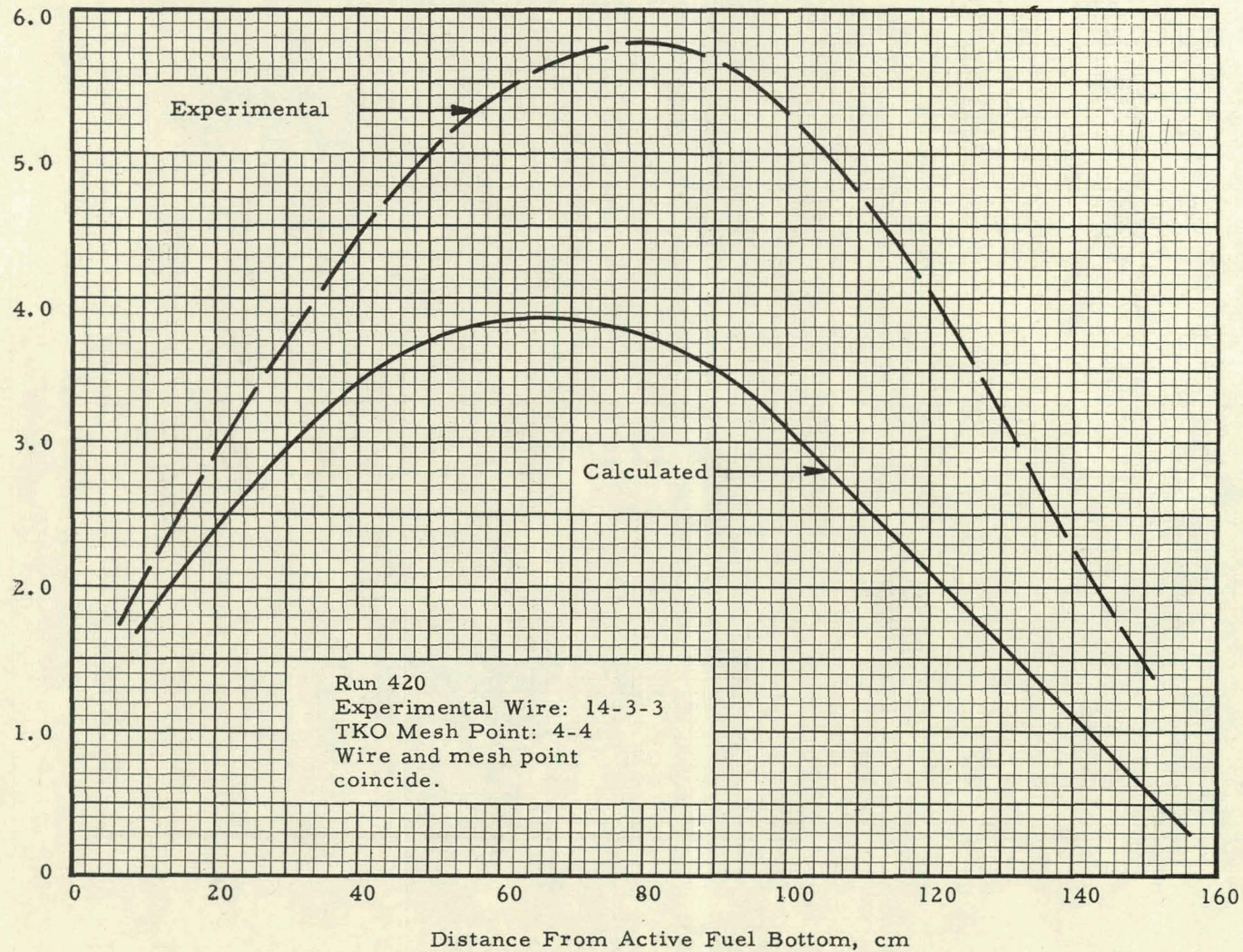


FIG. 99: AXIAL FLUX TRAVERSE

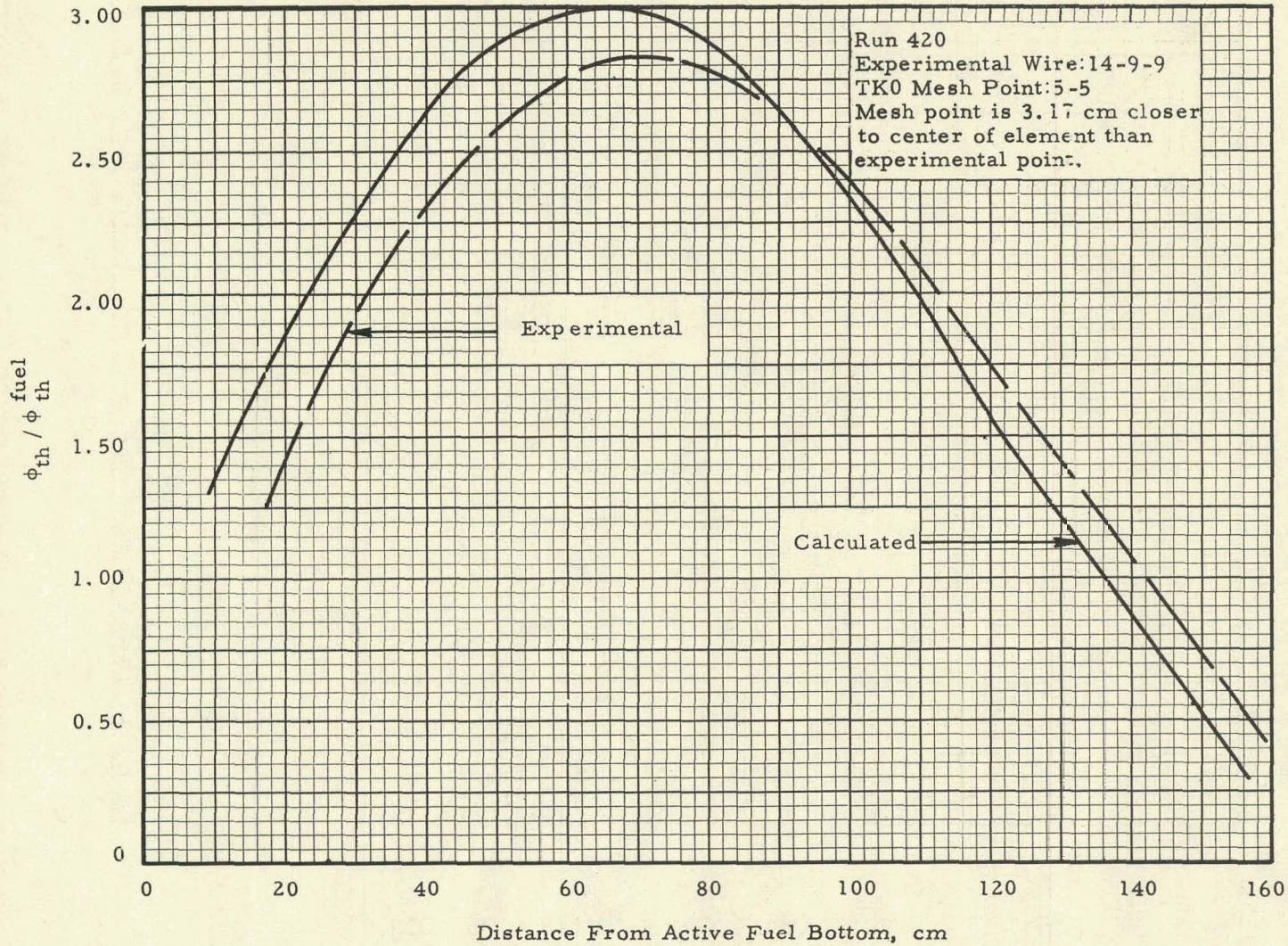
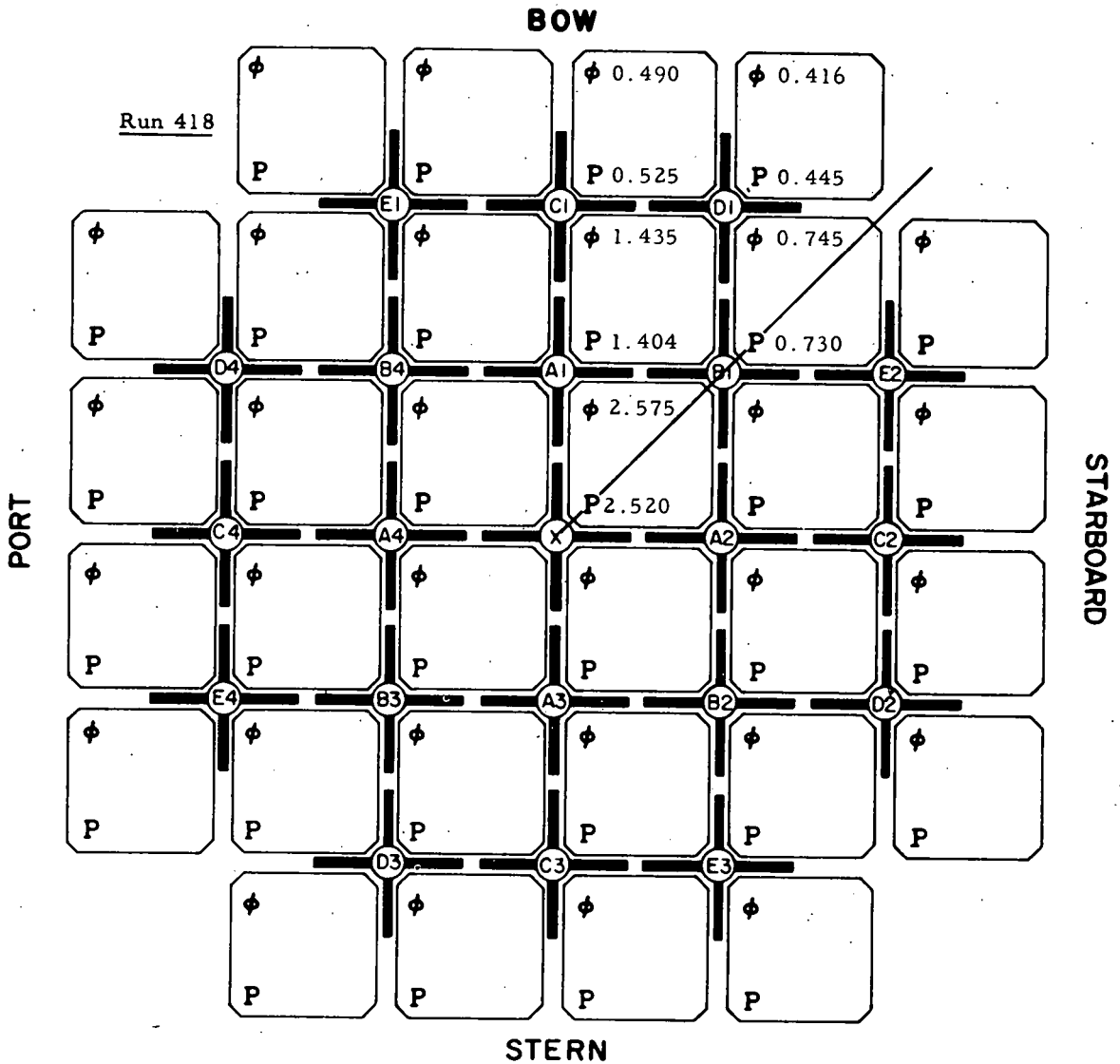


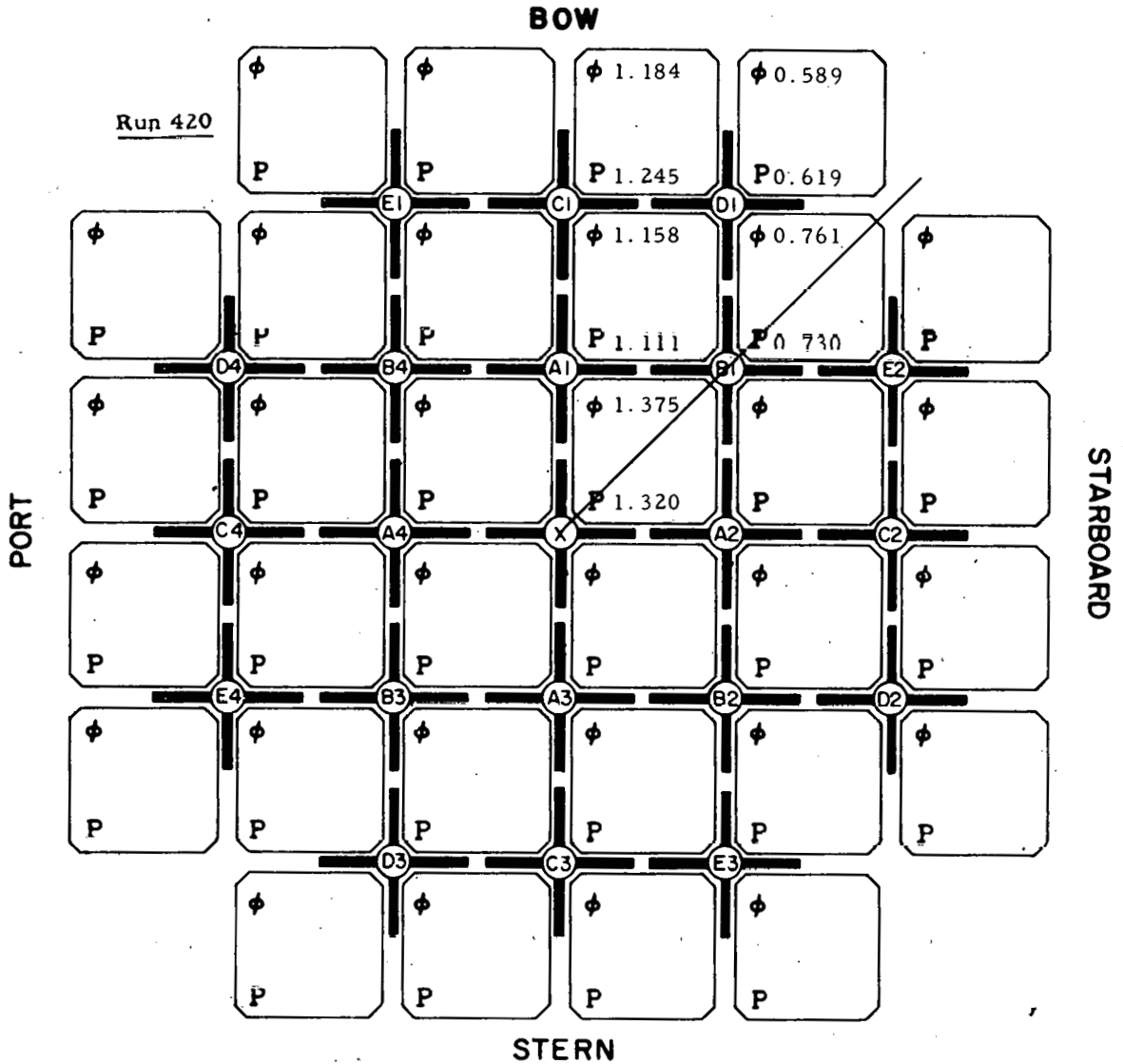
FIG. 100: CAN FLUX AND POWER AVERAGES



Rod Positions
(cm)

A1	79.0	B1	0	C1	0	D1	0	E1	0
A2	79.0	B2	0	C2	0	D2	0	E2	0
A3	79.0	B3	0	C3	0	D3	0	E3	0
A4	79.0	B4	0	C4	0	D4	0	E4	0
		X	0						

FIG. 101: CAN FLUX AND POWER AVERAGES



Rod Positions
(cm)

A1	0	B1	0	C1	108.0	D1	0	E1	0
A2	0	B2	0	C2	108.0	D2	0	E2	0
A3	0	B3	0	C3	108.0	D3	0	E3	0
A4	0	B4	0	C4	108.0	D4	0	E4	0
		X	150.0						

13. REFERENCES

REFERENCES

- ¹ Ball, R. M. and MacKinney, A. L., Nuclear Merchant Ship Reactor: Zero Power Tests - Core I, BAW-1202, The Babcock and Wilcox Company, Lynchburg, July 1960.
- ² Technical Manual for Nuclear Instrumentation and Safety Equipment - Volume I, NS SAVANNAH, Westinghouse Electric Corporation, East Pittsburgh, Pennsylvania.
- ³ Chapman, G. T. and Storrs, C. L., Effective Neutron Removal Cross Sections for Shielding, ORNL 1843, Oak Ridge National Laboratory, Oak Ridge Tennessee, 1955.
- ⁴ Weinberg, A. M. and Wigner, E. P., The Physical Theory of Neutron Chain Reactors, University of Chicago Press, 1958.
- ⁵ Heath, R. L., Scintillation Spectrometry - Gamma Ray Spectrum Catalogue, IDO-16408, Phillips Petroleum Company, Idaho Falls, Idaho.
- ⁶ Heath, R. L. and Schroeder, F., The Quantitative Techniques of Scintillation Spectrometry as Applied to the Calibration of Standard Sources, IDO-16149, Phillips Petroleum Company, Idaho Falls, Idaho.
- ⁷ Mortenson, J. H. and Ball, R. M., An Automatic Device for Power Mapping in Hetrogeneous Reactor Cores, Paper V-124, Joint Nuclear Congress, April 1959.
- ⁸ Nuclear Merchant Ship Reactor Project, Quarterly Technical Report, BAW-1124, The Babcock and Wilcox Company, Lynchburg, July-September 1958.
- ⁹ Caldwell, W. R., TKO, A Three Dimensional Neutron - Diffusion Code for the IBM-704, WAPD-TM-143, Westinghouse Electric Corporation, Bettis Field, Pittsburgh, Pennsylvania, 1959.

- ¹⁰ Hughes, D. J. and Harvey, J. A., Neutron Cross Sections
BNL-325, U. S. Atomic Energy Commission, 1955.
- ¹¹ Hodgman, C. D., et al., Handbook of Chemistry and Physics,
36th Edition, Chemical Rubber Publishing Company, Cleveland,
1954.